

Quantum transport through complex networks – from light-harvesting proteins to semiconductor devices



Dissertation

zur Erlangung des
Doktorgrades der Naturwissenschaften (Dr. rer. nat.)
der Fakultät für Physik
der Universität Regensburg

vorgelegt von
Christoph Kreisbeck
aus Lappersdorf
2012

Das Promotionsgesuch wurde eingereicht am 18.06.2012.

Die Arbeit wurde angeleitet von Dr. Tobias Kramer.

Prüfungsausschuss:	Vorsitzender:	Prof. Dr. John Lupton
	1. Gutachter:	Dr. Tobias Kramer
	2. Gutachter:	Prof. Dr. Thomas Niehaus
	weiterer Prüfer:	Prof. Dr. Milena Grifoni

Abstract

Electron transport through small systems in semiconductor devices plays an essential role for many applications in micro-electronics. One focus of current research lies on establishing conceptually new devices based on ballistic transport in high mobility AlGaAs/AlGa samples. In the ballistic regime, the transport characteristics are determined by coherent interference effects. In order to guide experimentalists to an improved device design, the characterization and understanding of intrinsic device properties is crucial. We develop a time-dependent approach that allows us to simulate experimentally fabricated, complex device-geometries with an extension of up to a few micrometers. Particularly, we explore the physical origin of unexpected effects that have been detected in recent experiments on transport through Aharonov-Bohm waveguide-interferometers. Such interferometers can be configured as detectors for transfer properties of embedded quantum systems. We demonstrate that a four-terminal waveguide-ring is a suitable setup for measuring the transmission phase of a harmonic quantum dot.

Quantum effects are not restricted exclusively to artificial devices but have been found in biological systems as well. Pioneering experiments reveal quantum effects in light-harvesting complexes, the building blocks of photosynthesis. We discuss the Fenna-Matthews-Olson complex, which is a network of coupled bacteriochlorophylls. It acts as an energy wire in the photosynthetic apparatus of green sulfur bacteria. Recent experimental findings suggest that energy transfer takes place in the form of coherent wave-like motion, rather than through classical hopping from one bacteriochlorophyll to the next. However, the question of why and how coherent transfer emerges in light-harvesting complexes is still open. The challenge is to merge seemingly contradictory features that are observed in experiments on two-dimensional spectroscopy into a consistent theory. Here, we provide such a theory based on a realistic model for the Fenna-Matthews-Olson complex. Up to now, realistic simulations of the two-dimensional spectra for large biomolecules have been out of computational reach. We overcome this limitation and establish an efficient algorithm using the new technology of graphics processing unit computation.

Contents

Introduction	1
I Energy transfer in light-harvesting complexes	12
1 Photosynthesis in green sulfur bacteria	15
2 The Fenna-Matthews-Olson (FMO) complex	19
2.1 Structure of the FMO complex	19
2.2 The Frenkel exciton Hamiltonian	21
3 Energy transfer dynamics in the FMO complex	25
3.1 Introduction	25
3.2 Theoretical description of the energy transfer	27
3.3 Hierarchical equation of motion (HEOM) approach	28
3.4 Energy funneling in the FMO complex	32
3.5 Weak coupling limit	37
3.6 Conclusion	38
4 Energy transfer efficiency	41
4.1 Introduction	41
4.2 Transfer and loss channel	42
4.3 Environment-assisted energy transfer	45
4.4 Trapping under the influence of non-Markovian noise	48
4.5 Optimal design of energy funneling in the FMO complex	51
4.6 Coherence and transfer efficiency	54
4.6.1 Introduction	54
4.6.2 Coherence measures and entanglement yield	56
4.6.3 Population beatings, coherence and transfer efficiency	56
4.6.4 Environmentally-induced redistribution of coherence	59
4.6.5 Summary	61
4.7 Conclusion and outlook	61

5	Two-dimensional spectroscopy	63
5.1	Introduction	63
5.2	Two-dimensional spectroscopy and its theoretical modeling	63
5.2.1	Experimental setup	63
5.2.2	Theoretical description	65
5.2.3	Two-exciton manifold	69
5.2.4	Rotational average over random orientations	70
5.3	Interpretation of 2d-echo spectra	72
5.3.1	Coherent dynamics	72
5.3.2	Dissipative dynamics	74
6	Entangled excitonic and vibrational dynamics	79
6.1	Introduction	79
6.2	Which oscillations are coherent and which are not	80
6.3	Bath-mediated quantum transport	82
6.4	Conclusion	84
7	Long-lived electronic coherence in the FMO complex	87
7.1	Introduction	87
7.2	Pure dephasing vs. relaxation rate	90
7.3	Implementing the HEOM approach on graphics-processing units .	92
7.4	Two-dimensional echo-spectra for the FMO complex	96
7.5	Static disorder	99
7.6	Transfer efficiency	102
7.7	Conclusion and outlook	103
II.	Ballistic transport through AlGaAs/GaAs semiconductor devices	105
1	Basic concepts of mesoscopic transport	107
2	A time-dependent approach for mesoscopic transport	111
2.1	Introduction	111
2.2	Wave-packet propagation and transmission amplitudes	113
2.3	Gaussian wave-packets and thermal electrons	118
2.3.1	Introduction	118
2.3.2	Relation between energy and momentum representation . .	119
2.3.3	Thermal wave packet representation of electron transport .	122
2.4	Numerical propagation Schemes	126
2.4.1	Introduction	126
2.4.2	Split-operator method	127

2.4.3	Graphics processing unit (GPU) implementation	129
2.5	Conclusion	135
3	Four-terminal waveguide Aharonov-Bohm interferometer	137
3.1	Introduction	137
3.2	Continuous phase drift and π phase-jumps in four-terminal rings .	140
3.2.1	Introduction	140
3.2.2	Experimental setup	141
3.2.3	Numerical simulations	143
3.2.4	Results for the linear transport regime	149
3.2.5	The non-linear regime and comparison with experiments .	154
3.2.6	Conclusion	158
3.3	Transmission phase of a quantum dot embedded in an AB-ring . .	158
3.4	Summary	164
	Summary and outlook	167
	Appendix	171
A	Energy transfer in light-harvesting complexes	173
A.1	Microscopic picture of the Frenkel exciton Hamiltonian	173
A.1.1	The Born-Oppenheimer approximation	173
A.1.2	Exciton model for coupled BChls	175
A.1.3	Coupling to the vibrational environment	177
A.2	Masterequation approach	181
A.2.1	Full Redfield equations	181
A.2.2	Secular approximation	185
A.3	Combined Masterequation – HEOM approach (ME-HEOM) . . .	188
A.3.1	ME-HEOM formalism	188
A.3.2	Application of ME-HEOM to a dimer	190
B	Lead eigenstates in the presence of a magnetic field	193
	References	195

Abbreviations

1d	one-dimensional
2d	two-dimensional
2DEG	two-dimensional electron gas
AB	Aharonov-Bohm
BChl	Bacteriochlorophyll
CPU	central processing unit
FFT	fast Fourier transform
FMO	Fenna-Matthews-Olson complex
GBR	generalized Bloch-Redfield
GPU	graphics processing unit
GPU-HEOM	graphics processing unit implementation of HEOM
HEOM	hierarchical equation of motion
LHC	light-harvesting complex
QUAPI	quasi adiabatic path integral
RC	reaction center
SSE	stochastic Schrödinger equation
t-DMRG	time-dependent renormalization group
TCL	time-convolutionless

Introduction

We investigate quantum transport through complex networks for different transport regimes. Depending on the physical realization as well as the temperature, transport regimes range from a purely coherent dynamics up to a strongly dissipative one. Part one of the present thesis deals with dissipative systems in quantum mechanics, which go back to the pioneering work of Caldeira and Leggett in Ref. [1], who incorporate dissipation by coupling the system to a large reservoir with an infinite number of degrees of freedom. The interplay of coherent transport, as discussed in the second part of the thesis, and dissipation is a widely discussed topic in electron transport [2, 3, 4, 5, 6, 7] and quantum information [8, 9, 10, 11]. The latter exploits quantum effects to establish new computational devices. Since fragile quantum effects are sensitive to any source of noise, the challenge in the field of quantum information is to develop scalable experimental setups that minimize noise, and ensure long-lasting coherence. The requirements on experimental setups for possible applications in quantum information are summarized in the famous DiVincenzo criteria [12].

Quantum effects are present not only in artificial devices, but they are exploited in biological systems as well [13]. The sense of smell, for example, is based on phonon-assisted tunneling [14, 15], a pure quantum effect without classical counterpart. Furthermore, two-dimensional (2d) spectroscopy reveals long-lived quantum coherence in the process of photosynthesis [16, 17, 18, 19, 20]. Photosynthesis is one of the most important processes in nature, and has been studied intensely during the last decades [21, 22]. Today the structure of the involved proteins, the light-harvesting complexes (LHCs), is well-known [22], and available in the protein data-base [23]. Up to recently, energy transfer has been described by classical incoherent Förster theory [24]. The prospect that nature might actively use quantum mechanics in the process of photosynthesis has revised the picture of energy transfer in LHCs. Greg Scholes, who contributed to one of the first pioneering experiments [19], speaks enthusiastically of green quantum computers [25]. The evidence of long-lived coherence in photosynthetic systems may inspire future applications ranging from blueprints for artificial light harvesting devices [26] to the fabrication of new generations of solar cells. Yet the exact role of coherence in the process of photosynthesis remains to be understood.

We discuss the Fenna-Matthews-Olson (FMO) complex [27, 28], which is fre-

quently studied as a prototype for LHCs. The FMO complex is part of the photosynthetic apparatus of green sulfur bacteria [29, 30, 31]. It acts as energy wire, and connects a huge light harvesting antenna with the reaction center where the final steps of energy conversion into chemical energy take place. The energy dynamics of the FMO complex is described by a Frenkel exciton model [32]. Experimentally, the information about the energy transfer process is obtained by 2d-spectroscopy [33, 34, 35, 36, 37]. This experiment illuminates an ensemble of FMO complexes by four laser pulses. The first two pulses create initial electronic excitations in the FMO complex, while a third pulse probes the system after a certain delay time. The fourth pulse is used as a reference for the outgoing signal, which facilitates to detect the phase-information of the signal [35, 38]. Repeated measurements for different delay times give information about the dynamics in the exciton system. The 2d-spectra provide a two-dimensional map of exciton populations in the energy domain, where the transfer process manifests itself in a landscape of diagonal- and cross-peaks. The line-shapes of the peaks reflect the nature of the coupling of the excitons to the vibrational environment of the protein mask. The dynamics of the peaks with advancing delay time yields information about the energy transfer. A coherent energy transfer shows unambiguous signatures in the cross-peaks in form of oscillations whose frequencies are given by the location of the peak in the energy map of the 2d-spectra. Experiments by Engel *et al.* in Ref. [20] reveal such an oscillatory signal in the cross-peaks which lasts up to delay times of 1.8 ps at temperature of 77 K, and even at a physiological temperature of 277 K oscillations up to 0.3 ps are detected. Those oscillations are interpreted as experimental evidence for long-lasting electronic coherence. Similar experiments show long-lasting coherence for a wide class of LHCs [16, 17, 18, 19].

At ambient temperatures long-lasting coherence cannot be expected in large biomolecules. For instance, for the parameter regime of light-harvesting complexes, perturbative methods based on rate equations do predict only very short-lived coherence lasting at most up to 50 fs [39, 40]. This mismatch between the experimental observations and the theoretical predictions asks for new concepts and mechanisms that are able to explain the measured long-lived electronic coherence. One of the outstanding questions is how quantum coherence can prevail in large biomolecules embedded in noisy environments. In fact, the experimental observations seem to contradict each other. The long lasting coherence does neither go along with the broad peak-shapes of the spectra [41] nor with the observed fast energy relaxation that occurs on the picosecond time-scale [42].

Theoretical simulations of the experimental setup of the 2d-spectra are numerically demanding. To reduce computational costs many works [43, 44, 40, 45] study the population dynamics, which keeps track of the probability to find the electronic energy at a certain position within the FMO complex. However, the population dynamics is not directly accessible in experiments, and comparison

with measured 2d-spectra requires to simulate the highly sophisticated four-wave mixing setup of the 2d-dimensional spectroscopy. In this context Ishizaki and Fleming [43] predict long lived quantum beatings provided that the finite time scale of temporal correlated vibrations is included in the model. The present thesis extends the ideas of Ishizaki and Fleming, and develops efficient numerical schemes that allow us to simulate the full experimental spectroscopic setup, and to compute 2d-spectra for the FMO complex for the same parameter as in Ref. [43]. In fact, the finite time scale in the vibrational environment turns out to influence the experimentally detected signal in a non-trivial way. The model proposed by Ishizaki and Fleming, however, does not reproduce the experimentally reported long lived electronic coherence, as is shown independently by Hein, Kreisbeck *et al.* in Ref. [46] and Chen *et al.* in Ref. [47]. Another drawback of the model in Ref. [43] is that for numerical convenience the authors employ a Drude-Lorentz spectral density describing the phonon-mode dependent coupling of the exciton system to the continuum of vibrational modes of the FMO complex. As we elaborate in this thesis, a Drude-Lorentz spectral density is too simplified to cover the structured spectral density of the FMO complex [48]. In particular, the Drude-Lorentz spectral density shows significant deviations regarding the coupling of the exciton system to the low energy vibrational modes [48, 49]. We show that a realistic spectral density for the FMO complex carries along different physical mechanisms in the energy transfer dynamics.

Since the experimental results are difficult to explain within the framework of electronic coherence, Christensson *et al.* [50] propose that the oscillatory signal in the experimental 2d-spectra is attributed to few strongly coupled vibrational modes. Within this interpretation the 2d-spectra would be explained in terms of molecular vibrations rather than long lived electronic coherent dynamics. Similar arguments are put forward by Plenio *et al.* in Ref. [45]. Thus, quantum effects might be less relevant than hypothesized. However, the picture of few strongly coupled modes relies on the assumption that the vibrations are tuned to very specific frequencies, which contradicts experiments carried out in the group of Engel [51]. In experiments with mutants, the authors of Ref. [51] alter the vibrational frequencies of the FMO complex, but do not obtain a significant change in the detected signal.

Energy transfer in LHCs comprises several aspects, such as fast energy relaxation, protection of electronic coherence, and robustness against variations in the vibrational structure. In order to explain experiments they all need to be assembled into a big picture. All previously proposed models have in common that they are able to reproduce some aspects, but none of them gives a complete explanation of the relevant physics. In this thesis we establish a mechanism that predicts long lasting electronic coherence in LHCs. Our results prove that for realistic conditions of energy transfer in LHCs, long lasting electronic coherence prevails despite a strong dissipative coupling to a vibrational environment. The

mechanism we develop is based on the superohmic nature [48, 49] of the coupling to the vibrational environment of the FMO complex. We show that the suppressed pure dephasing rate supports prolonged electronic coherence, while coupling to a continuum of higher phonon modes ensures fast energy relaxation. Moreover, our model reproduces the experimentally observed peak-shapes in reasonable agreement. We predict that the experimental broad peak-shapes are dominated by inhomogeneous broadening, which is caused by averaging over an ensemble of many individual molecules that slightly vary in their structure [34]. Additionally, we demonstrate that specific strongly coupled modes do not yield a significant influence on the 2d spectra, which is in line with the experimental observation of Ref. [51]. In summary, we introduce a physical mechanism which protects electronic coherence in the exciton dynamics despite strong coupling to a dissipative environment. So, as mentioned above, our mechanism brings together different experimentally observed aspects of the energy transfer in the FMO complex.

The natural question arising from the experimental signatures that long lasting coherence emerges in biological systems is the following: In what ways is coherence useful for energy transfer in the process of photosynthesis? Considering the history of biological selection and evolution in nature it appears to be unlikely that quantum coherence is there just by chance, but might be actively exploited. The functional role of quantum coherence in LHCs is an active field, and many theoretical investigation have been developed in recent years [52, 53, 54, 55, 56, 57, 58, 59, 60, 61, 62]. One idea is that coherence might be used for a quantum search [57], like the Grover algorithm [63] developed in quantum information, to achieve a quantum speed-up of the energy transfer. However, in Ref. [61], Hoyer *et al.* show that such a quantum speed-up is only attained during the first 50 to 70 fs, while a longer lasting coherent dynamics does not yield any further improvement concerning the quantum search. Thus, the investigations of how LHCs benefits from long-long lived electronic coherence continue. One proposal is that coherent energy transfer is advantageous in overcoming energy barriers present in the energy pathways in LHCs [64]. Other works suggest that coherence is used to achieve robustness of fast energy transfer [58, 60] with respect to changes in the local environment of LHCs. In Ref. [62] the authors vaguely formulate the idea that coherence might be exploited for the regulation of the energy transfer process. However how exactly long lived coherence helps to optimize the transfer is not yet completely understood.

Aspuru-Guzik *et al.* [57, 52] and Plenio *et al.* [54, 55] independently show that the interplay of coherence and dephasing assists fast energy transfer in the FMO complex. The studies are based on simple rate equations, and do not include the finite time-scale of the vibrational environment, which is known to influence the transfer dynamics [65, 43]. In order to include the temporal correlations in the vibrations we perform realistic simulations going beyond rate equations

[52, 53, 54, 55, 56, 57, 58, 62]. So far it has not been clear how to simulate the energy transfer to the reaction center while accounting for higher phonon processes and temporal correlations in the vibrational environment. We develop a hybrid approach where temporal correlations in the vibrations are incorporated but we assume that the irreversible trapping process in the reaction center, which is the final step of the transfer process, is based on the simpler to calculate master-equation formalism [3, 4]. The involved approximations for the trapping are appropriate, since details in the trapping process are not known, and trapping is commonly incorporated phenomenologically [52, 54, 56, 62]. We investigate the optimal transport conditions of the FMO complex, which helps to learn how artificial light harvesting systems need to be designed to optimize their performance. In fact, the optimal transport is an elaborate balance of resonant coherent energy transfer, dephasing, and thermal relaxation. Additionally, we separate different aspects of noise assisted transport by analyzing the temperature dependence of the transfer efficiency.

From the technical point of view the difficulty is to perform accurate numerical simulations of the large biomolecules with the presently available numerical resources. Simulations based on an atomistic level including all atoms are far from the computational scope. Thus, effective Hamiltonians such as the Frenkel exciton model have been developed [32]. The parameters of the Hamiltonian are extracted from fits to experiments [66, 67, 68] in combination with atomistic structure based calculations [49, 69, 70]. The spectral density, describing the nature of the coupling of the exciton system to the vibrational environment, is known by fluorescence line narrowing experiments [48]. Microscopic molecular dynamics simulations in combination with electronic structure calculations by Kleinekathöfer *et al.* in Ref. [71] and Aspuru-Guzik *et al.* in Ref. [72] yield first theoretical simulations of the spectral density, but are in their early stages, and have not yet reached convergence. In the recent years different elaborate approaches, such as the small polaron transform by Olaya-Castro *et al.* Ref. [73], the stochastic Schrödinger equation (SSE) by Eisfeld *et al.* Ref. [74, 75], the quasi adiabatic path integral (QUAPI) approach by Thorwart *et al.* Ref. [44] or the time-dependent renormalization group (t-DMRG) approach by Plenio *et al.* Ref. [76, 45] have been employed to simulate the energy transfer dynamics in LHCs within the Frenkel exciton model. While the simpler to compute population dynamics is accessible with these approaches, the simulation of the experimental four-wave mixing setup for the 2d-spectra has been off the present computational capability.

In this thesis we use the hierarchical equations of motion (HEOM) technique developed by Tanimura and Kubo in Ref. [77]. HEOM incorporates higher phonon processes as well as the finite time scale of the dynamics in the vibrational environment of LHCs [43]. The optimal performance of HEOM is obtained for high temperatures where the leading term of the temporal bath correlation

is given by a single function with exponential decay. The rate of the decay of this function describes the time scale of correlated vibrational dynamics. For the energy transfer in LHCs the high temperature approximation is valid for the experimentally relevant temperatures between 77 K and 277 K, see Kreisbeck *et al.* in Ref. [78] and Ishizaki and Fleming in Ref. [43]. Typical physiological temperatures of energy transfer in LHCs range between 268 K and 313 K [79]. HEOM is applied by Schulten *et al.* in Refs. [80, 81] to understand the energy transfer in large LHCs such as light harvesting complex II or to study inter-complex excitation transfer in purple photosynthetic bacteria. Such numerical simulations of the energy transfer dynamics in large LHCs with the HEOM formalism are extremely challenging, and require sophisticated parallelization schemes implemented on multiprocessor CPUs of large super computers [81]. However, the CPU implementation suffers from bandwidth limitations, and the large communication overhead for the HEOM approach sets strong limitations on the number of CPU-cores where parallelization remains efficient [81].

In this work we overcome the hardware restriction of CPUs by using the new technology of GPU (graphics processing unit) computing. We develop an elaborate algorithm utilizing the 448 streaming processors provided by the NVIDIA C2070 graphics board. GPU-HEOM scales linearly with the number of available streaming processors resulting in a 448-fold reduction of computation time. We obtain an enormous gain in performance. Studies of the transfer efficiency for the FMO complex for a wide range of parameters, for example, are done within hours of GPU computation time, while the same calculations would require several weeks on a single core CPU, Kreisbeck *et al.* Ref. [78]. Our GPU-HEOM algorithm opens a wide field for new opportunities to perform numerical simulations. Besides, investigations of the transfer efficiency within different regimes help to gain new insight into the underlying functional mechanisms. The GPU-HEOM provides an efficient implementation of the simulation of the experimentally measured 2d-spectra, see Hein, Kreisbeck *et al.* Ref. [46]. In particular, we extend the previous formulation of HEOM, which has been limited to a Drude-Lorentz spectral density, to more general structured spectral densities by employing the Meier-Tannor decomposition [82]. This allows us to investigate the role of specific strongly coupled vibrational modes to the transfer dynamics, see Kreisbeck and Kramer in Ref. [83]. To our knowledge, up to date, the GPU-HEOM is the only algorithm able to perform numerical simulations of 2d-spectra of experimental four-wave mixing signals of the FMO complex for a structured spectral density, while fully including higher order phonon processes and temporal correlations in the vibrations. This provides an efficient tool to study 2d-spectra, and to analyze the relevance of the continuous shape of the spectral density for prolonged coherence in LHCs.

The second part of this work is devoted to the investigation of electron trans-

port through AlGaAs/GaAs semiconductor heterostructures, which is governed by a transport regime different from the one underlying the energy transfer in LHCs discussed above. The process of photosynthesis is carried out at physiological temperatures so that the energy transfer is dominated by a strongly dissipative dynamics whereas in nano-electronics experiments are typically performed in dilution refrigerators at very low temperatures down to few milli-Kelvin. Another difference compared to biological systems is that experiments in semiconductor nano-electronics typically use rather pure samples. Sophisticated experimental techniques enable the fabrication of AlGaAs/GaAs based high mobility samples with large mean-free path up to 50 μm [84, 85, 86, 87, 88]. The mean-free path corresponds to the length scale where the electrons undergo a coherent motion without inelastic scattering. The mean-free path is typically larger than the extension of the device. As a consequence one observes ballistic electron transfer. In the ballistic regime, transport is dominated by coherent electron motion and elastic scattering at the device geometry. The transport characteristics are determined by sensitive interference effects. Thus, the theoretical simulation of ballistic electron transport requires an accurate modeling of the nanodevice geometry. In orthogonal micro-junctions, for example, such interference effects significantly influence the magneto transport leading to a negative Hall resistance [89] or the quenching of the Hall resistance for small magnetic fields [90, 91].

In AlGaAs/GaAs heterostructure the electron system is confined at the interface of the different layers along the direction perpendicular to the interface, and forms a two-dimensional electron gas (2DEG). A further confinement of the electron system to even lower dimensions is achieved in the device fabrication process by etching techniques or additional gate voltages [92, 93, 94]. This facilitates for instance the fabrication of quantum waveguides, quantum dots or quantum point contacts [92, 93, 94]. In fact, AlGaAs/GaAs based nano-devices show a rich variety of quantum effects. Some of the most prominent effects are the quantum Hall effect [95], conductance quantization in low-dimensional systems [96], magnetic focusing [97], and resonant tunneling [98, 99]. The idea of nano-electronics is to exploit quantum effects in semiconductor heterostructures, and to develop new devices such as single electron transistors [100] based on resonant tunneling. Ballistic transport offers the prospect of developing fast and low power consuming devices [101, 102, 103]. Possible applications range from side gated three terminal Y-junctions, which are used as switching devices [101], to quantum interference transistors [102]. Further magneto-ballistic effects are employed to design ballistic rectifiers [104].

Theoretical descriptions of ballistic transport are commonly based on the Landauer-Büttiker formalism [105, 106], where currents and voltages are expressed in terms of transmission amplitudes. The latter reflect the coherent scattering at the geometry of the device. A standard method to compute the transmission amplitudes is the recursive Green's function approach [107, 98].

These computations are numerically challenging. In recent years sophisticated implementations of the recursive Green's function algorithm [108, 109, 110, 111] have been developed, all of which speed up the algorithm. Nevertheless the recursive Green's function approach suffers from the problem that the transmission amplitude is attained for a single Fermi energy only, which makes it inefficient for experiments where the device characteristic is probed for a wide range of Fermi energies.

In this work we introduce a time-dependent approach based on wave-packet propagation. A related approach in mesoscopic transport is addressed in a recent article by Kramer, Heller and Parrott Ref. [112], who propagate a wave-packet pulse to describe experiments on magnetic focusing [97]. We extend concepts of quantum chemistry [113, 114, 115, 116, 117, 118] to ballistic transport, and show that the wave-packet propagation carries the information of the transmission amplitudes that are extracted by cross-correlation functions with suitable receiver wave-packets. The wave-packet approach yields several advantages for the simulation of ballistic electron transport in mesoscopic physics: (i) it gives efficient simulations of the transmission amplitudes for large and complicated multi-terminal devices geometries. For example in Kreisbeck *et al.* Ref. [119] we use the wave-packet approach to simulate the transmission amplitudes in four-terminal ring-structures with device sizes up to $3\ \mu\text{m} \times 2\ \mu\text{m}$. (ii) a single wave-packet propagation gives the energy-resolved transmission amplitudes for a large range of Fermi energies. (iii) the choreography of the propagated wave-packet reveals information about intrinsic scattering properties. (iv) the time-dependent approach is well-suited for GPU implementations. We develop an efficient GPU algorithm resulting in a 35-fold speed-up compared to a single-core CPU implementation. Recently, Krückl and Richter in Ref. [120] extended the time-dependent approach introduced here to describe transport in topological insulators.

We use the wave-packet approach to study ballistic transport in an Aharonov-Bohm (AB) interferometer. The AB effect is a pure quantum effect observed in double-slit like two-path interference devices [121]. The resulting interference pattern shows an oscillatory behavior. The period of these oscillations depends on the enclosed magnetic flux. The AB effect shows oscillations in the conductance measurements of waveguide-based ring-structures [122, 123, 124]. The pioneering work of Yacoby *et al.* in Ref. [125] has brought AB ring interferometers back into focus in mesoscopic physics. The authors of Ref. [125] propose that the AB interferometer can be configured as a detector of the transmission phase of a quantum dot that is embedded in one of the arms of the ring. While the transmission amplitude through quantum systems is accessible by means of conductance measurements, the AB interferometer offers the advantage of extracting additional phase information. Indeed, successive experiments by Schuster *et al.* in Ref. [126] and Avinun-Kalish *et al.* in Ref. [127] measure the transmission

phase of embedded quantum dots, which contributes to the phase of the AB oscillations. Following simple models such as the Friedel sum rule or the one-dimensional (1d) double barrier-well potential [128, 129], there is a continuous shift in the phase of the AB oscillations by π if the Fermi energy is scanned through a resonance of the quantum dot. Besides this continuous phase drift, the experiments [126, 127] show phase lapses of π between certain consecutive resonances, which have not been expected in the simple models mentioned above. For large occupation numbers of the quantum dot the phase lapses of π become universal, and appear between any consecutive resonance of the quantum dot. Those unexpected phase lapses have created a lot of interest. By now there are several theoretical investigations trying to understand the origin of the universal phase behavior [130, 131, 132, 133].

The first step toward a theoretical understanding of the complicated effects underlying the AB-setup with an embedded quantum dot is a characterization of the empty interferometer (without quantum dot). Not all quantum-ring setups are equally well-suited for measuring the transmission phase of quantum dots. For example, in two-terminal devices time reversal symmetry enforces phase rigidity, and the phase of the AB oscillations is restricted to 0 or π [122, 123, 124]. In this situation there is no continuous phase drift, while phase changes always appear in form of abrupt π phase-jumps. To overcome phase rigidity the experiments open the ring to additional terminals. In fact, for a suitable arrangement of current and voltage probes (non-local setup), four-terminal measurements in quantum waveguide rings by Kobayashi *et al.* in Ref. [134] show a continuous phase drift in the AB oscillations as function of the Fermi energy. However, for a different arrangement of current and voltage probes (local setup) there is no continuous phase drift, and the results resemble two-terminal measurements. The empty four-terminal interferometer shows complicated features in the phase of the AB oscillations, such as π phase-jumps that emerge both in the non-local and the local setup. The experimentally observed effects are universal, and detected in several experiments [135, 119, 103, 134]. The origin of these effects is not yet understood, and a profound microscopic understanding of four-terminal waveguide AB interferometers is inevitable. This may serve as a guideline for experimentalist to design improved setups.

In this thesis we provide accurate numerical simulations of the four-terminal waveguide rings. We use our wave-packet approach, which allows us to incorporate the 2d-potential landscape defining the device geometry. This way we manage to go beyond 1d-models [136, 137, 138, 139, 140, 141]. It turns out that the wave-packet approach is particularly well-suited for the problem at hand, since it simulates efficiently the scan through the Fermi energy. Our numerical simulations facilitate the comparison with recent experiments by Buchholz *et al.* in Refs. [142, 135, 119]. The idea of this experimental setup is to design an improved device that allows for a clear continuous phase drift in the AB oscil-

lations. Compared to previous experiments by Kobayashi *et al.* in Ref. [134] the device designed by Buchholz *et al.* in Refs. [142, 135, 119] is advantageous in several aspects [119]: (i) the ring is fabricated as a semi-circle, which breaks the symmetry in the path length of the two arms of the ring. This enables a continuous phase drift by changing the Fermi energy. (ii) the contacts feeding the leads are placed far away from the ring, and do not disturb the measurement setup. (iii) the electrons are injected into the ring via well-defined orthogonal cross-junctions to minimize reflections at the leads. Nevertheless, the improved design does not yield any improvement concerning the aim of avoiding abrupt π phase-jumps. Our numerical simulations reveal that the phase jumps are intrinsic features of the interference at the geometry of the four-terminal waveguide-ring. Multiple Fabry-Perot [143] like reflections in the arms of the ring result in resonances. Those resonances lead to a drastic change of the microscopic scattering properties of the cross-junction, which gives the experimentally detected abrupt π phase-jumps in the AB oscillations at certain Fermi energies. The back-coupling between resonances in the arms and the scattering of electron flow in the cross-junction is not captured in previous studies using 1d-models [136, 137, 138, 139, 140, 141].

Even though the empty AB waveguide rings show non-trivial interference effects, we demonstrate that devices like the one fabricated by Buchholz *et al.* in Refs. [142, 135, 119] are suited as transmission phase detectors, provided that there is a careful preparation of the setup. Indeed, we configure the AB interferometer as transmission phase detector, and place a harmonic quantum dot in one of the arms of the ring. To avoid disturbing multi-mode scattering we consider a transport regime where only two transversal modes of the waveguides contribute. The quantum dot couples to the ring via resonant tunneling. There is transport through both arms of the ring only if the Fermi energy hits a resonance of the embedded quantum dot. In the other cases one does not observe an AB interference pattern in the measured signal. The theoretical calculation is relevant to the experiments by Schuster *et al.* in Ref. [126] and Avinun-Kalish *et al.* in Ref. [127]. These experiments use a strongly confined quantum dot such that the magnetic flux does not penetrate the quantum dot. In this work we consider a different regime, and embed a less strongly confined harmonic quantum dot into the interferometer. This leads to a significant splitting of the energy levels of the quantum dot with increasing magnetic field. According to the Darwin-Fock spectrum [98] the individual resonances of the harmonic quantum dot at zero magnetic field split into several resonances corresponding to the angular momentum states for a finite magnetic field. In the resonant tunneling regime [107, 98, 99], the transmission phase undergoes a continuous π drift while scanning the Fermi energy through the resonances corresponding to the angular momentum states. Since the angular momentum states for the same main quantum number have the same parity, the transmission phase shows a phase

lapse of π between consecutive angular momentum states. The observed transmission phase behavior of the Darwin-Fock states is to some extent similar to the universal phase-behavior observed in Refs. [126, 127]. We perform numerical simulations for the AB interferometer with the embedded harmonic quantum dot. Our results demonstrate that the transmission phase of the Darwin-Fock spectra creates unambiguous features in the AB interference fringes as function of the Fermi energy. Precisely, the Darwin-Fock spectrum shows *cat's whisker* like interference pattern.

I Energy transfer in light-harvesting complexes

1 Photosynthesis in green sulfur bacteria

Photosynthesis converts sunlight into chemical energy and is one of the most important processes on earth. Worldwide, more than 100 billion tons of biomass [144] are produced each year and photosynthesis is the driving force in nature. Besides higher plants like trees and flowers 50 percent of the total photosynthesis is carried out by algae and Bacteria [145]. Cyanobacteria, purple bacteria, and green sulfur bacteria are among many others, the most prominent representatives of light-active bacteria [21]. The light absorbing pigments of photosynthetic bacteria are various bacteriochlorophylls (BChls) and carotenoids, which give the bacteria distinct colors, ranging from green and brownish-green to red and purple [21]. There are several types of BChls that have slightly different structures leading to variations in their absorption spectra. BChl *a*, for example, absorbs light in the infrared spectrum around 800 nm [146], whereas the absorption spectrum of BChl *c* [147] is similar to that of Chlorophylls. Chlorophylls are the light-active pigments of plants and show peaks in the absorption spectra for wavelength between 400 nm-500 nm (blue) and 600 nm-700 nm (red). This gives plants their unambiguous green color [148].

In the following, we are interested in the photosynthesis process of green sulfur bacteria. Green sulfur bacteria live under low light conditions and have evolved highly efficient strategies for catching available photons and storing the absorbed energy via chemical reactions in the form of chemical energy. Green sulfur bacteria are found in microbial mats around Octopus Springs in Yellowstone National Park [149, 150]. Recently, a brown-colored species of green sulfur bacteria was discovered in the Black Sea between 90 m and 120 m below the surface [151]. With their highly efficient photosynthesis system, green sulfur bacteria are perfectly adapted to a life under low light conditions where, on average, each BChl absorbs just a single photon in a period of approximately six hours [30]. Figure 1.1 shows a schematic sketch of the photosynthetic apparatus of green sulfur bacteria. The main functional building blocks [29, 30, 31] are the chlorosome antenna, where photons are absorbed and the reaction center (RC), where the energy is stored by chemical reactions. The reaction center protein is located in the membrane. Typically, there are about 50 reaction centers per chlorosome

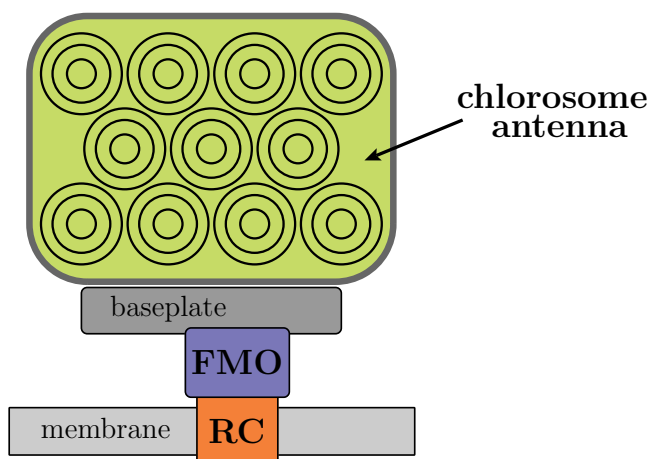


Figure 1.1: Sketch of the photosynthetic apparatus of green sulfur bacteria [29, 30, 31]. Light is absorbed in the huge chlorosome antenna which contains up to 250 000 BChl molecules. The absorbed energy creates electronic excitations in the BChls and accumulates in the baseplate. The latter is connected to the reaction center (RC) via the Fenna-Matthews-Olson (FMO) complex. The FMO complex acts as an energy wire and transfers the excitation energy with near-unity efficiency to the reaction center. In the reaction center, excitation energy is trapped by photochemical reactions and is stored in the form of chemical energy.

and, on average, 5,000 light absorbing BChls provide the energy for a single reaction center [31]. Plants only have 40 Chlorophylls per reaction center [152], which illustrates that green sulfur bacteria require an immense light harvesting antenna to collect photons under the extremely low light intensities. The BChls in the chlorosome antenna are organized by self-assembly and form cylindrical rods [31]. The cylindrical rods couple with each other and the electronic excitation is transferred within ~ 10 ps to the baseplate of the photosynthetic apparatus [31]. The baseplate is a dimer sandwich of CsmA-proteins containing BChl *a* molecules that form a two-dimensional crystalline structure [31, 29]. The baseplate is in contact with the Fenna-Matthews-Olson (FMO) complex, which finally transfers the energy to the reaction center. It is proposed [31] that the concept of coupling the reaction center to the baseplate via the FMO complex enhances the number of BChls that are linked to the reaction center. This yields a stronger connection between the antenna and the reaction center. Energy transfer through the FMO complex occurs with near unity efficiency [22] and almost the complete amount of excitation energy, accumulated in the baseplate, is transferred to the reaction

center.

In the reaction center, the photon energy induces a charge separation, forming an electrostatic potential $\Delta\Psi$ across the membrane. Predicted timescales for the process of charge separation in the reaction center range from 3 ps [152] to 25 ps [153]. Secondary electron donors and acceptors act as a proton pump and keep a proton gradient of ΔpH across the membrane, feeding an ATP circle [154], where energy is finally stored in the high-energy phosphate bonds of ATP [152, 153, 155].

2 The Fenna-Matthews-Olson (FMO) complex

2.1 Structure of the FMO complex

The FMO complex was discovered in 1962 by John M. Olson [27]. Roger Fenna and Brian W. Matthews resolved the structure of the FMO complex using X-ray crystallography with a 2.8 Å resolution [28]. A detailed analysis of the FMO complex was available in 1979 [156]. The structure of the FMO complex is listed in the protein data base [23]. For a review of the research history of the FMO complex, we refer the reader to Ref. [157].

The FMO complex is a trimer, composed of three identical subunits arranged around a three-fold symmetry axis. Since the different subunits only interact weakly with each other we restrict our studies to a single subunit. Each subunit contains seven coupled BChls, that are embedded in a protein mask formed by a polypeptide backbone. Fig. 2.1 illustrates the arrangement of the seven BChls within a single subunit [69]. Not much is known about the microscopic mechanisms of the linking of the FMO complex to the antenna and the reaction center, and the question of exactly which BChls are involved is still an open issue. Theoretical studies [69, 49] predict BChl 3 and BChl 4 to be the BChls with the lowest excitation energies. Therefore the BChl 3 side of the FMO complex is expected to be located close to the reaction center to enable energy funneling. Experimental evidence for the orientation of the FMO complex is given in 2009 by Wen et al. in Ref. [158], in which the authors confirm that the BChl 3 side of the protein interacts with the reaction center, while the BChl 1 side is in contact with the baseplate of the chlorosome antenna. Previous theoretical works [52, 59, 62] assume a strong interaction of BChl 3 with the reaction center and link BChl 1 and BChl 6 to the antenna. The energy to excite the electronic configuration of the BChls of the FMO complex is around the wavelength of 800 nm and is therefore in the infrared range. Under physiological conditions, the energy to create an initial excitation within the FMO complex is provided by the baseplate. The BChls are coupled via dipole-dipole interactions and the electronic excitation moves through the FMO complex [32]. Finally, energy is

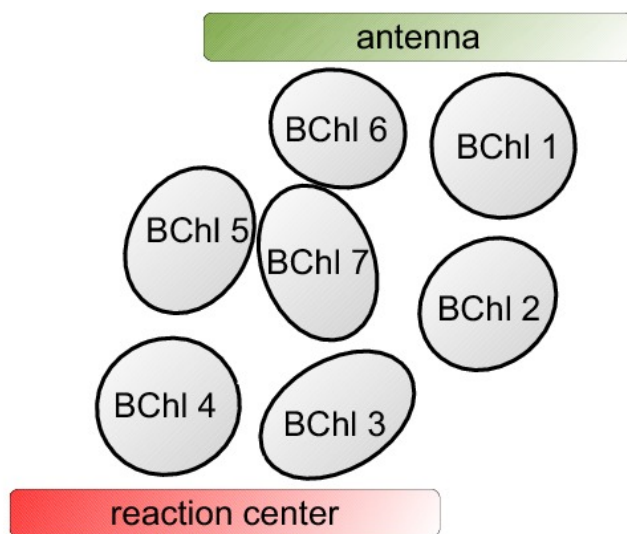


Figure 2.1: Arrangement of the seven core BChls of a single subunit of the FMO trimer. Initial excitations enter the FMO complex from the antenna either at BChl 1 or BChl 6. The BChls are coupled to each other and energy is transferred through the FMO complex to BChl 3 and BChl 4. These BChls are close to the reaction center where the excitation energy induces a charge separation. Recently, an eighth BChl has been discovered [159, 160] that is located close to the baseplate. It is suggested that this additional BChl enhances the coupling of the seven core BChls to the baseplate [159, 160, 40].

transferred to BChls 3 and 4. These are in contact with the reaction center where the energy is trapped.

The BChls are embedded in a protein environment and depending on the local structure of the protein mask, the electronic configuration varies from BChl to BChl. Quantum chemistry computations, based on time-dependent density functional theory in combination with classical electrostatics, yield theoretical predictions for the site energies and the coupling strengths between the BChls [69]. Peptide α -helices are responsible for BChl 3 having the lowest excitation energy [69]. The protein environment modulates the electronic properties of the BChls, which are tuned to yield fast energy transfer to the reaction center. To what extent the FMO complex has developed optimal transfer conditions is discussed in detail in chapter 4.

Novel structural analysis based on X-ray diffraction reveals an eighth BChl in the FMO complex. The eighth BChl is located in a cleft on the surface of the FMO complex and closes the gap between the baseplate and the seven core

BChls [159, 160]. The excitation energy of the eighth BChl has been extracted by theoretical simulations, taking into account the crystal structure on an atomistic level [40]. The excitation energy of the eighth BChl is reported to be the highest one. Since the eighth BChl is located close to the baseplate, it is suggested that the presence of the additional BChl enhances the interaction with the chlorosome antenna. We only include the eighth BChl on an elementary level. We assume that the additional eighth BChl acts as a linker between the baseplate and the seven core BChls, and distributes the initial excitation energy from the baseplate to BChl 1 or 6. For spectroscopic studies, the FMO complex is isolated from the chlorosome antenna and the reaction center. During this preparation procedure the loosely bound BChl 8 gets detached in most cases, and the BChl 8 is only present in 35% of the FMO complexes in the sample [40]. Hence, it is sufficient to consider the seven core BChls of the FMO complex for simulations of experimental spectra, the subject of chapters 5, 6 and 7.

2.2 The Frenkel exciton Hamiltonian

Theoretically, an atomistic model and an ab initio treatment of the energy transfer in LHCs describing the dynamics in full detail is computationally much too expensive. We use an effective description of the exciton dynamics within a Frenkel exciton Hamiltonian [32, 161, 162, 163]

$$\mathcal{H} = \mathcal{H}_{\text{ex}} + \mathcal{H}_{\text{phon}} + \mathcal{H}_{\text{ex-phon}} + \mathcal{H}_{\text{reorg}}. \quad (2.1)$$

The basic concepts of the microscopic picture behind the Frenkel Hamiltonian is given in Appendix A.1. The total Hamiltonian is composed of the exciton system \mathcal{H}_{ex} , the motion of the nuclei is modeled by harmonic vibrations $\mathcal{H}_{\text{phon}} = \sum_{m,\xi} \hbar\omega_{\xi,m} b_{\xi,m}^\dagger b_{\xi,m}$ and coupling terms between the exciton and vibrational degrees of freedom are expressed by the last two parts. We assume low light conditions where there is at most a single electronic excitation present in the coupled BChls. For a system with N BChls, the exciton Hamiltonian reads

$$\mathcal{H}_{\text{ex}} = \sum_{m=1}^N \varepsilon_m^0 a_m^\dagger a_m + \sum_{m>n} J_{mn} (a_m^\dagger a_n + a_n^\dagger a_m), \quad (2.2)$$

where a_m^\dagger (a_m) is defined as the creation (annihilation) operator of electronic excitations at BChl m . The state $|m\rangle = a_m^\dagger|0\rangle$ corresponds to an electronic excitation at BChl _{m} while the electronic configuration of all other BChls remains in the ground state. The state $|0\rangle$ is defined as the ground state without any electronic excitations (all BChls are in the electronic ground state). The energy required to create an electronic excitation is denoted by ε_m^0 . Electronic

excitations also induce molecular vibrations leading to the reorganization energy

$$\mathcal{H}_{\text{reorg}} = \sum_{m=1}^N \lambda_m a_m^\dagger a_m. \quad (2.3)$$

The reorganization energy is the energy that is dissipated in the protein environment to relax the vibrational coordinates to their new equilibrium configuration [32]. More details are given in Appendix A.1.3. We denote an electronic excitation at BChl m as a population of site m with corresponding site energy $\varepsilon_m = \varepsilon_m^0 + \lambda_m$. Dipole-dipole couplings between different BChls yield the inter-site couplings J_{mn} giving rise to delocalization of the excitation energy over all BChls. Information about the site energies and inter-site couplings can be extracted from fits to measured linear absorption spectra [164, 49, 68, 67].

We assume a linear coupling of the exciton system to the vibrational environment

$$\mathcal{H}_{\text{ex-phon}} = \sum_{m=1}^N V_m B_m, \quad (2.4)$$

with

$$V_m = a_m^\dagger a_m \quad \text{and} \quad B_m = \sum_{\xi} \hbar \omega_{\xi,m} d_{\xi,m} (b_{\xi,m}^\dagger + b_{\xi,m}). \quad (2.5)$$

The exciton-phonon coupling term originates from a vertical Franck-Condon transition between the potential energy surface of the electronic ground and the electronic excited state of the BChls. A detailed microscopic derivation and physical interpretation of the Frenkel exciton Hamiltonian is given in Refs. [32, 163]. The basic concepts are also summarized in Appendix A.1.

The parameters of the Frenkel exciton model for the FMO complex are extracted from fits to experimental data [66, 67, 68] in combination with crystal structure-based calculations [49, 69, 70]. The FMO complex is a part of the photosynthetic apparatus of green sulfur bacteria. During evolution, different species of green sulfur bacteria have emerged [21, 165]. The most prominent representatives of green sulfur bacteria are *C. tepidum* and *P. aestuarii*. The structure of the FMO complex of both bacteria is slightly different [49]. In the following, we use the parameter for *C. tepidum* given in Ref. [49] (table 4 (trimer column) and table 1 (column 4)) listed in Table 2.1. The extracted parameters for the Frenkel Hamiltonian depend on the theoretical model used. In the literature there are several numerical simulations resulting in slightly different site energies and inter-site couplings [68]. The parameters of the FMO complex are special in the sense that all parameters are of the same order of magnitude. For example, the difference in site energies $\varepsilon_m - \varepsilon_n$ and the inter-site couplings J_{mn} are in the same range as the reorganization energy $\lambda \approx 40 \text{ cm}^{-1}$ [49, 43]. Even the thermal activation energy $k_B T = 200 \text{ cm}^{-1}$ for $T = 300 \text{ K}$ is of the same

	BChl ₁	BChl ₂	BChl ₃	BChl ₄	BChl ₅	BChl ₆	BChl ₇
BChl ₁	12410	-87.7	5.5	-5.9	6.7	-13.7	-9.9
BChl ₂	-87.7	12530	30.8	8.2	0.7	11.8	4.3
BChl ₃	5.5	30.8	12210	-53.5	-2.2	-9.6	6.0
BChl ₄	-5.9	8.2	-53.5	12320	-70.7	-17.0	-63.3
BChl ₅	6.7	0.7	-2.2	-70.7	12480	81.1	-1.3
BChl ₆	-13.7	11.8	-9.6	-17.0	81.1	12630	39.7
BChl ₇	-9.9	4.3	6.0	-63.3	-1.3	39.7	12440

Table 2.1: The exciton Hamiltonian in the site basis in units of cm^{-1} . Bold font denotes the dominant inter-site couplings and site energies. Values are taken from [49]. The entries at line BChl_m and row $\text{BChl}_{m'}$ correspond to matrix elements $\langle m | \mathcal{H}_{\text{ex}} | m' \rangle$. The extracted site energies and inter-site couplings depend on the theoretical model used. There are several numerical simulations for the FMO complex which all predict slightly different site energies and inter-site couplings [68].

order of magnitude. That is, there is no small parameter that can be treated as a perturbation. Thus, numerical simulations of the transfer dynamics in the FMO complex require a non-perturbative approach [166]. More details about the energy transfer dynamics and the comparison with approximative theories based on second-order perturbation theory are given in chapter 3.

3 Energy transfer dynamics in the FMO complex

3.1 Introduction

The exciton system \mathcal{H}_{ex} is not isolated and couples to a vibrational environment. This gives rise to an energy exchange between excitonic and vibrational degrees of freedom and induces dephasing, dissipation and energy relaxation in the transfer dynamics [32]. In quantum mechanics dissipation is studied theoretically within a reduced density operator formalism [32, 3]. The reduced density operator describes the state of the exciton system and is obtained after averaging out the vibrational degrees of freedom. In site basis $\mathcal{B} = \{|m\rangle\}$ the reduced density operator is represented by localized electronic excitations at BChl m . The population dynamics, that is the time evolution of the diagonal entries of the reduced density matrix in the site basis, highlights the energy flow among the coupled BChls within light-harvesting complexes (LHCs) while the off-diagonal elements stand for the amount of coherence and delocalization within the exciton system [32]. An alternative basis set for the reduced density operator is given in terms of exciton eigenstates $\mathcal{B}_{\text{ex}} = \{|E_M\rangle\}$ with $\mathcal{H}_{\text{ex}}|E_M\rangle = E_M|E_M\rangle$.

The aim of this chapter is to provide theoretical techniques to explore the energy transfer in the FMO complex. A standard approach is given by the master-equation formalism [32, 3, 4], which is based on second-order perturbation theory with respect to the exciton-phonon coupling. Additionally, the master-equation formalism relies on the Markov approximation. The Markov approximation follows the assumption that the reorganization process is fast and that the vibrational coordinates relax instantaneously to thermal equilibrium [32, 166]. In this case, the temporal correlations in the vibrations are given by a Dirac delta function and the time evolution of the reduced density operator is expressed in terms of rate equations commonly referred to as Redfield equations [32]. A further simplification entails the secular approximation in which the rate equations attain Lindblad form [32, 3]. The advantage of the Redfield and the related Lindblad equations is that they are simple to handle, numerically easy to implement, and computationally efficient. This makes these approaches popular and they are

widely applied to energy transfer in LHCs [54, 57, 62, 167, 168, 169, 56].

However for the energy transfer process in LHCs, the parameters of the exciton-phonon coupling leave the range of validity of the Redfield equations [166]. For the FMO complex, phonon relaxation times are reported to be in the range between 35 fs [43] and 166 fs [39], which is of the same timescale as the exciton dynamics. Therefore, temporal correlations in the vibrations influence the energy transfer process [43, 170]. Moreover, the coupling strength between excitons and vibrations, quantified by the reorganization energy $\lambda = 35 \text{ cm}^{-1}$ [39], is large, and theoretical simulations have to go beyond second order perturbation theory. In section 3.3 we introduce the hierarchical equation of motion (HEOM) technique established by Tanimura and Kubo [77] and developed further in Refs. [171, 172, 173, 174, 175, 176, 177]. HEOM is a non-perturbative approach that properly incorporates higher-order phonon processes and temporal correlations in the phonon environment. The HEOM approach works best at physiological temperatures relevant for studying the functional role of LHCs. HEOM relies on a second-order cumulant expansion that is exact for a harmonic bath. In its original version, HEOM is limited to a Drude-Lorentz spectral density, defining the phonon-mode dependent exciton-phonon coupling strength. Furthermore HEOM is numerically extremely demanding, restricting the analysis of energy transfer in LHCs either to small systems [178, 179] or the discussion of very limited parameter sets [43, 47, 80].

We overcome this limitation by developing a graphics processing unit (GPU) implementation of the hierarchical equations of motion approach (GPU-HEOM). The idea behind the GPU-HEOM is to use up to 448 streaming processors provided by the NVIDIA C2070 graphics board in parallel. Our algorithm employs optimal work distribution, minimizes numerically expensive memory transfer and uses fast memory access via shared and constant memory provided by the GPU hardware architecture. These optimization strategies result in a 448-fold reduction of computation time as, illustrated in detail in Kreisbeck *et al.* Ref. [78]. Our GPU-HEOM cuts down the computation time drastically and sets the basis for the generalization of HEOM to more general spectral densities. We carry out this in chapter 7.3.

In section 3.2 we introduce the basic concepts of the reduced density operator description. In section 3.3 we follow the line of arguments of Ref. [174], and derive the HEOM approach, which rewrites the time-nonlocal equation of motion for the reduced density operator into hierarchically coupled equations of motions for a set of suitable defined auxiliary matrices. In section 3.4, we recapitulate the basic ideas of the energy transfer dynamics in the FMO complex [32]. We illustrate the electronic structure of the FMO complex and state the main pathways of energy flow. We further compare the HEOM results with approximative Redfield equations and investigate how the process of energy transfer is influenced by higher-order phonon processes and finite phonon relaxation timescales. Finally,

in section 3.5, we investigate limiting cases where HEOM goes into a Markovian weak coupling limit. In the weak coupling regime, the exciton dynamics is accurately described by the Redfield equations.

3.2 Theoretical description of the energy transfer

In the following, we introduce basic concepts of the reduced density matrix approach [32, 3, 4]. The time evolution of the total density operator $R(t)$, which characterizes the degrees of freedom of the exciton system as well as the degrees of freedom of the phonons, is governed by the Liouville equation. In the interaction picture, the Liouville equation is given by

$$\frac{d}{dt}\tilde{R}(t) = -\frac{i}{\hbar}[\tilde{\mathcal{H}}_{\text{ex-phon}}(t), \tilde{R}(t)] = -\frac{i}{\hbar}\tilde{\mathcal{L}}(t)\tilde{R}(t), \quad (3.1)$$

where we denote interaction picture operators by

$$\tilde{\mathcal{O}}(t) = \exp(\frac{it}{\hbar}\mathcal{H}_0)\mathcal{O}\exp(-\frac{it}{\hbar}\mathcal{H}_0), \quad (3.2)$$

with $\mathcal{H}_0 = \mathcal{H}_{\text{ex}} + \mathcal{H}_{\text{phon}} + \mathcal{H}_{\text{reorg}}$. We assume that the total density operator factorizes at initial time $t_0 = 0$ in system and vibrational degrees of freedom

$$R(t_0) = \rho(t_0) \otimes \rho_{\text{phon}}(t_0). \quad (3.3)$$

The protein is embedded in a thermal environment with temperature T . We treat the vibrations as a bosonic bath and the vibrational degrees of freedom are represented by the thermal state

$$\rho_{\text{phon}}(t) = \exp(-\beta\mathcal{H}_{\text{phon}}/k_{\text{B}}T) / \text{Tr}\{\exp(-\beta\mathcal{H}_{\text{phon}})\}, \quad (3.4)$$

with $\beta = 1/k_{\text{B}}T$. We express the coupling strength between excitons and phonons at BChl m by the spectral density

$$J_m(\omega) = \pi \sum_{\xi} \hbar^2 \omega_{\xi,m}^2 d_{\xi,m}^2 \delta(\omega - \omega_{\xi,m}). \quad (3.5)$$

A microscopic theory of the Frenkel exciton Hamiltonian reveals that the coupling strengths to the vibrations and the reorganization energy are in relation to each other, see Appendix A.1, eqs. (A.26) and (A.27). Thus, the spectral density is related to the reorganization energy by

$$\int_0^\infty d\omega \frac{J_m(\omega)}{\pi\hbar\omega} = \lambda_m. \quad (3.6)$$

The goal is to derive equations of motion for the reduced density operator which is obtained after tracing out the vibrational degrees of freedom

$$\rho(t) = \text{Tr}_{\text{phon}}\{R(t)\}. \quad (3.7)$$

By employing second-order perturbation theory in the exciton-phonon coupling, the time evolution of the reduced density operator is given in terms of simple rate equations for the entries of the reduced density matrix, see Appendix A.2. Without these approximations, the time evolution of the reduced density operator is, in general more involved and numerically demanding to handle.

3.3 Hierarchical equation of motion (HEOM) approach

In the following, we introduce the hierarchical equation of motion (HEOM) approach [77]. HEOM is neither based on perturbation theory nor does it rely on the Markov approximation. Within a Frenkel exciton model, HEOM gives an exact solution for the energy transfer in LHCs, even for a strong exciton-phonon coupling and slow phonon relaxation. As we discuss in section 2.2, for the FMO complex all parameters are of the same order of magnitude and one needs to go beyond second-order perturbation theory with respect to the exciton-phonon coupling. Furthermore, as Ishizaki and Fleming demonstrate [43], the slow phonon relaxation significantly influence the energy transfer dynamics. Both effects, higher order phonon processes and the finite timescale of the reorganization process of the phonon bath are accurately captured by the HEOM approach [174].

To derive HEOM, we start from the Liouville equation (3.1) and follow the arguments given by Ishizaki and Fleming in Ref. [174]. We assume that the exciton and vibrational degrees of freedom of the total density operator initially factorize. The total density operator at $t = t_0$ is given according to eq. (3.3). The factorization condition only holds for the initial time, while at later times the exciton and phonon dynamics become entangled [180]. Formal integration of the Liouville equation (3.1) and tracing out the phonon degrees of freedom yields

$$\tilde{\rho}(t) = \tilde{\mathcal{U}}(t)\tilde{\rho}(0) \quad (3.8)$$

with

$$\tilde{\mathcal{U}}(t) = \langle T_+ \exp \left(-\frac{i}{\hbar} \int_0^t ds \tilde{\mathcal{L}}(s) \right) \rangle. \quad (3.9)$$

Here $\langle \dots \rangle = \text{Tr}_{\text{phon}}\{ \dots \rho_{\text{phon}} \}$ stands for the bath expectation value and T_+ denotes the chronological time-ordering operator. We make use of the Gaussian

nature of the harmonic vibrations and reduce bath expectation values to products of two-time correlation functions

$$C_m(\tau) = \langle \tilde{B}_m(\tau) \tilde{B}_m(0) \rangle. \quad (3.10)$$

The operators B_m are defined in eq. (2.5). We assume that vibrations at different pigments are uncorrelated. The time evolution operator is then given by

$$\tilde{\mathcal{U}}(t) = T_+ \prod_m \exp \left(\int_0^t ds \tilde{W}_m(s) \right), \quad (3.11)$$

with

$$\tilde{W}_m(t) = -\frac{1}{\hbar^2} \int_0^t ds \tilde{V}_m(t)^\times [S_m(t-s) \tilde{V}_m(s)^\times - i \frac{\hbar}{2} \chi_m(t-s) \tilde{V}_m(s)^\circ]. \quad (3.12)$$

The influence of the environment is characterized by the symmetrized correlation

$$S_m(t) = \text{Re}\{C_m(t)\} \quad (3.13)$$

and response function

$$\chi_m(t) = -\frac{2}{\hbar} \text{Im}\{C_m(t)\}. \quad (3.14)$$

For a Drude-Lorentz spectral density

$$J(\omega) = 2\lambda \frac{\omega\nu}{\omega^2 + \nu^2}, \quad \text{with} \quad \nu^{-1} = \tau_c \quad (3.15)$$

the response function attains an exponential form

$$\chi(t) = \frac{2}{\hbar} \lambda \gamma e^{-t/\tau_c}, \quad (3.16)$$

where we introduced the phonon relaxation timescale $\tau_c = \nu^{-1}$. Here, we assume that all BChls couple with the same parameters to the vibrations, and we omit the subscript m from the notation. Using the Matsubara expansion for $C(t)$, see Appendix A.2.1, eq. (A.51), we expand the symmetrized correlation function into a series of exponential functions

$$S(t) = \lambda\nu \cot\left(\frac{\beta\hbar\nu}{2}\right) e^{-\nu t} + \frac{2\lambda}{\beta\hbar} \sum_{k=1}^{\infty} \frac{2\nu}{\gamma_k^2 - \nu^2} \gamma_k e^{-\gamma_k t}. \quad (3.17)$$

Here, we introduce the Matsubara frequencies $\gamma_k = 2\pi k/\beta\hbar$. Assuming high temperatures $\hbar\nu/k_B T < 1$, the symmetrized correlation function simplifies to

$$S(t) \simeq \frac{2\lambda}{\beta\hbar} e^{-t/\tau_c}. \quad (3.18)$$

For the FMO complex, phonon-relaxation times are reported to be in the range between $\tau_c = 35$ fs [43] and $\tau_c = 166$ fs [39]. For these parameters $\hbar\nu/k_B T$ ranges between 0.15 ($\tau_c = 166$ fs) and 0.75 ($\tau_c = 35$ fs) at physiological temperature $T = 300$ K. Hence, the high temperature approximation is justified in this regime.

Both the symmetrized correlation function $S_m(t)$ and response function $\chi_m(t)$ decay exponentially on the phonon-relaxation timescale τ_c . The exponential form is crucial to express the time-nonlocal eq. (3.8) as a hierarchy of coupled time-local equations of motion. This requirement ties HEOM to a Drude-Lorentz-shaped spectral density. In the following, we introduce the relaxation operator

$$\tilde{\theta}_m(t) = i \left(\frac{2\lambda}{k_B T \hbar} \tilde{V}_m^\times(t) - i\lambda\nu \tilde{V}_m^\circ(t) \right) \quad (3.19)$$

with $V_m^\times \bullet = [V_m, \bullet]$ and $V_m^\circ \bullet = \{V_m, \bullet\}$ and define auxiliary operators

$$\tilde{\sigma}^{(n_1, \dots, n_N)}(t) = T_+ \prod_m^N \left(\int_0^t ds e^{-\nu(t-s)} \tilde{\theta}_m(s) \right)^{n_m} \exp \left(\int_0^t ds \tilde{W}_m(s) \right). \quad (3.20)$$

The reduced density operator is expressed in terms of $\tilde{\rho}(t) = \tilde{\sigma}^{(0, \dots, 0)}(t)$, which follows immediately from the definition of the auxiliary operators. The time evolution of the auxiliary operators yields hierarchically coupled equations of motion. The equation of motion for the reduced density operator in the Schrödinger picture is given by

$$\frac{d}{dt} \rho(t) = -\frac{i}{\hbar} \mathcal{L}_{\text{ex}} \rho(t) + \sum_m \frac{i}{\hbar} V_m^\times \sigma^{(0, \dots, n_m=1, \dots, 0)}(t) \quad (3.21)$$

with

$$\begin{aligned} \frac{d}{dt} \sigma^{(n_1, \dots, n_N)}(t) = & \left(-\frac{i}{\hbar} \mathcal{L}_{\text{ex}} - \sum_m n_m \nu \right) \sigma^{(n_1, \dots, n_N)}(t) \\ & + \sum_m \frac{i}{\hbar} V_m^\times \sigma^{(n_1, \dots, n_m+1, \dots, n_N)}(t) \\ & + \sum_m n_m \theta_m \sigma^{(n_1, \dots, n_m-1, \dots, n_N)}(t). \end{aligned} \quad (3.22)$$

The HEOM approach rewrites the time-nonlocal effects into hierarchically coupled equations of motion eqs. (3.21) and (3.22). Instead of propagating a single density operator $\rho(t)$, a complete set of auxiliary operators has to be advanced in time. The set of auxiliary operators $\sigma^{(n_1, \dots, n_N)}(t)$ describe the state of the bath. Due to the structure of the hierarchically coupled equations of motion, information is exchanged between the exciton system and the bath [170]. Thus, entanglement between excitonic and vibrational degrees of freedom emerges [180]. We

assume that there are no correlations between excitons and vibrations at $t_0 = 0$, and we initially set all entries of the σ -matrices to zero.

For sufficiently large $N_{\max} = \sum_m n_m$, the diagonal coupling terms in the time evolution of auxiliary matrices become dominant and we truncate the hierarchy. This truncation sets the number of required auxiliary matrices $\#\sigma = (N + N_{\max})!/N_{\max}!N!$ which scales exponentially with both system size (number of coupled BChls N) and truncation N_{\max} . For the energy transfer in the FMO complex, typical truncations are of the order of $N_{\max} = 4$ to $N_{\max} = 12$ [78, 43, 46] which involves up to 50 388 auxiliary matrices in the hierarchy. Therefore, the computational effort increases tremendously for the HEOM approach when compared to the Redfield approach, in which only the density operator needs to be advanced in time. Reasonable computation times require efficient implementations like GPU-HEOM, Kreisbeck *et al.* Ref. [78].

The derivation of the hierarchy eqs. (3.21) and (3.22) relies on a high temperature approximation that is valid at $T = 300$ K. However, many experimental studies of LHCs are carried out at a temperature of $T = 77$ K [42, 16, 20]. For a comparison of numerical simulations with experimental results, further low temperature correction terms need to be employed. One possible route is to include more Matsubara frequencies in the correlation function. However, including more Matsubara frequencies increases the number of entries within the index tuple (n_1, \dots, n_N) [175, 176, 80, 177]. Hence, the number of auxiliary matrices $\sigma^{(n_1, \dots, n_N)}(t)$ increases tremendously, and with this, the numerical effort as well. We follow Ref. [43] and circumvent this increase in numerical costs by exploiting the fast relaxation timescale of the Matsubara frequencies, $\gamma_1 \approx 15$ fs at $T = 77$ K. Thus, we approximate $\gamma_k e^{-\gamma_k t} \sim \delta(t)$ by the Dirac delta distribution. Equation (3.17) then reduces to

$$S_m(t) = \frac{2\lambda}{\beta\hbar} e^{-\nu t} - \frac{2\lambda}{\beta\hbar} \sum_{k=1}^{\infty} \frac{2\nu}{\gamma_k^2 - \nu^2} (\nu e^{-\nu t} - \delta(t)), \quad (3.23)$$

where we further make use of the relation

$$\frac{2\lambda}{\beta\hbar} \sum_{k=1}^{\infty} \frac{2\nu}{\gamma_k^2 - \nu^2} = \frac{2\lambda}{\hbar\beta\nu} - \lambda \cot\left(\frac{\hbar\beta\nu}{2}\right). \quad (3.24)$$

In the following, we consider only the first Matsubara frequency

$$S_m(t) \simeq \frac{2\lambda}{\beta\hbar} \left(1 - \frac{2\nu}{\gamma_1^2 - \nu^2} \nu\right) e^{-\nu t} + \frac{2\lambda}{\beta\hbar} \frac{2\nu}{\gamma_1^2 - \nu^2} \delta(t). \quad (3.25)$$

Within this low temperature correction, there is no need to extend the index tuple of the auxiliary matrices. The hierarchically coupled equations of motion

eqs. (3.21) and (3.22) are only slightly modified by replacing [43]

$$\begin{aligned}\mathcal{L}_{\text{ex}} &\rightarrow \mathcal{L}_{\text{ex}} - \sum_{m=1}^N \frac{2\lambda}{\beta\hbar^2} \frac{2\nu}{\gamma_1^2 - \nu^2} V_m^\times V_m^\times \\ \Theta_m &\rightarrow \Theta_m - \frac{2\lambda}{\beta\hbar} \frac{2\nu^2}{\gamma_1^2 - \nu^2} V_m^\times.\end{aligned}\tag{3.26}$$

A further improvement of the low temperature correction can be attained by including the second γ_2 or higher Matsubara frequencies. Also, a Padé spectrum decomposition has been proposed [181, 182] that shows faster convergence than the Matsubara decomposition. The low temperature correction becomes particularly relevant for the simulation of electron transfer through nanostructures where many experiments are performed at temperatures below 1 K. HEOM in combination with a Padé spectrum decomposition was recently applied to study higher-order tunneling processes for transport through an interacting quantum dot system at a very low temperature of 0.3 K [182]. For energy transfer in LHC's, however, low temperature correction is only a minor issue, since *in vivo* conditions are around 300 K and experimentally relevant temperatures are above 77 K. Hence, correction terms of eq. (3.26) already give good results for the simulation of energy transfer in the FMO complex [78].

3.4 Energy funneling in the FMO complex

A sketch of the energetic structure of the FMO complex of *C. tepidum* (Table 2.1) is depicted in Fig. 3.1. The thick lines indicate the site energies of the seven BChls, whereas the arrows stand for the dominant inter-site couplings J_{mn} . Dipole-Dipole interaction between neighboring BChls leads to strongly coupled dimer pairs and forms the main pathways of possible energy transfer. BChl 7 couples to both BChl 4 and BChl 6. Initial excitation energy is provided by the antenna. We do not take into account the transfer process from the baseplate of the antenna to the FMO complex explicitly, but rather assume that initial excitations are created either at BChl 1 or BChl 6.

There are two possible pathways of energy transfer. For the first pathway (highlighted in red in Fig. 3.1), electronic excitations enter the FMO at BChl 1 and energy is transferred via BChl 2 to the target BChls 3 and 4. The second pathway (highlighted in blue in Fig. 3.1), starts at BChl 6 and involves BChls 5 and 7 as intermediate steps to pass energy to the target states. The energetic structure of the site energies forms an energy gradient toward the reaction center. Because of the coupling to the vibrational modes, there is an energy exchange between electronic excitations and vibrations, and energy is dissipated during

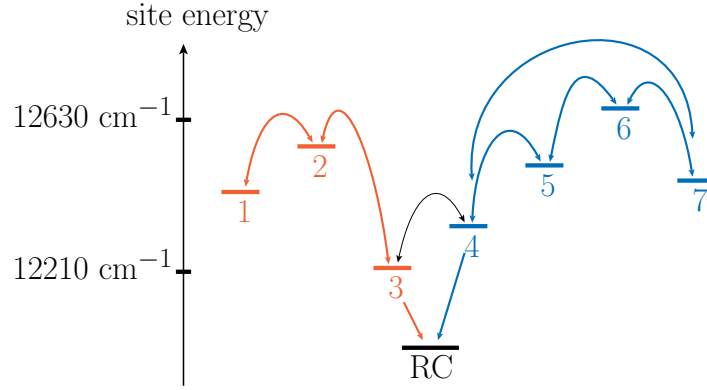


Figure 3.1: Sketch of the exciton energies of the FMO complex (Table 2.1). Each site, designated by a number, represents a BChl of the FMO complex. The arrows indicate the dominant inter-site couplings. Electronic excitation enters the FMO complex either at BChl 1 or BChl 6. This gives rise to two pathways of energy flow toward the reaction center. The coupling of BChl 3 and BChl 4 to the reaction center of BChl 3 and BChl 4 is indicated by the arrow pointing toward the site RC that represents the reaction center. For the first pathway (red), energy is transferred from BChls 1 via BChl 2 to BChl 3, which couples to the reaction center. The second pathway (blue) involves BChls 1, 4, 5, 6, and 7. The structure of the site energies form an energy funnel toward the reaction center.

the reorganization process. Thus, the exciton system thermalizes and energy is funneled to the low exciton states.

The excitation energy transfer process is best followed in terms of the population dynamics $\rho_{mm}(t) = \langle m | \rho(t) | m \rangle$. $\rho_{mm}(t)$ are the diagonal entries of the reduced density matrix in the site basis representation and correspond to the probabilities of finding an electronic excitation at BChl m . Fig. 3.2 shows the population dynamics for the FMO complex for the initial population at BChl 1 ($\rho_{11}(t_0 = 0) = 1$) at temperatures of $T = 77$ K and $T = 300$ K. The time evolution of the reduced density matrix is numerically implemented within the non-perturbative and non-Markovian HEOM approach, introduced in section 3.3. We describe the coupling of electronic excitations and vibrations at BChl m with a Drude-Lorentz spectral density with reorganization energy $\lambda_m = 35$ cm^{-1} and phonon relaxation timescale $\tau_c = 100$ fs. For the given parameters we truncate the hierarchy, eqs. (3.21) and (3.22), at $N_{\text{max}} = 12$. In order to check the convergence of the hierarchy level we compare the results of the population dynamics for truncation level $N_{\text{max}} = 12$ with truncation $N_{\text{max}} = 13$. Increasing the truncation

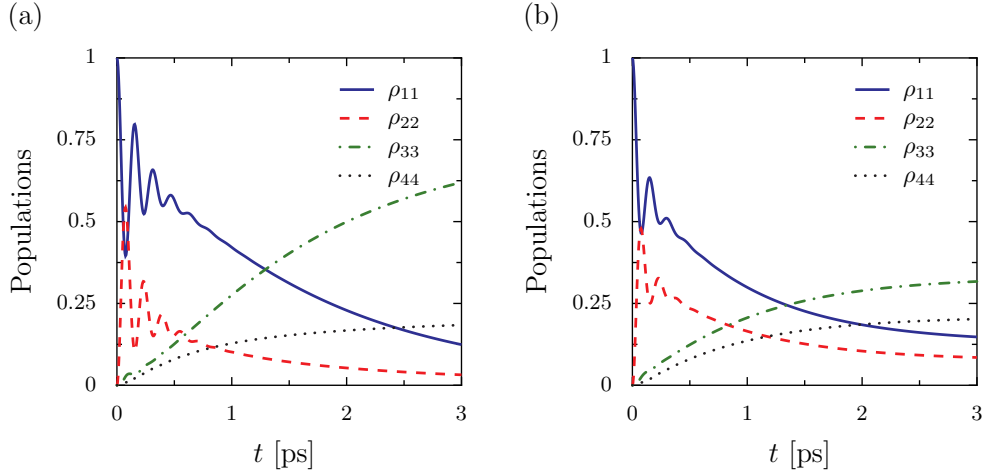


Figure 3.2: Excitation energy transfer (EET) in the FMO complex expressed by the population dynamics $\rho_{mm}(t) = \langle m | \rho(t) | m \rangle$. The density operator is numerically propagated with the HEOM technique introduced in section 3.3 with truncation $N_{\max} = 12$. Initial population is located at BChl₁. The exciton phonon-coupling is described by a Drude-Lorentz spectral density with $\lambda = 35 \text{ cm}^{-1}$ and $\tau_c = 100 \text{ fs}$. We depict the population dynamics at (a) $T = 77 \text{ K}$ and (b) $T = 300 \text{ K}$.

leads only to minor changes $|\rho_{m,m}(t, N_{\max} = 13) - \rho_{m,m}(t, N_{\max} = 12)| \leq 7 \times 10^{-6}$ ($\leq 1.5 \times 10^{-6}$) at $T = 77 \text{ K}$ ($T = 300 \text{ K}$).

Immediately after creating an initial excitation at BChl 1, there is energy transfer among the pigments toward the target BChl 3, and the population ρ_{33} steadily increases. The energy transfer process is accompanied by long-lasting oscillatory energy trade between populations ρ_{11} and ρ_{22} , that is, energy flows back and forth between the strongly coupled dimer pair BChl 1 and BChl 2.

At a temperature of 77 K these beatings last up to 0.7 ps, and at a physiological temperature of 300 K, beatings preserve up to 0.4 fs. These findings go back to Ishizaki and Fleming [43], who interpret these beatings as signatures of long-lasting electronic coherence [43, 183]. However, in chapter 6 we show that this interpretation is not correct. The careful and detailed analysis carried out in chapter 6 proves that the origin of the long-lasting beatings in the population dynamics originates from the complicated and non-trivial exchange of energy between the exciton system and the phonon bath.

Energy relaxation guides the populations from the high energy levels to the low energy states. In the long time limit, the exciton system thermalizes and approaches a stationary state where the populations are distributed according to the thermal state. For weak exciton-phonon couplings the thermal state of the

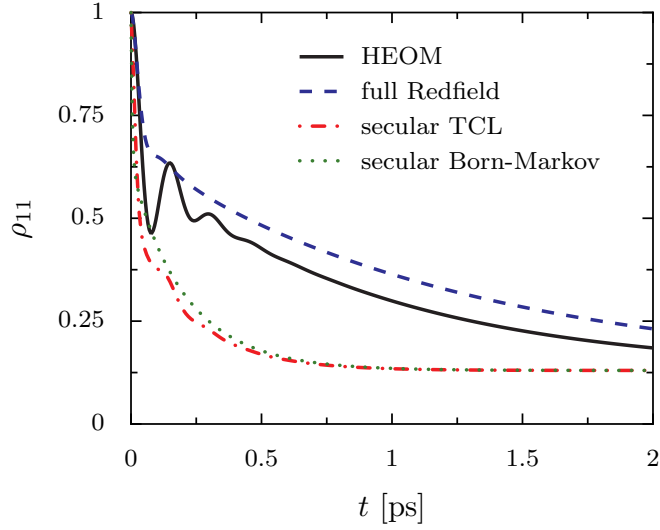


Figure 3.3: Time evolution of population ρ_{11} for different levels of approximations. Dashed line: full-Redfield equations (A.37), dashdotted line: secular time-convolutionless (TCL) master equation (A.63) and dotted line: secular Born-Markov approximation (Appendix A.2.2). None of the approximative approaches matches the exact HEOM result (solid line). Parameters used: $\lambda = 35 \text{ cm}^{-1}$, $\tau_c = 100 \text{ fs}$ and $T = 300 \text{ K}$.

single exciton manifold is given by the Boltzmann statistics

$$\rho_{\text{thermal}} = \frac{\exp(-\beta \mathcal{H}_{\text{ex}})}{\text{Tr}\{\exp(-\beta \mathcal{H}_{\text{ex}})\}}. \quad (3.27)$$

For stronger coupling to the phonon bath the stationary state deviates from the Boltzmann statistics [184]. A further analysis of the thermal population in the FMO complex for HEOM simulations is given by Kreisbeck *et al.* in Ref. [78]. For the temperature $T = 77 \text{ K}$, the stationary state is approached after approximately 10 ps where nearly the complete energy accumulates at the target states, $\rho_{33} + \rho_{44} = 0.95$. For the higher temperature $T = 300 \text{ K}$ thermalization occurs on a faster timescale and the stationary state is attained after 6 ps. At $T = 300 \text{ K}$, the thermal activation yields an enhanced probability for populating higher states, but the energetically lowest states BChl₃ or BChl₄ are still preferred, $\rho_{33} + \rho_{44} = 0.54$.

In the following we study the influence of non-Markovian effects and higher order phonon processes on the exciton dynamics. Fig. 3.3 shows the population dynamics within different levels of approximation. We use the parameters $\lambda = 35 \text{ cm}^{-1}$ and $\tau_c = 100 \text{ fs}$. The initial population is located at pigment BChl 1.

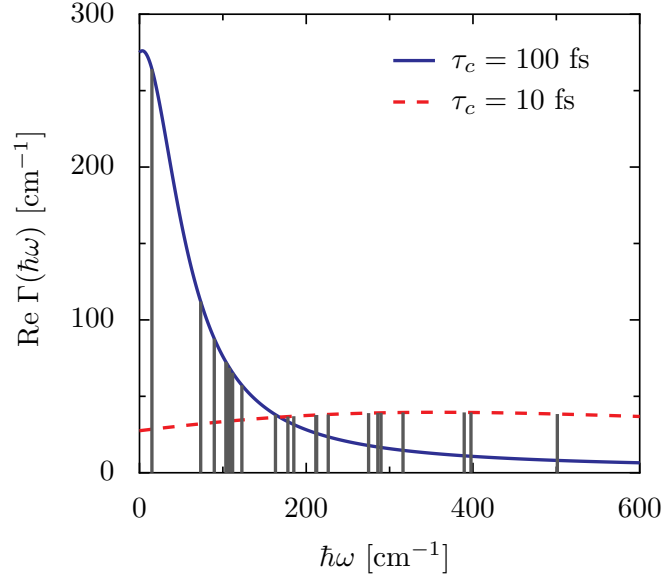


Figure 3.4: Real part of the Redfield rates for phonon relaxation timescales $\tau_c = 100$ fs and $\tau_c = 10$ fs. The vertical lines indicate the energy difference $E_M - E_N$ between the two eigenstates of the exciton Hamiltonian of the FMO complex, as stated in Table 2.1. Parameters used: $\lambda = 35$ cm $^{-1}$ and $T = 300$ K.

We compare the exact HEOM results at a temperature of $T = 300$ K with the full Redfield equations (A.37), the secular time-convolutionless (TCL) master equation (A.63), and the secular Born-Markov approximation (Appendix A.2.2). The latter is obtained from the secular TCL master equation by employing the Markov approximation. All of these approximations are based on second-order perturbation theory in the exciton-phonon coupling. See Appendix A.2. None of the approximative approaches agree sufficiently with the exact HEOM result. Markovian descriptions such as the full Redfield equation and the secular Born-Markov approximation do not capture the finite timescale of phonon relaxation and fail to reproduce long-lived beatings in the population dynamics [166]. Only the TCL secular Born approximation, which captures non-Markovian effects up to second-order perturbation theory, gives rise to long-lived beatings in the population dynamics [185]. The beatings are, however, reduced in amplitude compared to HEOM. None of the approximative approaches predict the correct thermal relaxation timescale. While the full Redfield equation predicts thermalization that is too slow, the secular approximation strongly overestimates the process of thermalization.

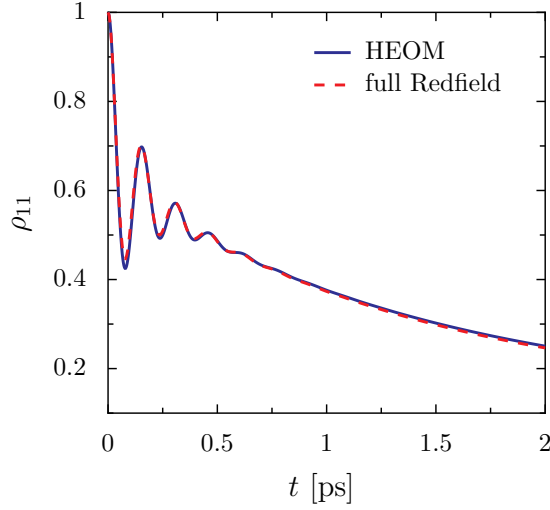


Figure 3.5: Comparison of the population dynamics ρ_{11} at $T = 300$ K evaluated in HEOM and with the full Redfield equation. The reorganization energy is given by $\lambda = 35$ cm $^{-1}$. The results for the fast phonon relaxation timescale $\tau_c = 10$ fs are shown, where the exciton dynamics is accurately described by Markovian-second order perturbation theory. The results of HEOM (solid line) and the full Redfield equation (dashed line) are almost on top of each other.

3.5 Weak coupling limit

According to the findings of section 3.4, the approximative full Redfield equations cannot reproduce the exact exciton dynamics for the parameter regime of the FMO complex. Nevertheless, there are certain weak coupling regimes in which the HEOM results are accurately described by Markovian second-order perturbation theory. The coupling strength between excitons and phonons is encoded in the spectral density. In particular, the reorganization energy λ is a global measure for the strength of the coupling to the phonon bath. For small reorganization energies, non-Markovian effects are of minor importance. Second-order perturbation theory is appropriate [174]. Here, we consider a different limit and discuss the case of fast phonon relaxation $\tau_c \lesssim 10$ fs, where the coupling with vibrations becomes more and more Markovian. We show that a fast phonon relaxation not only diminishes non-Markovian effects, but also effectively reduces the coupling strength to the vibrational modes for a Drude-Lorentz spectral density. Hence, the population dynamics obtained by HEOM is accurately reproduced by the full Redfield equations.

In the Redfield approach, the time evolution of the density operator is de-

scribed by rate equations. According to eq. (A.40), the rates $\Gamma((E_N - E_M)/\hbar)$ are evaluated at fixed energies $E_m - E_n$, corresponding to the energy difference between the two eigenstates of the exciton system. Since we use the same parameters for the exciton-phonon coupling for each sites, we omit the subscript m of the Redfield rates Γ . The Redfield rates are evaluated according to eq. (A.52), and depend on the phonon occupation and the spectral density. Since $\tau_c = \nu^{-1}$ explicitly enters the spectral density, changing the time scale of bath correlations also affects the rates Γ_m . Fig. (3.4) depicts the real part of $\Gamma_m(\omega)$ (see eq. (A.53)) for $\tau_c = 100$ fs and $\tau_c = 10$ fs. The reorganization energy is set to $\lambda = 35$ cm⁻¹, and we set the temperature to $T = 300$ K. The zero frequency component $\text{Re}\{\Gamma(\omega \rightarrow 0)\}$ corresponds to the dephasing rate $\Gamma^* = 4\lambda k_B T \tau_c$ which increases linearly with the temperature and the phonon relaxation timescale. The lines mark the energies $E_M - E_N$ where the rates are evaluated in the Redfield equations. For $\tau_c = 100$ fs, $\text{Re}\{\Gamma(\omega)\}$ decays monotonically with energy $\hbar\omega$. There is a large dephasing rate $\Gamma^* \approx 275$ cm⁻¹. Most of the energy differences $E_m - E_n$ are below 150 cm⁻¹, and we get a strong coupling with the vibrations. The situation is different for fast phonon relaxation $\tau_c = 10$ fs. The dephasing rate is reduced by a factor of ten compared to the situation with slow phonon relaxation $\tau_c = 100$ fs. Furthermore, $\text{Re}\{\Gamma(\omega)\}$ is broadened and always remains in the weak coupling regime.

Fig. (3.5) shows the corresponding population dynamics. For $\tau_c = 10$ fs, the full Redfield results almost appear on top of those for the HEOM. In the regime of fast phonon relaxation, the exciton-phonon coupling is weak, and second order perturbation theory yields accurate results. The weak coupling limit, is not approached for the larger phonon relaxation time $\tau_c = 100$ fs, where we obtain a significant deviation of the approximative Redfield results from the exact HEOM approach, see Fig. 3.3.

3.6 Conclusion

In this chapter we describe the dissipative dynamics in the exciton system with a reduced density operator approach. We introduce the HEOM technique [77] which properly includes the reorganization processes and yields an adequate description of energy transfer in LHCs [174]. We present the basic concepts of the energy transfer in the FMO complex. The exciton dynamics is analyzed by the site basis population dynamics $\rho_{mm}(t)$, keeping track of the probability of finding an electronic excitation at BChl m . Energy transfer is driven by thermal relaxation from high energy states close to the antenna to the low energy states. In the steady state the populations are in agreement with the thermal Boltzmann distribution.

Approximative methods based on second-order perturbation theory with re-

spect to the exciton-phonon coupling $\mathcal{H}_{\text{ex-phon}}$ are not valid for the parameter regime of energy transfer in LHCs [166]. It is only in the weak coupling limit that the transfer dynamics is adequately reproduced by the full Redfield equations. The weak coupling limit is approached for small reorganization energies [174]. Here, we show that, for the special case of a Drude-Lorentz spectral density, a fast phonon relaxation timescale also drives the exciton-phonon interaction into a weak coupling limit. This is because the phonon relaxation timescale strongly affects the shape of the spectral density. The latter determines the relaxation and dephasing behavior of the dissipative exciton dynamics.

4 Energy transfer efficiency

Parts of this chapter have been published in Kreisbeck *et al.* Ref. [78].

4.1 Introduction

Experimental measurements of two-dimensional spectroscopy of the FMO complex show coherent beatings [16, 20] that last up to 400 fs at physiological temperatures. Hence, coherence lasts up to timescales where the excitation energy in the FMO complex is transferred from the antenna to the reaction center. This provokes the idea that coherence is not just a by-product but rather improves the functionality of light-harvesting complexes [186, 25]. Mohseni *et al.* [57] propose that the high transfer efficiency of the FMO complex is based on quantum walks, resulting in a quantum speed-up of energy transfer analogous to quantum-search algorithms [63, 187]. However, a closer analysis reveals that, for the FMO complex, a quantum speed-up is only attained during the first 70 fs [61] of the transfer process. This finding suggests that long-lived coherence might improve the robustness [61] of the efficient energy transfer, or might be used for the regulation of light-harvesting functions [62] rather than supporting a quantum speed-up in the transfer process.

Fast energy transfer is ascribed to the coupling between the exciton system and the vibrational environment which assists the energy transfer in LHCs [52, 54, 55]. There are various mechanisms of environment-assisted transport, ranging from energy relaxation to the dephasing induced opening of indirect transport pathways between weakly connected parts of the FMO complex. In this chapter, we analyze ways in which coherence and environment-assisted transfer go along together. We show that both mechanisms are well balanced in the optimal transfer regime. Neither the extreme regime of strong coupling to the environment nor the extreme regime of purely coherent dynamics provide suitable conditions for efficient energy transfer. This determines the optimal parameter set for the reorganization energy, the phonon relaxation timescale and the exciton Hamiltonian of the FMO complex.

In section 4.2, we extend the exciton Hamiltonian introduced in chapter 2 and

include the reaction center and energy trapping. In section 4.3, we discuss basic concepts of environment assisted transfer within the Born-Markov approach for the exciton-phonon coupling. Studying the transfer efficiency of the energy transfer under the influence of a non-Markovian environment calls for the inclusion of exciton trapping and exciton recombination in the HEOM formalism. In section 4.4, we develop ME-HEOM that incorporates parts of the system like exciton trapping with a masterequation (ME) [4, 3] approach, while employing the exact HEOM approach for the exciton-phonon coupling. ME-HEOM allows us to study how non-Markovian effects influence transfer efficiency. A comparison with approximative approaches highlights the relevance of the sophisticated ME-HEOM approach. In section 4.5, we discuss the optimality of the electronic structure of the FMO complex. We propose a strategy of varying the site energies of the FMO complex to achieve optimal energy transfer to the reaction center. Such optimization strategies are relevant for the design of future artificial light-harvesting devices [26]. Furthermore we use variations in the structure of the FMO complex to highlight different transport regimes. In particular, the temperature dependency of the transfer efficiency reveals the interplay of different mechanisms of environment-assisted transfer. In section 4.6, we finally investigate the functional role of long-lived electronic coherence for the highly efficient energy transfer. We show that a certain amount of coherence is required to overcome exciton localization that hinders energy flow to the reaction center. We further illustrate that the coupling to the environment changes the distribution of coherence. A uniformly spread coherence is generated through the coupling to the phonon bath in the optimal transfer regime.

4.2 Transfer and loss channel

In section 3.4, we illustrate energy transfer within the isolated FMO complex that is detached from the reaction center. The coupling to the baseplate of the antenna is simulated by assuming that an initial population enters the complex either at BChl 1 or at BChl 6 bearing two pathways of energy flow. To investigate the functional role of the FMO complex as a highly efficient energy wire, and to educe the underlying mechanisms of fast energy transfer, we need to incorporate the process of population trapping in the reaction center (RC). We follow previous works [52, 57, 61, 162, 56, 188], and introduce the reaction center as an energy trapping state $\mathcal{H}_{\text{trap}} = E_{RC}|RC\rangle\langle RC|$. The process of energy trapping is then introduced by the leakage of populations from the FMO complex to the reaction center. The simple model of introducing an irreversible energy sink is sufficient for our studies since we focus on the timescales of energy transfer rather than on studying the microscopic details of the process of trapping in the reaction center.

During this section, we proceed along the ideas presented in Kreisbeck *et al.*

[78]. The coupling between the FMO complex and the reaction center is described by

$$\mathcal{H}_{\text{ex-RC}} = - \sum_{m=3}^4 \sum_{\xi_{RC}} (b_{\xi_{RC}} + b_{\xi_{RC}}^\dagger) \times \mu_{m,\xi_{RC}} (|RC\rangle\langle m| + |m\rangle\langle RC|), \quad (4.1)$$

where we introduce artificial photon modes $\mathcal{H}_{\text{phot}}^{RC} = \sum_{\xi_{RC}} \hbar\omega_{\xi_{RC}} b_{\xi_{RC}}^\dagger b_{\xi_{RC}}$ of the reaction center, representing a dissipative environment that ensures irreversible population trapping. We assume that BChl 3 and BChl 4 are the linker BChls between the FMO complex and the reaction center. The coupling strength is given by the coefficients $\mu_{m,\xi_{RC}}$, and can be embraced by the spectral density

$$J_{m,RC}(\omega) = \sum_{\xi_{RC}} |\mu_{m,\xi_{RC}}|^2 \delta(\hbar\omega - \hbar\omega_{\xi_{RC}}). \quad (4.2)$$

Apart from transfer to the reaction center, there is also a loss channel. Light-matter interaction induces exciton recombination that is the radiative decay of the electronic excitations of the BChls to the ground state. Excitation energy is released by emitting photons and the transported energy in the FMO complex is thus lost. The interaction with the radiation field reads in dipole approximation [189]

$$\mathcal{H}_{\text{ex-phot}} = - \sum_{m=1}^N \sum_{h\nu} (a_{h\nu} + a_{h\nu}^\dagger) \times \mu_{m,h\nu} (|0\rangle\langle m| + |m\rangle\langle 0|), \quad (4.3)$$

where we introduce the zero exciton state $\mathcal{H}_0 = E_0|0\rangle\langle 0|$. The photon modes are given by $\mathcal{H}_{\text{phot}} = \sum_{h\nu} h\nu a_{h\nu}^\dagger a_{h\nu}$. $\mu_{m,h\nu}$ are the dipole couplings between the external field and the electronic excitation at BChl m . The exciton-photon coupling strength is expressed by the spectral density

$$J_{m,\text{phot}}(\omega) = \sum_{h\nu} |\mu_{m,h\nu}|^2 \delta(\hbar\omega - h\nu). \quad (4.4)$$

We extend the Frenkel exciton Hamiltonian eq. (2.1) and include trapping $\mathcal{H}_{\text{ex-RC}} + \mathcal{H}_{\text{phot}}^{RC}$ and energy losses $\mathcal{H}_{\text{ex-phot}} + \mathcal{H}_{\text{phot}}$. Furthermore, we explicitly take into account the zero-exciton state \mathcal{H}_0 and the population trapping reaction center $\mathcal{H}_{\text{trap}}$. The reduced density matrix ρ , introduced in section 3.2, is then enlarged to a 9×9 matrix in which $\rho_{RC,RC} = \langle RC|\rho|RC\rangle$ keeps track of the number of the population trapped in the reaction center, and in which $\rho_{0,0} = \langle 0|\rho|0\rangle$ corresponds to the amount of energy that is lost during the transfer process.

In the following, we treat trapping and radiative losses within a secular Born-Markov approach. We introduce the operators

$$A_{m,RC}(\omega) = \sum_M c_m(E_M) \delta(\hbar\omega - E_M) |RC\rangle\langle E_M| \delta(\hbar\omega - E_M) \quad (4.5)$$

and

$$A_{m,\text{phot}}(\omega) = \sum_M c_m(E_M) \delta(\hbar\omega - E_M) |0\rangle\langle E_M| \delta(\hbar\omega - E_M), \quad (4.6)$$

where $|E_M\rangle$ denote the eigenstates of the single exciton manifold of the FMO complex. The $c_m(E_M)$ correspond to the unitary transformation coefficients that switch between the site- and the eigenbasis representation

$$|m\rangle = \sum_M c_m^*(E_M) |E_M\rangle. \quad (4.7)$$

Proceeding along the steps of Appendix A.2.2, we obtain the following contributions for the population trapping and for the loss channel to the Liouville equation for the reduced density operator

$$\mathcal{L}^{RC} = \sum_{m=3}^4 \sum_{E_M} \gamma_{m \rightarrow RC}(E_M) \mathcal{D}[A_{m,RC}(E_M)] + \sum_{m=1}^N \sum_{E_M} \gamma_{RC \rightarrow m}(E_M) \mathcal{D}[A_{m,RC}^\dagger(E_M)] \quad (4.8)$$

and

$$\mathcal{L}^{\text{phot}} = \sum_{m=1}^N \sum_{E_M} \gamma_{m \rightarrow 0}(E_M) \mathcal{D}[A_{m,\text{phot}}(E_M)] + \sum_{m=1}^N \sum_{E_M} \gamma_{0 \rightarrow m}(E_M) \mathcal{D}[A_{m,\text{phot}}^\dagger(E_M)]. \quad (4.9)$$

The Lindblad operators $\mathcal{D}[A]$ are defined as

$$\mathcal{D}[V]\rho = V\rho V^\dagger - \frac{1}{2}V^\dagger V\rho - \frac{1}{2}\rho V^\dagger V. \quad (4.10)$$

The transition rates $\gamma_{m \rightarrow RC}(E_M) = 2\pi J_{m,RC}(E_M)(n_{RC}(E_M) + 1)$ describe the transfer of population from the FMO complex to the reaction center. n_{RC} defines the occupation of the artificial photon modes of the reaction center. In the following, we assume that energy trapping is irreversible and, therefore, that there is no energy transfer from the reaction center to the exciton system. Hence, we set the corresponding rates to zero $\gamma_{RC \rightarrow m}(E_M) = 0$. Energy losses due to radiative decay are expressed in terms of transition rates $\gamma_{m \rightarrow 0}(E_M) = 2\pi J_{\text{phot}}(E_M)(n_{\text{phot}}(E_M) + 1)$, where n_{phot} defines the photon occupation. Since we assume that the initial excitation energy is only provided by the antenna we set $\gamma_{0 \rightarrow m}(E_M) = 0$. We further assume energy-independent trapping $\gamma_{m \rightarrow RC}(\omega) = \Gamma_{RC}$ and loss rates $\gamma_{m \rightarrow 0}(\omega) = \Gamma_{\text{loss}}$. The process of trapping and radiative decay is then expressed by

$$\mathcal{L}_{\text{ex-RC}} = \sum_{m=3}^4 \Gamma_{RC} \mathcal{D}[|RC\rangle\langle m|], \quad (4.11)$$

and

$$\mathcal{L}_{\text{ex-phot}} = \sum_{m=1}^N \Gamma_{\text{loss}} \mathcal{D}[|0\rangle\langle m|]. \quad (4.12)$$

Equations (4.11) and (4.12) are equivalent to introducing anti-Hermitian parts to the exciton Hamiltonian [52, 57, 190].

The transfer efficiency is defined as the total amount of the population that gets trapped in the reaction center

$$\eta = \rho_{RC\,RC}(t \rightarrow \infty). \quad (4.13)$$

Maximal efficiency $\eta = 1$ describes the situation in which the whole population is transferred to the reaction center. Zero efficiency $\eta = 0$ corresponds to the situation in which the exciton population radiatively decays before any of the population enters the reaction center. The timescale of the energy transfer is quantified by the average trapping time

$$\langle t \rangle = \int_0^\infty dt' t' \left(\frac{d}{dt} \rho_{RC,RC}(t) \right)_{t=t'}. \quad (4.14)$$

According to equations (4.13) and (4.14), we have to propagate until $t \rightarrow \infty$. However, in our numerical implementation we stop the propagation at t_{max} , a point at which the population in the system (excluding the reaction center and the electronic ground state) has dropped from 1 to below 10^{-5} .

4.3 Environment-assisted energy transfer

The transfer efficiency results as a combination of three different timescales: (i) the timescale of the loss channel Γ_{loss} , (ii) the timescale of trapping Γ_{RC}^{-1} , and (iii) the time scale of energy transfer within the FMO complex from an initial BChl 1 or BChl 6 to the target BChls 3 and 4. The exciton life time, expressed by Γ_{loss} , is of the order of 1 ns. The trapping rate Γ_{RC}^{-1} is in the range of a few picoseconds [52, 61, 59]. Hence, high transfer efficiency requires fast (picosecond timescale) transfer from the acceptors BChls 1 and 6 to the targets BChl 3 and BChl 4.

As is discussed in detail in section 3.4, energy dissipation drives the exciton system within a few picoseconds toward the thermal equilibrium with the protein environment. Fast thermalization and energy relaxation is a major mechanism for achieving high transfer efficiency, as is discussed in section 4.5 (see also Kreisbeck *et al.* Ref. [78]). That the coupling to a noisy environment aids transport in LCHs is developed independently by Aspuru-Guzik [52, 57] *et al.* and Plenio *et al.* [54, 55] using secular Born-Markov and even simpler Markovian models

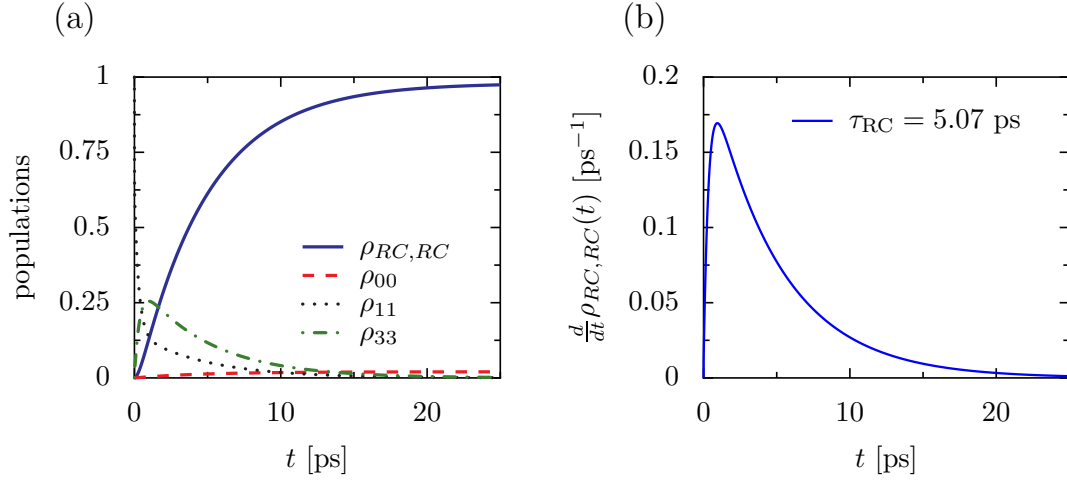


Figure 4.1: Energy transfer in the FMO complex evaluated in the secular Born-Markov approximation under the presence of trapping $\Gamma_{\text{RC}}^{-1} = 2.5$ ps and radiative losses $\Gamma_{\text{loss}}^{-1} = 0.25$ ns. (a) population dynamics and (b) energy flux $\frac{d}{dt}\rho_{\text{RC},\text{RC}}(t)$ from the FMO complex to the reaction center. Parameters used: $\lambda = 35$ cm $^{-1}$, $\tau_c = 166$ fs and $T = 300$ K.

such as Haken-Strobl or Lindblad equations. The aim of this section is to illustrate the very basic concepts of transfer efficiency, average trapping time and environment-assisted transfer. Throughout this section, we describe the exciton dynamics within the approximative, secular Redfield approach. A more realistic and more complex study of the transfer efficiency including higher-order phonon processes and non-Markovian effects in the phonon bath is carried out in full detail in section 4.4.

We describe the exciton-phonon coupling within a secular Born-Markov approach. The time evolution of the reduced density operator is given by

$$\frac{d}{dt}\rho(t) = -\frac{i}{\hbar}[\mathcal{H}_S, \rho(t)] + \mathcal{L}_{\text{ex-phon}}\rho(t) + \mathcal{L}_{\text{ex-phot}}\rho(t) + \mathcal{L}_{\text{ex-RC}}\rho(t), \quad (4.15)$$

where operators $\mathcal{L}_{\text{ex-phot}}$ and $\mathcal{L}_{\text{ex-RC}}$ are defined according to eqs. (4.11) and (4.12). The Liouville operator for the exciton-phonon coupling (Appendix A.2.2) is defined as

$$\mathcal{L}_{\text{ex-phon}} = \sum_{m,\omega} \gamma_m(\omega) \mathcal{D}[V_m(\omega)]. \quad (4.16)$$

The coherent dynamics is expressed by the system Hamiltonian

$$\mathcal{H}_S = \mathcal{H}_{\text{ex}} + \mathcal{H}_0 + \mathcal{H}_{\text{trap}}, \quad (4.17)$$

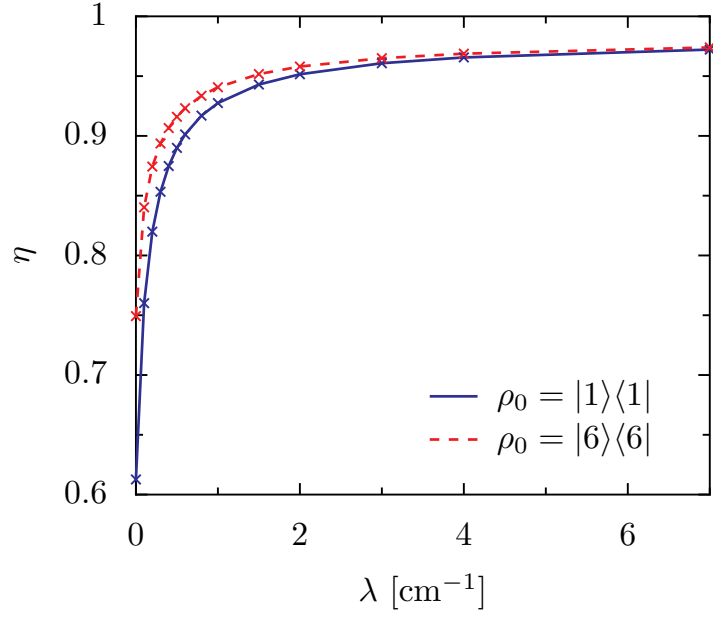


Figure 4.2: Transfer efficiency η , eq. (4.13), as a function of the reorganization energy for the two pathways of energy flow in the FMO complex, evaluated in the secular Born-Markov approximation. Solid line: initial population at BChl 1. Dashed line: initial population at BChl 6. Parameters used: $\tau_c = 166$ fs, $\Gamma_{RC}^{-1} = 2.5$ ps, $\Gamma_{loss}^{-1} = 0.25$ ns and $T = 300$ K.

including the exciton Hamiltonian \mathcal{H}_{ex} , the energy trap \mathcal{H}_{trap} , and the zero exciton state \mathcal{H}_0 .

Fig. 4.1(a) illustrates the population dynamics of the system under the presence of trapping and radiative decay. Initial population is located at BChl 1. We set the trapping and loss rate to $\Gamma^{RC} = (2.5 \text{ ps})^{-1}$ and $\Gamma^{loss} = (0.25 \text{ ns})^{-1}$. During the time evolution energy is dissipated and the population is transferred to BChl 3. Afterwards, trapping to the reaction center is the dominant process and the population in the reaction center $\rho_{RC,RC}$ steadily increases. Almost the whole population reaches the reaction center and only a small part of the electronic excitations gets lost due to exciton recombination. The population of the ground state ρ_{00} , counting energy losses, remains below 0.02. The population flux toward the reaction center is quantified by $\frac{d}{dt}\langle RC|\rho(t)|RC\rangle$, and is depicted in Fig. 4.1(b). The population flux to the reaction center increases rapidly for short times and reaches its maximum after approximately 1 ps, corresponding to the timescale of the thermal relaxation. $\frac{d}{dt}\langle RC|\rho(t)|RC\rangle$ is related to the average trapping time eq. (4.14). The average trapping time to the reaction center

$\langle t \rangle = 5.07$ ps obtained is much faster than the exciton lifetime, leading to the high transfer efficiency of 0.98.

High transfer efficiency is only attained in the presence of coupling to noise. For example a purely coherent dynamics yields a slow energy transfer $\langle t \rangle = 92.9$ ps and efficiency drops to $\eta = 0.61$. The reason is that the coherent exciton dynamics within the FMO complex takes place in nearly disjunct subspaces of the exciton system. For example, the subspace of the strongly coupled dimer pair BChl 1 and BChl 2 is nearly decoupled from the subspace of the targets BChl 3 and BChl 4. Coupling to noise opens an indirect transfer channel via energy exchange with the phonon bath and bridges these subspaces [52, 55, 56]. We illustrate environment-assisted transfer in Fig. 4.2, where we plot the transfer efficiency η , eq. (4.13) against reorganization energy λ . The coherent dynamics is represented by $\lambda = 0$ cm⁻¹. Both energy pathways (initial population at BChl 1 or BChl 6) show a higher transfer efficiency with increasing coupling to the environment. A small coupling $\lambda = 2$ cm⁻¹ is already enough to bridge the disjunct subspaces. This leads to a high transfer efficiency above 0.95.

4.4 Trapping under the influence of non-Markovian noise

Parts of this section have been published in Kreisbeck *et al.* [78].

Previous transfer efficiency studies of the FMO complex either rely on second order perturbation theory, such as the secular Born-Markov approximation [57, 62], or are based on an even more rudimentary level, such as the Haken-Strobl model [52, 60, 54, 55]. As we show in section 3.4, memory effects in the bath correlations, as well as the higher-order phonon processes, yield non-negligible contributions to the exciton dynamics. An accurate description of the exciton-phonon coupling is provided by HEOM. However, studying the transfer efficiency requires the incorporation of trapping and radiative decay, neither of which are captured in the original version of HEOM (section 3.3). In Appendix A.3, we derive a combined masterequation (ME)-HEOM approach that treats parts of the system, such as trapping and radiative decay, within a Markovian second order perturbation theory, while temporal correlations and higher-order phonon processes in the coupling to the phonon bath are incorporated within the HEOM technique. ME-HEOM gives accurate results for energy trapping in LCHs for a wide range of reorganization energies, ranging from the weak to the strong coupling regime.

We use ME-HEOM to investigate the influence of non-Markovian effects on the transfer efficiency. We show that, in the intermediate and strong coupling regimes

approximative methods such as the full Redfield equations and the secular Born-Markov approximation introduced in Appendix A.2 fail to predict correct results. We further explore the optimal transport condition with respect to the exciton-phonon coupling strength. The ME-HEOM yields qualitatively different results than previous studies of transport optimality in the FMO complex that employ the approximative generalized Bloch-Redfield (GBR) approach [59].

Within the ME-HEOM formalism, the hierarchically coupled equations of motion for the reduced density operator are given by

$$\begin{aligned} \frac{d}{dt}\rho(t) = & -\frac{i}{\hbar}[\mathcal{H}_S, \rho(t)] + (\mathcal{L}_{\text{ex-phot}} + \mathcal{L}_{\text{ex-RC}})\rho(t) \\ & + \sum_{m=1}^7 iV_{m,\text{phon}}^\times \sigma^{(0,\dots,n_m=1,\dots,0)}(t) \end{aligned} \quad (4.18)$$

with

$$\begin{aligned} \frac{d}{dt}\sigma^{(n_1,\dots,n_7)}(t) = & -\frac{i}{\hbar}[\mathcal{H}_S, \sigma^{(n_1,\dots,n_7)}(t)] \\ & + (\mathcal{L}_{\text{ex-phot}} + \mathcal{L}_{\text{ex-RC}} - \sum_{m=1}^7 n_m \gamma_m) \sigma^{(n_1,\dots,n_7)}(t) \\ & + \sum_{m=1}^7 iV_{m,\text{phon}}^\times \sigma^{(n_1,\dots,n_m+1,\dots,n_7)}(t) \\ & + \sum_{m=1}^7 n_m \theta_m \sigma^{(n_1,\dots,n_m-1,\dots,n_7)}(t). \end{aligned} \quad (4.19)$$

The ME-HEOM hierarchy basically corresponds to the one derived for the isolated FMO complex (detached from the reaction center, no trapping, no energy losses) eqs. (3.21) and (3.22). The influence of the loss and of the trapping channel leads to a slight modification of the hierarchy. The operators $\mathcal{L}_{\text{ex-RC}}$ and $\mathcal{L}_{\text{ex-phot}}$ (eqs. (4.11) and (4.12)) have to be applied in addition to the density operator $\rho(t)$. The same holds for the equation of motion of the auxiliary matrices that define the complete hierarchy. More details about the concepts of ME-HEOM are given in Appendix A.3 and Kreisbeck *et al.* Ref. [78].

Fig. 4.3 shows the average trapping time as a function of the reorganization energy. Initial population is located at BChl 1. Since increasing the coupling strength to the environment requires higher truncation levels in the hierarchy, we adapt the truncation $N_{\text{max}} = N$ in such a way that the difference in trapping time between $N_{\text{max}} = N$ and $N_{\text{max}} = N + 1$ is below 0.02 ps. Depending on the reorganization energy, the numerical effort is very demanding. For a large reorganization energy $\lambda = 300 \text{ cm}^{-1}$ we need a truncation level $N_{\text{max}} = 16$. The corresponding HEOM calculation would take more than one month on a single

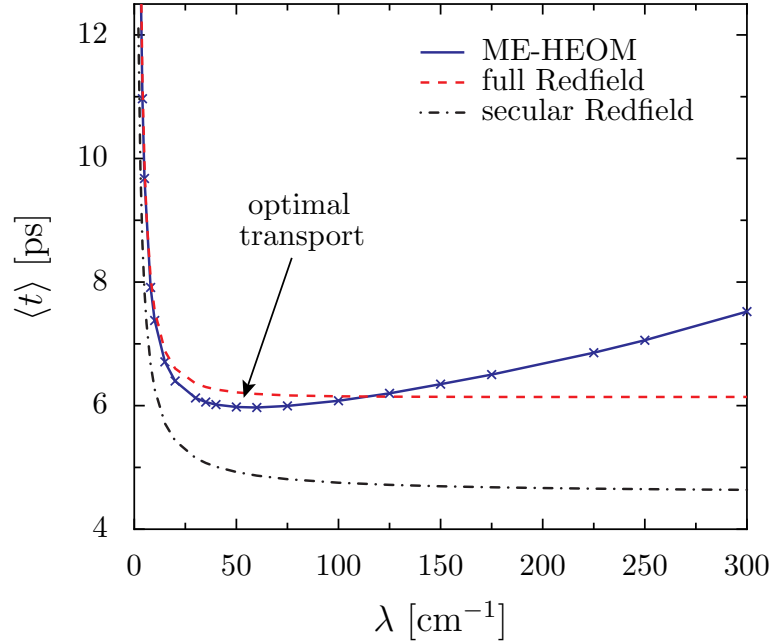


Figure 4.3: Average trapping time as a function of reorganization energy λ for the initial population at BChl 1. Comparison of ME-HEOM with the full Redfield equations and the secular Born-Markov approximation. Parameters used: $\tau_c = 166$ fs, $\Gamma_{\text{RC}} = 2.5$ ps, $\Gamma_{\text{loss}} = 0.25$ ns and $T = 300$ K.

CPU, which illustrates the numerical complexity of the results shown in Fig. 4.3. Such calculations are only accessible due to our efficient GPU implementation of the ME-HEOM approach that leads to a 450-fold reduction in computation time, see Kreisbeck *et al.* Ref. [78].

In Fig. 4.3 we plot the average trapping time as a function of the reorganization energy λ that adjusts the coupling strength to the phonon bath. Coupling to the phonon bath aids transport, and the transfer to the reaction center becomes faster with increasing reorganization energy. There is an optimal reorganization energy $\lambda_{\text{opt}} \approx 55 \text{ cm}^{-1}$ that corresponds to minimal trapping time $\langle t \rangle_{\text{opt}} = 6.0$ ps leading to a high transfer efficiency of $\eta = 0.976$. Only in the strong coupling regime does trapping time increase, and leaves the optimality condition. The optimality is robust against variations in reorganization energy. Between $\lambda = 20 \text{ cm}^{-1}$ and $\lambda = 150 \text{ cm}^{-1}$, for example, the average trapping time is below 6.4 ps and thus close to the minimal trapping time. Robustness of the efficient energy transfer is an important criterion since organisms like green sulfur bacteria live in diverse environments. Small changes in the environment must not result in dramatic effects in the functional role of the FMO complex. Neither the secular Born-Markov ap-

proximation nor the full Redfield equations yield the minimum average trapping time. In both cases, the average trapping time decreases monotonically with the reorganization energy. The secular Born-Markov approximation overestimates the timescale of thermalization, see section 3.4, which guides the population toward the low energy states of BChl 3 and 4. Hence, the secular Born-Markov approximation predicts transfer to the reaction center that is too fast compared to the exact ME-HEOM results. It is only in the weak coupling limit, that is for small reorganization energies below $\lambda = 10 \text{ cm}^{-1}$, that we find a good level of agreement between the full Redfield equations and ME-HEOM. Comparing our exact results with those obtained within the GBR approximation Ref. [59], Fig. 2(a), we find qualitative differences. Although GBR is able to reproduce the optimality of the average trapping time as a function of the reorganization energy, GBR fails to predict the strong increase in average trapping time for large reorganization energies.

4.5 Optimal design of energy funneling in the FMO complex

Parts of this section have been published in Kreisbeck *et al.* [78].

Evolution and natural selection force biological organisms to optimize their vitally important functions. For green sulfur bacteria, efficient light harvesting is essential to survive under extremely low light intensities. This suggests that the FMO complex is not just a random arrangement of BChls, but that the structure has evolved to optimize fast energy transfer. Here, we propose an optimization strategy based on a well-balanced detuning of the site energies. A large detuning is required to get a sufficiently large energy gradient. In this regime, the low energy states become highly populated in the thermal state, yielding efficient energy funneling. But on the other hand detuning must be kept as small as possible, because large detuning effectively decouples the BChls from each other, hindering efficient coherent energy flow. Coherent energy flow is most efficient if the site energies are in resonance; that is if all site energies are equal. This regime does not fulfill the criteria of energy funneling. In conclusion, transport optimality requires a compromise between resonant coherent energy transfer and environment-assisted energy funneling.

In order to investigate the interplay of coherent energy flow and environment-assisted energy funneling, we shift the site energies of BChl 3 and 4 by ΔE either to higher ($\Delta E > 0$) or lower energies ($\Delta E < 0$), $\varepsilon_{3/4} \rightarrow \varepsilon_{3/4} + \Delta E$. The upper panel of Figure 4.4 depicts the transfer efficiency as a function of the temperature and energy shift ΔE . The lower panel of Fig. 4.4 illustrates both

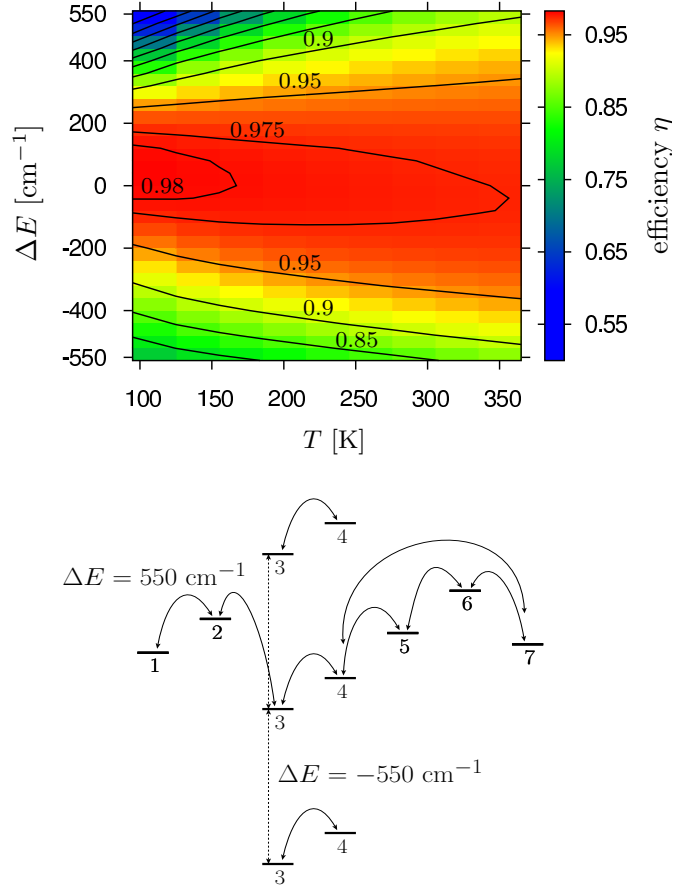


Figure 4.4: Upper panel: Transfer efficiency η as a function of the shifts ΔE in the site energies of BChl 3 and 4, $\varepsilon_{3/4} \rightarrow \varepsilon_{3/4} + \Delta E$ and temperature. Parameters used: $\lambda = 35 \text{ cm}^{-1}$, $\tau_c = 166 \text{ fs}$, $\Gamma_{RC} = 2.5 \text{ ps}$ and $\Gamma_{\text{loss}} = 0.25 \text{ ns}$. Lower panel: energetic structures of the original FMO complex and of the energy shifts $\Delta E = \pm 550 \text{ cm}^{-1}$.

the energetic structure of the original FMO complex (listed in Table 2.1) and the structure for large shifts $\Delta E = \pm 550 \text{ cm}^{-1}$. The energy transfer process is numerically simulated with ME-HEOM. There are three different transport regimes. In regime (i), the site energies $\varepsilon_{3/4}$ are shifted to very low energies ($\Delta E = -550 \text{ cm}^{-1}$). This gives rise to a large energy gradient, and the thermal state almost exclusively populates the target states BChl 3 and 4. However, since the target states are strongly detuned from the remaining BChls, the thermal state is approached slowly. Overall, the transfer efficiency is reduced compared to the original structure of the FMO complex ($\Delta E = 0 \text{ cm}^{-1}$). Regime (ii) corresponds to the intermediate configuration $\Delta E = +250 \text{ cm}^{-1}$ in which all

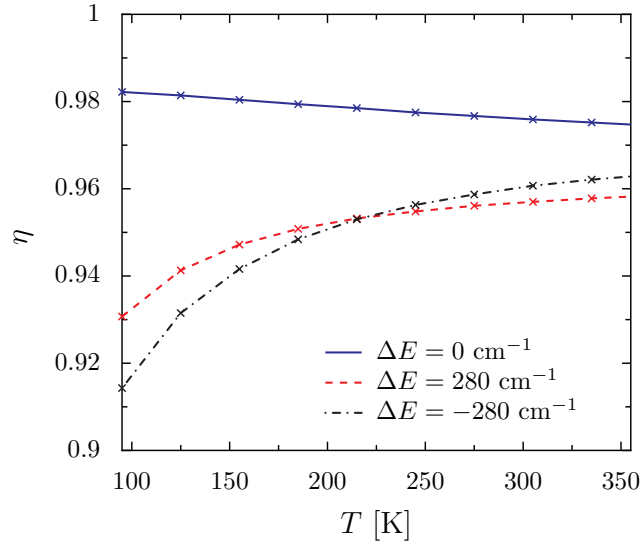


Figure 4.5: Efficiency η as a function of the temperature for different energy shifts ΔE . We use the same parameters as in Fig. 4.4. Depending on shifts to higher ($\Delta E = 280 \text{ cm}^{-1}$) or lower energies ($\Delta E = -280 \text{ cm}^{-1}$), either the thermal population of the target states BChls 3 and 4 or the temperature induced dephasing dominates. For the original structure of the FMO complex ($\Delta E = 0 \text{ cm}^{-1}$), the positive effect of the increasing dephasing rate with temperature, and the negative effect of the population of higher energy states due to thermal activation, compensate for each other and the transfer efficiency remains almost constant with temperature.

site energies are in the same range. In regime (ii), there is a dominant resonant coherent energy transfer, but the FMO complex loses its structure as an energy funnel. In regime (iii) ($\Delta E = +550 \text{ cm}^{-1}$), the site energies $\varepsilon_{3/4}$ are the highest and are detuned from the others. Thus, there is neither efficient energy funneling nor efficient resonant coherent energy transfer.

In conclusion, we find that the original structure of the FMO complex, which is a compromise between energy funneling (regime (i)) and resonant coherent energy flow (regime (ii)), matches the condition for optimal energy transfer to the reaction center. The optimality in the exciton structure of the FMO complex is robust against variations $\Delta E \pm 200 \text{ cm}^{-1}$. This is essential for the FMO complex, since slow fluctuations in the protein environment give rise to static disorder in the site energies. For the FMO complex, static disorder is estimated to be in the range between 60 cm^{-1} and 140 cm^{-1} [39, 41, 47].

We further explore the mechanisms of environment-assisted energy transfer.

Environment-assisted transfer involves two physical processes, (i) thermal relaxation to the low energy states, Kreisbeck *et al.* [78], and (ii) dephasing, which bridges disjunct subspaces of the FMO complex [52, 54]. The interplay of these mechanisms manifests itself in the temperature dependency of the transfer efficiency. In particular, the shifts in site energies $\varepsilon_{3/4}$ highlight the interplay of the two different mechanisms. In Fig. 4.5, we study the transfer efficiency as a function of temperature for positive and negative energy shifts $\Delta E = \pm 280 \text{ cm}^{-1}$, and for the original structure of the FMO complex $\Delta E = 0 \text{ cm}^{-1}$. For shifts to higher energies $\Delta E = +280 \text{ cm}^{-1}$, the targets BChl 3 and 4 are no longer the BChls with the lowest site energies. Hence, thermal activation is required to populate these states. Thus efficiency improves with higher temperature. Here, the population of the thermal state dominates the temperature dependency of the efficiency. For shifts to lower energies $\Delta E = -280 \text{ cm}^{-1}$, on the other hand, dephasing dominates the transfer process. The site energies $\varepsilon_{3/4}$ are strongly detuned from the others, and the subspace of the dimer pair BChl 3 and 4 is nearly decoupled from the other BChls. Hence, strong dephasing is required to bridge the nearly disjunct subspaces of the FMO complex. Since the dephasing rate increases linearly with temperature [59], the transfer efficiency increases with temperature as well, although thermal activation reduces the preference of the low energy states BChl 3 and 4. Depending on shifts to higher or lower energies, different mechanisms dominate. The original structure of the FMO complex ($\Delta E = 0 \text{ cm}^{-1}$) almost keeps the influence of dephasing and thermalization balanced. The negative influence of the thermally enhanced population of higher energy levels slightly outperforms the positive effect of stronger dephasing leading to a small decrease in efficiency with higher temperatures.

Summarizing this section, we have demonstrated that energy transfer in the FMO complex relies on an elaborate balance between coherent delocalized energy flow and environment-assisted transport channels. The latter is a combination of thermal relaxation and dephasing, for which the interplay of both processes determines the temperature dependency of the transfer efficiency. The alignment of the site energies in the FMO complex is optimized to match the conditions for efficient unidirectional energy flow. This involves coherent energy transfer, thermal relaxation and indirect transfer channels between disjunct subspaces via coupling to the phonon bath.

4.6 Coherence and transfer efficiency

4.6.1 Introduction

There are several qualitative and quantitative studies about the functional role of coherence [55, 61, 64, 62, 53] for fast energy transfer. Those works rely on Redfield

equations, the secular Born-Markov approximation or rudimentary Haken-Strobl models that describe the reorganization process inadequately. Moreover, within such approximative methods no long lasting coherent beatings are present in the exciton population dynamics. This is illustrated in chapter 3, Fig. 3.3. However, a proper incorporation of the sluggish phonon bath gives rise to long-lasting quantum beatings in the population dynamics [43]. The timescale of beatings in the population dynamics depends on the phonon relaxation timescale τ_c [43]. We use the ME-HEOM approach to study the transfer efficiency as a function of τ_c . This yields information about the relationship between fast energy transfer to the reaction center and long-lasting beatings in the population dynamics. Furthermore we follow the ideas of section 4.5 and carry out investigations about the interplay between noise and coherence. We show that noise is not just a source of decoherence, but also affects the distribution of coherence in the FMO complex in a subtle way. This influences the energy transfer process. We propose that the coupling to the environment induces a redistribution of coherence that enhances the transfer efficiency.

In section 4.6.2, we introduce measures to quantify coherence in the exciton system. We follow Fassioli and Olaya-Castro [62] and introduce the entanglement yield. The entanglement yield quantifies the amount of coherence within the exciton system during the process of energy transfer to the reaction center. In Ref. [62], Fassioli and Olaya-Castro use the entanglement yield to quantify the distribution of coherence in the FMO complex for the very weak coupling regime (close to the purely coherent dynamics) between the exciton system and the vibrational environment. In this section, we use the entanglement yield to characterize the influence of coherence for the energy transfer process within the FMO complex for the relevant intermediate and strong coupling regimes. In section 4.6.3, we use the timescale of temporal correlations as control parameter for generating long-lasting quantum beatings and for drawing conclusions about the ways in which the transfer is affected. We show that long-lasting quantum beatings in the population dynamics are not necessarily related to large amount of coherence in the exciton system. This is in contrast to previous interpretations of the long-lived quantum beatings in the population dynamics [43, 183]. Finally, in section 4.6.4, we use the entanglement yield to quantify the relevance of coherence in the transfer process. In particular, we study the entanglement yield as a function of the reorganization energy and demonstrate that coupling to noise rearranges the coherence within the BChls of the FMO complex. An equally distributed entanglement involving all BChls yields the optimal condition for efficient transport. We close this chapter with a short conclusion in section 4.6.5.

4.6.2 Coherence measures and entanglement yield

In this section we follow the ideas of Fassioli and Olaya-Castro [62]. We quantify coherence by bipartite concurrence [191]

$$C_{mn}(t) = 2|\rho_{mn}(t)|. \quad (4.20)$$

The sum of all bipartite tangles $\tau_{mn}(t) = (C_{mn}(t))^2$ is then a measure for the total amount of coherence

$$E_T(t) = 4 \sum_{n>m} \tau_{mn}(t) = 4 \sum_{n>m} |\rho_{mn}(t)|^2. \quad (4.21)$$

In order to measure the average coherence during the complete process of energy transfer to the reaction center, we define the entanglement yield introduced by Fassioli and Olaya-Castro [62]

$$\Phi_T = \frac{1}{\eta} \int_0^\infty dt' E_T(t') \left(\frac{d}{dt} \rho_{RC,RC}(t) \right)_{t=t'}. \quad (4.22)$$

The notation for the entanglement yield is historical and does not account for recent theoretical investigations that point out that coherence and entanglement are non-equivalent measures [192] in the single exciton dynamics of LHCs. Nevertheless we retain the nomenclature of the original work by Fassioli and Olaya-Castro. The entanglement yield describes the average amount of coherence for times at which trapping is most likely to occur and hence at which coherence significantly influences the transfer process. Analogous to eq. (4.22), we define the bipartite entanglement yield

$$\Phi_{nm} = \frac{1}{\eta} \int_0^\infty dt' \tau_{mn}(t') \left(\frac{d}{dt} \rho_{RC,RC}(t) \right)_{t=t'}. \quad (4.23)$$

This describes the amount of coherence shared between BChl n and BChl m during the energy transfer to the reaction center. Throughout this chapter, we use the Hamiltonian of table 2.1, and assume that BChl 3 is linked to the reaction center [52, 59, 62]. For the trapping and the recombination, we set the rates to $\Gamma_{\text{loss}}^{-1} = 1$ ns and $\Gamma_{\text{RC}}^{-1} = 1$ ps [52, 61, 59, 62].

4.6.3 Population beatings, coherence and transfer efficiency

From the theoretical side, it is a hard task to extract relationships between coherence and transfer efficiency. Indirect measures, like the entanglement yield [62], have been invented. The best case scenario would be if there were system parameters that allowed the direct control of the amount of coherence in the

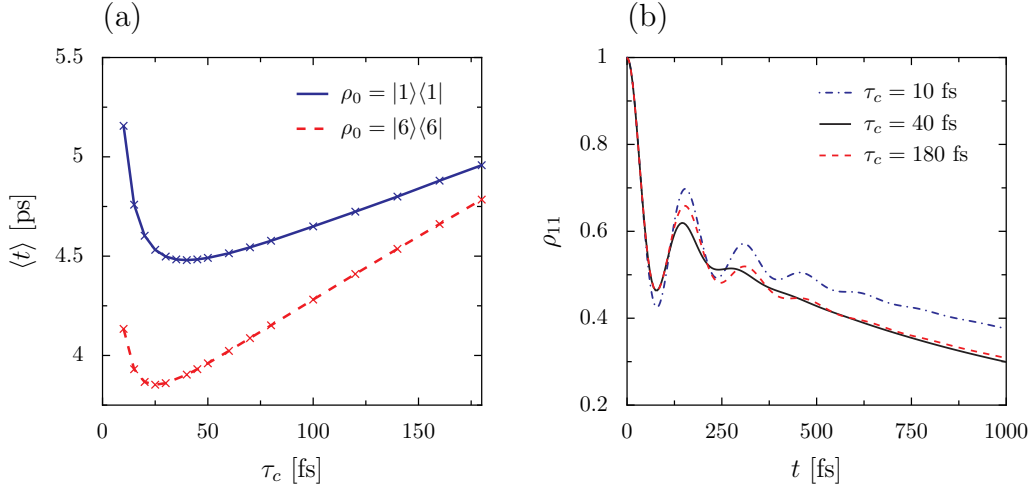


Figure 4.6: (a) average trapping time as a function of the phonon relaxation timescale τ_c . Solid line: initial population at BChl 1. Dashed line: initial population at BChl 6. (b) population dynamics of the isolated (no radiative decay, no trapping) FMO complex with the initial population at BChl 1 for different phonon relaxation timescales. Parameter used: $\lambda = 35 \text{ cm}^{-1}$, $\Gamma_{\text{RC}}^{-1} = 1 \text{ ps}$ and $\Gamma_{\text{phot}}^{-1} = 1 \text{ ns}$.

exciton system. The phonon relaxation timescale τ_c might be such a parameter. Ishizaki and Fleming point out that long-lived beatings in the population dynamics originate from a coherent interplay between the excitonic system and the sluggish vibrational environment [43, 174]. The slower the phonon relaxation becomes the longer the observed beatings in the population dynamics [43] are. The lifetime of those beatings in the population dynamics is interpreted as the life-time of the coherence in the exciton system [43, 183].

Our idea is to adjust the appearance of beatings in the population dynamics via the phonon relaxation timescale τ_c . We expect that, if coherence supports efficient energy transfer, the longer the beatings last, the better the efficiency will become. Fig. 4.6(a) depicts the average trapping time as a function of τ_c . Both pathways yield an optimal phonon relaxation timescale τ_c^{opt} corresponding to the minimal trapping time and, therefore, to the maximal transfer efficiency. For the initial population at BChl 1, we obtain $\tau_c^{\text{opt}} \approx 40 \text{ fs}$ and minimal trapping time $\langle t \rangle_{\text{min}} = 4.48 \text{ ps}$. The pathway with an initial excitation at BChl 6 yields faster population trapping $\langle t \rangle_{\text{min}} = 3.85 \text{ ps}$. In addition, optimal transfer is obtained for shorter correlation times $\tau_c^{\text{opt}} \approx 25 \text{ fs}$. Comparing the optimal transfer conditions for the initial population at BChl 1 with the corresponding population dynamics, shown in Fig. 4.6(b), we find that optimal energy transfer is related to the situation in which beatings in the population dynamics decay the

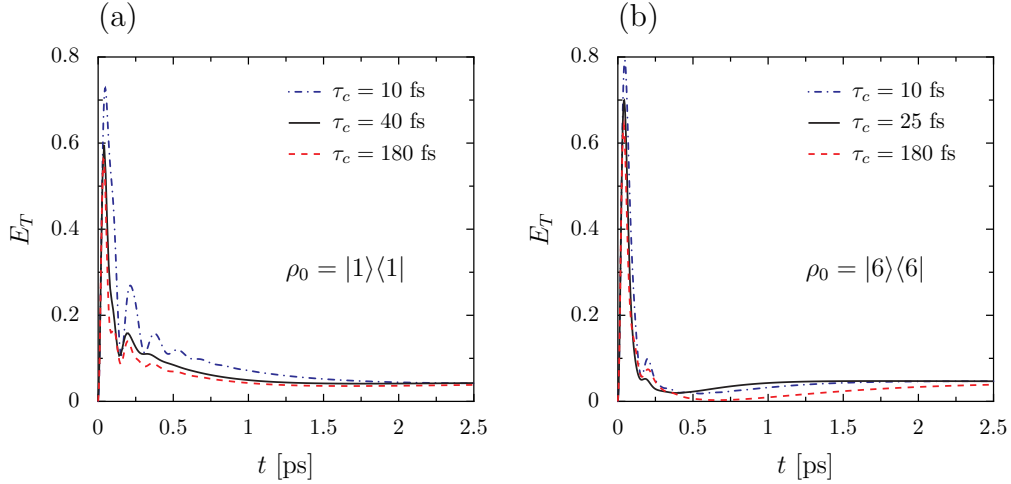


Figure 4.7: Measure for coherence E_T , eq. (4.21) during the energy transfer process within the isolated FMO complex for different phonon relaxation timescales τ_c . Parameters used: $T = 300$ K and $\lambda = 35$ cm $^{-1}$ (a) initial population at BChl 1 and (b) initial population at BChl 6.

fastest. It seems that coherence should be avoided to obtain maximal efficiency.

However, this conclusion is drawn too quickly. Considering the coherence measure $E_T(t)$, eq. (4.21), we obtain a monotonic decrease in coherence with an increasing phonon relaxation timescale τ_c (see Fig. 4.7). For example in Fig. 4.7(a), the coherence measure $E_T(t)$ for $\tau_c = 40$ fs is, for all times, larger than the one for $\tau_c = 180$ fs, although the latter shows beatings twice as long in the population dynamics. Hence, the conclusion that beatings in the population dynamics imply a strong coherence in the exciton system is misleading. Although stated otherwise [43, 183], long-lived beatings in the population dynamics do not necessarily imply long-lasting coherence in the exciton system.

For a slow phonon-relaxation timescale $\tau_c = 180$ fs the population beatings are due to an interplay between two physical processes. On the one hand, the parameter τ_c affects the spectral density and, in particular the dephasing rate $\Gamma^* = 4\lambda k_B T \tau_c$. The larger τ_c gets, the larger the dephasing rate becomes, enforcing a fast decoherence in the exciton dynamics. On the other hand, there is a flow of information between the exciton and the phonons [170]. Coherent information is stored in the bath memory. This information is played back to the exciton system at later times. The coherent energy trade between bath and system affects the exciton dynamics in a complex way, as is discussed in detail in chapter 6. In total, a slow phonon relaxation timescale τ_c results in a reduced coherence, superposed by long-lasting beatings in the populations dynamics.

In conclusion, we find that there is no one-to-one correspondence between co-

herence and population beatings. Therefore, our idea of controlling coherence with the phonon relaxation timescale does not work. Nevertheless, we can extract information from our analysis of the transfer efficiency as a function of τ_c in relation to the functional role of coherence to fast energy transfer. Fast phonon relaxation ($\tau_c=10$ fs) effectively reduces the coupling to the vibrations and a weak coupling regime is approached (see section 3.5). In this regime, noise-assisted transfer [57, 52, 54, 56] is inefficient, and energy funneling to the reaction center is slow. This explains the higher average trapping time for small τ_c obtained in Fig. 4.7(a). On the other hand, slow phonon relaxation ($\tau_c=180$ fs) induces strong decoherence. For the energy pathway starting from BChl 6, for instance, the populations become localized for a time interval between 0.5 ps and 1 ps, see Fig. 4.7(b), where the coherence measure E_T almost vanishes for $t \in [0.5, 1]$ ps. This localization hinders energy transfer through the BChls. This explains the fast increase in average trapping time for large τ_c . Optimal transfer is obtained for the intermediate regime $\sim \tau_c = 25-40$ fs. This corresponds to the situation in which the coherent exciton dynamics overcomes localization but coupling the environment is strong enough to allow for efficient environment-assisted transport.

4.6.4 Environmentally-induced redistribution of coherence

In section 4.6.3, optimal energy transfer results as an interplay between thermalization, generating unidirectional energy funneling toward the reaction center and coherent transfer to overcome energy localization. However, the nature of coherence is not necessarily helpful. For example, strong coherence between the initial excitation at BChl 1 and 2 gives rise to long-lasting Rabi oscillations between these BChls. In this case, there is hardly any transfer to the reaction center. Employing coherence for fast energy transfer requires a mechanism that destroys such Rabi oscillations. Instead a uniformly spread coherence involving all BChls needs to be generated. This would allow for a continuous energy flow through the BChls to the reaction center. Our idea is that the coupling to the vibrational environment arranges the coherence within the BChls of the FMO complex in a useful way. This idea is motivated by the fact that thermalization redistributes populations according to the thermal state. During this process, the coherences are also affected and distributed more uniformly within the complex. We quantify the influence of coherence on the transfer processes by the entanglement yield Φ , eq. (4.22). Comparing the changes in the entanglement yield with changes in the trapping time as a function of reorganization energy, depicted in Fig. 4.8(a), allows us to deduce conclusions about the influence of coherence on the functionality of fast energy transfer.

In the following, we focus on the idea that the coupling to the environment redistributes coherence in such a way that a fast and continuous energy flow to-

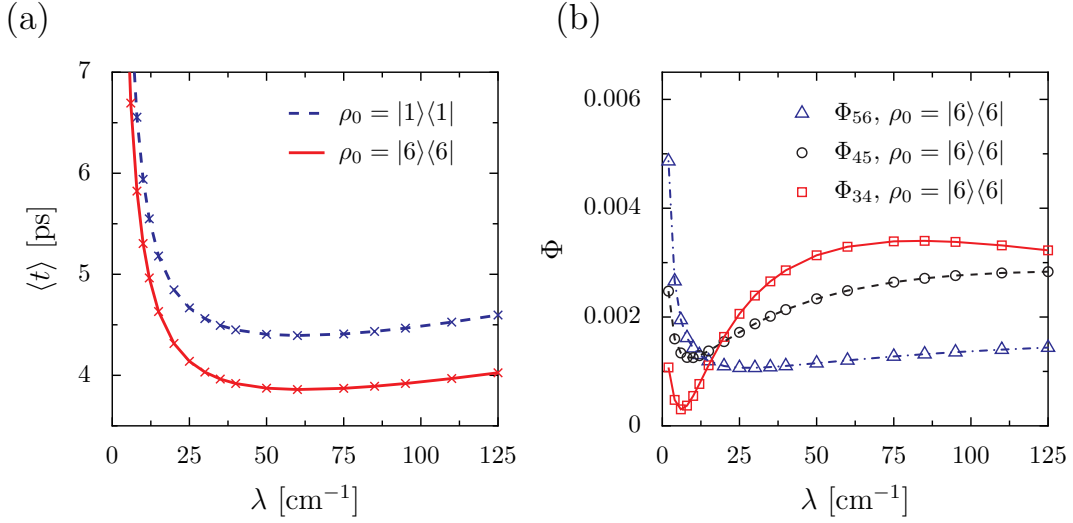


Figure 4.8: (a) trapping time as a function the of reorganization energy λ . Solid line: initial population at BChl 6. Dashed line: initial population at BChl 1. (b) bipartite entanglement yield Φ_{56} , Φ_{45} and Φ_{34} as a function of the reorganization energy λ for the initial population at BChl 6. Parameters used: $T = 300$ K and $\tau_c = 50$ fs, $\Gamma_{\text{RC}}^{-1} = 1$ ps, $\Gamma_{\text{phot}}^{-1} = 1$ ns.

ward the reaction center emerges. For the initial excitation at BChl 6 the main energy pathway goes via BChls 5, 4 and 3. Fig. 4.8(b) depicts the corresponding bipartite entanglement yield (eq. (4.23)) Φ_{56} , Φ_{45} and Φ_{34} as a function of reorganization energy. Increasing the coupling to the vibrational environment induces decoherence, and the entanglement yield Φ_{56} drops. Energy dissipation reshuffles the populations according to the thermal state. Since this process is not completely incoherent, distribution of coherence among the BChls is rearranged as well. With increasing the reorganization energy λ , the initially strong coherence of the donor dimer pair BChl 6 and BChl 5 is reduced, whereas the entanglement yield for the mediator dimer pair BChl 5 and 4, as well as for the acceptor dimer pair BChl 3 and 4 is simultaneously enhanced. In the optimal transfer regime, the reorganization energy λ is in the range between 40 cm^{-1} and 100 cm^{-1} (Fig. 4.8(a)). In this regime, the entanglement yield Φ_{34} shows a maximum. Furthermore Φ_{56} , Φ_{45} , and Φ_{34} are of the same order of magnitude and coherence is thus evenly distributed among BChls 6, 5 4 and 3. Spatially distributed coherence allows for a continuous energy flow from the antenna to the reaction center. The same mechanism holds for the initial population at BChl 1. Strong coherence between the donor dimer pair BChl 1 and 2 is destroyed, and coherence at the acceptor dimer pair BChl 3 and BChl 4 is generated.

4.6.5 Summary

For a Drude-Lorentz spectral density, beatings in the population dynamics are not related to purely electronic coherence, and arise from an entangled motion of the exciton system and the phonon bath. Hence, the optimality condition with respect to the phonon-relaxation time-scale τ_c is not related to the appearance of beatings in the population dynamics. Instead, the condition for an optimized energy transfer arises from mechanisms of environment-assisted transport. For the Drude-Lorentz spectral density, the phonon relaxation timescale adjusts the dephasing rate $\Gamma^* = 4\lambda k_B T \tau_c$. In the optimal transport regime, a sufficiently large dephasing rate bridges disjunct subspaces of the FMO complex. At the same time the dephasing rate is kept small enough, to avoid localization effects in the energy transfer.

We further analyze the entanglement yield as a function of the reorganization energy. The entanglement yield quantifies the relevance of coherence for the transfer process. In particular, we consider the bipartite entanglement yield that quantifies the coherence which is shared among neighboring BChls. We show that the coupling of the exciton system with the environment rearranges the distribution of coherence in the FMO complex. In the optimal transport regime, coherence is uniformly spread over all BChls of the FMO complex. This suggests that the unidirectional energy funneling is supported by a coherent delocalized energy transfer. This transfer is fast compared to a classical hopping. In particular, the presence of a strong coherence between BChls 3 and 4 illustrates the advantage of a coherent energy transfer. Energy funneling guides the excitons to the low energy levels BChl 3 and 4. However, only BChl 3 couples to the reaction center and a fast connection between BChl 4 and 3 is required. Within a classical picture, the excitons would be localized and the final step from BChl 4 to BChl 3 would be slow.

4.7 Conclusion and outlook

In this chapter, we incorporate trapping and exciton recombination and explore the efficiency of the energy transfer to the reaction center. We develop the ME-HEOM, a method that provides the advantage of including trapping and exciton recombination within the numerically efficient Born-Markov approach while fully capturing the non-Markovian and non-perturbative nature of the exciton-phonon coupling. Thus, the investigation of the energy transfer for the intermediate and strong coupling regimes, as well as for a slow phonon relaxation, becomes feasible.

Transfer optimality is found for parameter regimes in which the reorganization energy, the phonon relaxation timescale τ_c and the inter-site couplings J_{mn} are of the same order of magnitude. In summary, we find that the structure

of the exciton Hamiltonian of the FMO complex yields optimal energy transfer. The FMO complex balances the complementary coherent energy flow and environment-assisted transfer. Environment-assisted transfer is comprised of three mechanisms. Dephasing provides an indirect transport channel to bridge disjunct subspaces of the FMO complex [52, 54], and energy dissipation drives the exciton system to the low energy target states. Furthermore, coupling to the environment rearranges the distribution of coherence in the FMO complex. In the optimal transport regime, coherence is uniformly spread over all BChls of the FMO complex. All mechanisms together provide an unidirectional energy flow assisted by coherent transfer.

We demonstrate that coherent energy transfer supports a high transfer efficiency, and we explain underlying mechanisms. However, we cannot give quantitative statements about the relevance of coherence for the energy transfer. Hence, it remains unclear whether coherence is of vital importance for the energy transfer, or if coherence only leads to minor contributions. Rebentrost *et al.* in Ref. [53] estimate a contribution of coherence to the transfer efficiency of about 10 %. However, the investigations in Ref. [53] are based on the Born-Markov approach that underestimates the life-time of coherence but overestimates the influence of energy dissipation in the phonon bath. This suggests that coherence might even be more important. Quantifying the relevance of the coherence of the exciton dynamics to the transfer efficiency under realistic conditions is still an outstanding topic in the field.

5 Two-dimensional spectroscopy

5.1 Introduction

Mechanisms of the energy transfer in LHCs are experimentally studied by spectroscopic techniques. Linear spectroscopy provides information about the energetic structure of the coupled BChls, while the more advanced two-dimensional echo (2d-echo) spectroscopy is used to monitor the time-resolved exciton dynamics in LHCs. 2d-echo spectroscopy elucidates the process of thermal relaxation and, in particular, the nature of the coupling to a noisy environment manifests itself in the peak shapes of the spectra [42, 46, 34]. Furthermore, by varying the parameters of the applied laser pulses in a clever way, the full density matrix of the single exciton manifold can be reconstructed [193].

In section 5.2, we briefly discuss the concepts of the experimental setup and provide the theoretical framework for the simulation of 2d-echo spectra. The nonlinear response function formalism employed goes back to Mukamel and Loring [194]. In section 5.3, we recapitulate the basic features of 2d-echo spectra and illustrate how to read 2d-echo spectra. In particular, we highlight the effects of electronic coherence, dephasing, and energy relaxation. Those processes are the basic ingredients for the efficient energy transfer established in chapter 4.

5.2 Two-dimensional spectroscopy and its theoretical modeling

5.2.1 Experimental setup

Experimentally, 2-d spectra are obtained from third-order nonlinear spectroscopy, also called four-wave mixing. A schematic sketch of the setup is shown in Fig. 5.1. The system to be studied is probed by three incident laser pulses that hit the sample at times $\tau_1 = 0$, $\tau_2 = t_1$ and $\tau_3 = t_1 + T_{\text{delay}}$. The first two pulses are pump pulses that prepare the exciton system in a populating state. The third pulse probes the system and is separated from the second pump pulse by the delay time T_{delay} . Scanning through T_{delay} yields a time-resolved picture of the system

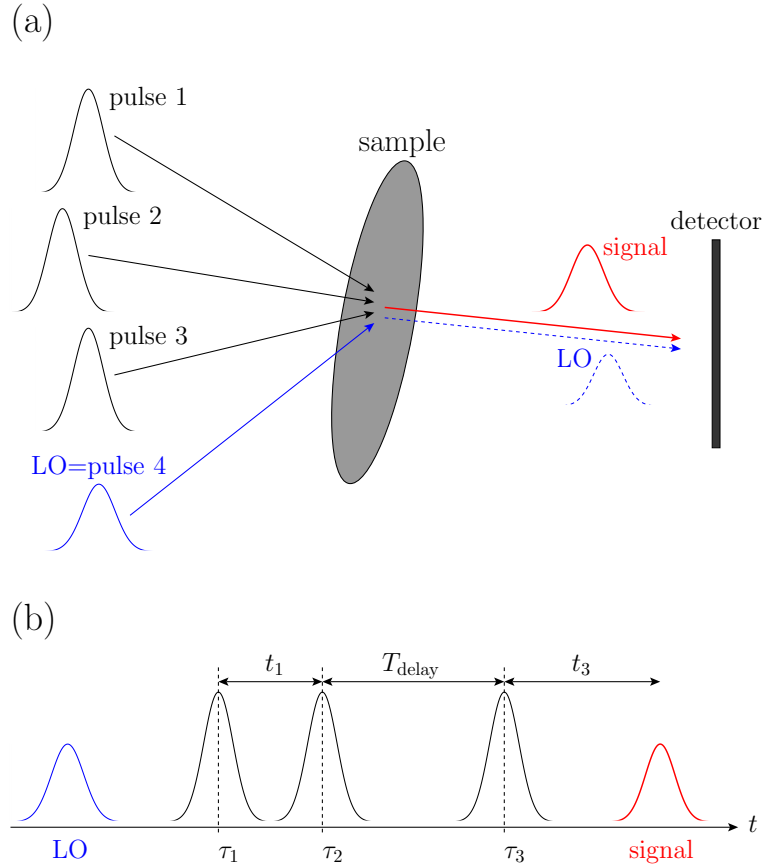


Figure 5.1: (a) sketch of the experimental setup of heterodyne third-order non-linear spectroscopy (four-wave mixing). Three incident laser pulses probe the sample. A fourth pulse, the local oscillator (LO), is used as a reference field for the outgoing signal. (b) sequence of the applied laser pulses in chronological order. The 2d-spectra are obtained by transforming the signal with respect to time t_1 and t_3 into the frequency domain. Scanning through delay time T_{delay} yields the time resolved exciton dynamics of the probed system.

dynamics. Heterodyne detection uses a fourth pulse, the local oscillator, as a reference field for the outgoing signal that is detected at time $t = t_1 + T_{\text{delay}} + t_3$. Heterodyne detection offers the advantage that the electric field carrying the complete phase information is measured [35, 38]. The sequence of laser pulses is illustrated in Fig. 5.1(b). The time intervals between the pulses have a physical meaning and can be interpreted as follows [35]: The first pulse creates a coherent superposition between the electronic ground state and the single exciton manifold. The time interval t_1 is called coherence time. The second pulse creates

a population in the exciton system and the corresponding dynamics is recorded by the delay time T_{delay} , also called population time. The third pulse initiates an outgoing signal and t_3 stands for the signal time. Further details about the experimental setup are given in [35, 36, 37].

Phase matching leads to two distinct directions of the outgoing signal and the total spectrum is divided into rephasing and non-rephasing parts [38]. Phase matching results from the much larger sample size in comparison to the optical wavelength. The sample consists of an ensemble of many molecules. The signals of the individual molecules superpose each other with random phases, giving rise to destructive interference in all directions that do not meet the phase matching condition [38]. Finally, the detected signal is Fourier transformed with respect to times t_1 and t_3 resulting in a two-dimensional *map* of the population of exciton states in the energy domain.

5.2.2 Theoretical description

The theoretical framework for the interpretation of 2d spectroscopy was developed in 1985 by Mukamel and Loring [194] who introduced a nonlinear response function formalism to simulate four-wave mixing signals. In the following, we briefly summarize the basic ideas behind this approach. For further reading, we refer the reader to a textbook by Mukamel [33], or to a more condensed outline of the fundamental concepts by Hamm [195].

The response of the probed system to an incident electric field is given by the macroscopic polarization. The polarization is given in dipole approximation by the expectation value of the dipole operator μ

$$P(t) = \text{Tr}\{\mu\rho(t)\}. \quad (5.1)$$

The density operator $\rho(t)$ describes the intrinsic dynamics of the probed system. We expand the polarization in powers of the electric field $E(t)$

$$P(t) = \sum_{i=1} \chi^{(i)} E(t)^i. \quad (5.2)$$

While in linear optics the polarization is characterized by the linear susceptibility $\chi^{(1)}$, in nonlinear optics higher orders in the electric field are relevant. In order to describe four-wave mixing signals, the polarization has to be expanded up to the third-order in the electric field. In dipole approximation, the interaction between the external electric field and the sample is given in dipole approximation by [189]

$$\mathcal{H}_{\text{field}} = \mu E(t). \quad (5.3)$$

We treat $\mathcal{H}_{\text{field}}$ as a perturbation and expand the dynamics of the density operator in powers of the electric field strength

$$\tilde{\rho}(t) = \tilde{\rho}_0 + \sum_{n=1} \left(-\frac{i}{\hbar}\right)^n \int_{t_0}^t d\tau_n \int_{t_0}^{\tau_n} d\tau_{n-1} \dots \int_{t_0}^{\tau_2} d\tau_1 E(\tau_n) E(\tau_{n-1}) \dots E(\tau_1) \times [\tilde{\mu}(\tau_n), [\tilde{\mu}(\tau_{n-1}), \dots [\tilde{\mu}(\tau_1), \rho_0] \dots]]. \quad (5.4)$$

Operators in the interaction picture with respect to the unperturbed system dynamic are denoted with a tilde. We set the initial preparation time $t_0 \rightarrow -\infty$, and substitute $t_1 = \tau_2 - \tau_1$, $t_2 = \tau_3 - \tau_2$ and $t_3 = t - \tau_3$. We insert eq. (5.4) into eq. (5.1) and collect all terms that are of third order in the electric field E . The third-order polarization is then given by

$$P^{(3)}(t) = \int_0^\infty dt_3 \int_0^\infty dt_2 \int_0^\infty dt_1 E(t - t_3) E(t - t_3 - t_2) E(t - t_3 - t_2 - t_1) \times S^{(3)}(t_3, t_2, t_1), \quad (5.5)$$

where we define the third-order response function as

$$S^{(3)}(t_3, t_2, t_1) = - \left(\frac{i}{\hbar}\right)^3 \text{Tr} \left\{ \tilde{\mu}(t_3 + t_2 + t_1) [\tilde{\mu}(t_2 + t_1), [\tilde{\mu}(t_1), [\tilde{\mu}(t_0), \rho(t_0)]]] \right\}. \quad (5.6)$$

The evaluation of the third-order response function requires that dipole operators be applied at four different times. The first three dipole operators (within the commutators) reflect the action of the three incident laser pulses on the system dynamics. The forth dipole operator has to be applied at time $t = t_3 + t_2 + t_1$, and appears in combination with the trace operation. This last operation describes the macroscopic response of the system according to eq. (5.1).

We assume that the laser pulses are separated in the time domain and, therefore, that time ordering is well defined. In this case, we can use the impulsive limit of delta-shaped envelopes for the three incident laser pulses

$$E_i(t) = E_i \delta(t - \tau_i) e^{\pm i \omega_i t} e^{\mp k_i r}. \quad (5.7)$$

The detected signal is then proportional to the third-order response function $S^{(3)}(t_3, T_{\text{delay}}, t_1)$, where t_1 , T_{delay} and t_3 correspond to the time intervals that define the sequence of the laser pulses (see Fig. 5.1). Since the sample size is much larger than the wavelength of the pulses, random phases interfere destructively and the outgoing signal is highly directed. In 2d spectroscopy, phase matching in combination with the rotating wave approximation, in which fast oscillatory terms are neglected, yields distinct outgoing signals $k_S = \pm k_1 \pm k_2 \pm k_3$.

Experimental setups commonly detect the rephasing (RP) component with a signal along the wave vector $k_S = -k_1 + k_2 + k_3$, and detect the non-rephasing

(NR) signal with $k_S = k_1 - k_2 + k_3$. The signal $S^{(3)}(t_3, T_{\text{delay}}, t_1)$ is Fourier transformed with respect to time intervals t_1 and t_3 . This gives the rephasing

$$I_{RP} = \int_0^\infty \int_0^\infty dt_1 dt_3 e^{i\omega_3 t_3 - i\omega_1 t_1} S_{RP}(t_3, T_{\text{delay}}, t_1) \quad (5.8)$$

and non-rephasing part

$$I_{NR} = \int_0^\infty \int_0^\infty dt_1 dt_3 e^{i\omega_3 t_3 + i\omega_1 t_1} S_{NR}(t_3, T_{\text{delay}}, t_1) \quad (5.9)$$

of the 2d-echo spectra [34, 33, 195]. The delay time T_{delay} between pump and probe pulses is used as a free parameter and probes the system dynamics.

The specific nature of the system comes into play via the response function $S^{(3)}(t_3, T_{\text{delay}}, t_1)$. The response function is obtained as a sequence of the time-evolution of the system that is interrupted by the application of dipole-operators at times when the laser pulses hit the sample. The incident pulses can either excite (μ_+) or deexcite (μ_-) the probed system, and we split the dipole operator accordingly, $\mu = \mu_+ + \mu_-$. The Liouville pathways, that is to say the system dynamics and the sequence of dipole operators, are encoded in the nested commutators in eq. (5.6) leading to 16 terms and 64 terms respectively, if we split the dipole operators into μ_+ and μ_- . Within the impulsive limit, only selected terms contribute to the response function. The rephasing and non-rephasing signals reduce then to six Liouville pathways. The Liouville pathways can be cast into double-sided Feynman diagrams, giving a clear scheme of how to interpret and evaluate the individual terms. The Feynman diagrams for the rephasing and non-rephasing signals are shown in Fig. 5.2. The rules of how to read the Feynman diagrams are given as follows [34, 33, 195]: The vertical lines correspond to the time line of the *ket* (left line) and *bra* (right line) of the density matrix, while the arrows display the action of the dipole operators. Arrows attached to the *ket*-line (*bra*-line) stand for the multiplication of the dipole operators from the left (right) to the density matrix. That dipole operators have to be applied from different sides to the density operator can easily be seen by explicitly expanding the commutators of eq. (5.6). Furthermore, the arrows pointing to the right (left) carry an electric field $e^{-i\omega t + ikr}$ ($e^{+i\omega t - ikr}$). If the arrows point to the right (left), the dipole operator μ_+ (μ_-) has to be applied. The application of μ_+ (μ_-) on the *ket*-line is associated with the physical process of excitation (deexcitation) of the exciton system. Since $\mu_+^\dagger = \mu_-$, the physical interpretation of μ_+ and μ_- interchanges while applying the dipole operators on the *bra*-line. After the last multiplication, which is always a deexcitation of the *ket*-line, one has to take the trace operation. Therefore, only such Feynman diagrams contribute to the signal, ending in a populating state. Each Feynman-diagram gets a sign $(-1)^n$, where n is the number of arrows attached to the *bra*-line.

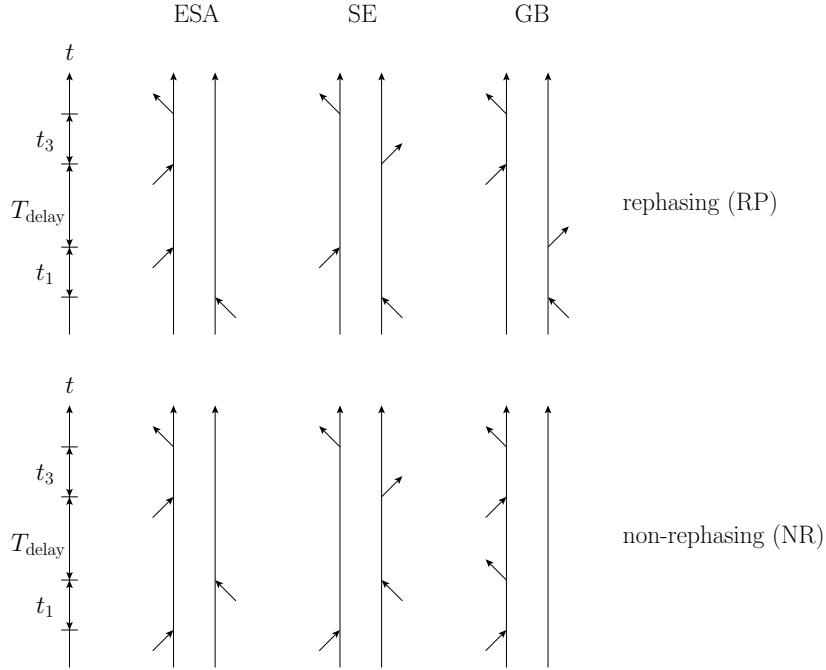


Figure 5.2: Feynman diagrams for the rephasing (RP) and non-rephasing (NR) Liouville pathways. The Liouville pathways are given by excited state absorption (ESA), stimulated emission (SE), and ground state bleach (GB). The sequence of the dipole operators that must be applied to the density operator is indicated by arrows. Arrows attached to the right (left) line of the double-sided Feynman diagrams require the multiplication of the dipole operators from the right (left) to the density operator. Arrows pointing to the right (left) require multiplication with dipole operator μ_+ (μ_-). Each diagram contributes with sign $(-1)^n$, where n is the number of arrows attached to the right line. ESA contributes to the signal with a negative sign, while SE and GB contribute with a positive sign.

Initially, the system is in the electronic ground state $\rho_0 = |0\rangle\langle 0|$. Hence, the first pulse has to be associated with an excitation. In addition, for all three RP (NR) pathways, the first laser pulse acts with μ_- (μ_+) on the *bra*-line (*ket*-line). The three diagrams reflect different information about the system dynamics during the delay time T_{delay} and are accordingly named ground state bleach (GB), stimulated emission (SE), and excited state absorption (ESA). For the GB pathway, the exciton system is in the ground state during the delay time T_{delay} . For the SE pathway, the first two pump pulses prepare the system into a populating state. Therefore, scanning through the delay time T_{delay} explicitly probes the

dynamics within the single exciton manifold. For the ESA pathway, all photons get absorbed by the system. This induces a coherent superposition between the single and the double exciton manifold after the third incident laser pulse. In the total 2d spectrum, the ESA pathway contributes to the signal with a negative sign, while SE and GB contribute with positive signs.

For an explicit evaluation of the pathways, the Feynman diagrams need to be translated back to Liouville pathways. For example, the SE-RP pathway is obtained by

$$S_{GB-NR}^{(3)}(t_3, T_{\text{delay}}, t_1) = \text{Tr} \left\{ \mu_- U(t_3) \left(\mu_+ U(T_{\text{delay}}) (\mu_- U(t_1) (\mu_+ \rho_0)) \right) \right\}, \quad (5.10)$$

where $U(t)$ defines the system's time evolution operator.

5.2.3 Two-exciton manifold

Apart from single excitations, the three incident laser pulses of the 2d-echo setup also create two excitons that are caused by two electronic excitations at two separate BChls. We do not take into account double excited electronic states at the same pigment. The inclusion of the two-exciton manifold is relevant for the ESA pathways and enhances the dimension of the Hamiltonian for N coupled BChls by $N(N-1)/2$. We define two-exciton states as

$$|m, n\rangle = a_m^\dagger a_m a_n^\dagger a_n |0\rangle, \quad (5.11)$$

where a_m^\dagger and a_m are the creation and annihilation operators of electronic excitations at BChl m . The zero exciton state $|0\rangle$ defines the situation in which all BChls are in the electronic ground state. The commutation relations between creation and annihilation operators are given by $[a_m^\dagger, a_n]_+ = \delta_{mn} + (1 - \delta_{mn})2a_m^\dagger a_n$ and $[a_m^\dagger, a_n^\dagger]_+ = (1 - \delta_{mn})2a_m^\dagger a_n^\dagger$ [32].

The Hamiltonian of the two-exciton manifold [32, 34, 196]

$$\mathcal{H}_{2\text{ex}} = \sum_{n>m} \left[(\varepsilon_m + \varepsilon_n) a_m^\dagger a_m a_n^\dagger a_n + \sum_{k \neq n} J_{kn} a_m^\dagger a_m a_k^\dagger a_n + \sum_{k \neq m} J_{km} a_k^\dagger a_m a_n^\dagger a_n \right] \quad (5.12)$$

is constructed from the single-exciton manifold introduced in section 2.2. Site energies and dipole couplings J_{km} are given according to the single-exciton Hamiltonian, eq. (2.2). The physical interpretation of eq. (5.12) is that one of the two excitons moves from one BChl to another, while the second exciton remains in its position. Higher coupling terms $J_{mn,kl} a_m^\dagger a_n a_k^\dagger a_l$ and exciton-exciton interactions are neglected. We define the two-exciton eigenstates as

$$\mathcal{H}_{2\text{ex}}|\chi\rangle = E_\chi|\chi\rangle. \quad (5.13)$$

We assume that the nature of the protein vibrations and of their coupling to the exciton system does not change in the presence of a second electronic excitation. The exciton-phonon coupling of the two-exciton manifold is then given by [39, 34]

$$\mathcal{H}_{2\text{ex-phon}} = \sum_m V_{2\text{ex}-m} B_m, \quad (5.14)$$

where $B_m = \sum_\xi \hbar\omega_{\xi,m} d_{\xi,m} (b_{\xi,m}^\dagger + b_{\xi,m})$ describes the coupling to the phonon modes at BChl m , defined in eq. (2.5). The operator $V_{2\text{ex}-m} = \sum_n a_m^\dagger a_m a_n^\dagger a_n$ takes into account two-exciton states. Equation (5.14) has a similar structure as the exciton-phonon coupling of the single exciton manifold eq. (2.4). Therefore, extending the hierarchical equations of motions introduced in section 3.3 is straight-forward. We just have to replace V_m by $V_{2\text{ex}-m}$ in eqs. (3.19) to (3.22). The same holds for the low temperature correction term eq. (3.26). Although there are only minor changes in the equations, the inclusion of the double-exciton manifold has huge implications for the numerical effort. This is due to the enlarged matrix dimension of the double-exciton manifold. For example, for the FMO complex, the matrix dimension of the reduced density operator and the auxiliary matrices (eqs. (3.21) and (3.22)) enhance from 7×7 to 29×29 . Due to the increase in numerical cost, some theoretical works do not include the ESA pathway in the simulation of 2d-echo spectra [41, 50]. However, the two-exciton dynamics changes the character of the 2d-echo spectra and needs to be taken into account in realistic simulations.

5.2.4 Rotational average over random orientations

The light-matter interaction in LHCs is given by the dipole vectors \vec{d}_m of the BChls. In the FMO complex, the dipole vectors are orientated along the nitrogen atoms $N_B - N_D$ [70] of the BChls. The positions of the nitrogen atoms are listed in the protein data-base [23]. While the orientations of dipole vectors depend on the orientation of the BChl's, we assume that the strengths of the dipoles are identical for each BChl, $|\vec{d}_m| = d$. The dipole orientations for the FMO complex are stated in Table 5.1.

The experiments simultaneously illuminate a large ensemble of randomly orientated proteins, and the detected signal represents a rotational average. The interaction between a probed protein and the laser pulses is given by the dipole moments $\mu_m(\phi, \theta) = \vec{d}_m \cdot \vec{l}(\phi, \theta)$, where $\vec{l}(\phi, \theta) = (\sin \theta \cos(\phi), \sin \theta \sin \phi, \cos \theta)$ corresponds to the polarization vector of the laser pulses. The dipole operator defined in eq. (5.3) for the single-exciton manifold reads

$$\mu_{1\text{ex}} = \begin{pmatrix} 0 & \mu_{1\text{ex}}^- \\ \mu_{1\text{ex}}^+ & 0 \end{pmatrix} \quad (5.15)$$

	BChl 1	BChl 2	BChl 3	BChl 4	BChl 5	BChl 6	BChl 7
d_x	-0.7410	-0.8571	-0.1971	-0.7992	-0.7369	-0.1350	-0.4951
d_y	-0.5606	0.5038	0.9574	-0.5336	0.6558	-0.8792	-0.7083
d_z	-0.3696	-0.1073	-0.2110	-0.2766	0.1641	0.4569	-0.5031

Table 5.1: The normalized dipole orientations of the FMO complex (*C. tepidum*) are listed. The dipole moment of BChl m points along the nitrogen atoms $N_B - N_D$. The positions of the nitrogen atoms are listed in the protein data base [23].

with

$$\mu_{1\text{ex}}^+ = \sum_m \mu_m(\phi, \theta) |m\rangle \langle 0| \quad \text{and} \quad \mu_{1\text{ex}}^- = (\mu_{1\text{ex}}^+)^\dagger. \quad (5.16)$$

In the simulation of 2d-echo spectroscopy the dipole moments appear in the fourth order (see eq. (5.6)) and one needs to perform rotational averages of the form[39]

$$\langle \mu_m^2 \mu_n^2 \rangle_{\text{rot}} = \int_0^{2\pi} \int_0^\pi d\theta d\phi \mu_m^2(\phi, \theta) \mu_n^2(\phi, \theta) \sin \theta. \quad (5.17)$$

In simple Redfield theories, the rotational average can be initialized [39, 196, 41] and explicitly incorporated in the equation of motion for the reduced density operator while propagating along the Liouville pathways. However, for the more sophisticated HEOM approach, this is no longer possible. Instead, Monte Carlo simulations are required for which many realizations corresponding to random orientations need to be calculated. Using such random shots requires that the order of hundreds 2d-echo spectra be simulated [46, 47]. In order to circumvent these numerically demanding procedure, we use a set of specific laser directions. The rotational average eq. (5.17) can be reproduced by sampling ten laser polarization-vectors [46]

$$\langle \mu_m^2 \mu_n^2 \rangle_{\text{rot}} = \sum_{k=1}^{10} (\vec{d}_m \cdot \vec{l}_k)^2 (\vec{d}_n \cdot \vec{l}_k)^2. \quad (5.18)$$

The directions $\vec{l}_k = \frac{1}{\sqrt{3}}(x_k, y_k, z_k)$ are listed in table 5.2. For the evaluation of the ESA pathways we extend the dipole operator eq. (5.15) to the two-exciton manifold [34]

$$\mu = \begin{pmatrix} 0 & \mu_{1\text{ex}}^- & 0 \\ \mu_{1\text{ex}}^+ & 0 & \mu_{2\text{ex}}^- \\ 0 & \mu_{2\text{ex}}^+ & 0 \end{pmatrix} \quad (5.19)$$

with

$$\langle m, n | \mu_{2\text{ex}}^+ | k \rangle = \delta_{m,k} \langle n | \mu_{1\text{ex}}^+ | 0 \rangle + \delta_{n,k} \langle m | \mu_{1\text{ex}}^+ | 0 \rangle \quad \text{and} \quad \mu_{2\text{ex}}^- = (\mu_{2\text{ex}}^+)^\dagger. \quad (5.20)$$

	\vec{l}_1	\vec{l}_2	\vec{l}_3	\vec{l}_4	\vec{l}_5	\vec{l}_6	\vec{l}_7	\vec{l}_8	\vec{l}_9	\vec{l}_{10}
x_k	1	1	-1	-1	0	0	φ^{-1}	$-\varphi^{-1}$	φ	$-\varphi$
y_k	1	-1	1	-1	φ^{-1}	$-\varphi^{-1}$	φ	φ	0	0
z_k	1	1	1	1	φ	φ	0	0	φ^{-1}	φ^{-1}

Table 5.2: Laser polarization vectors for the 10-shot rotational average [46], $\varphi = \frac{1}{2}(1 + \sqrt{5})$. The polarization vectors correspond to the normal vectors of a dodecahedron approximation of the sphere.

5.3 Interpretation of 2d-echo spectra

In this section, we recapitulate how the basic features of the energy transfer in LHCs show up in the dynamics of 2d-echo spectra, while scanning through the delay time. The 2d-echo spectra reflect a two dimensional map of the exciton population in LHCs. The coherent exciton dynamics leads to oscillations in cross-peaks, the frequency of which depends on the corresponding exciton energies. Coupling to the vibrational modes induces dephasing, giving rise to broadening of peaks in the spectra. Energy relaxation leads to an increasing amplitude of peaks that correspond to lower exciton states, while the amplitude at peaks associated with higher exciton states decreases. For further reading, we refer the reader to Ref. [34]. In addition, we set the duration of the electronic coherence in the single exciton manifold in relation to the damping of oscillations in cross-peaks of the 2d-echo spectra.

5.3.1 Coherent dynamics

We illustrate the effects of a purely coherent dynamics in the 2d-echo spectra of a general system of N coupled BCHs. In the following, we discuss the rephasing SE pathway. The other pathways are evaluated in the same manner and show a similar behavior. For the SE pathway, the exciton system remains within the single exciton manifold and we expand the dipole operators in the single-exciton eigenbasis. Inserting eq. (4.7) into eq. (5.16) yields

$$\mu_{1\text{ex}}^+ = \sum_M \mu_M |M\rangle \langle 0| \quad \text{with} \quad \mu_M = \sum_m \mu_m c_m^*(E_M). \quad (5.21)$$

We evaluate the rephasing SE pathway according to the Feynman diagram in Fig. 5.2. Initially, the system is in the electronic ground state $\rho(0) = |0\rangle \langle 0|$. The first pulse creates an excitation of the *bra* state and prepares the system in a coherent superposition between the zero and the single exciton manifold

$$\rho(0)\mu_{1\text{ex}}^- = \sum_M \mu_M^* |0\rangle \langle M|. \quad (5.22)$$

After the second pulse hits the sample, the system is in the state

$$\mu_{1\text{ex}}^+ \rho(t_1) = \sum_{M,N} \mu_N \mu_M^* |N\rangle \langle M| e^{\frac{i}{\hbar} E_M t_1}, \quad (5.23)$$

where the phase $e^{\frac{i}{\hbar} E_M t_1}$ reflects the coherent dynamics during the time interval t_1 between the first and the second laser pulse. The first two laser pulses prepare the system in a populating state. Scanning through the delay time T_{delay} then probes the single exciton dynamics. The coherent dynamics

$$\rho(t_1 + T_{\text{delay}}) = \sum_{M,N} \mu_N \mu_M^* |N\rangle \langle M| e^{\frac{i}{\hbar} E_M t_1} e^{-\frac{i}{\hbar} (E_N - E_M) T_{\text{delay}}}, \quad (5.24)$$

gives rise to an oscillatory signal, the frequency of which is determined by the difference of the eigenenergies $E_N - E_M$. We proceed with the evaluation of the remaining parts of the Liouville pathway. Performing the trace after applying the last dipole operator in the Feynman diagram yields

$$S_{SE-RP}^3(t_3, T_{\text{delay}}, t_1) = \sum_{M,N} |\mu_N|^2 |\mu_M|^2 e^{-\frac{i}{\hbar} E_N t_3} e^{\frac{i}{\hbar} E_M t_1} e^{-\frac{i}{\hbar} (E_N - E_M) T_{\text{delay}}}. \quad (5.25)$$

Finally, the rephasing SE spectrum is obtained after performing the Fourier transform, eq. (5.8), with respect to t_1 and t_3

$$I_{SE-RP}^3(\omega_1, T_{\text{delay}}, \omega_3) = \sum_{M,N} |\mu_N|^2 |\mu_M|^2 e^{-\frac{i}{\hbar} (E_N - E_M) T_{\text{delay}}} \delta(\omega_1 - E_M) \delta(\omega_3 - E_N). \quad (5.26)$$

The spectrum shows peaks located at the position of the eigenenergies of the exciton system. The intensity of the peaks is given by the dipole moments. For a purely coherent dynamics, diagonal peaks DP(N, N) ($\omega_1 = \omega_3 = E_N$) do not evolve with the delay time while cross-peaks CP(N, M) ($\omega_1 = E_M$ and $\omega_3 = E_N$) oscillate with a frequency of

$$\omega_{N,M} = (E_N - E_M)/\hbar. \quad (5.27)$$

The ESA pathways involve two-exciton states in the time evolution during the time interval t_3 . This changes the peak positions along ω_3 axis. Peaks are located at energy differences between single-exciton and two-exciton states, $\omega_3 = E_\chi - E_M$. Since the energies for the two-exciton manifold, eq. (5.12), are close to the sum of two single-exciton energies, the ESA peaks in the spectrum are almost on top of the peaks of the single-exciton pathways SE and GB. Because of the Feynman rules, the ESA pathway gets a global negative sign, and the coherent oscillations $e^{-\frac{i}{\hbar} (E_N - E_M) T_{\text{delay}}}$ of the ESA and SE pathways are phase-shifted by π . In the total signal of the 2d-echo spectra (sum of ESA, SE, and GB pathways) the SE and ESA pathways interfere destructively diminishing the visibility of the coherent oscillatory signal in the cross-peaks.

5.3.2 Dissipative dynamics

In light harvesting complexes, the exciton system does not evolve in a purely coherent fashion, but couples to a dissipative phonon bath. For the FMO complex, such a coupling to an environment is crucial for the fast energy transfer to the reaction center, see chapter 4. In this section we discuss the signatures of the dissipative dynamics in the 2d-echo spectra. Decoherence yields a damping of the cross-peak oscillations in the 2d-echo spectra. We relate the life-time of cross-peak oscillations to the coherence life-times in the single-exciton manifold. Finally, we illustrate the process of thermal relaxation. This process shows up in the form of an increasing spectral weight at the lower exciton states in the 2d spectra with advancing delay time T_{delay} [42].

We consider a model trimer that consists of three coupled BChls. A trimer is the smallest system in which (i) the coherent dynamics involves multiple frequencies and (ii) where the double excitons are delocalized. The spectrum of a trimer is less convoluted than that of the seven-site FMO complex. Therefore, the trimer allows us to study basic mechanisms in a clearer way. Realistic simulations of 2d-echo spectra for the full FMO complex are discussed later in chapter 7. We consider the three coupled BChls 1, 2, and 3 of the FMO complex. The Hamiltonian of the single exciton manifold for the trimer is given in units of cm^{-1} by

$$\mathcal{H}_{\text{ex,tri}} = \begin{pmatrix} 280 & -106 & 8 \\ -106 & 420 & 28 \\ 8 & 28 & 0 \end{pmatrix}, \quad (5.28)$$

where the site energies and inter-site couplings are taken from Ref. [39]. The double exciton manifold is constructed according to eq. (5.12). We set the orientations of the dipole moments for the three BChls of the trimer to the values of BChl 1, BChl 2 and BChl 3 listed in Table 5.1. Averaging over random orientations is included by the ten-shot rotational average, eq. (5.18). Compared to a realistic reorganization energy of $\lambda = 35 \text{ cm}^{-1}$, we reduce the coupling to the vibronic modes and set $\lambda = 10 \text{ cm}^{-1}$. We use a Drude-Lorentz spectral density eq. (3.15) with a phonon relaxation timescale $\tau_c = 50 \text{ fs}$. Due to the reduced reorganization energy, the exciton system and the phonon bath are less entangled [170, 180]. The situation is more complex for larger reorganization energies, as is discussed below in chapter 6.

Figure 5.3(a) depicts the real part of the rotationally averaged spectrum of the trimer for $T_{\text{delay}} = 560 \text{ fs}$, including all six rephasing and non-rephasing Feynman diagrams at temperature $T = 150 \text{ K}$. The coupling to the phonon bath induces dissipation in the exciton dynamics, resulting in broadened peaks in the 2d-spectra. This kind of broadening of the peaks is referred to as homogeneous broadening. In order to extract information about the coherence life-times in the single exciton manifold, we track the peak amplitudes of cross-peaks CP(1,2) and

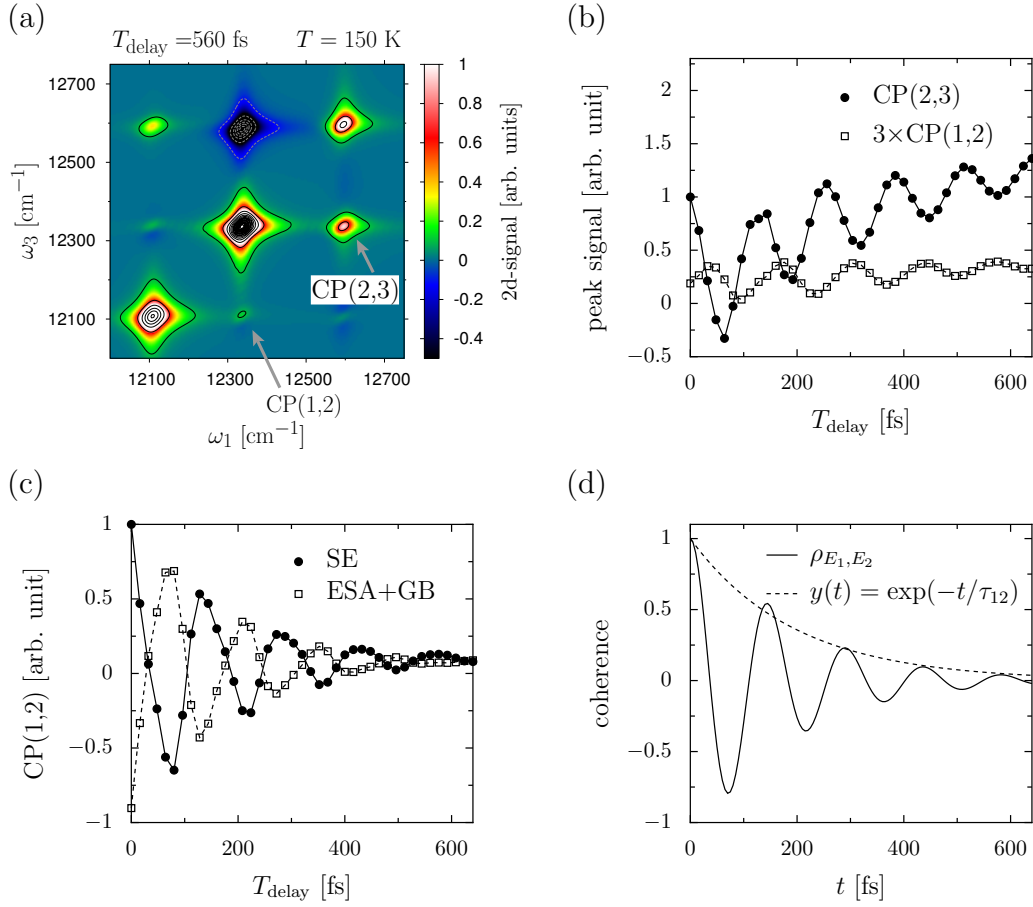


Figure 5.3: (a) the real part of the rephasing and non-rephasing 2d-echo spectrum for delay time $T_{\text{delay}} = 560$ fs. ω_1 corresponds to the pump, and ω_3 corresponds to the probe frequency of the four-wave mixing setup. The signal is color-coded and given in arbitrary units. The arrows mark the cross-peaks CP(1,2) and CP(2,3). (b) cross-peak dynamics CP(1,2) and CP(2,3). The amplitude is normalized to CP(2,3). (c) phase shift of π between SE and ESA pathways. Circles depict the rephasing and non-rephasing SE pathways, while the squares correspond to the rephasing and non-rephasing ESA and GB pathways. (d) coherence $\rho_{E_1, E_2}(t) = \langle E_1 | \rho(t) | E_2 \rangle$ with fit of the exponential decay, $\rho_{E_1, E_2}(t) \sim \exp(-t/\tau_{12})$, yielding the coherence life-time $\tau_{12} = 194$ fs. Parameters used: $\lambda = 10$ cm⁻¹, $\tau_c = 50$ fs and $T = 150$ K.

CP(2,3) as a function of the delay time T_{delay} , depicted in Fig. 5.3(b). The signal amplitude is normalized to the initial value of CP(2,3). Both peaks undergo

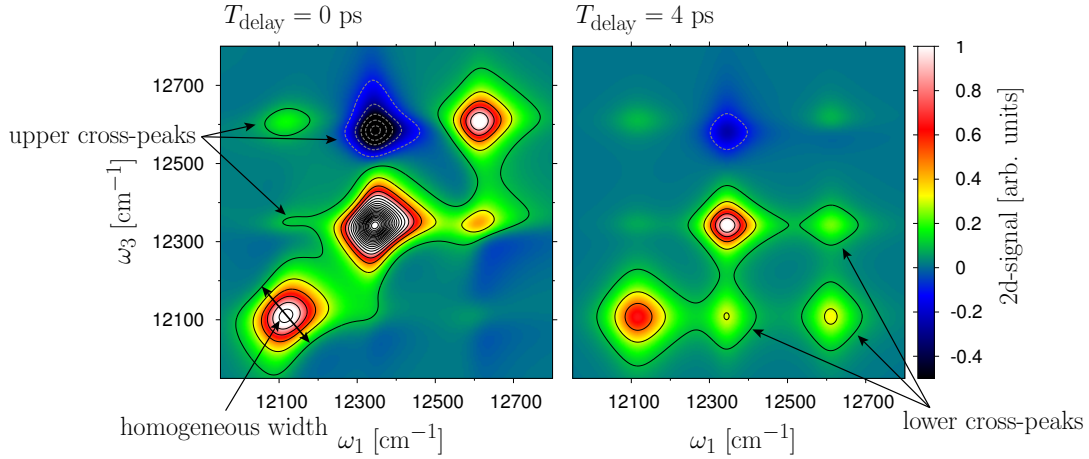


Figure 5.4: Illustration of the thermalization process in the 2d-echo spectrum. The real part of the rephasing and non-rephasing pathways for delay times $T_{\text{delay}} = 0$ ps and $T_{\text{delay}} = 4$ ps is shown. Peaks corresponding to higher exciton states fall down along the ω_3 axis. In the thermal state, approached for $T_{\text{delay}} = 4$ ps, spectral weight is located in the lower-right plane of the spectrum. Parameters used: $\lambda = 35$ cm $^{-1}$, $\tau_c = 50$ fs and $T = 150$ K.

oscillations, the periods $t_{1,2} = 145$ fs and $t_{2,3} = 130$ fs which, for cross-peaks CP(1,2) and CP(2,3), matches the expected period of 147 fs and 132 fs of the coherent dynamics given by eq. (5.27). The periods are extracted from fits of the SE pathways. Furthermore the SE and ESA pathways are phase shifted by π , as illustrated in Fig. 5.3(c) for CP(1,2). This phase shift of π is characteristic of an coherent electronic dynamics [39]. In Fig. 5.3(c) we add the GB to the ESA pathway which inducing a constant shift in amplitude. This brings the ESA amplitude into the range of the SE one, and allows for a better comparison.

The dynamics of the cross-peak CP(N,M) is related to the time evolution of the off-diagonal entries in the single exciton manifold of the reduced density operator in the eigenbasis representation, $\rho_{E_N,E_M}(t) = \langle E_N | \rho(t) | E_M \rangle$. These elements are referred to as coherences [197]. Decoherence in the exciton dynamics induces an exponential decay ($\sim \exp(-t/\tau_{NM})$) of the coherence ρ_{E_N,E_M} . For example, coherence ρ_{E_1,E_2} decays with coherence life-time $\tau_{12} = 194$ fs, as illustrated in Fig. 5.3(d). The duration of the beatings in the dynamics of CP(N,M) in the 2d-echo spectra is related to the coherence life-time τ_{NM} . For the SE pathway of CP(1,2) the life-time of the oscillatory signal given by $\tau_{\text{CP}(1,2)} = 197$ fs is in an excellent level of agreement with the associated coherence life time $\tau_{12} = 194$ fs.

Besides decoherence, coupling to a thermal environment also gives rise to the thermalization of the exciton system. Energy relaxation drives the system from

its initial state to the lower energy states. The initial state at $T_{\text{delay}} = 0$ ps is determined by the interaction with the first two laser pulses, and depends on the dipole moments of the BChls. With an increasing delay time, the amplitude in the 2d-echo spectra relaxes to lower energy states. Since information about the dynamics during the delay time is only available in the signal time t_3 , energy relaxation only affects the signal frequency ω_3 . Hence with increasing delay time, peaks fall down along the ω_3 axis and thermalization drives the amplitude in the spectra to the cross-peaks in the lower-right half-plane of the 2d-echo spectra [39, 198]. Fig. 5.4 illustrates the thermalization process for the trimer, eq. (5.28) for reorganization energy $\lambda = 35 \text{ cm}^{-1}$ at temperature $T = 150 \text{ K}$. We show the 2d-echo spectrum for delay times $T_{\text{delay}} = 0$ ps and $T_{\text{delay}} = 4$ ps. The thermalization drives the amplitude in the 2d-spectra to the lower exciton states. In the thermal state, which is approached after approximately 4 ps, there is a significant increase in the amplitude of the lower cross-peaks in the 2d-spectrum.

6 Entangled excitonic and vibrational dynamics

6.1 Introduction

Simple Redfield approaches do not explain the rich experimental features found in the 2d-echo spectra of LCHs [16, 19, 20, 197]. Thus, suggestions have emerged that a strong coupling to the vibrational environment influences the exciton dynamics in a non-trivial way [174]. Strong coupling in combination with a slow timescale of phonon relaxation prolongs quantum beatings in the site basis population dynamics [43] and entangles the excitonic with the phonon degrees of freedom [180]. The latter gives rise to an information flow between the environment and the exciton system [170]. The experimental evidence for a reversible energy flow between the exciton system and the vibrational environment in the FMO complex is pointed out by a detailed analysis in Ref. [197].

The highly efficient GPU-HEOM implementation facilitates studies for both large exciton phonon coupling and slow phonon relaxation, which are the key ingredients for achieving a strong entanglement between excitonic and vibrational degrees of freedom. This enables us to give a quantitative analysis of the reversible energy flow that manifests itself in unique features in the peak dynamics of the 2d-echo spectra of LHCs.

In section 6.2, we investigate the origin of the sitebasis population dynamics of Ref. [43]. Those beatings are not purely coherent, but are induced by the non-Markovian interaction with the phonon environment. This is a specific feature of the employed Drude-Lorentz spectral density. The prolonged beatings in the site basis population dynamics for a sluggish phonon bath obtained by Ishizaki and Fleming [43] do not prove the existence of long-lived electronic coherence in the exciton dynamics of LHCs, but rather highlight the reversible energy flow between the exciton system and the phonon bath. In section 6.3, we show that the interaction of the exciton system with the phonon-bath couples exciton populations with exciton coherences. This yields a bath mediated quantum transport from diagonal-peaks to cross-peaks of the 2d-echo spectra. The signatures of the bath mediated quantum transport show up in the 2d-echo spectra as an

unambiguous phase-relation between cross- and diagonal peak- oscillations, and is experimentally observed in the FMO complex by Panitchayangkoon *et al.* in Ref. [197]. We estimate the expected order of magnitude of the bath-mediated quantum transport from the dynamics of the single exciton manifold.

6.2 Which oscillations are coherent and which are not

In the following, we set the site basis population dynamics discussed in chapter 3.4 in relation to the exciton populations, coherences and oscillatory signals in the 2d-echo spectra. Simulations using a Drude-Lorentz spectral density

$$J(\omega) = 2\lambda \frac{\omega\nu}{\omega^2 + \nu^2}, \quad \nu^{-1} = \tau_c, \quad (6.1)$$

and including the finite phonon relaxation timescale τ_c , reveal long lived beatings in the site basis population-dynamics. These are interpreted as the signature of electronic coherence in LHCs [174, 43]. Here, we demonstrate that these beatings are not purely of a coherent origin, but are induced by non-Markovian bath effects. The slower the phonon relaxation gets, the more pronounced the memory effects in the phonon bath are. This explains why the amplitude and duration of the obtained site basis population-beatings increase with phonon relaxation timescale τ_c .

We use a Drude-Lorentz spectral density eq. (3.15) with parameters $\tau_c = 166$ fs and $\lambda = 35$ cm⁻¹, and discuss the dynamics of the trimer defined in eq. (5.28). Throughout this section, we set the temperature to 150 K. The trimer is comprised of BChl 1, BChl 2, and BChl 3 of the FMO complex, and hence defines one of the two pathways of energy transfer to the reaction center. For the initial population at BChl 1, the sitebasis population dynamics shows beatings that last up to 0.8 ps. We prove that these oscillations are not related to purely electronic coherence. For this, we study the energy transfer in the exciton eigenbasis. This is also the suitable basis for the interpretation of 2d-echo spectra (see section 5.3). We analyze exciton coherences ρ_{E_N, E_M} yielding the life-time of electronic coherence and exciton populations ρ_{E_M, E_M} that are affected by the reversible energy exchange with the phonon bath. The reversible interplay of the phonon bath and the exciton dynamics leads to significant beatings in exciton populations ρ_{E_2, E_2} and ρ_{E_3, E_3} , see Fig. 6.1(a). Within Markovian Redfield approaches, the exciton populations decay toward the thermal state but do not show oscillations. The oscillations in the exciton populations translate into a oscillatory signal in diagonal peaks of the rephasing 2d-echo spectra. The duration and amplitude of the oscillations in the diagonal peaks, depicted in Fig. 6.1(b), are in a good level of agreement with the dynamics of the corresponding exciton populations,

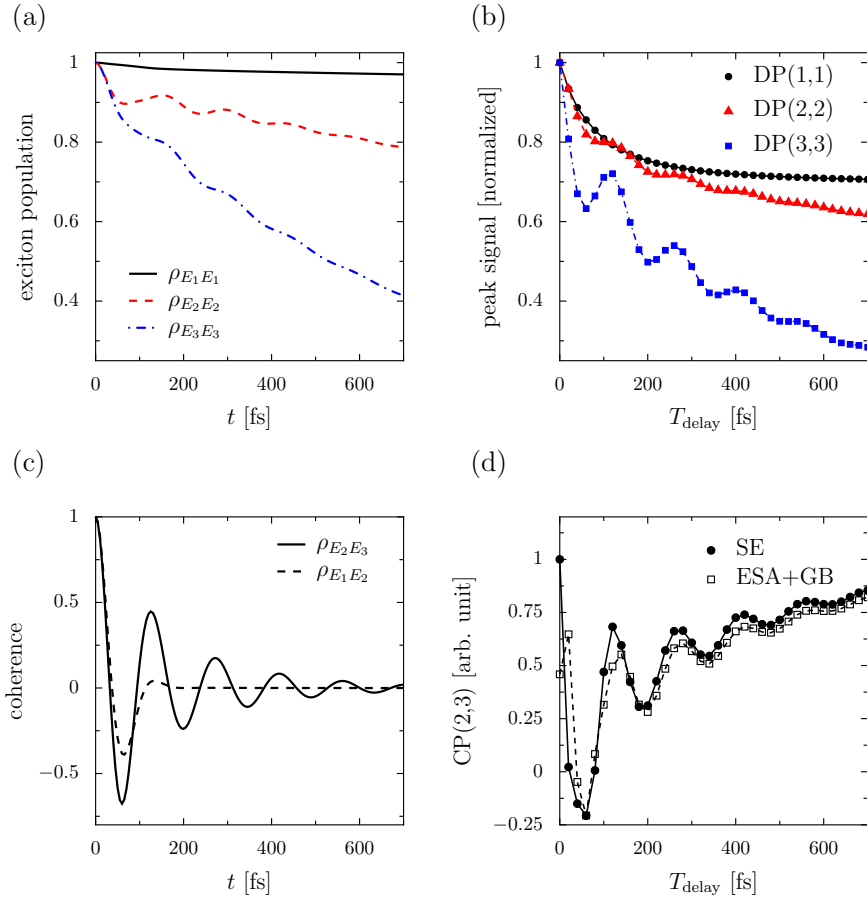


Figure 6.1: (a) non-Markovian effects lead to oscillations in the exciton populations ρ_{E_2, E_2} and ρ_{E_3, E_3} (b) exciton populations are related to diagonal peaks in the 2d-echo spectra. DP(2,2) and DP(3,3) of the rephasing and non-rephasing 2d-echo spectra (real part) show long-lasting oscillations. (c) dynamics of the coherences ρ_{E_1, E_2} and ρ_{E_2, E_3} . For the Durde-Lorentz spectra density, only the coherence ρ_{E_2, E_3} is long-lived, while coherence ρ_{E_1, E_2} only lasts for about 200 fs. (d) SE and ESA pathways of CP(2,3) (rephasing and non-rephasing, real part). Both oscillate *in phase*. This is opposed to what is expected from a purely electronic coherent dynamics. Parameters used: $\lambda = 35 \text{ cm}^{-1}$, $\tau_c = 166 \text{ fs}$ and $T = 150 \text{ K}$.

Fig. 6.1(a). The life times of the exciton coherences are depicted in Fig. 6.1(c). Prolonged electronic coherence exists only for ρ_{E_2, E_3} in which beatings last up to 0.8 ps. The remaining coherences ρ_{E_1, E_2} and ρ_{E_1, E_3} are short-lived and last only up to on quarter of the duration of the obtained beatings in the site basis

population dynamics.

From the single exciton dynamics alone one cannot distinguish whether the physical origin of the long-lived oscillations in the coherence ρ_{E_2,E_3} is due to purely electronic coherence, or if the coupling to the phonon bath plays a crucial role for the prolonged oscillations. Here, studying the 2d-echo spectra, which provide precise criteria for electronic coherence, yields further information. Purely electronic coherence shows up as an oscillatory signal in the cross-peaks. The oscillation frequency is determined by the location of the peaks in the exciton energy grid. But, more importantly for a coherent dynamics, the SE and ESA pathways oscillate with an opposite phase (see the discussion in section 5.3). However, this is not the case for cross-peak CP(2,3), as depicted in Fig. 6.1(d). The SE and ESA pathways show long-lasting beatings as are expected from the dynamics of ρ_{E_2,E_3} , but both pathways oscillate *in* phase. Thus, these beatings do not reflect purely electronic coherence. The long-lasting coherence ρ_{E_2,E_3} involves interaction with the phonon bath.

6.3 Bath-mediated quantum transport

The total rephasing and non-rephasing cross-peak signal CP(1,2) (all SE, GB, and ESA pathways included), depicted in Fig. 6.2(a), shows long lasting oscillations (up to 600 fs) on top of a non-oscillatory background. Long-lasting beatings are not expected from the analysis of the corresponding coherence ρ_{E_1,E_2} , Fig. 6.1(c). Hence, electronic coherence does not explain the observed oscillatory signal in CP(1,2). In the following, we prove that these beatings are caused by the bath mediated quantum transport of beatings in the exciton populations to exciton coherences. In the 2d-echo spectra bath mediated quantum transport transfers the oscillations in the diagonal peak DP(2,2) to cross-peak CP(1,2).

We start with a simple Redfield argument that is also used to interpret the experimentally obtained quantum transport in the exciton dynamics of the FMO complex [197]. Within the full Redfield equation (Appendix eq. (A.37)), the interaction with the vibrational environment couples exciton populations ρ_{E_i,E_i} with coherences ρ_{E_i,E_j} . Formally, the full Redfield equation can be written in terms of rate equations for the entries of the reduced density operator. We keep the notation of Ref. [197] eq.(3)

$$\frac{d}{dt}\rho_{E_i,E_j}(t) = -\frac{i}{\hbar}(E_i - E_j)\rho_{E_i,E_j}(t) - \sum_{k \neq l} \kappa_{ij,kl}\rho_{E_k,E_l}(t) - \sum_k \kappa_{ij,kk}\rho_{E_k,E_k}(t). \quad (6.2)$$

The rates $\kappa_{ij,kl}$ depend on the exciton system, temperature, and exciton-phonon coupling described by the spectral density. The explicit form of the rates is obtained by expanding eq. (A.37) into the exciton eigenbasis. The last term

describes the coupling between exciton populations $\rho_{E_k, E_k}(t)$ and coherences $\rho_{E_i, E_j}(t)$. Assuming an oscillatory dynamics of the exciton populations $\rho_{E_k, E_k}(t) \sim \cos(\omega t)$, integration of eq. (6.2) yields an oscillatory contribution to the coherence $\rho_{E_i, E_j}(t) \sim \sin(\omega t)$. Therefore, the bath mediated transfer from exciton populations to coherences yields a phase shift in the oscillations of $\pi/2$.

In Fig. 6.2(c), we extract the oscillatory components of DP(2,2), which are related to beatings in the exciton population ρ_{E_2, E_2} and CP(1,2), which are related to the coherence ρ_{E_1, E_2} . DP(2,2) and CP(1,2) show oscillations with the same frequency, the same life-time and the expected phase shift of $\pi/2$. This analysis confirms the interpretation of the long-lived cross-peak oscillations in CP(1,2) in terms of bath mediated quantum transport. In contrast to the interpretation of the experimental results Ref. [197], which proposes that diagonal peaks inherit their beatings from cross-peaks, we obtain quantum transport in the opposite direction. Cross-peak CP(1,2) inherits its beatings from the diagonal peak DP(2,2).

The amplitude of the long lasting beatings in CP(1,2) is about ten times smaller than the one for DP(2,2). Hence, we expect that quantum transport works with about 10% efficiency. To prove this, we show that exciton populations couple with exciton coherences and we also provide a quantitative estimate for the relevance of bath-mediated quantum transport. We prepare the system in the exciton populating state ρ_{E_2, E_2} , and keep track of the dynamics of the coherence ρ_{E_1, E_2} , as depicted in Fig. 6.2(b). There is a small amount of amplitude (note the scaling factor of 20 in Fig. 6.2(b)) that is transferred through the coupling to the phonon-bath from the population ρ_{E_2, E_2} to the coherence ρ_{E_1, E_2} .

For a purely coherent dynamics, no such transfer would occur and the coherence $\rho_{E_1, E_2}(t)$ would remain at zero. For our analysis, we are interested in the oscillatory components of $\rho_{E_1, E_2}(t)$ and $\rho_{E_2, E_2}(t)$, which are depicted in Fig. 6.2(d). The oscillatory components of $\rho_{E_1, E_2}(t)$ appear with two different timescales. There is a short-lived oscillatory signal up to 200 fs, and there are long lived oscillations with a much smaller amplitude. The small, long-lasting oscillations coincide with the oscillatory components of the exciton population-dynamics $\rho_{E_2, E_2}(t)$ in frequency and life-time. Furthermore, the oscillations are phase-shifted by approximately $\pi/2$. Thus, we identify the small, long lasting oscillations as a bath-mediated quantum transport from exciton population ρ_{E_2, E_2} to exciton coherence ρ_{E_1, E_2} . Oscillations in ρ_{E_1, E_2} are about 30 times smaller than the corresponding oscillations in ρ_{E_2, E_2} , indicating that bath-mediated quantum transport works with about 3% efficiency. Up to a factor of three in the efficiency of the estimated bath-mediated quantum transport, we obtain reasonable agreement with the correlated oscillations observed in DP(2,2) and CP(1,2) in the 2d-echo spectra (Fig. 6.2(b)).

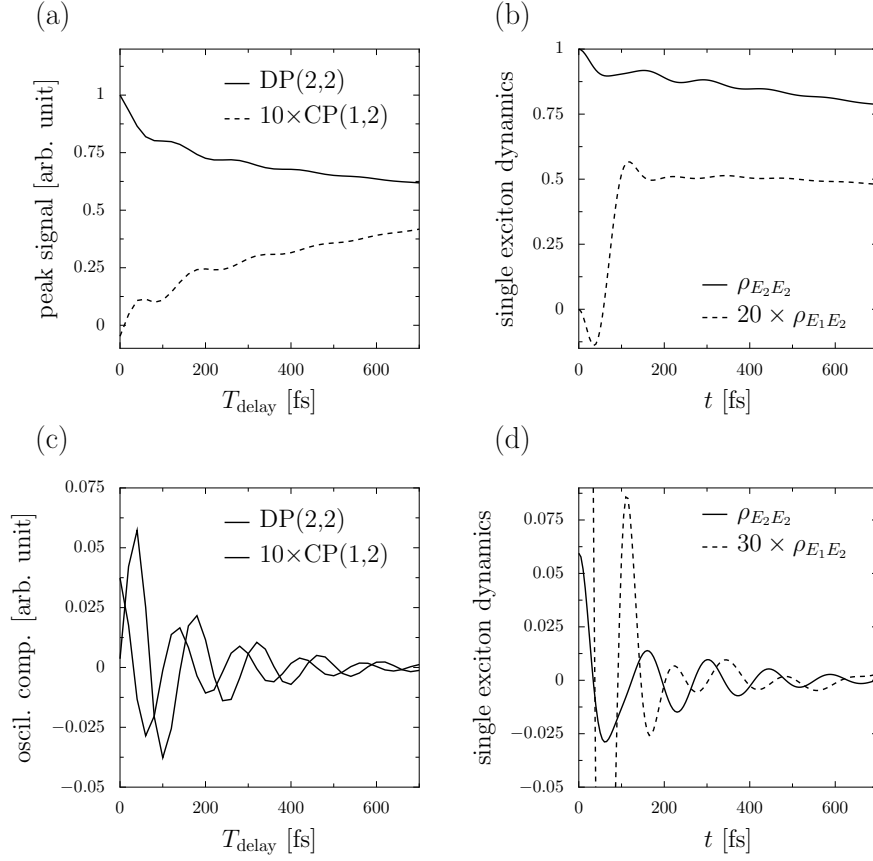


Figure 6.2: Illustration of bath-mediated quantum transport. (a) dynamics of cross-peak CP(1,2) and diagonal peak DP(2,2) (real part of the rephasing and non-rephasing signal). The oscillatory components are depicted in (c). (b) population dynamics of coherences ρ_{E_1, E_2} and ρ_{E_2, E_2} . The oscillatory components are depicted in (d). Parameters used: $\lambda = 35 \text{ cm}^{-1}$, $\tau_c = 166 \text{ fs}$ and $T = 150 \text{ K}$.

6.4 Conclusion

We investigate the influence of the finite phonon relaxation timescale, giving rise to an entangled motion between the exciton system and the vibrational environment. We find that the long-lived site basis population beatings obtained by Ishizaki and Fleming [43, 174] are mainly related to oscillations in the exciton populations (diagonal entries ρ_{E_i, E_i}) that are induced by a reversible energy trade between the phonon bath and the exciton system. In the 2d-echo spectra, such effects show up as oscillations in the diagonal peaks in the rephasing signal. Thus, the previous interpretation of the site basis population beatings in terms of purely

electronic coherence [43, 183] has several failings: The beatings in the site basis population dynamics are mainly due to oscillations in the exciton populations. These are not expected to oscillate in a purely electronic coherent dynamics. Most exciton coherences are short-lived, while only very specific coherences are prolonged by the entangled dynamics with the environment. The relevance of the phonon bath in prolonging specific coherences leaves its signature in the corresponding cross-peak dynamics of the 2d-echo spectra in which SE and ESA pathways oscillate *in* phase. This is in contrast to a purely coherent dynamics in which SE and ESA pathways oscillate in opposite phase.

Furthermore, our simulation demonstrates that bath-mediated quantum transport in the exciton dynamics of LCHs. This bath-mediated quantum transport is experimentally obtained in the FMO complex [197]. However, in contrast to the experimental interpretation in which cross-peak oscillations are transferred to diagonal-peak oscillations, our theoretical study shows exactly the reversed situation. Diagonal-peak oscillations are transferred to cross peak oscillations. We show that the energy exchange between the bath and the exciton motion induces oscillations in the exciton populations. In the 2d-echo spectra the exciton-population beatings show up as an oscillatory signal in the diagonal peaks. The coupling to the vibrational environment couples exciton populations with exciton coherences. Beatings in the diagonal peaks are transferred to beatings in the cross peaks.

In conclusion, our analysis provides exact numerical simulations within a Drude-Lorentz spectral density and proves the existence of a reversible energy exchange between the exciton system and the protein vibrations for a realistic parameter regime of energy transfer in LHCs. Our findings highlight that non-Markovian quantum processes show up as unambiguous signatures in the 2d-spectra of LHCs. Information of coherence is exchanged between the phonon bath and the exciton system, inducing beatings in diagonal peaks of the 2d-spectra. Those beatings are also experimentally detected in 2d-spectra of the FMO complex [197].

7 Long-lived electronic coherence in the FMO complex

Parts of this chapter have been published in Kreisbeck *et al.* arxiv:1203.1485.

7.1 Introduction

The experimentally observed long-lasting coherence in the 2d-echo spectra of LHCs [16, 17, 18, 19] revises the picture of energy transfer in photosynthesis. For the FMO complex, a coherence life-time of up to 1.8 ps at a temperature of 77 K is reported [20]. Instead of classical hopping from one BChl to the next, quantum coherence prevails for long enough to influence the energy transfer process [26]. So far, the microscopic origin of, as well as the physical mechanisms supporting, long-lasting coherence are still unclear. Microscopic theories based on molecular dynamics simulations have not yet led to unambiguous conclusions [72, 199, 71]. Understanding the nature of the interaction of the exciton system with the vibrational environment and its consequences for coherence remains one of the outstanding questions in the field [26].

The difficulty of reproducing the experiments lies in the nature of two seemingly contradictory observations. The experiments predict long-lived electronic coherence, but at the same time, fast thermalization occurs, indicating a strong coupling to a noisy environment. In this regime, fast decoherence is expected. Brixner *et al* in Ref. [42] show that thermal relaxation takes place in the FMO complex within a few picoseconds at 77 K. Thermalization leads to an increasing population of lower exciton peaks in the 2d-echo spectra, see section 5.3.2. Coupling to noise is an important ingredient for the functioning of the FMO complex as an efficient energy wire, since thermalization drives the exciton population along the energy gradient toward the reaction center. Thermal noise aids transport [52, 54, 78] as we discuss in chapter 4. The parameters of approximate Redfield approaches can be adjusted to reproduce the timescale of the thermalization process and the line shapes of the peaks in the 2d-echo spectra. But then, long-lived coherent oscillations are absent in the peak dynamics of the 2d-echo spectra [39, 42, 198]. In 2009, Ishizaki and Fleming propose that

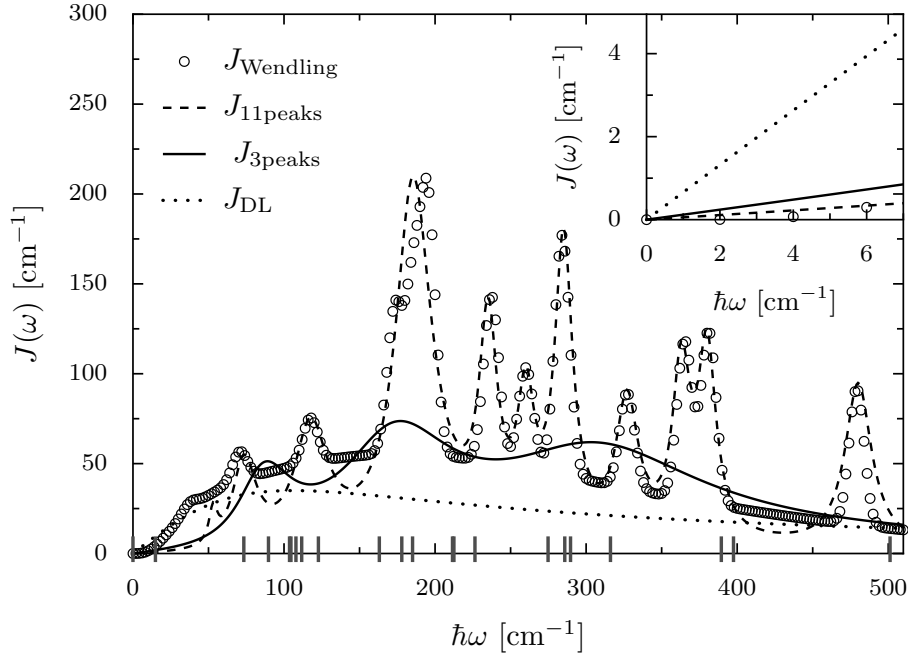


Figure 7.1: Spectral density of the FMO complex. J_{Wendling} corresponds to the experimentally measured spectral density of the FMO complex [48]. $J_{11\text{peaks}}$ ($J_{3\text{peaks}}$) approximates J_{Wendling} by eleven (three) shifted Drude-Lorentz peaks, eq. (7.6). J_{DL} depicts the Drude-Lorentz spectral density for $\lambda = 35 \text{ cm}^{-1}$ and $\tau_c = 50 \text{ fs}$. The marks on the frequency axis indicate the energy difference between two exciton eigenstates of the FMO complex, where the spectral density is evaluated within Redfield approaches. Inset: comparison of the slope of the different spectral densities around zero-frequency, defining the pure dephasing rate γ_d , eq. (7.4). $\gamma_d = 0$ for the super-Ohmic spectral density J_{Wendling} . For $J_{11\text{peaks}}$ ($J_{3\text{peaks}}$), the pure dephasing rate is suppressed by a factor of 12 (5.5) compared to J_{DL} .

the finite time scale of phonon relaxation prolongs electronic coherence in LHCs [43, 174]. As we discuss in section 6, a sluggish phonon bath yields a reversible energy exchange between the bath and the exciton system, but does not produce long-lived, purely electronic coherence. Simulated 2d-echo spectra for the FMO by Hein and Kreisbeck *et al.* in Ref. [46] predict for the same parameters used in Ref. [43] coherence life-times of the lower exciton peaks that are approximately six times shorter than observed in experiments at a temperature of 150 K. For a larger phonon relaxation timescale $\tau_c = 100 \text{ fs}$, Chen *et al.* do not observe signatures of coherence even at a low temperature of 77 K [47].

Although the work of Ishizaki and Fleming does not yield the answer for long-lasting coherence, their findings show that the finite timescale of the reorganization process influences the population dynamics of LHCs and requires the inclusion of non-perturbative and non-Markovian effects in numerical simulations. This highlights the importance of a careful and realistic modeling of the exciton-phonon coupling. The nature of the exciton-phonon coupling is characterized by the spectral density. The most realistic spectral density for the energy transfer in LHCs is given by Wendling *et al.* in Ref. [48], who extract the spectral density for the FMO complex from fluorescence line-narrowing experiments at a temperature of 4 K. The Wendling spectral density J_{Wendling} is shown in Fig. 7.1. There are specific, strongly coupled modes, visible as peaks in J_{Wendling} , for example around 180 cm^{-1} . It has been proposed that the cross-peak oscillations are induced by the strongly coupled discrete modes [50, 45], rather than by purely electronic coherence. This interpretation implies that the discrete vibronic modes are specifically tuned to reproduce cross-peak oscillations, whose frequencies match the exciton-energy differences. The interpretation of Refs. [50, 45] relies on the hypothesis that evolution in nature has tuned discrete vibrational modes and exciton frequencies into a balanced condition. But experiments altering the vibronic structure of the FMO complex by partial deuteration, by ^{13}C substitution and by creating native mutants do not yield major differences in the peak dynamics of the 2d-echo spectra [51], and does not confirm the hypothesis of specifically tuned vibronic modes.

In this chapter, we demonstrate an alternative mechanism that supports long-lived, purely electronic coherence in the FMO complex. The mechanism depends on the continuous part of the spectral density. We also show that strongly coupled, discrete phonon modes do have a minor influence in the exciton dynamics. We use the realistic Wendling spectral density J_{Wendling} . The continuum part of J_{Wendling} has been parameterized by Adolphs and Renger [49]. Apart from the strongly coupled discrete modes, the major difference of J_{Wendling} compared to the frequently used Drude-Lorentz spectral density [78, 43, 178, 47, 80, 46] is that J_{Wendling} is super-Ohmic. As we demonstrate below, the super-Ohmic behavior is crucial to obtain long-lived, purely electronic coherence. We further show that the coupling to the continuum of higher phonon modes ensures the fast thermalization required for efficient energy transfer. Indeed, the Wendling spectral density yields an even faster transfer to the reaction center than the Drude-Lorentz one.

In section 7.2, we introduce the basic concepts of a super-Ohmic spectral density, and discuss its implications for the dephasing mechanism in the exciton dynamics. Approximative Redfield approaches do not capture the relevant physics in LHCs, which requires an exact technique to solve the exciton dynamics. In the literature, there exist various non-Markovian approaches that can treat general spectral densities [200, 75, 45]. However, so far, none of them is able to perform

the extremely numerically challenging 2d-echo spectra for the FMO complex. We develop the numerically efficient GPU-HEOM, see also Kreisbeck *et al.* Ref. [78], which makes non-Markovian simulations of the 2d-echo spectra for the FMO complex possible, as shown by Hein, Kreisbeck *et al.* Ref. [46]. HEOM in its original version is limited to a Drude-Lorentz spectral density [77, 175]. In section 7.3, we overcome this restriction and generalize GPU-HEOM to more complex shaped spectral densities like J_{Wendling} by using a superposition of shifted Drude-Lorentz peaks [82]. Numerical simulations of 2d-echo spectra become more demanding than for a single Drude-Lorentz spectral density, but remain computationally feasible due to the high performance GPU implementation. In section 7.4, we investigate coherence life-times of the FMO complex and analyze the oscillation duration in the corresponding peak dynamics in the 2d-echo spectra. A super-Ohmic spectral density yields a prolonged electronic coherence that is accompanied by sharp lineshapes in the 2d-echo spectra. In section 7.5, we include the static disorder in order to achieve a better agreement with the experimentally observed lineshapes. Finally, in section 7.6, we discuss the consequences of a super-Ohmic spectral density and its impact on the transfer efficiency of the FMO complex. We summarize the results of this chapter in section 7.7.

7.2 Pure dephasing vs. relaxation rate

Within the Redfield approach (Appendix A.2), the time evolution of the entries of the reduced density matrix is given in the form of rate equations. The Redfield rates defined in Appendix A.2, eq. (A.52) determine thermal relaxation and decoherence. These rates depend on the spectral density. The rates need to be evaluated at energies that correspond to the difference of exciton energies. In Fig. 7.1, we mark the energies where the spectral density is probed by the Redfield rates along the frequency axis. We use the exciton Hamiltonian Table 2.1 for the FMO complex.

In the following, we recapitulate textbook concepts [201] (chapter 21.4.2) for the decoherence rate

$$\gamma = \gamma_r/2 + \gamma_d. \quad (7.1)$$

The decoherence rate γ determines the life-time of the coherence in the exciton system, and consists of the relaxation rate γ_r and the pure dephasing rate γ_d . Both γ_r and γ_d depend on the exciton system, the spectral density, and the temperature. Let us consider a Spin-Boson model for a coupled two-site system

that couples to a common harmonic bath

$$\begin{aligned} \mathcal{H}_{\text{Spin-Boson}} = & \varepsilon/2(c_1^\dagger c_1 - c_2^\dagger c_2) + d/2(c_1^\dagger c_2 + c_2^\dagger c_1) + \sum_{\xi} \hbar\omega_{\xi} b_{\xi}^{\dagger} b_{\xi} \\ & + \frac{1}{2}(c_1^\dagger c_1 - c_2^\dagger c_2) \sum_{\xi} \hbar\omega_{\xi} d_{\xi} (b_{\xi}^{\dagger} + b_{\xi}). \end{aligned} \quad (7.2)$$

Here, c_m^\dagger creates a population at site m , with site energies $\pm\varepsilon/2$. We use a inter-site coupling of $d/2$. b_{ξ}^\dagger creates a vibronic mode with a frequency of ω_{ξ} in the harmonic bath and d_{ξ} corresponds to the strength of the exciton phonon-coupling. The latter is characterized by the spectral density $J(\omega) = \pi \sum_{\xi} \hbar^2 \omega_{\xi}^2 d_{\xi}^2 \delta(\omega - \omega_{\xi})$. The relaxation rates γ_r and γ_d are then given by [201] (chapter 21.4.2)

$$\gamma_r \approx d^2 S(b)/(2b^2) \quad \text{and} \quad \gamma_d = \varepsilon^2 S(0)/(2b^2). \quad (7.3)$$

Here, we define $b^2 = \varepsilon^2 + d^2$ and $S(\omega) = J(\omega) \coth(\hbar\omega/2k_bT)$. We evaluate the zero frequency limit $S(\omega \rightarrow 0)$ by using l'Hospital's rule and show that the pure dephasing rate is related to the slope of the spectral density at zero frequency and goes linearly in temperature

$$\gamma_d = \varepsilon^2/(2b^2) \frac{d}{d\omega} J(\omega)|_{\omega=0} k_b T. \quad (7.4)$$

In the high temperature limit $k_b T > b$, the relaxation rate grows linearly with temperature

$$\gamma_r \approx d^2/(b^3) J(b) k_b T. \quad (7.5)$$

Next we illustrate the different contributions of the pure dephasing and the relaxation rate for the decoherence rate. In particular, we compare the situation of the Drude-Lorentz spectral density with the one of the measured super-Ohmic spectral density for the FMO complex J_{Wendling} . For the Drude-Lorentz spectral density we use a reorganization energy $\lambda = 35 \text{ cm}^{-1}$ and a phonon relaxation timescale $\tau_c = 50 \text{ fs}$. We consider the dimer pair BCHs 1 and 2 of the FMO complex with $\varepsilon = 120 \text{ cm}^{-1}$ and $d = -175.4 \text{ cm}^{-1}$ (BChl₁ and BChl₂ of Table 2.1). The pure dephasing rate $\gamma_d/T = 0.15 \text{ cm}^{-1}\text{K}^{-1}$ dominates the decoherence rate γ for the Drude-Lorentz spectral density, while the relaxation rate $\gamma_r/(2T) = 0.032 \text{ cm}^{-1}\text{K}^{-1}$ (high temperature approximation eq. (7.3)) is one order of magnitude smaller than the pure dephasing rate. For the Wendling spectral density J_{Wendling} , we obtain a different picture. Since the Wendling spectral density is super-Ohmic $S(0) = 0$ [49], the pure dephasing rate vanishes $\gamma_d = 0 \text{ cm}^{-1}$. Decoherence is solely driven by the small relaxation rate $\gamma_r/T = 0.06 \text{ cm}^{-1}\text{K}^{-1}$. We propose that the absence of the pure dephasing rate γ_d leads to a prolonged electronic coherence in the exciton dynamics of LHCs.

The analysis of the Spin-Boson model provides an estimate and gives an intuitive physical picture for decoherence in the exciton dynamics. In the following, we carry out non-Markovian simulations of the exciton dynamics and calculate 2d-echo spectra for the FMO complex. We demonstrate that the super-Ohmic Wendling spectral density indeed supports long-lived electronic coherence in the FMO complex. In addition, we show that although pure dephasing is suppressed, the coupling to the vibrational environment is strong, and the fast energy dissipation is retained.

7.3 Implementing the HEOM approach on graphics-processing units

Exact numerical simulations of 2d-echo spectra for the FMO complex for structured spectral densities, such as J_{Wendling} , are very challenging. In recent years, several approaches have been developed and refined to perform non-perturbative and non-Markovian simulations for the exciton dynamics of LHCs [200, 76, 75, 73]. However, all methods struggle with various difficulties. Either they rely on additional approximations [75, 73] that need further validation or only yield reliable results for temperatures around $T = 0$ K [76, 200], which are irrelevant for biological systems. State-of-the-art techniques [45, 44] are able to perform simulations of the population dynamics of the FMO complex at a temperature of $T = 77$ K by using the continuous part of the Wendling spectral density and taking into account one strongly coupled vibronic mode at 180 cm^{-1} . However, more accurate simulations that either incorporate all of the strongly coupled vibronic modes of J_{Wendling} or the simulations of 2d-spectra relevant for the comparison with experiments, have been beyond the numerical capability of the approaches developed in Refs. [200, 76, 75, 73, 45, 44].

To our knowledge, HEOM is the only method in which non-perturbative and non-Markovian simulations of 2d-echo spectra for the seven-site FMO complex are accessible [46, 47]. Since HEOM relies on a Drude-Lorentz spectral density (see section 3.3), only simulations for this specifically shaped spectral density have been performed before. In this chapter, we overcome this limitation and we extend the HEOM approach to general spectral densities. We employ the Meier-Tannor decomposition [82] and represent general spectral densities as superpositions of shifted Drude-Lorentz peaks. Together with the highly efficient GPU-HEOM implementation, see Kreisbeck *et al.* [78]), we develop a powerful tool for simulating the energy transfer in LHCs for structured spectral densities.

According to Meier and Tannor [82], general spectral densities are constructed

	$J_{3\text{peaks}}$
λ_k in cm^{-1}	10, 15, 13
ν_k^{-1} in fs	250, 120, 65
Ω_k in cm^{-1}	85, 170, 300

	$J_{11\text{peaks}}$
λ_k in cm^{-1}	1.2, 6.4, 7.4, 15.6, 3.4, 1.8, 4.0, 2.0, 1.8, 1.9, 2.0
ν_k^{-1} in fs	1600, 550, 400, 370, 750, 800, 750, 600, 750, 750, 500
Ω_k in cm^{-1}	53, 73, 117, 185, 235, 260, 285, 327, 363, 380, 480

Table 7.1: Parameter set for the spectral densities $J_{3\text{peaks}}$ and $J_{11\text{peaks}}$. The reorganization energies λ_k , relaxation timescales ν_k^{-1} , and the energy shift Ω_k of the contributing shifted Drude-Lorentz peaks to the total spectral density eq. (7.6) are shown.

by

$$J(\omega) = \sum_{k=1}^M \frac{\nu_k \lambda_k \omega}{\nu_k^2 + (\omega \pm \Omega_k)^2}. \quad (7.6)$$

We approximate the spectral density of the FMO complex J_{Wendling} by a sum of eleven shifted Drude-Lorentz peaks $J_{11\text{peaks}}$. This reproduces the super-Ohmic onset and takes into account all the strongly coupled vibronic modes. The continuous part of J_{Wendling} is represented by three Drude-Lorentz peaks $J_{3\text{peaks}}$. $J_{11\text{peaks}}$ and $J_{3\text{peaks}}$ are depicted in Fig. 7.1, and the corresponding parameters are listed in Table 7.1. The HEOM technique (see chapter 3.3) relies on the exponential form of the symmetrized correlation $S(t)$, and the response function $\chi(t)$, eqs. (3.16) and (3.18). The exponential form remains intact for a shifted Drude-Lorentz peak. For the spectral density eq. (7.6), we obtain within the high temperature approximation ($\hbar\nu_k\beta < 1$)

$$S(t) \simeq \sum_{k=1}^M \frac{\lambda_k}{\hbar\beta} e^{-\nu_k t} \underbrace{e^{\pm i\Omega_k t}}_{\text{oscil. comp.}} \quad (7.7)$$

and

$$\chi(t) = \sum_{k=1}^M 2\lambda_k/\hbar \underbrace{(\nu_k \pm i\Omega)}_{\text{imag. frequ.}} e^{-\nu_k t} e^{\pm i\Omega_k t}. \quad (7.8)$$

Compared to the original version of the bath correlation functions for a single, non-shifted Drude-Lorentz spectral density eqs. (3.16) and (3.18), the shifted position of the Drude-Lorentz peaks gives rise to an oscillatory component with

a frequency of Ω_k . We proceed along similar arguments as in chapter 3.3, and introduce $\theta_{m,k,s=\pm}(t)$. $\theta_{m,k,s=\pm}(t)$ is defined as being analogous to eq. (3.19), but we replace $\nu \rightarrow \nu_k \pm i\Omega_k$. The hierarchy eqs. (3.21) and (3.22) the changes accordingly

$$\frac{d}{dt}\rho(t) = -\frac{i}{\hbar}\mathcal{L}_{\text{ex}}\rho(t) + \sum_m^N \frac{i}{\hbar}V_m^\times \sum_{k=1,s=\pm}^M \sigma^{(0,\dots,n_{m,k,s=1},\dots,0)}(t) \quad (7.9)$$

with

$$\begin{aligned} \frac{d}{dt}\sigma^{(n_{1,1,s},\dots,n_{1,M,s},\dots,n_{N,1,s},\dots,n_{N,M,s})}(t) = & \\ = \left(-\frac{i}{\hbar}\mathcal{L}_{\text{ex}} - \sum_{m,k=1,s=\pm}^{N,M} n_{m,k}(\nu_k + s i\Omega_k) \right) \sigma^{(n_{1,1,s},\dots,n_{1,M,s},\dots,n_{N,1,s},\dots,n_{N,M,s})}(t) & \\ + \sum_{m,k=1,s=\pm}^{N,M} \frac{i}{\hbar}V_m^\times \sigma^{(n_{1,k,s},\dots,n_{m,k,s+1},\dots,n_{N,M,s})}(t) & \\ + \sum_{m,k=1,s=\pm}^{N,M} n_{m,k,s}\theta_{m,k,s} \sigma^{(n_{1,k,s},\dots,n_{m,k,s-1},\dots,n_{N,M,s})}(t). & \end{aligned} \quad (7.10)$$

The main difference compared to the original version of the hierarchy introduced in chapter 3.3 is that the superposition of M shifted Drude-Lorentz peaks enlarges the index tuple $\vec{n} = (n_{1,1,s}, \dots, n_{1,M,s}, \dots, n_{N,1,s}, \dots, n_{N,M,s})$ of the auxiliary matrices. The previously single index for each site increases to M indexes. Furthermore, there is an additional factor of two in the number of indexes, taking into account the sign s in the shifts $\pm\Omega$ of the Drude-Lorentz peaks. The seven original indexes $\vec{n} = (n_1, \dots, n_7)$ for the FMO complex for a single non-shifted Drude-Lorentz spectral density blow up to 42 (154) indexes for the spectral density J_{3peaks} (J_{11peaks}). This increases the number of auxiliary matrices considerably. For example, the truncation $N_{\text{max}} = 4$ requires that 330 auxiliary matrices need to be propagated for a single non-shifted Drude-Lorentz spectral density. However, J_{3peaks} already requires that 163 185 auxiliary matrices need to be propagated for the same truncation level. There is a huge increase in the computational costs for each additional shifted Drude-Lorentz peak of eq. (7.6) that is added. Thus, HEOM simulations for structured spectral densities like J_{3peaks} , or the even more involved J_{11peaks} for the FMO complex, are computationally very expensive.

The break-through for overcoming the computational limitations is provided by GPU-HEOM, our highly efficient graphics processing unit (GPU) implementation of the hierarchical equations of motion. Our idea is to parallelize the HEOM propagation scheme and to use the 448 streaming processors (1.15 GHz)

provided by the NVIDIA C2050 graphics board in parallel. The HEOM approach is well-suited to a GPU implementation since many computational tasks can be evaluated in parallel resulting in efficient latency hiding [202]. Hiding long latency operations by processing many small tasks is one of the fundamental concepts of GPU computing. To overcome bandwidth limitations, we minimize the memory transfer between GPU memory and CPU memory. The auxiliary matrices are only available on the GPU memory. For the final storage of the data the files, only the 49 entries of the reduced density matrix of the FMO complex need to be transferred from GPU memory to CPU memory. We overcome bandwidth limitations with the suitable work distribution of small tasks to the 448 streaming processors. In addition, we establish concepts to make use of the shared and constant memory of the GPU hardware. This allows fast L1 cache memory access. With these optimization strategies, the communication overhead of the HOEM, which renders CPU based parallelization schemes inefficient [80, 81], is not an issue for the GPU implementation. The performance increase obtained with the GPU-HEOM scales linearly with the number of streaming processors, resulting in a 450-fold reduction in computation time when compared to a single core CPU implementation, see Kreisbeck *et al.* Ref. [78].

In Table 7.2, we provide a comparison between the computation times of the CPU (Intel 2.40 GHz) and the GPU-HEOM implementation. We use a fourth-order Runge-Kutta propagation scheme. The computation times for the population dynamics of the FMO complex for a single non-shifted Drude-Lorentz spectral density are shown. We propagate the system of auxiliary matrices over 1000 time steps. The GPU computation is done in single precision, providing sufficient accuracy for a single non-shifted Drude-Lorentz spectral density. More complex spectral densities, such as $J_{3\text{peaks}}$ and $J_{11\text{peaks}}$, require double precision. Switching from single to double precision approximately gives a factor of two in the computation times. With the increasing depth of the hierarchy N_{max} , more and more auxiliary matrices need to be propagated, and the GPU-HEOM becomes more and more efficient. For the truncation $N_{\text{max}} = 12$, GPU-HEOM achieves a 458-fold speed-up when compared to the single-core CPU implementation.

Our efficient GPU-HEOM enables us to perform simulations of the exciton population dynamics for the FMO complex for the accurate representation of the Wendling spectral density $J_{11\text{peaks}}$. For $J_{3\text{peaks}}$ we can even perform numerically demanding 2d-echo spectra. This requires that the system of auxiliary matrices is propagated for about 1000 times more time steps than for the exciton population dynamics. Simulations of 2d-echo spectra for the spectral density $J_{11\text{peaks}}$ are, however, still beyond present capabilities. We verify the convergence of the hierarchy by increasing the truncation depth and by the inclusion of the low-temperature correction terms. The latter are derived for the extended hierarchy eqs. (7.9) and (7.10) in the same way as in chapter 3.3. The population dynamics

N_{\max}	$\#\sigma\text{-matr.}$	CPU	GPU	speed up	GPU utilization
8	6 435	2 636 s	7 s	$\times 376$	82%
10	19 448	8 275 s	19 s	$\times 435$	93%
12	50 388	21 972 s	48 s	$\times 458$	97%

Table 7.2: Comparison of the computation times between the CPU and GPU-HEOM implementation. The computation times for a fourth-order Runge-Kutta propagation of the population dynamics of the FMO complex over 1000 time steps are shown. We use a single, non-shifted Drude-Lorentz spectral density. The GPU-HEOM calculation is done on a NVIDIA C2050 graphics board (448 streaming processors) within single precision. Using double precision increases the GPU computation time by a factor of two.

for the spectral density $J_{3\text{peaks}}$ and the initial population at BChl 1 ($\rho_{11}(t_0 = 0) = 1$) converges for truncation level $N_{\max} = 3$, $|\rho_{11}^{N_{\max}=3}(t) - \rho_{11}^{N_{\max}=4}(t)| < 10^{-3}$ ($T = 150$ K).

7.4 Two-dimensional echo-spectra for the FMO complex

In this section, we show that a super-Ohmic spectral density supports long lived electronic coherence. We also demonstrate that coherence is robust against thermal noise. We analyze the cross-peak dynamics of 2d-echo spectra for the FMO complex (parameters are given in Table 2.1) for the spectral density $J_{3\text{peaks}}$. We include the rotational average by sampling four laser directions $\vec{l}_1 = (1, 1, 1)$, $\vec{l}_2 = (-1, 1, 1)$, $\vec{l}_3 = (-1, -1, 1)$ and $\vec{l}_4 = (1, -1, 1)$. Figure 7.2 shows a typical 2d-echo spectra, including all six rephasing and non-rephasing pathways for delay time $T_{\text{delay}} = 100$ fs at a temperature of 277 K.

In order to study coherence life-times, we consider cross-peak CP(1,5) (marked by the arrow in Fig. 7.2). Figure 7.3 depicts the normalized amplitude of CP(1,5) for the spectral density $J_{3\text{peaks}}$ as a function of the delay time T_{delay} for temperatures of 150 K and 277 K. We also provide a comparison with the results for the Drude-Lorentz spectral density with the parameters $\lambda = 35$ cm $^{-1}$ and $\tau_c = 50$ fs. The left panel of Fig. 7.3 shows the total signal, including all six rephasing and non-rephasing pathways, while the right panel depicts the cross-peak dynamics for the rephasing and non-rephasing SE pathways only. The total signal shows a small oscillatory component on top of a larger background. The oscillatory signal originates from the SE and ESA pathways. Both pathways show coherent

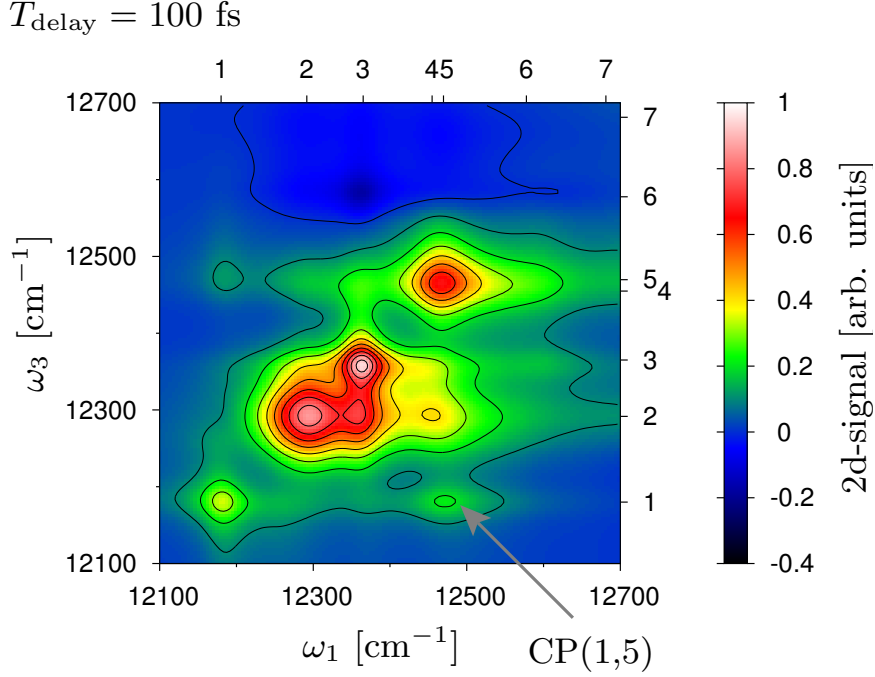


Figure 7.2: GPU-HEOM calculations of the 2d-echo spectrum for the FMO complex for the spectral density $J_{3\text{peaks}}$ at temperature $T = 277$ K. The real part of the signal is shown, including all six rephasing and non-rephasing pathways for delay time $T_{\text{delay}} = 100$ fs. The eigenenergies of the exciton system are marked by the labels 1-7. The arrow points to the cross-peak CP(1,5).

oscillations, the frequency of which matches the difference in the corresponding exciton energies $\omega_{1,5} = (E_1 - E_5)/\hbar$. Oscillations in the ESA and the SE pathways are phase-shifted by π as expected from a coherent dynamics (see section 5.3.2). Since destructive interference diminishes the oscillatory components in the total spectrum, the life-time of the coherence is best analyzed if the SE pathways are considered separately. The rephasing and non-rephasing SE pathways, depicted in Fig. 7.3(b), yield long-lived electronic coherence up to 0.6 ps (0.3 ps) at $T = 150$ K ($T = 277$ K), which is in the range of the experimentally reported coherence life-times for the FMO complex [20]. Compared to the spectral density $J_{3\text{peaks}}$, the coherence life-time for the Drude-Lorentz spectral density (red circles in Fig. 7.3) is two times shorter. At a higher temperature of $T = 277$ K, the Drude-Lorentz spectral density does not yield signatures of long lived coherence. This is in agreement with previous simulations of 2d-echo spectra for a Drude-Lorentz spectral density, Hein and Kreisbeck *et al.* Ref. [46].

We isolate the relevance of discrete, strongly coupled vibronic modes by com-

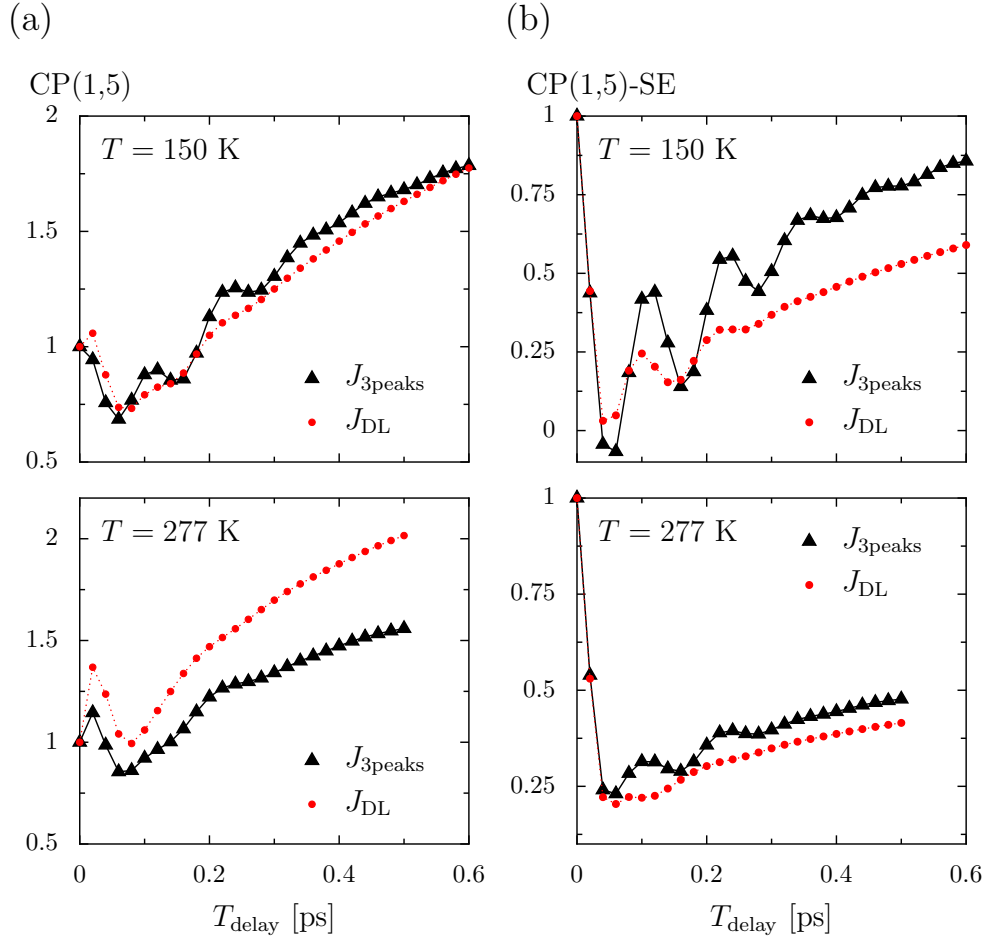


Figure 7.3: Normalized cross-peak oscillations of CP(1,5) of the FMO complex for temperatures of $T = 150$ K (upper panels) and $T = 277$ K (lower panels). The triangles correspond to the spectral density $J_{3\text{peaks}}$. The circles depict the results of the Drude-Lorentz spectral density with $\lambda = 35 \text{ cm}^{-1}$ and $\tau_c = 50 \text{ fs}$. (a) real part of the total rephasing and non-rephasing signal including GB, SE, and ESA pathways. (b) real part of the rephasing and non-rephasing SE pathways.

paring the exciton dynamics for the spectral density $J_{11\text{peaks}}$ with $J_{3\text{peaks}}$. Since 2d-echo spectra are not accessible for $J_{11\text{peaks}}$ we study the coherences ρ_{E_i, E_j} , which are related to the peak dynamics in 2d-echo spectra (see section 5.3.2). Fig. 7.4 depicts the coherence $\rho_{E_1, E_5}(t)$. The presence of strongly coupled discrete modes in $J_{11\text{peaks}}$ does not change the coherence life-times. We conclude that the super-Ohmic Wendling spectral density J_{Wendling} supports long lasting coherence in the FMO complex. Specific, strongly coupled vibronic modes, such as the one

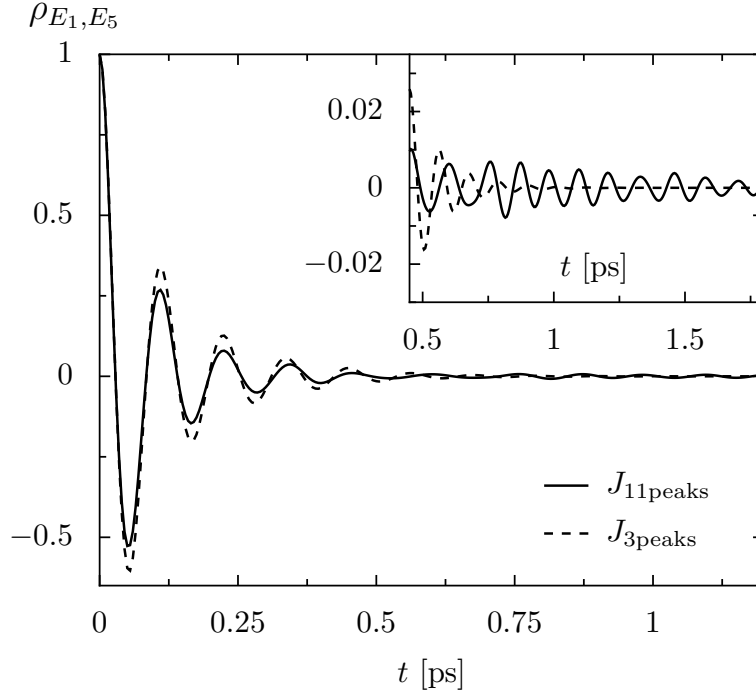


Figure 7.4: Dynamics of the coherence $\rho_{1,5} = \langle E_1 | \rho(t) | E_5 \rangle$ for spectral densities $J_{11\text{peaks}}$ (solid lines) and $J_{3\text{peaks}}$ (dashed lines). Strongly coupled vibronic modes in $J_{11\text{peaks}}$ do not change the coherence life-time. Inset: vibronic mode induced oscillations for $J_{11\text{peaks}}$ with a small amplitude.

around 180 cm^{-1} show up in the spectral density as peaks and give rise to small oscillations in the coherence ρ_{E_1, E_5} . The amplitude of vibronic mode-induced oscillations remains below ≤ 0.01 . The oscillation period depends on the frequency of the discrete, strongly coupled modes and, therefore on the peak positions in the spectral density. The width of the peaks in the spectral density determines the life time of the vibronic mode-induced oscillations in ρ_{E_1, E_5} .

7.5 Static disorder

The super-Ohmic Wendling spectral density reproduces the experimentally observed long-lived electronic coherence. However, the long-lasting coherence is accompanied by sharper peaks in the 2d-echo spectra. These do not agree with the broad spectra of the FMO complex that have been measured in Ref. [20], Fig. 1. In LCHs, there are two mechanisms that lead to broadened peaks in the 2d-echo spectra. These are homogeneous broadening (due to the coupling to a thermal environment), and inhomogeneous broadening. Inhomogeneous broad-

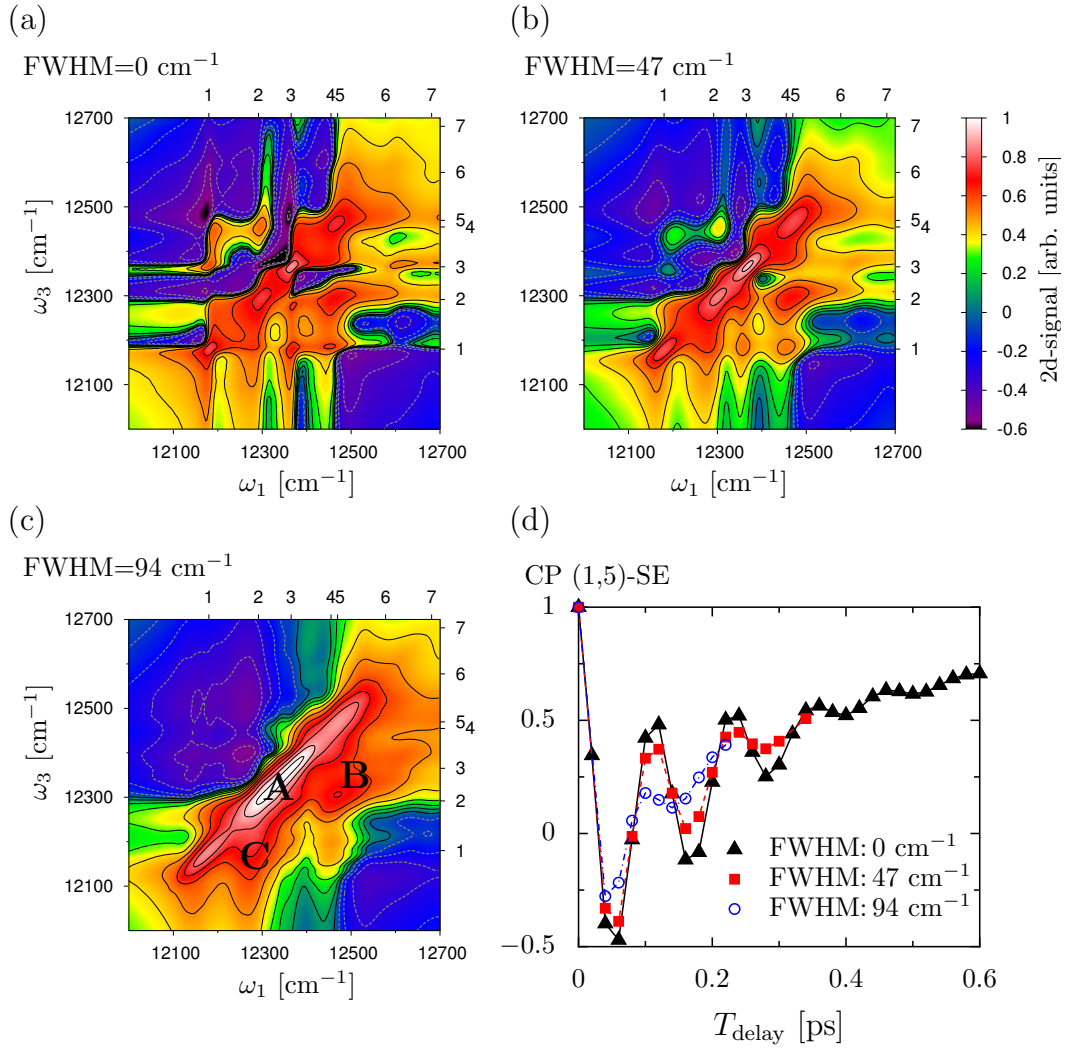


Figure 7.5: Real part of the rephasing SE 2d-echo spectra for delay time $T_{\text{delay}} = 200$ fs at a temperature of $T = 150$ K for different static disorder values. The Monte-Carlo simulations comprise 200 realizations. The exciton energies are marked by the labels 1-7. (a) no static disorder, (b) FWHM = 47 cm⁻¹, and (c) FWHM = 94 cm⁻¹. (d) normalized dynamics of CP(1,5) (real part, rephasing SE) for different static disorder values. The Monte-Carlo simulations comprise 100 (200) realizations for FWHM = 47 cm⁻¹ (FWHM = 94 cm⁻¹).

ening has its origin in slow protein vibrations that induce static disorder in the site energies [34]. In the 2d-echo spectra, this static disorder elongates diagonal peaks along the diagonal axis. The ratio of the diagonal to the off-diagonal width

of the diagonal peaks in the 2d-echo spectra gives an estimate for the relevance of the static disorder compared to that of homogeneous broadening [41].

We model static disorder as Gaussian fluctuations of the site energies $\varepsilon_j \rightarrow \varepsilon_j + \Delta\varepsilon_j$. The probability density for disorder value $\Delta\varepsilon_j$ is given by

$$p(\Delta\varepsilon_j) = \frac{1}{\sigma\sqrt{2\pi}} \exp\left(-\frac{\Delta\varepsilon_j^2}{2\sigma^2}\right). \quad (7.11)$$

The disorder strength is characterized by the full width at half maximum (FWHM), which is related to the standard deviation σ , $\text{FWHM}=2\sqrt{2\ln 2}\sigma$. While static disorder can be analytically incorporated for approximative Redfield approaches [195], this is not possible for HEOM, which requires that Monte-Carlo simulations need to be carried out for many individual realizations of the FMO complex. For each realization, we throw a coin to get a random set of site energies. We include the rotational average by taking samples over four laser directions introduced in section 7.4. The inclusion of the static disorder in the 2d-echo spectra is numerically demanding and each delay time requires the simulation of up to 200 realizations of the FMO complex.

Since the effects of static disorder, such as elongation of the diagonal peaks and changes in the cross-peak dynamics, are already present in the SE pathway, we consider the rephasing SE pathway only. Fig. 7.5 shows 2d-echo spectra (real part, rephasing SE) for the different disorder values $\text{FWHM}=0 \text{ cm}^{-1}$, 47 cm^{-1} , and 94 cm^{-1} for the delay time $T_{\text{delay}} = 200 \text{ fs}$ and a temperature of $T = 150 \text{ K}$. For better comparison with the experiments [20], Fig. 1., we use an arcsinh scale. This scale is used for the experimental data to emphasize structures in 2d-echo spectra with small amplitudes. Without static disorder ($\text{FWHM}=0 \text{ cm}^{-1}$), the peaks in the 2d-echo spectra are individually resolved. This is not observed in the experimental data where the 2d-echo spectra is strongly convoluted. With increasing static disorder, diagonal peaks get elongated, and for $\text{FWHM}=94 \text{ cm}^{-1}$, we reproduce basic features of the experimental data. Diagonal peaks coalesce and there is a large diagonal peak marked by region A in Fig. 7.5(c). Furthermore, the finer structures present for $\text{FWHM}=0 \text{ cm}^{-1}$ and $\text{FWHM}=47 \text{ cm}^{-1}$ smear out, and the individual peaks are no longer resolved, resulting in an outspread amplitude in regions B and C. Disorder $\text{FWHM}=94 \text{ cm}^{-1}$ turns out to be a realistic parameter for reproducing the experimental line shapes in 2d-echo spectra. This observation is in agreement with previous estimates of static disorder $\text{FWHM}=80 \text{ cm}^{-1}$ from linear absorption spectra [203].

In order to study the effects of static disorder for the cross-peak oscillations, we consider the dynamics of CP(1,5) (real part, rephasing SE) at a temperature of $T = 150 \text{ K}$. Fig. 7.5(d) shows the normalized amplitude of CP(1,5) as a function of the delay time for different static disorder values. Static disorder leads to an additional damping of the oscillatory signal in CP(1,5). Coherent beatings are robust against static disorder and remain largely intact for $\text{FWHM}=47 \text{ cm}^{-1}$.

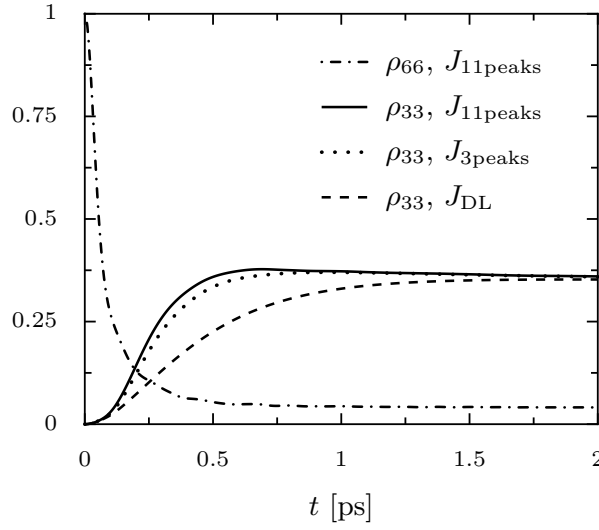


Figure 7.6: Population dynamics for the initial population at BChl 6 at a temperature of $T = 277$ K for different spectral densities.

For a larger disorder $\text{FWHM} = 94 \text{ cm}^{-1}$ oscillations are present but suppressed to a greater extent.

7.6 Transfer efficiency

The functional role of the FMO complex is to enable fast energy transfer toward the reaction center. Energy transfer is noise assisted and relies on fast thermalization. This drives the population along the energy gradient to the target BChl 3, which couples to the reaction center (see chapter 4).

Here, we demonstrate that the suppressed dephasing rate yields long-lived electronic coherence, but does not drive the system toward a weak coupling limit, of which transfer to the reaction center is inefficient. Indeed, the spectral densities $J_{11\text{peaks}}$ and $J_{3\text{peaks}}$ support the conditions for fast energy transfer. We exemplify the transfer efficiency for the energy pathway with an initial population at BChl 6 of the FMO complex at a physiological temperature of $T = 277$ K. Fig. 7.6 depicts the corresponding population dynamics. For comparison, the dynamics for the Drude-Lorentz spectral density ($\lambda = 35 \text{ cm}^{-1}$, $\tau_c = 50 \text{ fs}$) is shown. For $J_{11\text{peaks}}$, the initial population at BChl 6 drops very quickly, and after 2 ps the exciton system reaches the thermal state with a preferred occupation of the target BChl 3. Compared to the Drude-Lorentz spectral density, we find that $J_{11\text{peaks}}$ yields even faster transfer to the target BChl 3. For intermediate time $\sim 0.7 \text{ ps}$, the population at BChl 3 *overshoots* and ρ_{33} is larger than its

thermal population. Similar observations are obtained for the spectral density $J_{3\text{peaks}}$, the thermal relaxation rate of which is almost the same as for $J_{11\text{peaks}}$.

We include trapping to the reaction center and exciton recombination in the same way as introduced in chapter 4. We use a trapping rate to the reaction center of $\Gamma_{\text{RC}}^{-1} = 1$ ps and a loss rate of $\Gamma_{\text{loss}}^{-1} = 1$ ps. For the spectral density $J_{3\text{peaks}}$ and for the initial population at BChl 6, we obtain an average trapping time (eq. (4.14)) of 3.4 ps. Hence, energy transfer is about 10% faster than for the Drude-Lorentz spectral density, yielding an average transfer time of 3.8 ps.

7.7 Conclusion and outlook

We extend the HEOM approach to general spectral densities, where we use the Meier and Tannor decomposition of the spectral density in terms of shifted Drude-Lorentz peaks. In combination with the GPU (graphics processing unit) implementation for HEOM (GPU-HEOM), we develop a numerically efficient tool for exact simulations of the exciton dynamics in LHCs. This offers the opportunity of performing simulations for an accurate representation of the experimentally measured spectral density of the FMO complex. To our knowledge, this is the most realistic model of energy transfer in the FMO complex.

In order to reproduce the experimental observations for the FMO complex obtained from 2d-echo spectroscopy, the reproduction of three aspects is required: (i) long-lasting coherence, (ii) fast thermalization, and (iii) broad line shapes in the spectra. The parameters of the Redfield approaches can be fitted to fulfill the last two conditions, but then no long-lasting electronic coherence remains. Condition (i) is achieved in a trivial way by reducing the coupling strength to the phonon-bath. But then, both conditions (ii) and (iii) are violated. This indicates the difficulty of bringing together the three contradictory experimental findings.

Here, we demonstrate a mechanism for matching all three requirements. The super-Ohmic spectral density of the FMO complex ensures long-lasting coherence, while the strong coupling to a continuum of higher phonon modes ensures fast thermalization. By including static disorder, we reproduce the basic features in the experimentally obtained line shapes in the 2d-echo spectra. Our simulations imply that the measured broad line shapes in the 2d-echo spectra of the FMO complex are dominated by the static disorder. Concerning the proposal that strongly coupled vibronic modes might be responsible for the experimentally obtained cross-peak dynamics in 2d-spectra, we demonstrate that those strongly coupled modes do not have a significant influence on the cross-peak dynamics of the 2d-spectra.

Finally, we show that the super-Ohmic spectral density supports fast energy transfer to the reaction center. Energy transfer is even faster than for the Drude-Lorentz spectral density. To what extent long-lived electronic coherence is re-

sponsible for the enhanced efficiency remains an interesting question for future works.

II. Ballistic transport through AlGaAs/GaAs semiconductor devices

1 Basic concepts of mesoscopic transport

In the energy transfer in LHCs discussed in Part I, the coherent dynamics in the exciton system is simple. The coupling to the vibrational environment, however, induces rather complex effects in the exciton dynamics. The situation in electron transport through semiconductor devices is different. There is a large mean-free path and electrons undergo a coherent motion up to $50\text{ }\mu\text{m}$ in high mobility samples [84, 85, 86, 87, 88]. Typically, the mean free-path is larger than the extension of the device. Therefore non-trivial coherent interference effects due to elastic scattering at the device geometry are responsible for the transport characteristics of semiconductor devices.

In the following, we recapitulate the basic ideas behind ballistic electron transport through semiconductor devices that are presented in many textbooks [92, 93, 94, 107, 98, 204]. Semiconductor devices consist of macroscopic contacts acting as electron reservoirs, that feed currents to a mesoscopic system such as quantum dots or quantum waveguide structures. In general, the system can be seen as a scattering region, whose length scale ranges from the nanometer scale up to a few microns. The mesoscopic system and the macroscopic contacts are connected via leads. Ballistic transport phenomena in mesoscopic systems are commonly described within the Landauer-Büttiker formalism [105, 106]. This approach relates experimental observables, such as current and voltages, to transmission amplitudes. This is discussed in more details below.

Despite the complexity of semiconductor heterostructures, many applications of electron transport can be reduced to an effectively non-interacting, particle picture. The electron-electron interaction and the positive background charges of the donors of the bulk material reduce to an effective potential. Transport is then described in terms of wave scattering and driven by the coherent motion of the electrons. The Bloch theorem for the electronic wave function in periodic potentials results in the formation of band structures for the density of states in the lattice. The band structure comprises of band gaps and depends on the bulk material. The population of the available states of the bands is determined by the number of electrons and the thermal occupation according to the Fermi-Dirac distribution. For the electron transport, only a small region around the

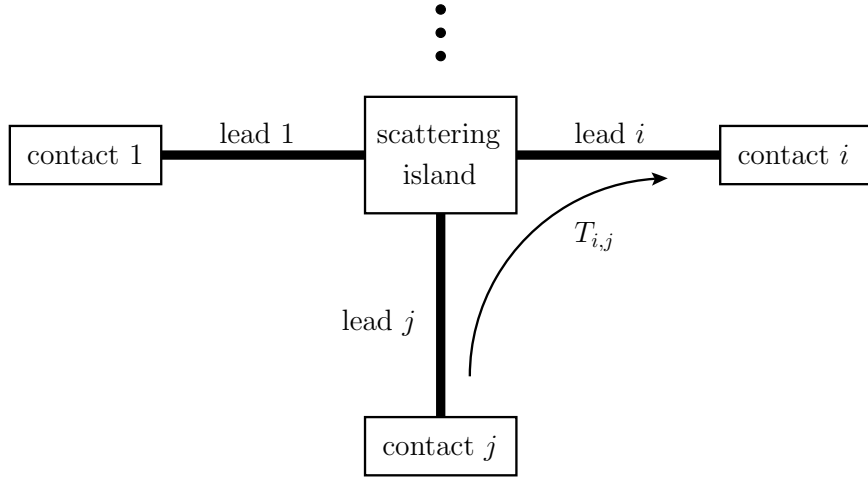


Figure 1.1: Schematic sketch of a multi-terminal device. Macroscopic contacts feed electrons into the leads. The leads are connected by a scattering island. Interference effects due to elastic scattering determine the transmission probabilities $T_{i,j}$. $T_{i,j}$ stands for the probability of injected electrons in lead j being transferred to lead i , where the electrons are then absorbed in contact i .

Fermi energy is relevant. In this case the electron motion can be described by free carriers with effective mass m^* . Within the effective mass approximation, the electronic wavefunction is given by the solution of an effective single-particle Hamiltonian

$$\mathcal{H} = \frac{\mathbf{p}^2}{2m^*} + V(\mathbf{r}) \quad (1.1)$$

where \mathbf{p} is the momentum operator. The scattering potential $V(\mathbf{r})$ takes into account the device geometry.

In the following, we consider the transport through AlGaAs/GaAs heterostructures. At the interface of the AlGaAs and GaAs layers, the electron motion is confined along the direction perpendicular to the interface and the electrons form a quasi two-dimensional electron-gas (2DEG) along the remaining directions. A further confinement into, for example, quantum waveguides or quantum dots, is achieved with etching techniques or the alignment of gate voltages. We describe the transport through the AlGaAs/GaAs-based nano-devices within the Landauer-Büttiker formalism. The total system is composed of three parts. There are macroscopic contacts, asymptotic leads, and a scattering island that connects the leads. Each lead in combination with a macroscopic contact is commonly referred to as terminal. A schematic sketch of a multi-terminal device is shown in Fig. 1.1. The physics of ballistic transport in multi-terminal devices

is determined by coherent elastic scattering at the geometry of the scattering island. The transport is described by the scattering matrix whose entries correspond to the transmission amplitudes $t_{i,j}$ for an incoming electron in lead j to be scattered to an outgoing electron in lead i . The corresponding transmission probability is given by $T_{i,j} = |t_{i,j}|^2$. The transmission probabilities $T_{i,j}$ are the key ingredients and determine the transfer characteristics of the device. In general, $T_{i,j}(E)$ depends on the energy E of the electrons. In Chapter 2, we discuss in detail numerical methods for calculating the transmission probabilities $T_{i,j}(E)$. The microscopic current in each lead is given by the Landauer formula

$$I_i = \frac{e}{h} \int dE \sum_j T_{i,j}(E) (f_i(E) - f_j(E)), \quad (1.2)$$

which relates the current to the transmission probabilities $T_{i,j}(E)$. The Fermi functions $f_i(E) = (e^{(E-\mu_i)/k_B T} + 1)^{-1}$, with chemical potentials μ_i , characterize the electron occupation of the macroscopic contacts.

Depending on the experimental setup, the macroscopic contacts act either as voltage or current probes. This enforces different boundary conditions for the currents I_i . When contact i is used as a current probe, the macroscopic contact feeds lead i with a continuous current flow $I_i = I$. If contact i acts as voltage probe, the situation is different. All incoming electrons in lead i are then absorbed by contact i . At the same time, however, the absorbed electron is replaced by an outgoing electron injected by the contact i . Thus, there is no net current in the voltage probes and the system enforces the condition $I_i = 0$. In general, the boundary conditions yield non-linear equations that determine the chemical potentials μ_i and hence the state of the macroscopic contacts. This allows one finally to calculate the experimentally observed currents and voltages.

2 A time-dependent approach for mesoscopic transport

2.1 Introduction

Ballistic transport in semiconductor devices is described within the Landauer-Büttiker formalism [107, 98, 105]. The device is divided into semi-infinite leads connected by a scattering island. The microscopic currents in the leads are expressed in terms of the transmission amplitudes which correspond to the entries of the scattering matrix.

Standard methods in mesoscopic transport are based on the Keldysh Green's function formalism [107, 98, 205, 206, 207]. The scattering matrix is related to the Green's function via the Fisher-Lee relation [208]. The Green's function for a non-interacting system is often numerically implemented using a recursive algorithm [98]. The underlying Hamiltonian is approximated by a tight-binding ansatz with nearest-neighbor hopping. The Green's function is defined on discrete lattice points. The semi-infinite leads are expressed in the form of self-energies, which reduces the open system to the finite sized scattering region. The lattice is then divided into slices and the Green's function is calculated recursively. Recently, various groups have invented elaborate tricks to speed up the naive algorithm. For example in Refs. [108, 109], the total system is classified into certain modules. The Green's function is then evaluated for each module separately. Besides the modular approach which is optimized for special geometries, more general methods have also been developed. Instead of dividing the lattice into slices, the so called *knitting algorithm* adds the grid points one by one, like knitting a sweater [110]. Another method of optimization uses a clever way of ordering the grid points, giving rise to an optimal block-tridiagonal form of the corresponding tight-binding Hamiltonian [111]. All of these different methods improve the numerical performance, but nevertheless the scattering matrix, is only evaluated for a single energy. That is, whenever transport properties are studied for large devices and for a wide range of Fermi energies, the recursive Green's function approach becomes computationally inefficient.

In this chapter, we go another way and develop a time-dependent approach

based on wave-packet propagation to compute the stationary transmission amplitudes. For many applications, it is more convenient to solve the time-dependent Schrödinger equation than its time-independent pendant [209, 210]. Several numerical methods are available for solving the time-dependent Schrödinger equation, such as the split-operator method [211, 212] or the polynomial expansion approaches [213, 214, 215]. The wave-packet methods have been established in theoretical chemistry to simulate coherent reactive scattering [113, 114, 115, 116, 117, 118]. Nevertheless, so far time-dependent descriptions have been used only rarely in condensed matter physics. The situation has changed in recent years, when wave packet methods have started to become employed in mesoscopic transport as well [216, 217, 218, 219]. For example, wave-packet propagation is used to simulate experiments of the magnetic focusing of electron waves [97, 112]. Wave packet-propagation methods are not restricted to semiconductor heterostructures but are also applied to new materials like graphene [220, 221].

The previous wave-packet applications for mesoscopic physics have in common that merely a pulse is propagated. However, in order to simulate real devices, the wave packets have to be associated with physical meanings. This is achieved, for example, in applications where the electrons are subjected to strong potential gradients and enter the device as localized states at certain injection points, the so-called hot spots [221]. The electrons are also represented by localized wave packets in situations where electrons are injected via a scanning tunneling microscope (STM) tip [222] that acts as a point-like electron source. In mesoscopic transport, electrons can be represented by thermal wave packets that in turn represent the average behavior of a certain thermal energy distribution [216]. However for low temperatures, the energy distribution of the electrons becomes narrow and thermal wave packets are strongly extended in the position domain leading, to numerical limitations.

The key point of this chapter is to overcome previous limitations and to introduce an approach that fully reconstructs the scattering matrix. Having the transmission amplitudes at hand allows us to perform simulations of current and voltage measurements of arbitrarily shaped multi-terminal devices. In this chapter, we introduce a time-dependent approach based on the Fourier analysis of cross-correlation functions, defined as the overlap between suitable sender and receiver wave packets. This approach allows us to describe electron transport in mesoscopic systems. The basic ideas for the application of the wave packet approach in mesoscopic physics are given by Kramer, Kreisbeck, and Krueckl in Ref. [223]. The time-dependent approach has several advantages. Firstly, the quantum choreography of the propagated pulse (sender) gives an intuitive physical picture of the scattering mechanisms involved in the transfer process. Secondly, the wave packet propagation efficiently computes the energy-resolved transmission amplitudes for a large range of energies. Thirdly, our time-dependent approach allows us to simulate general multi-terminal devices

with complicated geometries and topologies. Finally, the time-dependent approach is suited for high performance graphics processing unit (GPU) computation, yielding a 35 fold speed-up (double precision) compared to the CPU (central processing unit) implementation. The GPU algorithm is explained in detail in section 2.4.

In section 2.2, we formulate the scattering problem and define the scattering matrix. We illustrate how information about the scattering matrix is incorporated within the wave-packet propagation and revealed by suitable correlations with stationary receiver wave-packets. This yields the energy-resolved transmission amplitudes. In section 2.3, we follow the ideas of Heller *et al.* [216] who represents the thermal average behavior of electrons in terms of thermal wave packets. The thermal average of electrons is represented by a suitable choice of the shape of the wave packets used. We carry out a flux analysis and relate the observed currents in a two-terminal device to the quantum mechanical flux of the propagated wave packet. In section 2.4 we introduce numerical techniques for efficient wave packet propagation and establish our efficient GPU implementation. We close with a summary in section 2.5.

2.2 Wave-packet propagation and transmission amplitudes

The total system is composed of a microscopic scattering island that is coupled to macroscopic contacts via semi-infinite leads. That is the total Hamiltonian

$$\mathcal{H} = \sum_i \mathcal{H}_i^{\text{asym}} + \mathcal{H}^{\text{scat}} \quad (2.1)$$

splits into asymptotic parts $\mathcal{H}_i^{\text{asym}}$, describing the leads and a scattering part $\mathcal{H}^{\text{scat}}$. A sketch is given in Fig. 2.1. The leads are semi-infinite quasi one-dimensional objects that are quantized in transversal direction. In this section, we introduce a time-dependent approach based on wave packet propagation to compute the transmission amplitude t_{in_i, jn_j} , which corresponds to the probability amplitude of scattering from lead j populating transversal mode n_j to lead i populating transversal mode n_i . Within the Landauer-Büttiker formalism, the microscopic current in each lead i eq. (1.2) is then related to the transmission probability $T_{i,j} = \sum_{n_i, n_j} |t_{in_i, jn_j}|^2$.

We adapt time-dependent approaches established in theoretical chemistry to describe reactive scattering [210, 113, 114, 115, 116, 117, 118] to mesoscopic transport. We extend the concepts of Tannor *et al.* [210, 113, 116] and incorporate a homogeneous external magnetic field perpendicular to the plane of the scattering potential, see Fig. 2.1. In mesoscopic transport homogeneous magnetic fields

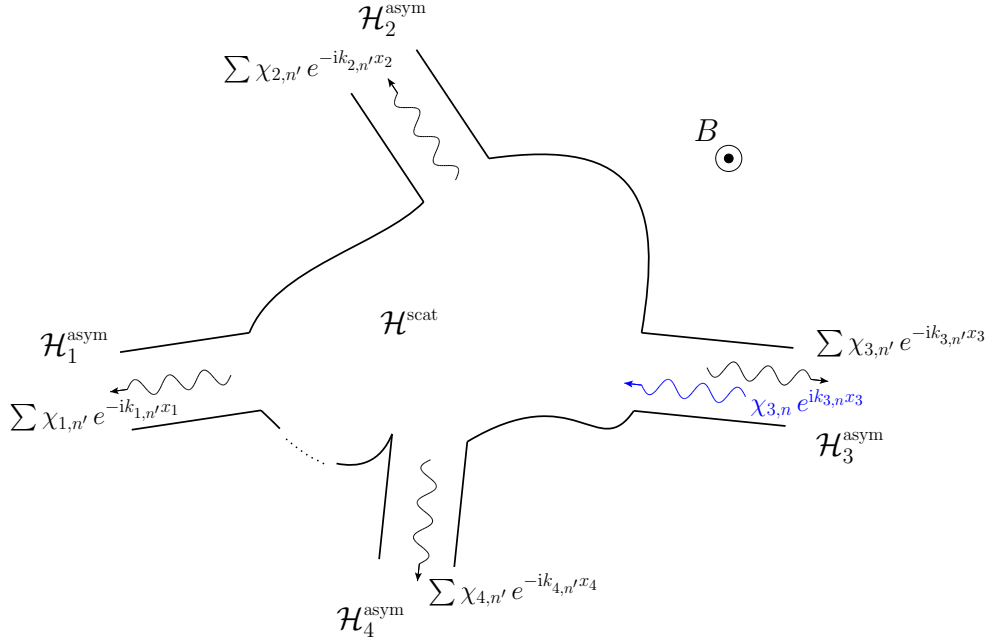


Figure 2.1: Sketch of a multi-terminal device. The scattering region described by $\mathcal{H}^{\text{scat}}$ is attached to semi-infinite leads $\mathcal{H}_i^{\text{asym}}$. The waves illustrate the scattering eigenstate $\psi_{3,n}^+(E)$ in the asymptotic regions, where $\psi_{3,n}^+(E)$ can be expressed in terms of asymptotic lead eigenstates $\psi_{i,n_i,\pm}(E)$, eq. (2.4). $\psi_{3,n}^+(E)$ is related to an incoming wave in lead 3 populating transversal mode $\chi_{3,n}$ with longitudinal momentum $k_{3,n}$. This wave is either reflected or transmitted to outgoing waves in all other leads, which may also populate different modes as a consequence of inter-mode scattering. The homogeneous magnetic field B is perpendicular to the plane of the scattering region.

play an important role. Prominent examples are Aharonov-Bohm interference devices [119, 126, 124, 134] or four-terminal Hall-junctions [105, 223, 91, 104]. For clarity, we show the B -field dependency explicitly in our notation when new physics is involved, but suppress it otherwise.

We identify the scattering eigenstates of the full Hamiltonian with the corresponding eigenstates of the asymptotic leads. The leads are transversally confined and hence quantized in transversal direction. The lead eigenstates are defined as follows

$$\mathcal{H}_i^{\text{asym}} \psi_{i,n_i,\pm}(E) = E \psi_{i,n_i,\pm}(E) \quad (2.2)$$

with

$$E = \frac{\hbar^2 k_i^2}{2m^*} + E_{i,n_i,\pm k_i} \quad (2.3)$$

and

$$\psi_{i,n_i,\pm}(E) = \left(\frac{\partial E}{\partial k_i} \right)^{-\frac{1}{2}} \chi_{i,n_i,\pm k_i} e^{\pm i k_i x_i}. \quad (2.4)$$

Here, $\chi_{i,n_i,\pm k_i}$ is the n_i -th transversal mode of lead i with transversal energy $E_{i,n_i,\pm k_i}$. The remaining energy goes into the longitudinal kinetic energy part $E_{\text{kin}} = \hbar^2 k_i^2 / 2m^*$. The longitudinal orientation of the leads points along coordinate \hat{x}_i . Positive longitudinal wave vectors k_i correspond to incoming waves. That is, its momentum points toward the scattering region, whereas negative wave vectors correspond to outgoing waves leaving the scattering region. In the presence of a magnetic field, the transversal modes also depend on the longitudinal momentum (see appendix B). The factor $(\partial E / \partial k_i)^{-\frac{1}{2}}$ ensures the normalization condition

$$\langle \psi_{i,n,\pm}(E) | \psi_{i,n',\pm}(E') \rangle = \delta_{nn',\pm\pm} \delta(E - E'). \quad (2.5)$$

The asymptotic eigenfunctions form a complete orthonormal set in lead i .

Scattering eigenstates of the total Hamiltonian are solutions of the Schrödinger equation that is restricted to the asymptotic regions. Thus, we categorize scattering eigenstates in terms of their behavior in the asymptotic leads. We define

$$\mathcal{H} \psi_{i,n_i}^{\pm}(E) = \left(\frac{\hbar^2 k_i^2}{2m^*} + E_{i,n_i,\pm k_i} \right) \psi_{i,n_i}^{\pm}(E) = E \psi_{i,n_i}^{\pm}(E), \quad (2.6)$$

where $\psi_{i,n_i}^{\pm}(E)$ is related to the asymptotic eigenstates $\psi_{i,n_i,\pm}(E)$ of lead i . In the corresponding time picture, $\psi_{i,n}^+$ starts with an incoming wave in lead i with fixed momentum k_i populating transversal mode n_i . After the wave hits the scattering region it gets either reflected in lead i or transmitted to outgoing waves in other asymptotic leads $j \neq i$. Due to inter-mode scattering, the reflected and transmitted parts are superpositions of different transversal modes. Fig. 2.1 exemplifies the situation for ψ_{3,n_3}^+ . The scattering eigenstates ψ_{i,n_i}^- correspond to the time-reversed situation

$$\psi_{i,n_i}^-(B) = (\psi_{i,n_i}^+(-B))^*. \quad (2.7)$$

All scattered parts unify in a single outgoing wave with wave vector k_i and transversal mode n_i . $\psi_{i,n}^+$ describes the history, whereas $\psi_{i,n}^-$ describes the destiny of the states. This gives an intuitive picture of the definition of the scattering matrix

$$t_{in_i,jn_j}(E) \delta(E - E') = \langle \psi_{i,n_i}^-(E) | \psi_{j,n_j}^+(E') \rangle, \quad (2.8)$$

which can be interpreted as the projection of the *destiny* on the *history*. The elements $t_{in_i,jn_j}(E)$ of the scattering matrix define the transmission amplitudes

entering the Landauer formula eq. (1.2). Each $\psi_{i,n_i}^+(E)$ and $\psi_{i,n_i}^-(E)$ form a complete orthonormal set of scattering eigenstates

$$\langle \psi_{i,n_i}^+(E) | \psi_{j,n_j}^+(E) \rangle = \delta_{i,j} \delta_{n_i,n_j} \delta(E - E') \quad (2.9)$$

$$\langle \psi_{i,n_i}^-(E) | \psi_{j,n_j}^-(E) \rangle = \delta_{i,j} \delta_{n_i,n_j} \delta(E - E'). \quad (2.10)$$

A detailed proof of these orthonormalization relations is given in Ref. [210], appendix C.

So far, we have recapitulated the definition of the scattering matrix. We have defined the setup and introduced the notation. In the following, we establish the concepts behind the wave-packet approach. Let us now define an incoming sender wave packet that fulfills the following criteria: The wave packet is located in one of the asymptotic leads where it populates a specific transversal mode. Moreover, it is composed of purely incoming longitudinal momenta. Such a sender wave-packet is represented in terms of scattering eigenstates $\psi_{j,n}^+(E)$,

$$\phi_{j,n_j}^{\text{send}} = \int dE \mu_{j,n_j}^{\text{send}}(E) \psi_{j,n_j}^+(E). \quad (2.11)$$

In an analogous manner, we define a receiver wave-packet that is located in lead i where it populates transversal mode n_i . The receiver wave-packet is composed of purely outgoing longitudinal momenta. Thus, the receiver is constructed as a superposition of scattering eigenstates $\psi_{i,n_i}^-(E)$,

$$\phi_{i,n_i}^{\text{rec}} = \int dE \mu_{i,n_i}^{\text{rec}}(E) \psi_{i,n_i}^-(E). \quad (2.12)$$

The receiver represents the destiny of the scattered wave and can be interpreted as a detector. The scattering eigenstates are recovered by

$$\psi_{i,n_i}^\pm(E) = \frac{(2\pi\hbar)^{-1}}{\mu_{i,n_i}^{\text{send/rec}}(E)} \int_{-\infty}^{\infty} dt \phi_{i,n_i}^{\text{send/rec}}(t) e^{iEt/\hbar}, \quad (2.13)$$

where

$$\phi_{i,n}^{\text{send/rec}}(t) = e^{-i\mathcal{H}t/\hbar} \phi_{i,n}^{\text{send/rec}}(t_0 = 0) \quad (2.14)$$

corresponds to the time evolution of the wave packets. During the propagation of the wave packet, it successively traverses the potential landscape and its time-correlation function recovers the stationary solutions of the underlying Hamiltonian. We insert eq. (2.13) into the definition of the scattering matrix eq. (2.8) and express the transmission amplitudes

$$t_{in_i,jn_j}(E) = \frac{(2\pi\hbar)^{-1}}{(\mu_{i,n_i}^{\text{rec}}(E))^* \mu_{j,n_j}^{\text{send}}(E)} \int_{-\infty}^{\infty} dt C_{in_i,jn_j}(t) e^{iEt/\hbar} \quad (2.15)$$

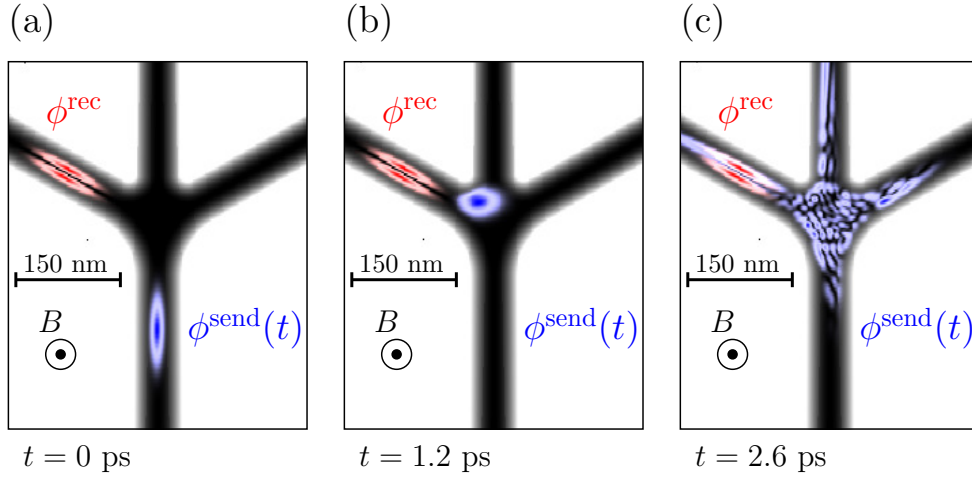


Figure 2.2: Illustration of the basic steps for computing the transmission amplitudes. As an example, we consider the scattering from the lower lead (populating the transversal ground state) to the left lead (populating the first excited transversal mode) of a non-centrosymmetric junction in the presence of a perpendicular magnetic field with $B = 0.4$ T. The red wave packet illustrates the receiver wave-packet, whereas the blue wave packet corresponds to the sender wave-packet. During the time evolution of the sender wave-packet, depicted for (a) the initial situation $t=0$, (b) $t=1.2$ ps and (c) $t=2.6$ ps, we record the cross-correlation function. Transforming the cross correlation to the energy domain then gives the corresponding transmission amplitudes.

in terms of the cross-correlation function

$$C_{in_i, jn_j}(t) = \langle \phi_{i,n_i}^{\text{rec}} | e^{i\mathcal{H}t/\hbar} | \phi_{j,n_j}^{\text{send}} \rangle = \langle \phi_{i,n_i}^{\text{rec}} | \phi_{j,n_j}^{\text{send}}(t) \rangle. \quad (2.16)$$

The cross-correlation function is given as the projection of the receiver wave-packet on the propagated sender wave-packet. Equation (2.15) relates the mode-resolved transmission amplitudes to the time evolution of the sender wave-packets and is the central result of this section. The factors $\mu_{i,n}^{\text{send/rec}}$ in eq. (2.15) are correction terms. These depend on the wave packets used and describe with which weights the individual scattering eigenstates contribute to the wave packets used. They are defined in eq. (2.11) and eq. (2.12) respectively, and are given by projecting the scattering eigenstates on the wave packets

$$\mu_{i,n_i}^{\text{send/rec}}(E) = \langle \psi_{i,n_i}^{+/-}(E) | \phi_{i,n_i}^{\text{send/rec}} \rangle. \quad (2.17)$$

Since the wave packets $\phi_{i,n_i}^{\text{send/rec}}$ are located in the asymptotic channels, the scattering eigenstates are associated with lead eigenstates defined in eq. (2.4). Thus

eq. (2.17) reduces to

$$\mu_{i,n_i}^{\text{send/rec}}(E) = \left(\frac{\partial E}{\partial k_i} \right)^{-\frac{1}{2}} \langle \chi_{i,n_i,\pm k_i} e^{\pm i k_i x_i} | \phi_{i,n_i}^{\text{send/rec}} \rangle. \quad (2.18)$$

The basic steps for computing the transfer matrix are illustrated in Fig. 2.2 for a non-centrosymmetric junction. We consider the process of scattering from the lower lead populating the transversal ground state to the left lead populating the first excited transversal mode. We define an outgoing receiver state corresponding to the destination that is located in the left lead (indicated by the red wave packet) and an incoming sender wave-packet (indicated by the blue wave packet). The sender wave-packet describes the history and is initially ($t = 0$ ps) located in the lower lead. During the time evolution, the sender scatters into the different arms and we detect all parts reaching the destination by computing the overlap between sender and receiver. The corresponding scattering matrix element is then given according to eq. (2.15) by the energy representation of the cross-correlation function. An explicit example of the application of the wave-packet approach and the typical shape of the cross-correlation function is given in Chapter 3 for ballistic transport through a four-terminal quantum-waveguide ring.

2.3 Gaussian wave-packets and thermal electrons

2.3.1 Introduction

In section 2.2, we introduce sender and receiver wave-packets for computing the transmission amplitudes. The explicit form of the receiver and sender wave-packets has not yet been specified, and there is a certain degree of freedom in the choice of the wave packets. The wave packets have to satisfy just three restrictions. Firstly, the wave packets need to be located in one of the asymptotic leads. For the sender, this condition has to be fulfilled only at initial time $t = 0$. Secondly, the transversal shape of the wave packets needs to represent a lead mode. Thirdly, the wave packets are composed of either purely incoming (sender) or purely outgoing (receiver) longitudinal momenta.

The longitudinal momentum distribution of the wave packets is related to the factors $\mu_{i,n_i}^{\text{send/rec}}(E)$ which correspond to the energy representation of the wave packets, eqs. (2.11) and (2.12). This facilitates the design of optimized wave packets for the requirements of the specific physical situation. For example, the wave packets can be designed to represent the thermal average behavior of

transport in semiconductor devices. This is the idea behind thermal wave packets [216]. The wave packet then gains a physical meaning and its time evolution is interpreted as a thermal electron that is transported through the device. Thermal wave packets are used, for example, to study temperature dependencies of interference phenomena [216, 112] in mesoscopic devices.

In section 2.3.2, we relate the energy distribution $\mu_{i,n_i}^{\text{send/rec}}(E)$ of the wave packets to their longitudinal momentum distribution. This yields a well-defined way of controlling the energy distribution by adjusting the longitudinal shape of the wave packets as we show for Gaussian wave-packets. In section 2.3.3, we then consider a two-terminal device and describe transport in terms of thermal wave packets. We show that thermal averages are represented in a good approximation by Gaussian wave-packets. Thus, for suitable parameter choices the choreography of a Gaussian pulse visualizes the transport through the device [216, 112].

2.3.2 Relation between energy and momentum representation

The energy representation of the sender and receiver wave-packets $\mu_{i,n_i}^{\text{send/rec}}(E)$ appears as correction terms in the formula for the transmission amplitudes eq. (2.15). The transmission amplitudes are obtained for energies which are well-represented by the wave packets and, hence, $\mu_{i,n_i}^{\text{send/rec}}(E)$ determines the energy range covered by the wave packets where the transmission amplitudes are accessible within a single wave-packet run. In the following, we relate the covered energy range to the longitudinal momentum distribution of the sender and receiver wave-packets. We show that the parameters of Gaussian wave-packets can be adjusted to cover any energy range. However, in practice, numerical limitations induce additional constraints on the wave-packet parameters. Both grid discretization and wave-packet dispersion set numerical limits to the spatial extension of the wave packets. Position and momentum representation are related by Heisenberg's uncertainty principle. Since the energy range, which is covered by the wave packet, depends on the momentum representation, the grid size limitations set restrictions for the treatable energy range of a single wave-packet run. For the transport problems discussed in this thesis, the energy representation of the wave packets typically covers 5 meV to 15 meV. We start with the characterization of the asymptotic lead eigenfunctions. We assume that the asymptotic leads are represented by harmonic waveguides. Lead i points along the x_i -direction, and the transversal confinement goes along the y_i -direction. The magnetic field is incorporated in Landau gauge

$$\mathbf{A}(x_i, y_i) = (-By_i, 0, 0). \quad (2.19)$$

The solution for the transversal mode n_i in lead i is given analytically by [98]

$$\chi_{i,n_i,k}(y_i) = \frac{\exp\left(-\frac{(y_i-y_c)^2}{2l^2}\right)}{\sqrt{2^n n_i!} \sqrt{\pi} l} H_{n_i}\left(\frac{y_i-y_c}{l}\right), \quad (2.20)$$

where H_{n_i} are the Hermite Polynomials. We further define

$$l = \sqrt{\frac{\hbar}{m^* \Omega}} \quad \text{and} \quad y_c = \frac{\hbar \omega_c k}{m^* \Omega^2}, \quad (2.21)$$

where ω is the frequency of the harmonic confinement, $\omega_c = eB/m^*$ denotes the cyclotron frequency and $\Omega = \sqrt{\omega^2 + \omega_c^2}$. According to eq. (2.4), the lead eigenstates read

$$\psi_{i,n,\pm} = \sqrt{\frac{m^* \Omega^2}{\hbar^2 k \omega^2}} e^{\pm i k x_i} \chi_{i,n,k}(y_i). \quad (2.22)$$

The total energy of the lead eigenstates

$$E = \hbar \Omega \left(n + \frac{1}{2}\right) + \frac{\hbar^2 k^2 \omega^2}{2 m^* \Omega^2} \equiv E_n + E_{\text{kin}} \quad (2.23)$$

splits into the transversal energy required to populate a transversal mode of the harmonic confinement and into longitudinal kinetic energy. The transversal shape of the wave packet is fixed, but there is freedom in the choice of the longitudinal component. Since the transversal lead modes depend on the longitudinal momentum, it is convenient to express the longitudinal part in the momentum representation $\phi(k)$. The sender and receiver wave-packets are then expressed by

$$\phi_{i,n_i}^{\text{send/rec}}(x_i, y_i) = \frac{1}{\sqrt{2\pi}} \int_0^\infty dk \phi(k) \chi_{i,n_i,k}(y_i) e^{\pm i k x_i}. \quad (2.24)$$

The integration goes only over positive values of k which ensure purely outgoing (incoming) sender (receiver) wave-packets, depending on the sign in the exponential function of the integrand. The spectral weights $\mu_{i,n_i}^{\text{send/rec}}(E)$ are evaluated according to eq. (2.18) and read

$$\mu_{i,n_i}^{\text{send/rec}}(E) = \left(\frac{m^* \Omega^2}{2 \hbar^2 \omega^2 (E - E_{n_i})} \right)^{\frac{1}{4}} \phi(k_E), \quad (2.25)$$

Here, E_{n_i} is the transversal energy for populating the transversal mode n_i and

$$k_E = \frac{\Omega}{\omega} \sqrt{\frac{2 m^* (E - E_{n_i})}{\hbar^2}} \quad (2.26)$$

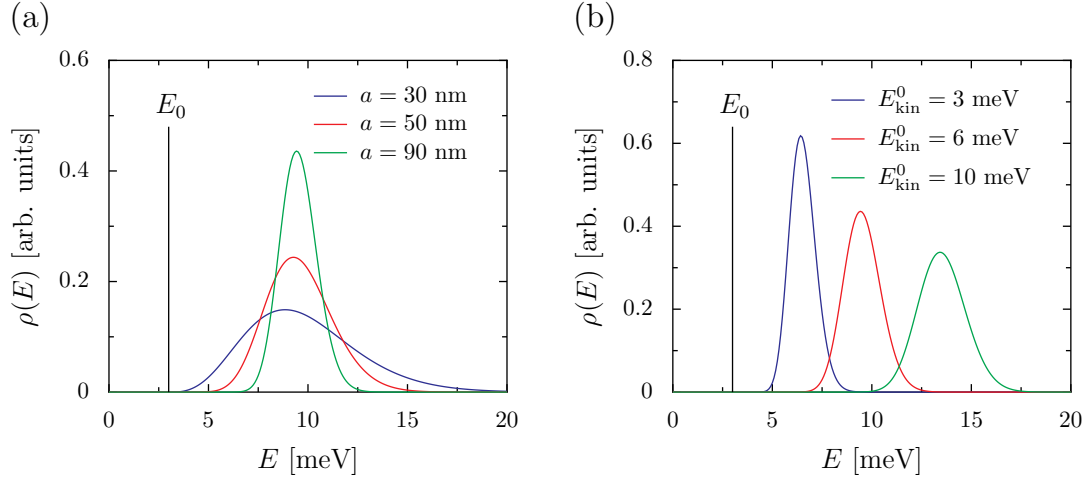


Figure 2.3: Energy density $\rho(E)$, eq. (2.27) for kicked Gaussian wave-packets at $B = 0$. The transversal harmonic confinement is set to $\hbar\omega = 6$ meV. Since the shape of the energy distribution does not depend on the transversal mode, the results shown are evaluated for the transversal ground state with transversal energy $E_0 = 3$ meV. The energy density $\rho_n(E)$ for transversal mode n is obtained by a constant energy shift $\rho_n(E) = \rho(E - n\hbar\omega)$. (a) evaluates the energy density $\rho(E)$ for the different Gaussian width a . The initial kick is set to $\hbar^2 k_0^2 / 2m^* = 3$ meV, (b) depicts $\rho(E)$ for the different initial kinetic energies $E_{\text{kin}}^0 = \hbar^2 k_0^2 / 2m^*$. The Gaussian width is set to $a = 90$ nm.

corresponds to the longitudinal momentum carrying the kinetic energy $E_{\text{kin}} = E - E_{n_i}$. The energy density of the wave packet, that is the probability of populating the scattering eigenstate $\psi_{i,n}^\pm(E)$, is given by

$$\rho(E) = |\mu_{i,n_i}^{\text{send/rec}}|^2. \quad (2.27)$$

Thus, $\rho(E)$ is related to the momentum distribution of the wave packets.

In the following, we choose Gaussian wave-packets

$$\phi(k) = \sqrt{\frac{a}{\sqrt{\pi}}} \exp\left(-\frac{a^2(k - k_0)^2}{2} - ikx_0\right), \quad (2.28)$$

which minimize the momentum-position uncertainty relation. The wave packet is kicked with initial momentum k_0 and centered around x_0 . Although Gaussian wave-packets are extended to the whole position domain, most parts are centered with a Gaussian width a around x_0 . Hence, we choose the center x_0 of the wave packet, such that the parts extended into the scattering region can be neglected.

The same argument holds for the momentum representation. If the initial kick k_0 is large enough, Gaussian wave-packets represent, in good approximation, purely outgoing ($k_0 > 0$) respectively purely incoming ($k_0 < 0$) wave packets, as required.

We adjust the energy representation with a suitable choice of the wave-packet parameters. For Gaussian wave-packets, there are two free parameters, the Gaussian width a and the initial momentum k_0 . The more localized the wave packet is in position space, the more extended it becomes in the momentum representation and also in the energy domain. Localized wave packets with Gaussian width $a = 30$ nm cover an energy range between 4 meV and 18 meV, as depicted in Fig. 2.3(a). The energy distribution with initial momentum $\hbar^2 k_0^2 / 2m^* = 3$ meV is shown for the first transversal mode for a harmonic transversal confinement with $\hbar\omega = 6$ meV. The initial kick k_0 adjusts the position of the peak in the energy density along the energy axis, as is shown in Fig. 2.3(b). Fig. 2.3(b) depicts the energy distribution for Gaussian wave packets with Gaussian width $a = 90$ nm for different initial kinetic energies $E_{\text{kin}}^0 = \hbar^2 k_0^2 / 2m^*$. The kinetic energy E_{kin}^0 sets the position of the maximum of the energy distribution. In conclusion, by adjusting the parameter of the wave packets, we are able to cover any energy range which is relevant for the transport regime under consideration.

2.3.3 Thermal wave packet representation of electron transport

In the following, we introduce the concepts of thermal wave packets [216]. Thermal wave packets are designed in such a way that their energy representation corresponds to the transport window around the Fermi energy of the 2DEG. For simplicity, we consider a two-terminal device. A sketch is given in Fig. (2.4). We further restrict our discussion to a single open transversal mode χ_n . The generalization of the subsequent ideas to multi-terminal devices and inter-mode scattering does not involve any new ideas.

Within the limit of small bias voltages the current in lead 2 reduces to

$$I_2 = \frac{e^2}{h} V_{\text{bias}} \int_{-\infty}^{\infty} dE \left. \frac{-\partial f_{\text{T}}(E)}{\partial E} \right|_{E=E_F} T_{21}(E) \quad (2.29)$$

where $f_{\text{T}}(E)$ is the Fermi function at temperature T and $T_{12} = |t_{2n,1n}(E)|^2$ is the transmission probability of scattering from lead 1 to lead 2. According to eq. (2.15), the transmission amplitude $t_{2n,1n}(E)$ is given by the Fourier transform of the cross correlation function between suitable sender and receiver wave-packets. In addition the correction factor $\mu^{\text{send/rec}}$ appears, which is related to the longitudinal momentum distribution of the used wave packets, see eq. (2.25). The idea is to adjust the wave packets in such a way that the thermal averaging

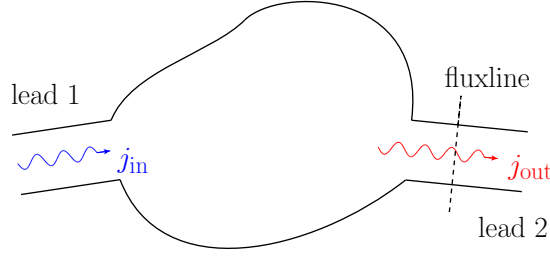


Figure 2.4: Sketch of a two-terminal device where the transmission probability T_{21} from lead 1 and 2 is described in terms of incoming (j_{in}) and outgoing (j_{out}) flux, eq. (2.30). The incoming flux j_{in} is determined by the flux of the sender wave-packet within asymptotic lead 1, while the outgoing flux j_{out} is detected during the scattering process by the fluxline in lead 2.

$-\partial f_{\text{T}}(E)/\partial E$ is already embedded in the spectral components $\mu^{\text{send/rec}}$ of the wave packets. The current flow is then given by the wave packet propagation without further correction, and the sender wave-packet is interpreted as thermal electron moving through the device. This picture is further emphasized if we express the transmission probability

$$T_{21}(E) = \frac{j_{\text{out}}(E)}{j_{\text{in}}(E)} \quad (2.30)$$

in terms of incoming flux j_{in} in lead 1 and outgoing flux j_{out} in lead 2. In the following lines of argument, we put forward explicit expressions for j_{out} and j_{in} . Both incoming and outgoing fluxes are detected in the asymptotic leads. The electron flux in lead i goes along the longitudinal direction x_i and is given for electronic state ψ by

$$j_i = \frac{\hbar}{m} \text{Im}(\psi^* \frac{\partial}{\partial x_i} \psi). \quad (2.31)$$

In section 2.2, we set the history of the scattering process in relation to the scattering eigenstates $\psi_{i,n}^+(E)$ defined in eq. (2.6). Scattering eigenstate $\psi_{1,n}^+(E)$ is associated to the lead eigenstate $\psi_{1,n,+}(E)$, eq. (2.4). Hence, $\psi_{1,n}^+(E)$ initially populates transversal mode n in lead 1 and corresponds to a plane wave that impinges on the scattering region with flux

$$j_{\text{in}}(y_1, E) = \frac{\Omega^2}{\omega^2} \frac{1}{\hbar} \chi_{1,n}(y_1)^* \chi_{1,n}(y_1). \quad (2.32)$$

The total incoming flux in lead 1 is obtained by integrating $j_{\text{in}}(y_1, E)$ along the

transversal direction y_1

$$j_{\text{in}}(E) = \frac{\Omega^2}{\omega^2} \frac{1}{2\pi\hbar}, \quad (2.33)$$

where we used the normalization condition $\langle \chi_{1,n} | \chi_{1,n} \rangle = 1/2\pi$. In order to detect the total outgoing flux, we place a fluxline across lead 2 at position x_0 . The fluxline is indicated by the dashed line in Fig. (2.4). The total outgoing flux is then obtained by integrating the flux along the fluxline

$$j_{\text{out}}(x_0, E) = \int dy_2 j(x_0, y_2, E), \quad (2.34)$$

with

$$j(x, y, E) = \frac{\hbar}{m^*} \text{Im}(\psi_{1,n}^+(x, y, E)^* \frac{\partial}{\partial x} \psi_{1,n}^+(x, y, E)). \quad (2.35)$$

In analogy to the cross-correlation approach introduced in section 2.2, we construct an incoming sender wave packet $\phi_{1,n}^{\text{send}}$, which populates the transversal mode n in lead 1. According to eq. (2.11), this wave packet is composed of scattering eigenstates $\psi_{1,n}^+(E)$. During the time evolution of the sender wave-packet we detect the flux crossing the fluxline. By using the spectral composition of the sender wave-packet eq. (2.11), the definition of j_{out} , eq. (2.34) and eq. (2.30) we obtain

$$j_{\text{out}}^{\text{send}}(x_0, E) = 2\pi\hbar \frac{\Omega^2}{\omega^2} |\mu_{1,n}^{\text{send}}(E)|^2 T_{21}(E) \quad (2.36)$$

which relates the flux through the fluxline $j_{\text{out}}^{\text{send}}(x_0, E)$ to the transmission probability $T_{21}(E)$. By engineering a thermal wave packet whose energy representation fits the thermal distribution

$$|\mu_{1,n}^{\text{send}}(E)|^2 = |\mu_{\text{th}}(E)|^2 = \frac{1}{2\pi\hbar} \frac{\omega^2}{\Omega^2} \left. \frac{-\partial f_T(E)}{\partial E} \right|_{E=E_F}, \quad (2.37)$$

the measured current in the device is associated with the detected flux along the fluxline in lead 2 by

$$I_2 = \frac{e^2}{h} V_{\text{bias}} \int_{-\infty}^{\infty} dE j_{\text{out}}^{\text{send}}(x_0, E). \quad (2.38)$$

The time evolution of the sender wave-packet is then interpreted as a thermal electron moving through the device.

According to eq. (2.25), the spectral components of the wave packets are related to the longitudinal momentum distribution. By inverting eq. (2.25)

$$|\phi_{\text{th}}(k)|^2 = \frac{\hbar^2 |k| \omega^2}{m^* \Omega^2} \rho_{\text{th}}\left(E_n + \frac{\hbar^2 k^2 \omega^2}{2m^* \Omega^2}\right), \quad (2.39)$$

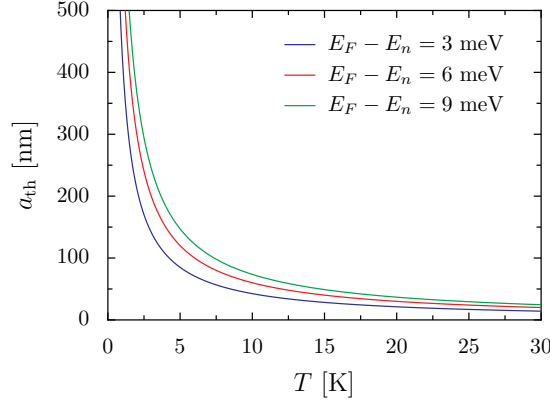


Figure 2.5: The thermal width a_{th} is shown as a function of temperature for different energy difference between the Fermi energy E_F and the transversal energy E_n . We describe thermal electrons in an AlGaAs/-GaAs heterostructure with an effective mass $m^* = 0.067m_e$. The magnetic field is set to zero, $B = 0$.

we obtain an expression for the longitudinal momentum representation for thermal wave packets corresponding to the energy distribution $\rho_{\text{th}}(E) = |\mu_{\text{th}}(E)|^2$. The solution of eq. (2.39) is not unique, and can be realized with incoming as well as outgoing wave packets. For an incoming wave packet we find

$$\phi_{\text{th}}(k) = e^{i\theta(k)} \sqrt{\frac{\hbar^2 |k| \omega^2}{m^* \Omega^2} \rho_{\text{th}}(E_n + \frac{\hbar^2 k^2 \omega^2}{2m^* \Omega^2})} \quad \text{with } k \geq 0. \quad (2.40)$$

There is an additional degree of freedom in the choice of the phase $\theta(k)$. Of practical interest is $\theta(k) = kx_0$, which allows us to shift the position of the wave packet by x_0 along the longitudinal direction. We approximate the thermal distribution, defined in eq. (2.37),

$$\rho_{\text{th}}(E) \approx \frac{1}{2\pi\hbar} \frac{\omega^2}{\Omega^2} \frac{1}{4k_B T} \exp\left(-\frac{(E - E_F)^2 \pi}{(4k_B T)^2}\right), \quad (2.41)$$

with a Gaussian shape. This results in a fourth-order Gaussian for the corresponding thermal momentum representation

$$\phi_{\text{th}}(k) = \sqrt{\frac{\hbar |k| \omega^4}{2\pi m^* \Omega^4 4k_B T}} \exp\left[-\frac{(\frac{\hbar^2 k^2 \omega^2}{2m^* \Omega^2} - (E_F - E_n))^2 \pi}{2(4k_B T)^2}\right]. \quad (2.42)$$

In order to estimate the spatial extension of the thermal wave packet, we expand the exponent in second order of k around $k_0 = \Omega \sqrt{2m^*(E_F - E_n)}/\hbar\omega$. This

gives a Gaussian fit of $\phi_{\text{th}}(k)$ with thermal width

$$a_{\text{th}} = \sqrt{\frac{(E_F - E_n) \pi}{2m^*}} \frac{\hbar \omega}{2k_B T \Omega}. \quad (2.43)$$

Fig. 2.5 shows a_{th} for different longitudinal energies, which are in AlGaAs/GaAs-based semiconductor devices typically of the order of few meV. The plots are evaluated for an effective mass $m^* = 0.067m_e$, where m_e stands for the electron mass. The thermal width a_{th} increases with increasing longitudinal kinetic energy $E_{\text{kin}} = E_F - E_n$. For low temperatures, the transport window, opened by $\frac{-\partial f_T(E)}{\partial E}$, narrows and the thermal wave packets become localized in momentum space. The Heisenberg position-momentum uncertainty principle then leads to spatially extended thermal wave packets and the thermal width a_{th} , which scales with $1/T$, rises to 500 nm for $T = 1.5$ K. Since we have to ensure that the thermal sender wave-packet is initially located in the asymptotic lead, the propagation routine requires long leads and hence demands numerically large grid sizes. This causes numerical limitations for thermal wave packets at very low temperatures. But for a wide range of experimentally relevant temperatures $T \gtrsim 2.5$ K, the thermal width is below 300 nm and remains numerically treatable.

2.4 Numerical propagation Schemes

2.4.1 Introduction

The generic steps of the wave-packet approach are comprised of the time evolution of a suitable chosen sender wave-packet and the evaluation of the cross-correlation function, defined as the overlap between the propagated sender wave-packet and the receiver states. Finally, the cross-correlation function is transformed to the energy domain. According to section 2.2 eq. (2.15), the scattering matrix elements are then obtained after applying correction terms, taking into account the specific shape of the used wave packets.

In section 2.4.2, we introduce schemes to solve the time-dependent Schrödinger equation. For our numerical algorithm, we use the split-operator method [211, 212], which has recently been successfully implemented using the new technology of graphics processing unit (GPU) computation[224]. In Ref [224], the authors report a 40-fold (single precision) speed-up of their NVIDIA GeForce GTX 480 GPU implementation, compared to an Intel i7 CPU version. In section 2.4.3, we set up an efficient numerical scheme for the wave-packet approach introduced in section 2.2 which we implemented on a NVIDIA GPU hardware platform. Besides the propagation of the sender wave-packet, the main numerical effort lies in the computation of cross-correlation functions. This effectively corresponds to the computation of inner products. This is a bandwidth limited problem and

therefore, our main focus is on developing efficient memory strategies using coalesced memory access and shared memory. GPU computation requires some elaborate techniques to squeeze out the best performance that is provided by the computational capabilities of the GPU hardware. An important lesson learned is that developing an efficient GPU algorithm requires more than just transferring an existing CPU code to the GPU hardware, as we demonstrate in this section. We close this section with a performance analysis of the implemented GPU algorithm. We gain a 35-fold speed-up within double precision compared to a single core CPU implementation. Our GPU implementation is based on CUDA, a programming language for GPU-computing delivered by NVIDIA.

2.4.2 Split-operator method

The key ingredient of time-dependent approaches is the propagation of wave packets, and we need to solve the time-dependent Schrödinger equation

$$i\hbar \frac{d}{dt} \psi(t) = \mathcal{H} \psi(t). \quad (2.44)$$

The formal solution for initial state $\psi(t_0)$ in terms of the time-evolution operator is given by

$$\psi(t) = U(t, t_0) \psi(t_0) = e^{-i\mathcal{H}(t-t_0)/\hbar} \psi(t_0), \quad (2.45)$$

where we assume a time-independent Hamiltonian. We divide the complete propagation into N small time steps $\Delta t = (t - t_0)/N$

$$\psi(t_0 + N\Delta t) = (e^{-i\mathcal{H}\Delta t/\hbar})^N \psi(t_0). \quad (2.46)$$

The simplest possible propagation scheme relies on a Taylor expansion of the exponential function up to the first order in the Hamiltonian \mathcal{H}

$$e^{-i\mathcal{H}\Delta t/\hbar} \approx 1 - i\mathcal{H}\Delta t/\hbar \quad (2.47)$$

resulting in the Euler method

$$\psi(t + \Delta t) = \psi(t) - \frac{i}{\hbar} \Delta t \mathcal{H} \psi(t). \quad (2.48)$$

The Euler method is of first order, that is the global error scales with $\mathcal{O}(\Delta t)$. Thus, the Euler method exhibits slow convergence and requires small time steps to ensure accurate results. To overcome this limitation we use the split-operator method [211, 212]. The total Hamiltonian $\mathcal{H} = \mathcal{T} + \mathcal{V}$ is divided into the kinetic energy and the scattering potential. Using the Baker-Campbell-Hausdorff formula, we split the time-evolution operator into

$$e^{-i(\mathcal{V}/2 + \mathcal{T} + \mathcal{V}/2)\Delta t/\hbar} = e^{-i\Delta t \mathcal{V}/2\hbar} e^{-i\Delta t \mathcal{T}/\hbar} e^{-i\Delta t \mathcal{V}/2\hbar} e^{\mathcal{O}(\Delta t^3)}. \quad (2.49)$$

Due to the symmetrized application of the potential energy, terms of the order of $e^{\mathcal{O}(\Delta t^2)}$ do not contribute, resulting in higher accuracy $e^{\mathcal{O}(\Delta t^3)}$. The explicit application of the kinetic and potential energy depends on the choice of the basis set in which the quantum state is represented. In position space, the application of the potential energy is just a multiplication, whereas the kinetic energy is more demanding and involves second-order derivatives with respect to the spatial coordinates. For the evaluation of the kinetic energy, the momentum representation is more convenient. The kinetic energy part then also reduces to multiplications. The idea is to transform the wave packet back and forth between position and momentum space, which is numerically efficiently done by the Fast Fourier Transform (FFT).

In the following, we restrict our studies to a two-dimensional system with an additional homogeneous magnetic field perpendicular to the plane of the potential landscape. The magnetic field is included by minimal coupling. The Hamiltonian now gets a more complex structure and in particular, the momentum and position coordinates get coupled. In symmetric gauge $\mathbf{A}(x, y) = (-B/2y, B/2x, 0)$ we obtain

$$\mathcal{H} = \mathcal{T}_{p_x, y} + \mathcal{T}_{p_y, x} + \frac{1}{2}\omega_L^2(x^2 + y^2) + V(x, y), \quad (2.50)$$

where we follow Kramer *et al.* [112] and divide the kinetic energy into

$$\mathcal{T}_{p_x, y} = \frac{p_x^2}{2m^*} - \omega_L p_x y \quad \text{and} \quad \mathcal{T}_{p_y, x} = \frac{p_y^2}{2m^*} + \omega_L p_y x \quad (2.51)$$

with $\omega_L = eB/2m$. The last two terms of eq. (2.50) are incorporated in the effective potential

$$V_{\text{eff}}(x, y) = \frac{1}{2}\omega_L^2(x^2 + y^2) + V(x, y). \quad (2.52)$$

Since both operators, p_x and y , commute $[p_x, y] = 0$, we can go to a mixed representation in which the momentum representation is used for the extension of the wave packet in x -direction, whereas we remain in position space for the y -coordinate. Although position and momentum operators couple to each other, the application of $\mathcal{T}_{p_x, y}$ still simplifies to a multiplication for the mixed representation. The same arguments hold for the application of $\mathcal{T}_{p_y, x}$. The only difference is that now the y -direction is transformed to momentum space and the x -direction is expressed in position space. The split-operator scheme to advance the wave packet one time step Δt is then given by

$$\psi(t + \Delta t) = e^{-\frac{i\Delta t}{2\hbar}V_{\text{eff}}} \mathcal{F}_x^{-1} e^{-\frac{i\Delta t}{2\hbar}\mathcal{T}_{p_x, y}} \mathcal{F}_x \mathcal{F}_y^{-1} e^{-\frac{i\Delta t}{\hbar}\mathcal{T}_{p_y, x}} \mathcal{F}_y \mathcal{F}_x^{-1} e^{-\frac{i\Delta t}{2\hbar}\mathcal{T}_{p_x, y}} \mathcal{F}_x e^{-\frac{i\Delta t}{2\hbar}V_{\text{eff}}} \psi(t). \quad (2.53)$$

Compared to the propagation scheme stated by Kramer *et al.* in Ref. [112], we achieve higher accuracy by symmetrizing the kinetic energy part with respect

to x - and y -direction. Equation (2.53) is the central result of this section and corresponds to the propagation method implemented in our numerical algorithm. The Fourier transform from position to momentum space is defined as

$$\mathcal{F}_x = \frac{1}{\sqrt{2\pi\hbar}} \int dx e^{-ip_x x}, \quad \mathcal{F}_y = \frac{1}{\sqrt{2\pi\hbar}} \int dy e^{-ip_y y} \quad (2.54)$$

The inverse transformation from momentum to position space is given by

$$\mathcal{F}_x^{-1} = \frac{1}{\sqrt{2\pi\hbar}} \int dp_x e^{ip_x x}, \quad \mathcal{F}_y^{-1} = \frac{1}{\sqrt{2\pi\hbar}} \int dp_y e^{ip_y y}. \quad (2.55)$$

In order to simulate open boundary conditions which ensure purely outgoing wave packets in the semi-infinite leads, we introduce a complex absorbing potential (CAP) [225, 226, 227]. The CAP has to be properly chosen to minimize reflections at the absorbing potential. Moreover, the CAP has to be localized along the edges of the simulated device such that the relevant region of the scattering potential is not affected by the absorber. We use the following CAP, which has proven to be a suitable choice [112]

$$V_{\text{abs}}(x, y) = iV_0 \left(\cosh^{-2} \left(\frac{(x - x_{\text{edge}})^2}{d^2} \right) + \cosh^{-2} \left(\frac{(y - y_{\text{edge}})^2}{d^2} \right) \right). \quad (2.56)$$

V_0 sets the strength of the absorber and d the spatial extension. Typical values used for applications in mesoscopic transport are $V_0 = 50$ meV and $d = 50$ nm. Note that the propagation scheme of eq. (2.53) remains unchanged and we incorporate the absorbing potential V_{abs} in the effective potential V_{eff} which then gets complex-valued.

2.4.3 Graphics processing unit (GPU) implementation

The idea of our GPU implementation of the wave-packet approach is to do the initialization of wave packets, the final data manipulation and the data storage on the CPU, whereas the numerically demanding time propagation and computation of cross-correlation functions is done massively parallelized by the GPU. In the following, we introduce an elaborate scheme for evaluating the cross-correlation function eq. (2.16). We distribute the workload into 128 blocks, each containing 64 threads that execute individual tasks in parallel. The reason for our more complicated implementation lies in the GPU architecture that can schedule tasks and hides latencies much more efficiently when the computational work is divided into many small tasks [202]. In our GPU implementation, we launch 8,192 partial summations which are distributed to 448 streaming processors provided by the NVIDIA C2070 graphics board.

Figure 2.6 shows a schematic sketch of the program flow of the implemented algorithm. At first, the relevant region of the simulated device is discretized into

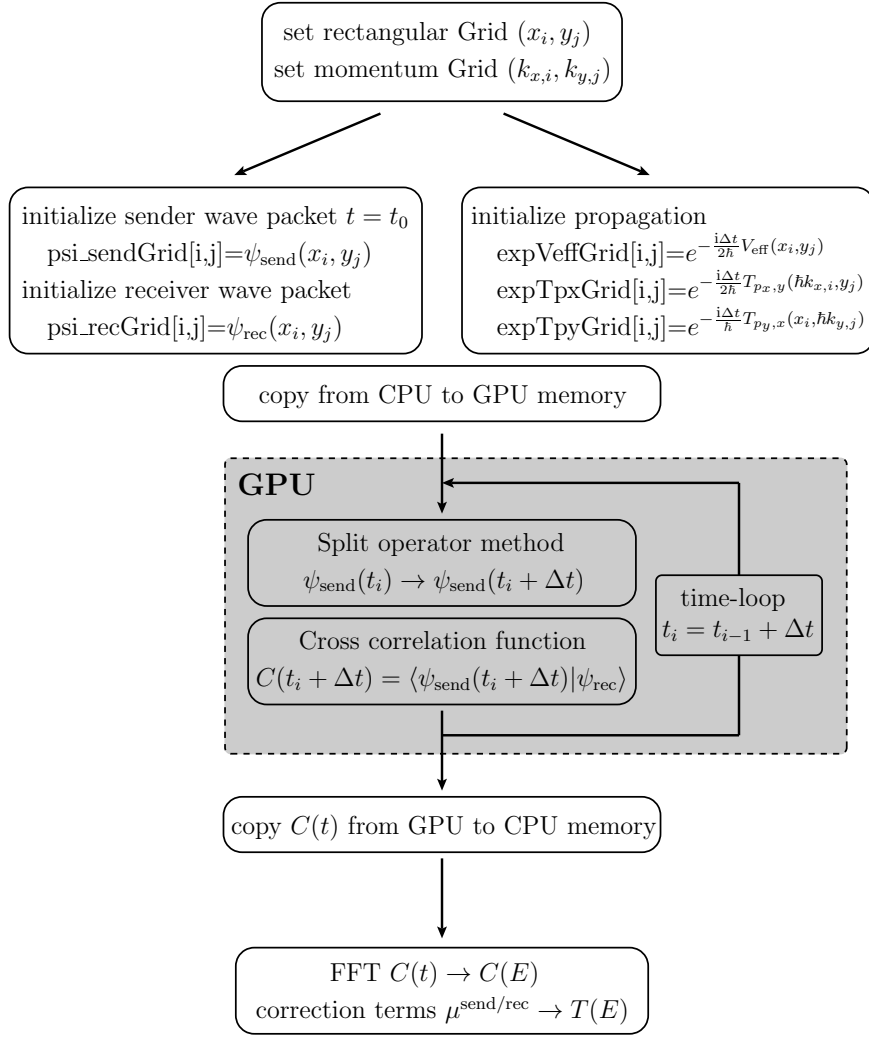


Figure 2.6: Program flow of the GPU implementation of the wave packet approach introduced in section 2.2. Initialization of the potential and the wave packets on a discrete finite grid as well as the final output is done on the CPU. The numerically time-consuming propagation according to the split-operator method eq. (2.53) and the evaluation of the cross-correlation function is implemented on the GPU. Slow communication between CPU and GPU is required only within the initialization procedure and after the end of the propagation loop.

a finite mesh of grid points (x_i, y_j) . Note that a discrete grid in position space implies a discrete grid in momentum space $(k_{x,i}, k_{y,j})$ as well. We denote the number of grid points in x-direction and y-direction by N_x and N_y , respectively.

In order to get the best performance out of the Fast Fourier Transform, N_x and N_y are set to 2^{n_x} and 2^{n_y} . For the discussed applications for transport in mesoscopic devices, spatial extensions are typically in the micrometer scale. Thus, 256 up to 2048 grid points are required for each spatial direction. The required resolution of the grid discretization varies with the device size and the strength of the applied magnetic field. The discretized version of sender and receiver wave-packets can be interpreted as $N_x \times N_y$ matrices $\text{psi_sendGrid}[i, j] = \psi_{\text{send}}(x_i, y_j)$ and $\text{psi_recGrid}[i, j] = \psi_{\text{rec}}(x_i, y_j)$. In the same way, the operator valued exponential functions appearing in eq. (2.53) are replaced by matrices $\text{expVeffGrid}[i, j]$, $\text{expTpxGrid}[i, j]$ and $\text{expTpyGrid}[i, j]$. After initializing the required objects on the CPU, the memory is transferred from CPU to GPU. Memory transfer between host and device is slow, but once the copy is done the time consuming propagation is carried out on the GPU without further communication between GPU and CPU. Only the final results are copied back to CPU and the numerical cost of the memory transactions is insignificant.

To advance the wave packet one time step, we use the split-operator method defined in eq. (2.53) which basically contains two building blocks: (i) the application of exponential functions and (ii) the fast Fourier transform. The application of the exponential functions essentially corresponds to complex-valued element wise matrix multiplication. To perform the FFTs, we use CUFFT provided by NVIDIAs CUDA library [228]. The split-operator method has recently been implemented on GPUs to solve both the time-dependent Schrödinger and the time-dependent Dirac equation [224].

Finally, we have to compute cross-correlation functions between sender and receiver states. This corresponds to performing an inner product between two complex-valued functions defined on a discrete grid. We evaluate the cross-correlation at intermediate propagation times t_i

$$C(t_i) = \left(\sum_{k,l=1}^{N_x, N_y} \text{psi_recGrid}[k, l]^* \text{psi_sendGrid}[k, l] \right) \Delta x \Delta y. \quad (2.57)$$

Note that the $N_x \times N_y$ entries of psi_sendGrid and psi_recGrid are stored in linear address space of global memory. Wave packets are complex-valued, and we emulate complex numbers by double2 variables, which are intrinsic data types provided by CUDA for optimized memory access for objects with two entries. Δx and Δy correspond to the grid discretization. Equation (2.57) demands two memory calls, whereas there are only two floating point operations, one summation and one multiplication. Thus, memory bandwidth limits the performance. An efficient scheme for parallel reduction – parallel execution of large summations – has been developed by Harris (NVIDIA Developer Technology) [229] who introduces schemes to optimize coalesced memory transfer and reduces the number of global memory calls by using shared memory. The idea is to split the

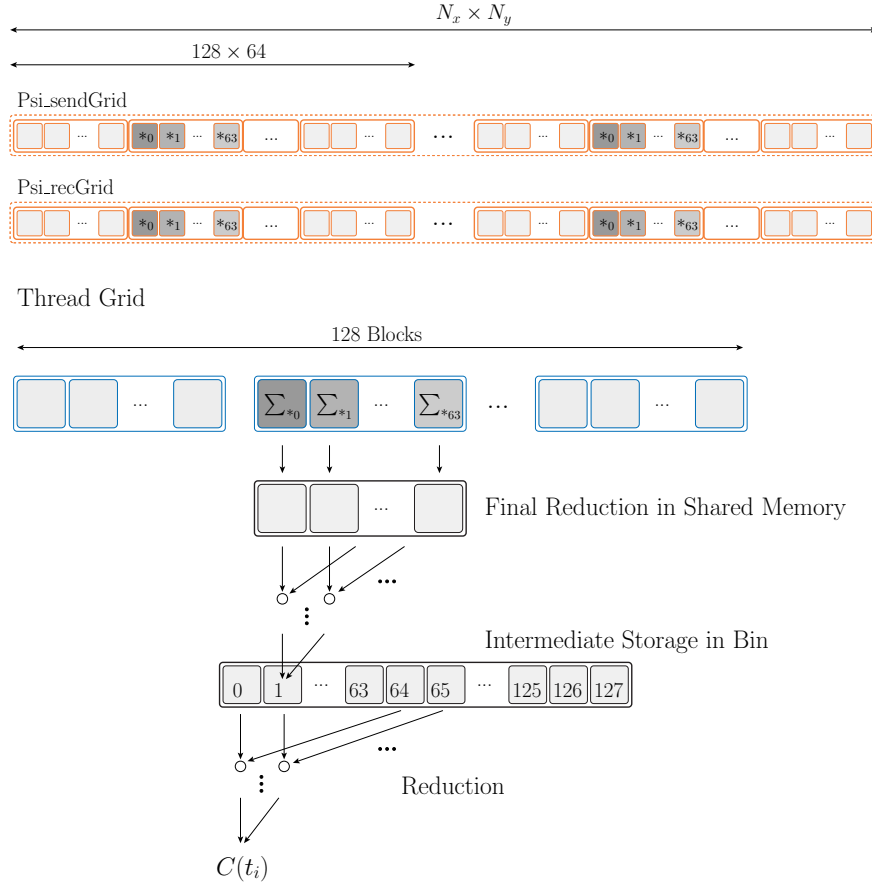


Figure 2.7: Schematic sketch of work distribution and memory layout for parallelized evaluation of cross-correlation function. The $N_x \times N_y$ complex-valued data points of the discretized sender and receiver wave-packets are aligned in linear memory space. The linear memory is divided into consecutive segments of 128×64 data points. The workload is organized in 128 blocks, each containing 64 threads. Each thread evaluates a partial summation. For example the first thread in the second block, labeled thr. 0, multiplies the entries of the sender and receiver for all data points highlighted in dark gray and labeled by $*_0$, and performs the partial summation eq (2.58). Afterwards, we use a final reduction in shared memory [229] and store the results in global memory d_Bin. Finally, summation of the entries in d_Bin gives the result for the cross-correlation function.

complete summation into smaller partial sums that are evaluated in parallel. The final reduction of the individual sums is then done by pair-wise summation. During this final reduction, more and more processors are idle. In the last step

just one processor is actually active. However, for the discussed applications, the relevant grid sizes are large enough such that the advantage of the parallel execution of partial sums is larger than the problem that some processors are idle in the last steps of the summation process.

A schematic sketch of the layout of our implementation to perform cross-correlation functions is given in Fig. 2.7. We organize the workload along a one-dimensional grid containing 128 blocks, where each block is built up of 64 threads. We assign to each thread on partial summation. Thus, in total, we divide the complete summation into $128 \times 64 = 8,192$ smaller sums. The wave packets are discretized according to the position grid, and the $N_x \times N_y$ entries are stored in linear global memory space. We divide this linear address space into segments containing 128×64 data points. In total, we get $N_{\text{seg}} = N_x * N_y / (128 * 64)$ such segments. Each of the 128 blocks of the grid with its 64 threads accesses the memory in packages of 64 data points. The complete grid then calls the entries of a complete 128×64 memory segment where the discretized wave packet is stored. Adding up the partial sums goes sequentially through the linear address space of the wave packets until all N_{seg} memory segments have been serviced. That is, in the end, each thread has completed a partial summation over N_{seg} data points contributing to the cross-correlation function. For example, as illustrated in Fig. 2.7, the first thread of the second block performs the partial summation over all grid points of the wave packets stored in the memory position assigned with '*0'. That is this specific thread evaluates the partial summation

$$\sum_{*0} \text{psi_recGrid}[*0] * \text{psi_sendGrid}[*0]. \quad (2.58)$$

The second thread performs the summation for the memory position *1. The remaining threads proceed in the same way. Since all threads of a block access memory within a consecutive memory section containing 64 data points, this kind of memory access ensures optimal coalesced memory transfer. We store the results of the partial sums obtained by the threads in shared memory. Shared memory is L1 cache and provides fast memory access to all threads within the same block. This yields fast memory access for the final reduction of the partial sums as we show below. Note that we need to wait until all threads have finished their work. That is, after the evaluation of the partial sums, we need to synchronize the threads. The final reduction, that is the summation of the partial results obtained from the 64 threads in the block, will now be done in shared memory. Therefore, the final reduction does not require any time-consuming global memory access. After final reduction, the results of each block are stored in d_Bin. Since threads of different blocks cannot access the same shared memory, d_Bin is defined in global memory. The last step is to perform the sum over all 128 entries stored in d_Bin.

For the applications of the wave-packet approach introduced in section 2.2,

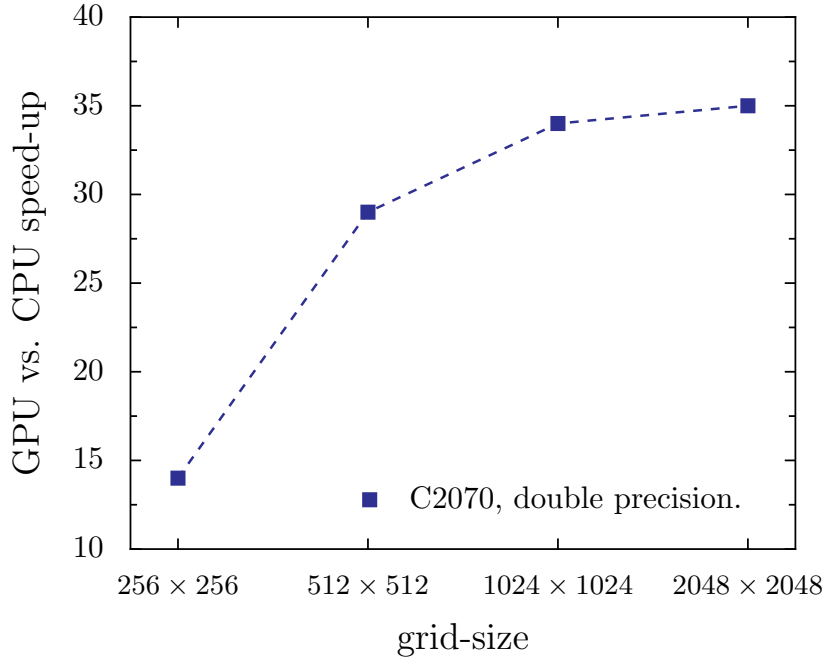


Figure 2.8: Performance analysis of the GPU implementation of the wave-packet approach. The speed-up of the GPU (NVIDIA C2070) implementation when compared to a single core CPU (Intel 2.40 GHz) implementation is shown as a function of the grid size $N_x \times N_y$. The calculations are done in double precision, and comprise the wave-packet propagation of the sender wave-packet, as well as the evaluation of the cross-correlation function for 12 receiver states. This is the typical number of required cross-correlation functions for four-terminal measurements with 3 open transversal modes. Typical propagation times for the wave-packet approach requires that 60 000 time steps need to be propagated. For a grid size of 1024×1024 , the GPU calculation takes 15 minutes, while the same calculation takes 8 hours on the single core CPU.

there is not only a single receiver wave-packet but there are typically 12 to 40 receiver states, depending on the number of terminals and open transversal modes. The evaluation of multiple correlation functions, corresponding to different receiver wave-packets, can be also done in parallel on the GPU. In our numerical implementation, we enlarge the grid of thread blocks by a further dimension, labeling the corresponding receiver wave-packets. Otherwise, for each receive we proceed along the presented steps above.

In Fig. 2.8 we depict the achieved speed-up when compared to a single core

CPU (Intel 2.40 GHz) implementation as a function of the grid size. The calculations are done in double precision on a NVIDIA C2070 graphics board. Due to the concept of latency hiding, the GPU algorithm requires some numerical workload to reveal its best performance. Thus, the larger the grid size becomes, the higher is the obtained speed-up compared to the CPU implementation. In contrast to our GPU-HEOM algorithm, which we establish in Part I of this thesis, the wave-packet approach is bandwidth limited and our algorithm does not fully reveal the computational capability provided by the 448 streaming processors of the NVIDIA C2070 graphics board. Nevertheless, using the GPU algorithm for the wave-packet approach, we obtain a 30- to 35-fold reduction in computation time, simply by using the new hardware technology provided by GPUs. For the transport problems in semiconductor nanostructures discussed in Chapter 3, the typical grid sizes are between 512×512 and 1024×1024 grid points. Typical computation times for the wave-packet approach are reduced from 8 hours to 15 minutes (propagation over 60 000 time steps, grid size 1024×1024).

2.5 Conclusion

In this section, we introduced a time-dependent approach to transport in mesoscopic physics. The idea of the introduced method is to compute the energy-dependent transmission amplitudes t_{in_i,jn_j} based on a wave-packet propagation. The transfer characteristics of ballistic electron transfer in mesoscopic systems fabricated in semi-conductor heterostructures is then obtained by the Landauer-Büttiker approach. This approach relates the transmission amplitudes to currents and voltages.

Compared to the recursive Green's function approach, one of the standard approaches in mesoscopic transport [107, 98], our wave-packet approach is advantageous in several aspects. Firstly, the time evolution of a wave packet gives a physical intuitive picture of scattering mechanisms involved in the ballistic transport through the device. As we show in section 2.3, under certain conditions, wave-packet propagation is associated with the motion of thermal electrons. In this regime, the time evolution of the wave packets acquires a physical meaning. Secondly, the wave packet holds the information of a whole set of scattering eigenstates for a large range of energies. For mesoscopic systems in AlGaAs/GaAs heterostructures, a single wave packet run yields the transmission amplitudes for energy ranges that are typically extended over 5 meV to 15 meV. This is of particular interest when the experimental setup scans the transport characteristic of a wide range of Fermi energies. And thirdly, the time-dependent approach is well suited for the new GPU hardware technology which is still gaining in computational power. Within our GPU implementation of the wave packet approach which we establish in section 2.4, we obtain an up to 35-fold reduction in

computation time when compared to the CPU version. Our efficient wave-packet approach allows us to perform simulations for large devices sizes. For example in Chapter 3, we simulate large four-terminal quantum waveguide rings that require typical grid extensions of $3\mu\text{m}\times 2\mu\text{m}$.

3 Four-terminal waveguide Aharonov-Bohm interferometer

3.1 Introduction

One of the most fundamental interference effects in quantum mechanics is given by the Aharonov-Bohm (AB) effect [121]. The AB effect is a quantum mechanical phenomenon and does not have a corresponding counterpart in classical physics. In their original work, Aharonov and Bohm propose a double-slit experiment where the two incident electron beams enclose a magnetic flux. The magnetic field is confined to a region that cannot be approached by the electron beam. Even though the magnetic field does not reach the trajectories, the detected amplitude of the two interfering beams shows an oscillatory interference pattern that depends on the enclosed magnetic flux Φ .

The focus of this chapter is to apply the AB effect to control observables like currents and voltages by small variations in the magnetic flux. Early experiments by Ford *et al.* [103] pioneered the usage of the AB interference fringes for electronic devices. Possible applications could include fast switches with low energy consumption [103]. Recently, AB rings have also been used as measurement devices for detecting the transmission phase of embedded nanostructures like quantum dots [126, 127, 230]. In this applications the external homogeneous magnetic field is extended over the complete device. This is different compared to the original setup of the AB effect [121] in which the magnetic field B is localized to a region which is not approached by the electron beams. A sketch of the setup is given in Fig. 3.1. The different path lengths s_1 and s_2 allow one to vary the phase of the AB oscillations continuously by adjusting the Fermi wave vector k_F of the incident electrons

$$|\psi_1 + \psi_2|^2 \sim \cos\left(2\pi\frac{\Phi}{\Phi_0} + k_F(s_1 - s_2)\right), \quad \text{with} \quad E_F = \hbar^2 k_F^2 / 2m. \quad (3.1)$$

Φ denotes the magnetic flux and $\Phi_0 = h/e$ stands for the magnetic flux quantum. In quantum rings fabricated in semiconductor heterostructures [103, 122, 123, 124, 134, 142, 135], the Fermi wave vector k_F is controlled via gate voltages

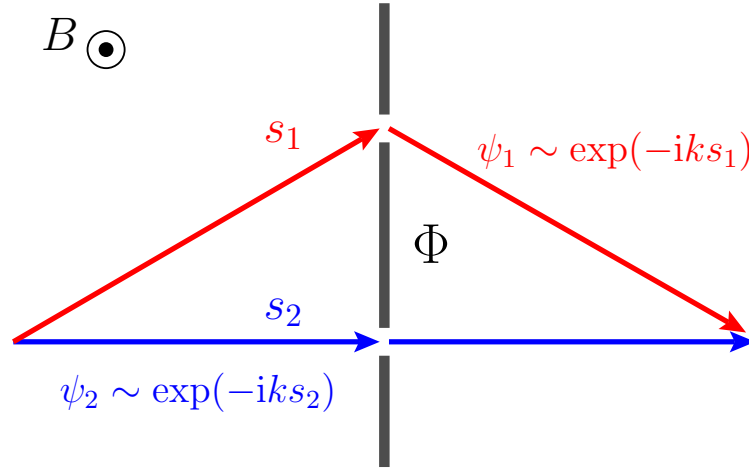


Figure 3.1: Sketch of the double-slit Aharonov-Bohm setup. Two electron beams with different path length s_1 and s_2 enclose a magnetic flux Φ . The homogeneous magnetic field B is perpendicular to the plane of the electron beams. Opposed to the original setup of Aharonov and Bohm [121], we assume that the magnetic field is extended over the complete device. The two-path interference results in an oscillatory interference pattern whose frequency depends on the enclosed magnetic flux Φ .

that adjust the Fermi energy E_F within the 2DEG. In real devices, the picture is not as simple as drawn in eq. (3.1), as we investigate in detail in this chapter. For example, in fabricated ring structures, electrons travel around the ring several times. This yields higher frequencies in the AB oscillations [124, 231]. Furthermore, time-reversal symmetry imprints symmetry relations into the transmission probability $T_{12}(\Phi) = T_{21}(-\Phi)$ [232]. Therefore, in two-terminal measurement setups like the one sketched in Fig. 3.1, the phase of the AB oscillations is locked to 0 or π [122, 123, 124], and the expected linear phase drift with the Fermi wave vector k_F is not observed. In order to break the phase rigidity, experimental setups attach additional leads to perform multi-terminal measurements [103, 134, 142, 135].

Four-terminal measurements only show a continuous phase drift with Fermi wave vector k_F for a specific arrangement of the current and voltage probes [134, 142, 135]. The Fermi energy E_F and, hence, the Fermi wave vector k_F are adjusted by an external gate voltage. At certain gate voltages, the continuous phase drift is interrupted by abrupt phase jumps of π . Such phase jumps are a source of noise in the application of AB interferometers as transmission-phase detectors or low power consuming switching devices. Thus, understanding the

microscopic origin of the phase jumps is crucial and may guide an improved device design. In this chapter, we show that higher frequencies in the AB oscillations and abrupt phase jumps by sweeping through the Fermi energy E_F are intrinsic properties determined by the device geometry. Multiple Fabry-Perot like interference in the arms of the ring changes the scattering behavior on a fast energy scale of the Fermi energy E_F . Commonly, one-dimensional (1d) models are used to describe transport through multi-terminal ring structures [136, 137, 138, 139, 140]. However, 1d-models can only phenomenologically include the scattering properties at the cross-junctions connecting the arms of the rings to the leads. The injection of electrons from the leads to the ring is modeled by energy-independent transmission amplitudes. This phenomenological description does not resolve the back-coupling between resonances in the arms (due to multiple reflections at the junction) and the transmission properties of the cross-junctions. Indeed, it turns out that exactly this back-coupling of resonant scattering in the arms of the ring and the character of the transmission at the cross junctions, is responsible for the characteristics of the detected signal in four-terminal quantum waveguide AB interferometers. This also explains the rich features in the AB interference pattern, as we point out in section 3.2.

The experiments fabricate the ring structures in a 2d potential landscape within the 2DEG of the AlGaAs/GaAs heterostructure [103, 126, 127, 230, 122, 123, 124, 134, 142, 135]. We use the time-dependent approach introduced in chapter 2. With our time-dependent approach, we are able to go beyond 1d-models and to compute the energy-dependent transmission amplitudes for the 2d-device setup. Furthermore the experimental scan over the Fermi energy E_F is done by a single wave-packet run. In combination with our high-performance GPU implementation developed in chapter 2, the time-dependent approach is numerically very efficient. Thus, our algorithm is well suited to simulate the large experimental ring-structures that have ring radii ranging from $0.5 - 1 \mu\text{m}$ [126, 127, 134, 142]. Previous calculations for quantum rings based on the recursive Green's function, for example, manage to simulate only very small ring structures with a radius of 54.5 nm [233].

In section 3.2, we simulate transport measurements in a four-terminal AB ring fabricated in a AlGaAs/GaAs heterostructure. We provide a detailed comparison of theoretical outcome and the experimental results. Parts of this section have been published in Kreisbeck *et al.* Ref. [119]. The experiments are done by Buchholz and Fischer *et al.* in Refs. [119, 135]. Finally, in section 3.3, we configure the AB ring as transmission phase detector of a quantum dot embedded in one arm of the ring. The simulations for this configuration are motivated by experiments by Schuster *et al.* Ref. [126] and Avinun-Kalish *et al.* Ref. [127] who demonstrate that such a setup yields information about resonances and the transmission-phase of the embedded quantum dot. We discuss the transmission phase of a harmonic quantum dot in the presence of a magnetic field and il-

illustrate how the Darwin-Fock spectrum [107] emerges within the interference fringes of a four-terminal AB interferometer.

3.2 Continuous phase drift and π phase-jumps in four-terminal rings

Parts of this section have been published in Kreisbeck, Buchholz (experimental part) *et al.* [119].

3.2.1 Introduction

The development of new devices based on the AB effect for applications such as the measurement of the transmission phase of embedded quantum systems, requires clean systems. Therefore in such devices, the mean-free path $\ell_e \sim 8 - 15 \mu\text{m}$ [126, 127, 134, 142] is larger than the size of the device geometry. Four terminal AB-interference experiments use typically waveguide ring-structures with radii of $0.5 - 1 \mu\text{m}$ [126, 127, 134, 142]. This ensures coherent electron transport along the ring and minimizes scattering at impurities and inelastic scattering. Changing the Fermi energy E_F of the electrons in the 2DEG of the device is then expected to yield a continuous phase drift of the AB oscillations eq. (3.1). However, in four-terminal measurements done by Kobayashi *et al.* [134], the AB interference fringes show more complicated features. In particular, phase jumps of π interrupt the continuous phase drift. The detected behavior of the AB oscillations is universal and present in various measurements in four-terminal quantum rings [135, 119, 103, 134].

In this section, we perform realistic simulations based on the wave-packet approach established in chapter 2. We incorporate the 2d potential landscape as well as details in the measurement setup such as the integrated signal of the lock-in amplifier. We relate the experimentally observed features in the phase behavior of the AB oscillations to non-trivial interference effects at the device geometry. While the specific character of the phase behavior of the AB oscillations depends on the explicit geometry, fundamental features like π phase-jumps are intrinsic universal features of waveguide ring structures.

In section 3.2.2, we introduce the experimental setup discussed in Kreisbeck, Buchholz *et al.* Ref. [119], and summarize the basic findings of the experimental measurements. In particular, we introduce the local and non-local measurement setup commonly used in four-terminal measurements in nanostructure quantum rings [119, 134, 142, 135]. Both setups differ in the arrangement of voltage and current probes. In section 3.2.3, we establish the numerical model for simulating the experimental setup. We use the effective mass approximation and describe

the electron transport in terms of a single particle picture. We compute the transmission amplitudes according to the wave-packet approach of chapter 2. Basic features of the scattering process at the device geometry are already visible in the transmission probabilities $|t_{in_i,jn_j}|^2$. We identify fundamental scattering properties by analyzing snap-shots during the wave packet propagation. In section 3.2.4, we evaluate the experimentally observed current and voltages within the Landauer-Büttiker formalism. We show results for the linear transport regime, within which analytical results for the experimental observables are available [107, 98, 105]. We explain the qualitatively different observations for the local and non-local setup. We relate the appearance of π phase-jumps to the back-action of Fabry-Perot like resonant scattering in the arms of the ring to the scattering properties of the cross-junctions linking the ring to the asymptotic leads. Finally, in section 3.2.5, we refine our numerical simulations, include the lock-in amplifier, and evaluate the currents and voltages within the non-linear regime. The Landauer-Büttiker formalism then leads to a system of non-linear equations which we solve with the Newton-Raphson method. We reproduce the experimental results to a highly detailed level. Thus, we conclude that the detected phase behavior of the AB oscillations as a function of Fermi energy reflects complicated interference effects due to scattering at the device geometry.

3.2.2 Experimental setup

In the following, we discuss the experimental setup of Buchholz *et al.* [142, 135, 119] which provides a better-defined device architecture than the previous experiments by Kobayashi *et al.* in Ref. [134]. The four-terminal ring-structure with a radius of $1\ \mu\text{m}$ is etched into a high mobility sample, based on a AlGaAs/GaAs heterostructure, with free-mean path length $\ell_e = 9.5\ \mu\text{m}$. A scanning electron micrograph of the sample is given in Buchholz *et al.* [142], and a schematic sketch is depicted in Fig. 3.2. The contacts which feed the 2DEG with electrons are placed far from the ring structure so that the electrons are guided by asymptotic leads toward orthogonal cross-junctions which connect the leads to the ring. This provides a well-defined injection of electrons into the ring of the AB interferometer that is not achieved in the experimental setup of Kobayashi *et al.* Ref. [134]. The geometry is designed to give a maximal difference in the path length of the upper arm s_1 and the lower arm s_2 . This breaks the symmetry between the upper and lower arms, facilitating a continuous phase shift in the AB oscillations with Fermi energy E_F , see eq. (3.1). The Fermi energy is controlled by a top-gate electrode. The idea is that the improved setup reduces the abrupt phase jumps in the AB oscillations obtained by Kobayashi *et al.* Ref. [134].

The device is measured in a dilution refrigerator at a base temperature of $T_{\text{base}} < 30\ \text{mK}$. Temperature-dependent AB experiments [135] and thermal noise measurements [234] for a similar setup estimate the electron temperature to

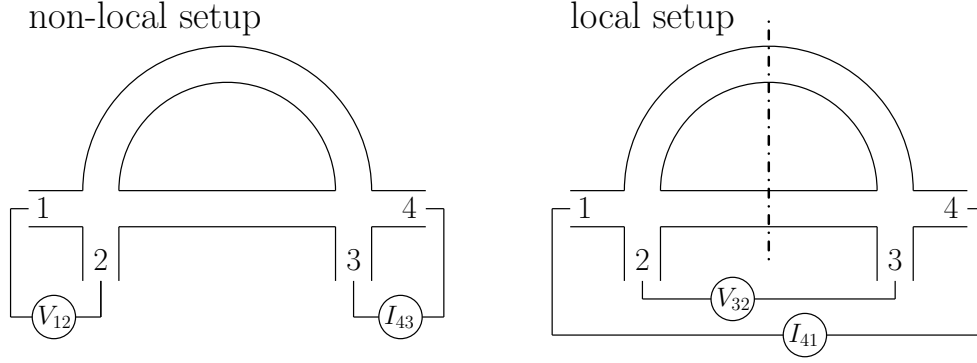


Figure 3.2: Sketch of the experimental four-terminal measurement setup. Depending on the arrangement of voltage and current probes, we distinguish between non-local and local measurement setup. In the non-local setup, current flows between leads 3 and 4 and the voltage drop is detected across leads 2 and 1. In the local setup, current flows between leads 1 and 4, while the voltage is probed across leads 2 and 3. The dash-dotted line shows the axis of symmetry of the local setup. The experimental setup consists of well-defined clean waveguides, and electrons are injected into the ring via orthogonal cross-junctions. A scanning micrograph of the experimental ring structure is given in Buchholz *et al.* Ref. [142, 135].

be 0.1 – 0.2 K. Typically, 3 – 12 transversal modes are populated in the leads [119, 135]. There are two experimental measurement setups, the local and non-local setup. Both setups differ in the arrangement of the voltage and current probes. In the non-local, setup the current I_{43} flows between lead 3 and lead 4, while the voltage drop V_{12} is detected at lead 2 and lead 3. In the non-local setup, the current and voltage probes are spatially separated. We define the non-local resistance

$$R_{43,12} = \frac{V_1 - V_2}{I_{43}} = \frac{V_{12}}{I_{43}}. \quad (3.2)$$

In the local setup current I_{41} is injected at leads 1 and 4, and the voltage drop V_{32} is detected at leads 2 and 3. The local resistance is given by

$$R_{41,32} = \frac{V_3 - V_2}{I_{41}} = \frac{V_{32}}{I_{41}}. \quad (3.3)$$

The experiment is performed by lock-in measurements with an ac current of 12 nA (root mean square (rms)) at 73.3 Hz. The voltage drop is probed by the lock-in amplifier as an integrated (rms) signal

$$V_{kl}^{\text{rms}} = \frac{\omega}{\sqrt{2}\pi} \int_0^{2\pi/\omega} V_{kl}(I_{ij}(t)) \cos \omega t \, dt. \quad (3.4)$$

The detected local and non-local resistance is then given by

$$R_{ij,kl}^{\text{rms}} = V_{kl}^{\text{rms}} / I_{ij}^{\text{rms}}. \quad (3.5)$$

The radius of the fabricated ring is $1 \mu\text{m}$, and the enclosed flux yields a h/e -period of the AB oscillations of $\Delta B = 2.28 \text{ mT}$. In the experiment, the h/e AB oscillations are detected with approximately 10 percent visibility. That is, both local and non-local resistance show an oscillatory component with a small amplitude on top of a larger, non-oscillatory background [142, 135]. Scanning through the Fermi energy of the electrons in the 2DEG is done by sweeping through the top-gate voltage. The experimental results are shown in Kreisbeck, Buchholz *et al.* [119], Fig. 1. In the non-local setup, changing the Fermi energy results in a continuous phase drift of the AB oscillations in the lock-in integrated non-local $R_{43,12}^{\text{rms}}$ resistance. Despite the improved device design, the continuous phase drift is interrupted by abrupt phase jumps of π , and there is no qualitative difference compared to the measurements of Kobayashi *et al.* Ref.[134]. At the Fermi energies where the phase jumps take place, the amplitude of the h/e frequency is suppressed, and the higher frequency $h/2e$ dominates the oscillatory component of $R_{43,12}^{\text{rms}}$. In the local setup, the local resistance $R_{41,32}^{\text{rms}}$ shows many phase jumps of π occurring on a fast energy scale, but there is no preferred phase drift. The results for the local setup resemble two-terminal devices that are governed by phase-rigidity [122, 123, 124], where the phase of the AB oscillations is locked to 0 or π . The results obtained for the local setup are in agreement with previous results of local four-terminal measurements [103, 134].

3.2.3 Numerical simulations

Several questions arise from the experimental results. What causes the qualitatively different findings for the local and non-local setup, and what restricts the phase of the AB oscillations in the local setup from a continuous drift? The most pressing question is what causes the phase jumps present in both the local and the non-local setup. In the following, we perform numerical simulations of the experimental setup. We describe the electron transport within the ballistic regime and interpret the experimental outcome in terms of elastic scattering.

We use the effective mass approximation introduced in chapter 1 in which transport is described by the single particle Hamiltonian eq. (1.1). The effective mass for the AlGaAs/GaAs heterostructure is given by $m^* = 0.067m_e$, where m_e stands for the electron mass. We include the magnetic field by minimal coupling and we replace $\mathbf{p} \rightarrow -i\hbar\nabla + e\mathbf{A}(x, y)$ in eq. (1.1). The experiments apply small magnetic fields of the order of few milli-Tesla. Therefore, we neglect the Zeeman splitting which is of the order of $\Delta E_{\text{Zeeman}} \sim \mu_B B \sim 10^{-3} \text{ meV}$. We do not include spin effects and the current in the leads is given by the Landauer formula eq. (1.2). In the ballistic transport, regime the observed currents and voltages

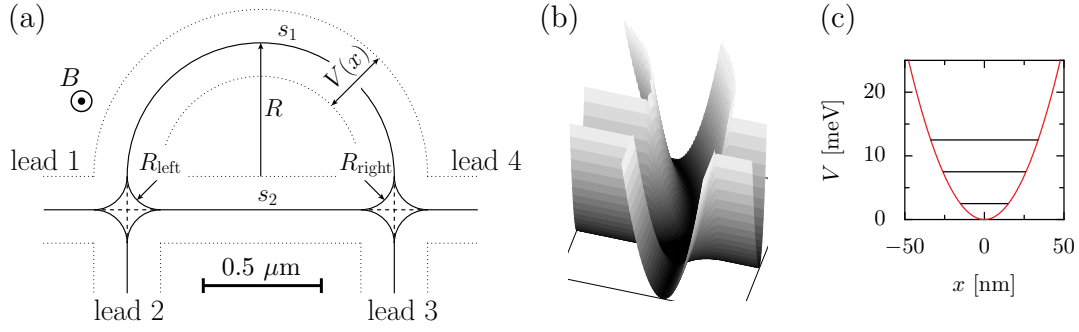


Figure 3.3: (a) schematic sketch of the simulated device geometry. We include depletion effects and assume a harmonic confinement for the leads and arms of the ring s_1 and s_2 . The confining frequency is set to $\hbar\omega = 5$ meV. Furthermore we use rounded cross-junctions with radii of $R_{\text{right}} = R_{\text{left}} = 70$ nm. The radius of the complete ring is given by $R = 0.5 \mu\text{m}$. (b) zoom into the confining potential of the orthogonal cross-junctions. (c) energy spacing of the modes of the transversal confining potential V .

are determined by scattering at the device geometry. We model the asymptotic leads of the experiments as harmonic waveguides with a confining frequency $\hbar\omega = 5$ meV. We include depletion effects in the device and accurately model the rounded orthogonal cross-junctions. Rounded junctions induce collimation effects that significantly change the scattering behavior [91]. Fig. 3.3(a) shows the geometry of the ring. We set the radius of the ring to $R = 0.5 \mu\text{m}$. The arms of the ring s_1 and s_2 are connected to the asymptotic leads by orthogonal rounded cross-junctions with radius $R_{\text{left}} = R_{\text{right}} = 70$ nm. Fig. 3.3(b) depicts a zoom into the potential of the right cross-junction. Fig. 3.3(c) illustrates the transversal confining potential with subband spacing $\Delta E = \hbar\omega = 5$ meV of the quantum waveguides defining the arms s_1 and s_2 and the asymptotic leads.

We use the time-dependent approach introduced in chapter 2 to numerically compute the energy-dependent transmission amplitudes. The time-dependent approach is based on wave-packet propagation. While the transversal shape of the wave packets is governed by the transversal confinement of the leads, we are free to choose the longitudinal component. In the following, we use Gaussian wave packets which can be designed to cover a certain energy range, as is demonstrated in section 2.3. For the numerical propagation, we use our efficient GPU implementation described in detail in section 2.4.

Numerical limitations like grid size and grid discretization set numerical constraints on the longitudinal shape of the wave packets. Typically the extension of the two-dimensional grid is $3 \mu\text{m} \times 2 \mu\text{m}$. Adjusting the parameters of the

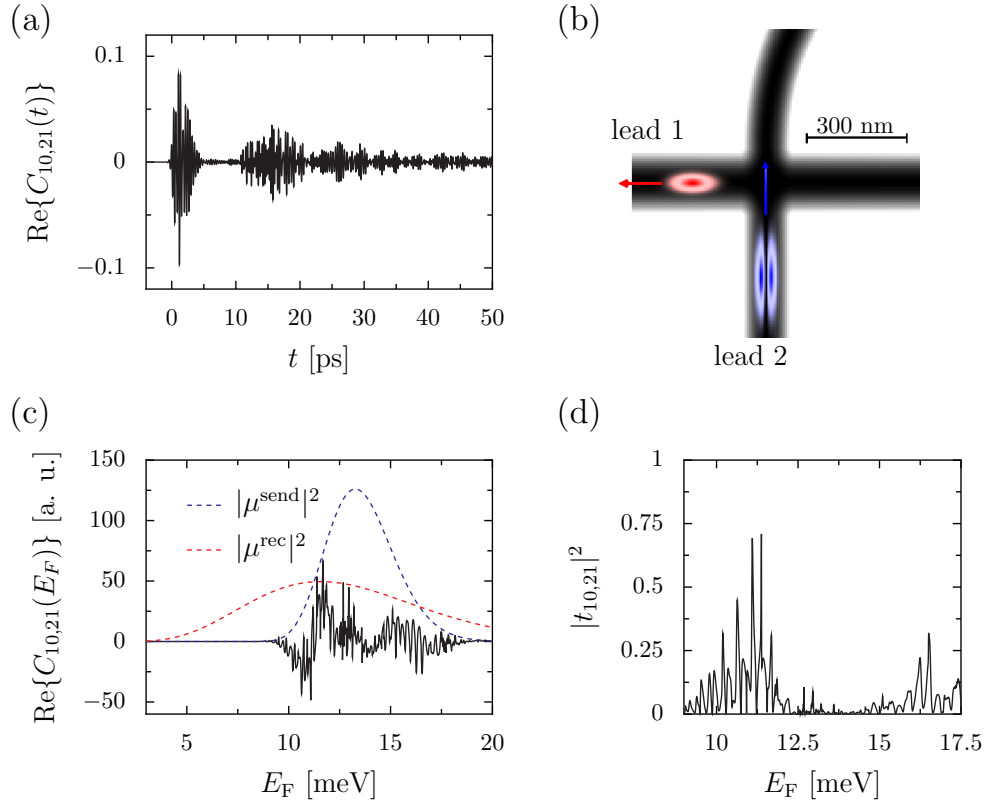


Figure 3.4: Illustration of the steps involved in the wave-packet approach to get the transmission probability $|t_{10,21}|^2$, which describes inter-mode scattering from lead 2 with transversal mode 1 to lead 1 in transversal mode 0. (a) time correlation function evaluated defined in eq. (2.16). (b) visualizes the extension of the receiver wave-packet (red) located in lead 1, and the sender wave-packet (blue) which is located in lead 2 for initial time $t = 0$ ps. (c) real part of the energy representation of the cross-correlation function after Fourier transform in arbitrary units. The dashed lines correspond to the energy density of the receiver $|\mu^{\text{rec}}|^2$ (red) and sender $|\mu^{\text{send}}|^2$ (blue) wave packet. (d) transmission probability $|t_{10,21}|^2$ is obtained from the energy representation of the cross-correlation function after employing the correction terms $|\mu^{\text{rec}}|^2$ and $|\mu^{\text{send}}|^2$ (see eq. (2.15)).

sender wave-packet results in a compromise between covering a large energy range and keeping the dispersion of the wave packet small enough to ensure that the sender wave-packet enters the scattering region as a localized wave packet. Since the receiver wave-packet remains stationary, dispersion is not an issue and the receiver wave-packet covers a larger energy range than the sender wave-

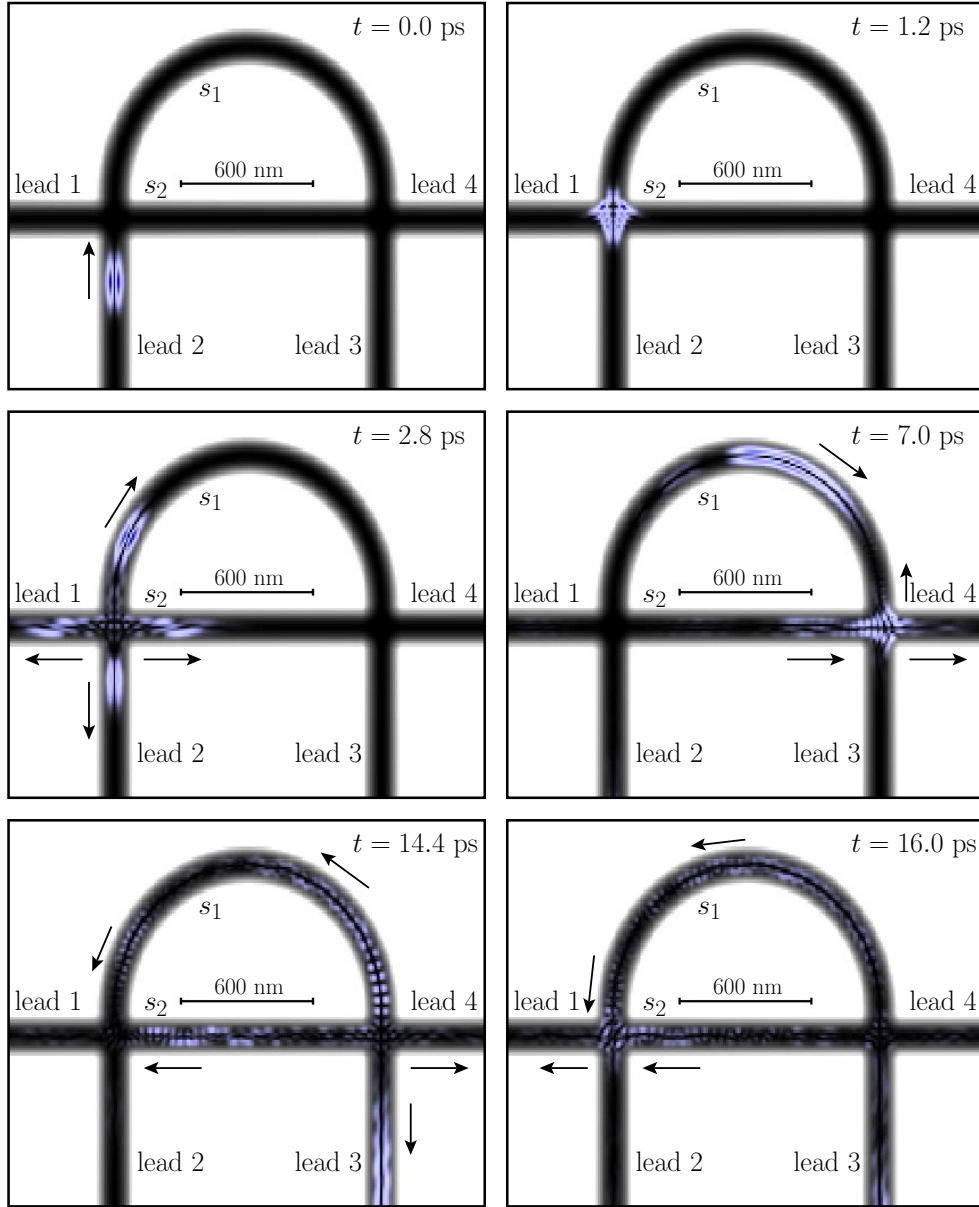


Figure 3.5: Snap-shots of the wave packet propagation for different times. The time evolution of the sender wave-packet is illustrated by the blue wave. The darkness encodes the amplitude of the wave packet. During the time evolution, the wave undergoes multiple scattering events. The arrows indicate the motion of the scattered parts.

packet. The dashed lines in Fig. 3.4(c) show the energy density, eq. (2.27), of the used sender and receiver wave-packets $\rho_{\text{send/rec}}(E)$. The sender covers an energy

range between 9 meV and 17.5 meV, while the receiver is extended in the energy domain over 5 meV to 25 meV. The shown results correspond to the lowest transversal mode of the receiver and the first transversal mode for the sender wave-packet. Higher transversal modes shift the energy density by the subband spacing $\hbar\omega = 5$ meV to higher energies. Measurements of the AB interference pattern in quantum wave-guide ring structures in Refs. [135, 119] use a top-gate voltage to probe a typical energy range of 1.6 meV. Hence, a single wave-packet run for each lead and open transversal mode is sufficient to cover the complete scan through the gate voltage.

Fig. 3.4 illustrates inter-mode scattering from lead 2 in transversal mode 1 to lead 1 in transversal mode 0. That is, we compute the transmission amplitude $t_{10,21}(E)$. The corresponding receiver wave-packet is illustrated by the red wave packet in Fig. 3.4(b). The spatial extension in position space of the wave packet is color-coded. The darker the color, the higher the probability of the wave packet to be located at the specific position is. The receiver is located in lead 1, populates the transversal mode 0, and is composed of purely outgoing momenta indicated by the arrow. The sender at time $t = 0.0$ ps is illustrated by the blue wave packet. The sender is located in lead 2 and populates the first excited transversal mode. During the propagation of the sender wave-packet, we keep track of the cross-correlation function $C_{10,21}(t)$ evaluated according to eq. (2.16).

The cross-correlation function $C_{10,21}(t)$ is depicted in Fig. 3.4(c). $C_{10,21}(t)$ shows a rich structure with revivals in the amplitude. In the following, we illustrate the scattering process of the wave packet that leads to the structure in the cross-correlation function. Fig. 3.5 shows snap-shots of the time evolution of the sender wave-packet. The arrows indicate the motion of the wave packet components. Initially ($t = 0.0$ ps), the sender is located within the asymptotic lead 2 and propagates toward the left cross-junction. At $t = 1.2$ ps, the sender approaches the center of the junction and scatters in different directions. The wave packet splits into four parts as is illustrated in the snap-shot at $t = 2.8$ ps. Some parts get reflected into an outgoing wave in lead 2. Other parts scatter to lead 1 and are detected by the receiver state. This leads to the large amplitude in $C_{10,21}(t)$ for the time interval between 1 ps and 5 ps. The remaining parts scatter either to the upper arm s_1 or to the lower arm s_2 of the ring. These parts travel along the ring toward the right cross-junction. The path s_2 is shorter than the path s_1 . Hence, the wave components traveling in the lower arm approach the right junction earlier than the components traveling along path s_1 . At $t = 7.0$ ps, the wave packet in the lower arm enters the right junction where parts leave the ring into lead 4. However, an amount of the wave packet gets transferred into the upper arm which then travel multiple times around the ring. This process induces higher frequencies in the AB oscillations. Apart from transport through the right cross-junctions, parts of the wave packet also get reflected and propagates along arm s_2 back to the left cross-junction, as depicted in snap-shot

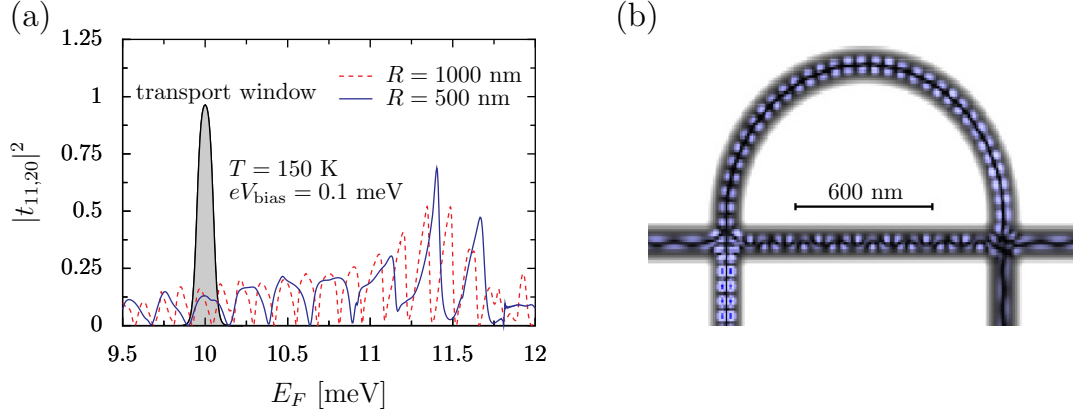


Figure 3.6: (a) transmission probability $|t_{11,20}|(E_F)$ for inter-mode scattering from lead 2 in the transversal ground state to lead 1 in the first excited transversal mode as function of Fermi energy E_F . Multiple reflections in the arms of the ring induces Fabry-Perot like resonances, resulting in fast fluctuations in the transmission probability. The larger the radius R of the ring, the faster these fluctuations become. The fluctuations occur on a smaller energy scale than the typical transport window of the experimental measurements. The experiments are performed for an electron temperature of 150 mK and apply typical bias voltages of $eV_{\text{bias}} = 0.1$ meV. The slope of the Fermi energy dependency of $|t_{11,20}|(E_F)$ reflects the transmission property of the cross-junctions. (b) amplitude of the scattering eigenstate $\psi_{2,1}^+(E)$, eq. (2.13), for energy $E = 9.84$ meV and $B = 4.5$ mT. Multiple reflections induce longitudinal nodes of the scattering eigenstates within the arms of the ring.

$t = 14.4$ ps. The wave then hits the left cross-junction at $t = 16.0$ ps for the second time, and the receiver again detects the outgoing waves in lead 1. We obtain a revival in the amplitude of the cross-correlation function $C_{10,21}(t)$.

In conclusion, we find that the sender wave-packet undergoes multiple reflections at the cross-junctions. This leads to an oscillatory pattern in the slope of the cross-correlation function. With advanced time, more and more parts of the sender wave-packet enter one of the asymptotic leads where they get absorbed by the macroscopic contacts simulated by the complex absorbing potential eq. (2.56). After a propagation time of 480 ps, the amplitude of the cross-correlation function drops below 0.5×10^{-3} and we stop the propagation. A discrete Fourier transform then yields the energy representation of the cross-correlation function $C_{10,21}(E)$ depicted in Fig. 3.4(c). The amplitude of $C_{10,21}(E)$ covers the energy range which is represented by the sender wave-packet. We

follow eq. (2.15) and employ the correction terms. This then results in the transmission probability $|t_{10,21}(E)|^2$ which is plotted in Fig. 3.4(d). The total propagation time determines the resolution of the transmission amplitudes in the energy domain. The propagation time of 480 ps yields an energy resolution of $\Delta E = 0.004$ meV for the transmission probabilities $|t_{10,21}(E)|^2$. Fig. 3.4(d) includes 1974 transmission amplitudes which are provided by the single wave-packet run.

The energy dependency of the transmission amplitude $|t_{10,21}(E)|^2$ contains two energy scales. There is a slow varying slope that reflects the scattering behavior of the orthogonal cross-junctions. The fast energy fluctuations are due to multiple reflections at the cross-junctions which induces Fabry-Perot like interference patterns in the arms of the ring. The resonance condition in a Fabry-Perot interferometer depends on the arm length s_i . Maximal transmission in an Fabry-Perot interferometer is given for energies matching the condition [143]

$$E - E_n = \frac{\hbar^2}{2m^*} \left(\frac{\pi}{s_i} \right)^2 k^2, \quad k \in \mathbb{N}, \quad (3.6)$$

where E_n stands for the energy of transversal mode n . The larger the radius of the ring, the faster the energy scale of the Fabry-Perot resonances becomes. A comparison of the transmission probability $|t_{10,21}(E)|^2$ for radius $R = 0.5 \mu\text{m}$ and $R = 1.0 \mu\text{m}$ is provided in Fig. 3.6(a). While the larger arm length for the larger ring $R = 1.0 \mu\text{m}$ induces faster fluctuations in $|t_{10,21}(E)|^2$, the overall slope, which is determined by the scattering behavior of the cross-junctions, remains unchanged. Multiple reflections also leave their trace in the scattering eigenstate $\psi_{i,n_i}^\pm(E)$, which is extracted from the wave-packet propagation according to eq. (2.13). Fig. 3.6(b) depicts the scattering eigenstate $\psi_{2,1}^+(E)$ for energy $E = 9.84$ meV and magnetic field $B = 4.5$ mT. Multiple reflections of the wave packet induces resonances which are visible in the longitudinal nodes of the scattering eigenstate in the arms of the ring.

3.2.4 Results for the linear transport regime

So far, we have computed the transmission amplitudes. In the following we employ the Landauer formula eq. (1.2) and we model the experimental setup within the linear regime. That is, we assume very small applied voltages and low temperatures. The transport window opened by the difference of the Fermi functions in eq. (1.2) is then smaller than the energy scale of the changes in the transmission amplitudes. Within the linear regime, the currents in the leads are expressed by the transmission amplitude at the Fermi energy E_F [107, 98, 105]

$$I_i = \frac{e}{h} \left((1 - T_{ii}(E_F)) \mu_i - \sum_{j \neq i} T_{ij}(E_F) \mu_j \right), \quad (3.7)$$

where μ_i corresponds to the chemical potentials of the macroscopic contact connected to lead i , and $T_{ij}(E) = \sum_{n_i n_j} |t_{in_i, jn_j}(E)|^2$ defines the probability for electrons to get transferred from lead j to lead i . The local and non-local resistances are evaluated analytically. We follow Büttiker Ref. [105], and obtain an analytical expression for the resistance $R_{ij,kl} = V_{kl}/I_{ij}$

$$R_{ij,kl}(E_F) = \frac{h}{e^2} \frac{T_{ki}(E_F)T_{lj}(E_F) - T_{kj}(E_F)T_{li}(E_F)}{D(E_F)} \quad (3.8)$$

with

$$\begin{aligned} D(E) &= \frac{h^2}{e^4} (\alpha_{11}(E)\alpha_{22}(E) - \alpha_{12}(E)\alpha_{21}(E))S(E) \\ \alpha_{11}(E) &= \frac{e^2}{h} \left((1 - T_{11}(E))S(E) - (T_{14}(E) + T_{12}(E))(T_{41}(E) + T_{21}(E)) \right) / S(E) \\ \alpha_{22}(E) &= \frac{e^2}{h} \left((1 - T_{22}(E))S(E) - (T_{21}(E) + T_{23}(E))(T_{32}(E) + T_{12}(E)) \right) / S(E) \\ \alpha_{12}(E) &= \frac{e^2}{h} \left(T_{12}(E)T_{34}(E) - T_{14}(E)T_{32}(E) \right) / S(E) \\ \alpha_{21}(E) &= \frac{e^2}{h} \left(T_{21}(E)T_{43}(E) - T_{23}(E)T_{41}(E) \right) / S(E) \\ S(E) &= T_{12}(E) + T_{14}(E) + T_{32}(E) + T_{34}(E). \end{aligned} \quad (3.9)$$

Fig. 3.7(a) shows the non-local resistance $R_{43,12}(B)$, eq (3.2), evaluated for the linear regime at Fermi energy $E_F = 9.47$ meV. The non-local resistance shows an oscillatory signal as a function of the magnetic field. Those oscillations are due to the AB effect. The AB oscillations show an amplitude of approximately 4.8 k Ω on top of a constant background of 7.1 k Ω . The constant background originates from the scattering process in the cross-junctions where the electron wave is transferred directly to the asymptotic leads without traveling through the ring. The Lorentz force changes the scattering at the orthogonal cross-junctions and we obtain an asymmetry in the amplitude of the AB oscillations with respect to the sign of the magnetic field. The asymmetry between the positive and negative magnetic fields gets stronger with the increasing magnetic field strength. We extract the frequency of the AB oscillations by performing the Fourier transform of the non-local resistance $R_{43,12}(B)$. To get a clear signal in the frequency domain, we fold $R_{43,12}(B)$ by a Gaussian, leading to broadened peaks in the Fourier transform $\mathcal{F}(R_{43,12})$. Fig. 3.7(b) shows the absolute value of $\mathcal{F}(R_{43,12})$. The peaks correspond to the different frequencies in the AB oscillations. The constant background of the AB oscillations is represented by the peak around $\omega_{AB} = 0$ mT $^{-1}$. The enclosed area of the ring results in an h/e -frequency of the AB oscillations with a period $\Delta B = 8.75$ mT, resulting in a frequency of $\omega_{AB} = 2\pi/\Delta B = 0.72$ mT $^{-1}$. Apart from the dominant h/e frequency, higher

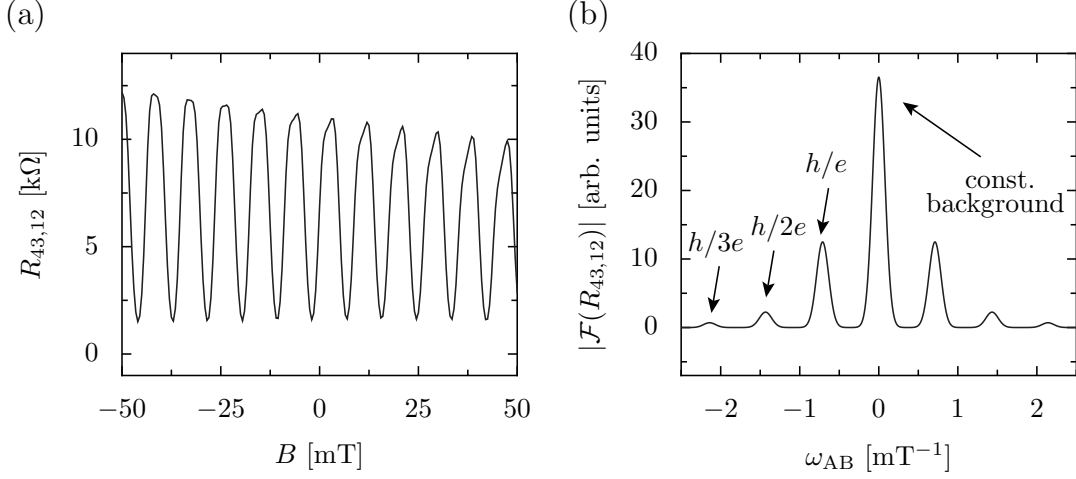


Figure 3.7: Results for the non-local setup in the linear regime for Fermi energy $E_F = 9.47$ meV. (a) AB oscillations of the non-local resistance $R_{43,12}(B)$. Due to the Lorentz force, the amplitude of the AB oscillations depends slightly on the magnetic field B . (b) Fourier analysis of the AB oscillations of $R_{43,12}(B)$. The absolute value is shown in arbitrary units. We use a Gaussian damping, and the peaks in the Fourier spectrum are broadened. Apart from the constant background, the AB oscillations are composed of multiple frequencies. The dominant frequency is given by the h/e frequency. The corresponding period, for the system under consideration, is given by $\omega_{AB} = 0.72$ mT^{-1} . Higher frequencies $h/2e$ and $h/3e$ emerge since parts of the electron wave travel several times around the ring.

frequencies, such as the $h/2e$ ($\omega_{AB} = 2 \times 0.72$ mT^{-1}) and $h/3e$ ($\omega_{AB} = 3 \times 0.72$ mT^{-1}) frequencies, also appear. Higher frequencies emerge when parts of the electron wave circle multiple times around the ring [231].

In the following, we consider the phase dependency of the AB oscillations with respect to changes in the Fermi energy. The transmission amplitudes, see Fig. 3.6, show fast fluctuations due to Fabry-Perot like interference in the arms of the ring. Those fast fluctuations are also present in the amplitude and in the phase behavior of the AB oscillations. We plot the non-local and local resistance as a function of the Fermi energy and the magnetic field. Fig. 3.8 shows a gray-scale plot of the oscillatory component (without constant background). The amplitude is color encoded. Dark regions correspond to maxima, and the white regions correspond to minima in the AB oscillations. We consider a range of Fermi energies of $E_F \in [8.5, 10.1]$ meV, within which two transversal lead modes contribute to the transport. The two measurement setups show qualitatively

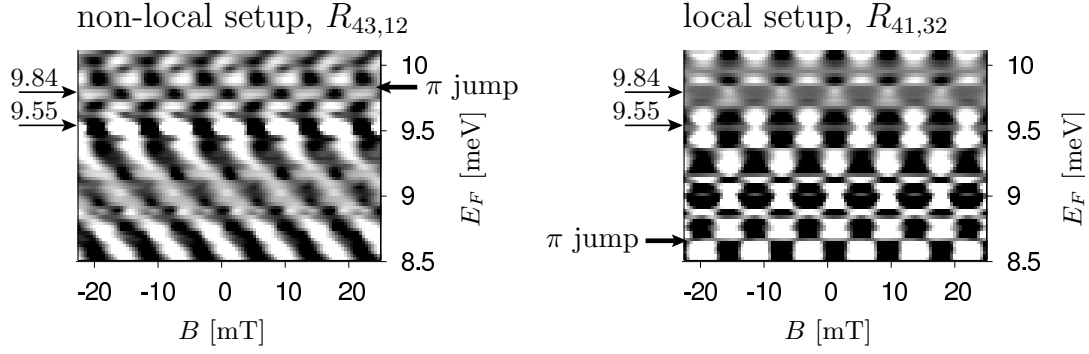


Figure 3.8: Gray-scale plots of the AB oscillations as a function of Fermi energy E_F for the non-local $R_{43,12}$ and local $R_{41,32}$ resistance evaluated in the linear regime. The non-local setup shows a continuous phase drift in the range $E_F \in [8.5, 9.5]$ meV. Around $E_F \approx 9.8$ meV, the continuous drift is interrupted by a sequence of π phase-jumps. The symmetric arrangement of the current and voltage probes induces phase-rigidity in the local resistance. Here, the phase is locked at either 0 or π . The local setup is governed by many phase jumps which appear on the energy scale of the Fabry-Perot like resonances.

different behavior. While the phase of the AB oscillations exhibits a continuous phase drift by changing the Fermi energy in the non-local setup (the maxima shift to the left with increasing Fermi energy), the phase of the AB oscillations is locked to zero or π in the local setup. The local setup shows a chess-board pattern with many phase jumps of π in the phase of the AB oscillations while scanning through the Fermi energy. The reason for the phase-rigidity of the local setup lies in the symmetry of the setup. Current and voltage probes are placed in such a manner that the mirror symmetry of the device prevails (Fig. 3.2). This enforces the local resistance to be an even function in the magnetic field, $R_{41,32}(B) = R_{41,32}(-B)$. The mirror symmetry of the measurement setup is broken in the non-local setup, allowing for a continuous phase drift in the AB oscillations. Nevertheless, the continuous phase drift is interrupted at certain Fermi energies by abrupt phase jumps of π . For example, there is a sequence of phase jumps around $E_F \approx 9.8$ meV in the non-local setup.

The phase jumps are related to the resonances in the arms of the ring, influencing the scattering behavior of the cross-junctions in a drastic way. The resonances in the arms appear because of the Fabry-Perot like multiple reflections at the cross-junctions. They occur on a fast energy scale. This explains the fast energy scale of the abrupt phase jumps in the local setup as well as the sequence of phase-jumps in the non-local setup around $E_F \approx 9.8$ meV. In order to get a

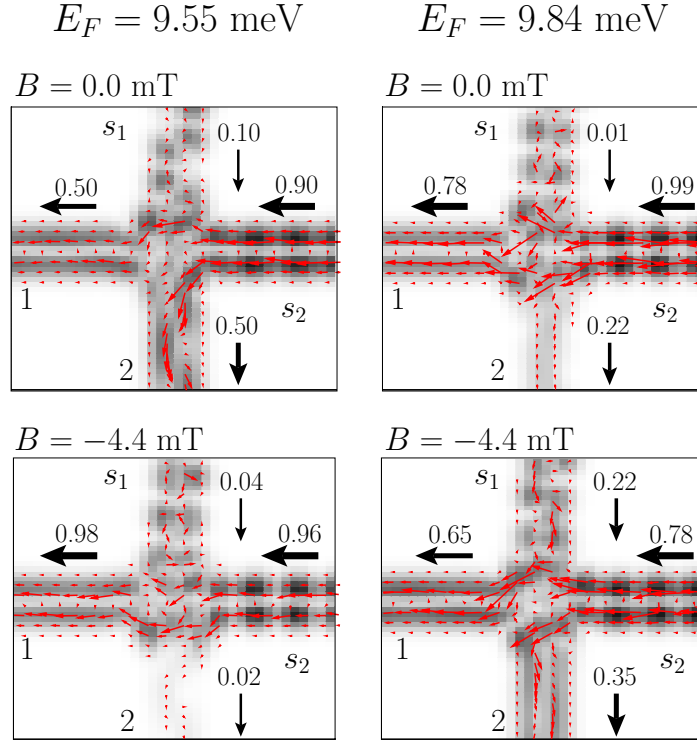


Figure 3.9: Microscopic scattering property at the left cross-junction of the quantum ring. The figure shows the probability density of scattering the eigenstate $\psi_{4,1}^+(E_F)$ for Fermi energies $E_F = 9.55$ meV and $E_F = 9.84$ meV enclosing a π -phase jump in the non-local resistance, see Fig. 3.8. The small arrows indicate the flux density eq. 3.10. The thick black arrows correspond to the normalized, integrated flux along the transversal direction of the waveguides. The opening and blocking of transport to lead 2 at the left cross-junction is detailed for the magnetic fields $B = 0$ mT and $B = -4.4$ mT. The magnitude of the latter approximately corresponds to half of the h/e period $\Delta B = 8.75$ mT.

microscopic picture of the scattering behavior at the cross-junctions, we consider the scattering eigenstate $\psi_{4,1}^+(E_F)$, which corresponds in a time-dependent picture to an incoming electron in lead 4, populating the first transversal mode. The electron scatters at the right cross-junction and the wave splits into components that travel along the upper arm s_1 and the lower arm s_2 of the ring. At the left junction, both parts interfere, and the AB interference pattern is probed in the non-local setup by the voltage probes at lead 1 and lead 2. Fig. 3.9 depicts the probability density of $\psi_{4,1}^+(E_F)$ in the vicinity of the left junction. We consider the Fermi energies $E_F = 9.55$ meV and $E_F = 9.84$ meV which enclose a phase

jump of π in the non-local setup at $E_F = 9.75$ meV. We further illustrate the scattering behavior for two different magnetic fields, $B = 0$ mT and $B = 4.4$ mT. The latter corresponds approximately to half of the h/e period $\Delta B = 8.75$ mT. The thin (red) arrows indicate the flux density

$$\vec{j}(\mathbf{r}) = \frac{\hbar}{m^*} \text{Im}(\psi_{4,1}^+(\mathbf{r}, E_F)^* \vec{\nabla} \psi_{4,1}^+(\mathbf{r}, E_F)), \quad (3.10)$$

and the thick (black) arrows correspond to the normalized, integrated flux along the transversal direction of the waveguides. At first, we discuss the situation for $E_F = 9.55$ meV. For $B = 0$ mT, the left junction distributes the electron flux evenly to lead 1 and lead 2. For $B = 4.4$ mT, the AB interference changes in such a way that there is a dominant electron transfer to lead 1, while transport to lead 2 is blocked. For Fermi energy $E_F = 9.75$ meV, the magnetic field dependency of the scattering is exactly reversed. For $B = 0$ mT, transport to lead 1 dominates, and scattering to lead 2 is suppressed. For $B = 4.4$ mT, however, the left cross-junction distributes the incoming flux more evenly to both leads 1 and 2. Compared to $E_F = 9.55$ meV, we obtain a phase shift of π in the magnetic field dependency of the scattering process. The opening and blocking of the flux with magnetic field B is less prominent for $E_F = 9.75$ meV, reducing the amplitude of the AB oscillations when compared to the situation $E_F = 9.55$ meV.

3.2.5 The non-linear regime and comparison with experiments

In the following, we compare the numerical simulations with the experimental results. The confining potential of the 1d-waveguides of the leads and arms of the ring influences the scattering property of the cross-junction which yields significant effects on the AB oscillations, especially in the case of single-mode scattering. In the experiments, 3-12 modes are typically populated. Single-mode effects superpose each other and the experiments detect an averaged signal, see Kreisbeck, Buchholz *et al.* Ref. [119] and Buchholz *et al.* Ref. [135]. Our simulation takes into account 3 open transversal modes. In order to reduce the numerical effort, we reduce the radius of the ring to $R = 0.5 \mu\text{m}$, compared to the experimental device size with a radius of $R = 1 \mu\text{m}$. The smaller radius reduces the enclosed area of the flux, and the period of the h/e AB oscillations of $\Delta B = 8.75$ mT is about four times larger than the experimental one with $\Delta B = 2.28$ mT. Furthermore, in sections 3.2.3 and 3.2.4, we illustrate that the Fabry-Perot like resonances in the arms of the ring change the distribution of the electron flux within the cross-junctions to the leads. Blocking and opening with the magnetic field depends on the Fermi energy, and the transport changes drastically even for small changes in the Fermi energy, see Fig. 3.9. The energy scale

of the fluctuations in the transmission probabilities is faster in the experimental geometry with a radius of $R = 1 \mu\text{m}$ than for our numerically simulated device geometry with $R = 0.5 \mu\text{m}$, as illustrated in Fig 3.6. The basic features such as the overall phase drift and the occurrence of π phase-jumps are not affected by the reduced size of the ring, though.

The experiments detect the integrated signal of the lock-in amplifier, eqs. (3.4) and (3.5). The experiments inject a current of 12 nA, which leads to bias voltages between $V_{\text{bias}} = 0.03$ and $V_{\text{bias}} = 0.1$ mV. The electron temperature is estimated to be 150 mK with a thermal broadening of $4k_{\text{B}}T \approx 0.05$ meV. The corresponding transport window, defined by the difference of the Fermi functions of the contacts, is indicated in Fig. 3.6 by the gray area ($V_{\text{bias}} = 0.1$ meV, $T = 150$ mK). Since the transport window is larger than the fluctuations in the transmission amplitude, the linear regime of the Landauer-Büttiker formalism employed in section 3.2.4 is not applicable for the parameter regime of the experimental setup. We need to evaluate the Landauer formula within its non-linear formulation. To evaluate the resistance $R_{ij,kl}$, we proceed as follows: The experimental setup feeds lead i with the ac-current

$$I_i(t) = I^{\text{max}} \cos \omega t, \quad I^{\text{max}} = \sqrt{2} I^{\text{rms}}. \quad (3.11)$$

Current conservation enforces $I_j(t) = -I_i(t)$, and the contacts k and l act as perfect voltage probes ($I_{k/l} = 0$). The chemical potentials of the contacts are then obtained as the solution for the system of non-linear equations

$$\begin{aligned} I_i &= \frac{e}{h} \int dE \sum_{\ell} T_{i,\ell}(E) (f_i(\mu_i, E) - f_{\ell}(\mu_{\ell}, E)) = I_i(t) \\ I_k &= \frac{e}{h} \int dE \sum_{\ell} T_{k,\ell}(E) (f_k(\mu_i, E) - f_{\ell}(\mu_{\ell}, E)) = 0 \\ I_l &= \frac{e}{h} \int dE \sum_{\ell} T_{l,\ell}(E) (f_l(\mu_i, E) - f_{\ell}(\mu_{\ell}, E)) = 0. \end{aligned} \quad (3.12)$$

The chemical potential of the contact j , where the current is injected, is fixed to the Fermi energy $\mu_j = E_F$. All other chemical potentials are extracted by solving the non-linear system eq. (3.12) which is carried out numerically within the Newton-Raphson method. This then yields the voltage drop

$$V_{kl}(t) = \frac{1}{e} (\mu_k(t) - \mu_l(t)). \quad (3.13)$$

Integration according to eq. (3.4) and inserting in eq (3.5) then gives the experimentally detected resistance $R_{ij,kl}^{\text{rms}}$.

In the experiments, the phase rigidity of the local setup is not as distinct as that obtained in our simulations in the linear regime, shown in Fig 3.8. Although the

finite current and the evaluation of the local resistance in the non-linear regime eq. (3.12) slightly lifts the strict phase locking to 0 or π , the experimentally detected small energy domains with a continuous phase drift in the local setup are not explained by finite-current effects, see Kreisbeck, Buchholz *et al.* Ref. [119]. Phase rigidity is a consequence of the perfect mirror symmetry of the simulated device geometry. However, the fabrication of a perfect symmetric device is not possible. There are deficiencies in the device fabrication and, in particular, the orthogonal cross-junctions are not identical in every little detail. In the following, we break the mirror symmetry of the device and assume that the rounding of the two cross-junctions is different. We set the radii of the cross-junctions to $R_{\text{left}} = 75$ nm and $R_{\text{right}} = 65$ nm.

Fig. 3.10 shows the numerical results for the non-local and local resistance. The gray-scale plots of the oscillatory component (without constant background) of the AB oscillations as a function of the Fermi energy E_F are depicted. The AB oscillations are visible in the alternating black and white-regions that correspond to maxima and minima in the resistances $R_{43,12}$ and $R_{41,32}$ while sweeping through the magnetic field B . With increasing Fermi energy, there are areas of reduced resolution and areas with a pronounced amplitude in the AB oscillations. Those structures in the gray-scale plots reflect the energy-dependent scattering properties of the orthogonal cross-junctions. There is also a fast varying structure with changes in the Fermi energy. This is especially visible in the local setup in which the interference pattern is interrupted by several π phase-jumps. The energy scale of those fluctuations is given by the Fabry-Perot like resonances that are due to multiple reflections at the junctions. These reflections are already observed in section 3.2.4 in the linear regime. Compared to the linear regime, finer structures in the energy dependency of the AB oscillations are smeared out because of the finite current and the finite temperature.

The non-local setup shows a continuous phase drift with the Fermi energy and, for example, the phase shifts continuously from 0 to π for Fermi energies between $E_F = 14.31$ meV and $E_F = 14.64$ meV, as illustrated in the upper panel of Fig. 3.10(a). Beside the continuous phase drift, there are also energies like $E_F \approx 13.9$ meV, marked by the arrow, with an abrupt phase-jump of π . The broken device symmetry allows for a continuous phase drift in the local setup for certain energy ranges, see Fig. 3.10(b). However, π -phase jumps still occur and, in particular, there is no preferred direction of the phase drift. The upper panel of Fig. 3.10(b) shows the AB oscillations at Fermi energies $E_F = 15.60$ meV, and $E_F = 15.93$ meV enclosing a phase jump of π at $E_F = 15.75$ meV. For the Fermi energy in which the phase jump occurs, the amplitude of the h/e period is suppressed and the $h/2e$ period dominates the AB oscillations. Our numerical simulations accurately reproduce the experimentally observed phase behavior of the AB oscillations. The experimental results are given in Kreisbeck, Buchholz *et al.* Ref. [119] Fig. 1.

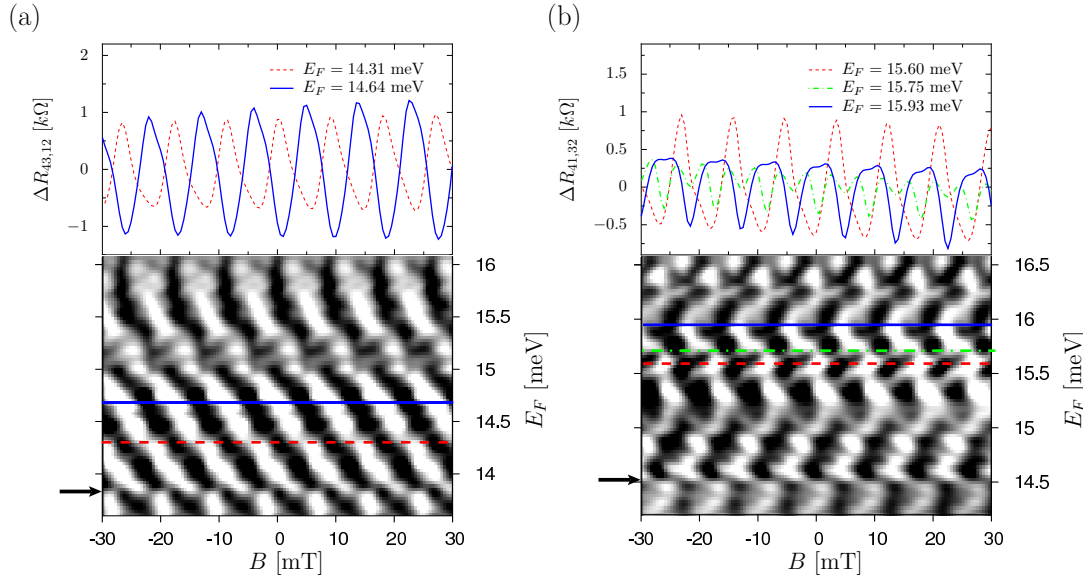


Figure 3.10: Oscillatory component of the (a) non-local ($\Delta R_{43,12}$) and the (b) local ($\Delta R_{41,32}$) setup. We incorporate asymmetries due to the device fabrication process and use different radii $R_{\text{left}} = 75$ nm and $R_{\text{right}} = 65$ nm for the orthogonal cross-junctions. To allow for a comparison with the experimental results of Kreisbeck, Buchholz *et al.* in Ref. [119], Fig. [1], we evaluate currents and voltages within the non-linear regime and include the ac lock-in amplifier (peak current of 6 nA, $T = 150$ K). Both setups show π phase-jumps as marked by the arrows. (a) The non-local setup yields a continuous phase-drift of π within the energy range $E_F \in [14.31, 14.64]$ meV. The corresponding oscillatory component of the non-local AB oscillations for Fermi energies $E_F = 14.31$ meV and $E_F = 14.64$ meV, marked by the dashed and solid lines, are depicted in the upper panel. (b) The asymmetric device geometry slightly lifts the phase rigidity of the local setup, but there is no overall phase drift. At the Fermi energy where phase jumps occur, the h/e frequency is suppressed and the $h/2e$ dominates, as illustrated in the upper panel. The Fermi-energies considered are marked in the lower panel by the dashed, dash-dotted, and solid lines.

While we reproduce the phase behavior of the AB oscillations, there are deviations between our simulations and the experiments in the amplitude of the AB oscillations. Compared to our simulations in Fig. 3.10, the experimental AB oscillations exhibit a much lower amplitude on top of a larger constant back-

ground. We ascribe the reduced amplitude in the experiments to electron-phonon interactions that induce dissipation and decoherence. Incoherent electrons are not subjected to the AB interference and contribute to the constant background. This process is not incorporated in the numerical simulations since we are mainly interested in the phase behavior of the AB oscillations which is not affected by incoherent electrons.

3.2.6 Conclusion

In summary, our simulations accurately reproduce the experimentally observed π phase-jumps in both the non-local and the local setup. Phase-jumps and fast fluctuations in the phase dependency of the AB oscillations with Fermi energy originate from Fabry-Perot like resonances in the arms of the ring, drastically redirecting the electron flow at the orthogonal cross-junctions. Thus, the appearance of π -phase jumps is an intrinsic property of the device geometry and a universal feature of the experimental setup. The energy scale of the π -jumps is given by the size of the ring.

Furthermore we explain the qualitatively different results of the non-local and the local setup by the different placement of voltage and current probes. The local setup supports the symmetry of the device, and the phase behavior resembles the results of two-terminal measurements which are governed by phase rigidity. Asymmetries in the device fabrication gives rise to certain energy regions within which the phase of the AB oscillations changes continuously with the Fermi energy. There is no overall phase tendency in the local setup.

3.3 Transmission phase of a quantum dot embedded in an AB-ring

In this section, we configure the AB ring as a transmission phase detector. Recent experiments [126, 127, 230, 235] use AB interference devices to characterize embedded quantum systems, such as quantum dots, that are placed in one of the arms of the ring. Compared to conductance measurements which yield information about the transmission amplitude of quantum systems, the setup of the AB interferometer yields additional information about the transmission phase of the embedded system. Theoretical simulations of such a setup are based on a very fundamental level and are described by phenomenological 1d-models [139, 140, 141]. Our wave-packet approach goes beyond such simple models and we perform realistic simulations which take into account the two-dimensional character of the device geometry. As we have demonstrated in section 3.2, this yields realistic simulations of the experimental setup which accurately reproduce

the experimental measurement setup.

In contrast to previous experiments which have fabricated small quantum dots embedded in much larger rings to ensure that the magnetic flux does not penetrate the quantum dot, we investigate a larger quantum dot, where the magnetic field induces a significant splitting of the energy levels. We demonstrate that the non-local setup of the AB interferometer, characterized in detail in section 3.2, is appropriate for a transmission phase detector for the embedded quantum dot. We consider a harmonic quantum dot and show how the Darwin-Fock spectrum [98] emerges as a unique pattern in the interference fringes of the AB oscillations.

Since the empty device already shows complicated effects like phase-jumps, a suitable and careful preparation of the setup is required. To avoid disturbing multi-mode effects, we configure the interferometer into a transport regime where only two open modes contribute to the transport. A mode-filtered electron injection allows experimentalists to perform even single-mode transport in a multi-mode waveguide structure [236]. Furthermore, we carefully adjust the range of the Fermi energy under consideration. Visualization of the transmission phase of the embedded quantum dot requires a continuous phase drift of the AB oscillations while scanning through the Fermi energy [127]. It is crucial to break phase rigidity because if the phase is locked to 0 or π , then the information of the transmission phase gets lost. This is also the reason why 2-terminal measurements, which exhibit phase rigidity [122, 123, 124], are not suitable as transmission phase detectors. A continuous phase drift of the AB oscillations is provided by the non-local four-terminal setup discussed in detail in section 3.2. For example, for Fermi energies in the range between 8.5 meV and 9.5 meV, the non-local setup shows a well-defined continuous phase drift without disturbing phase jumps of π , see section 3.2.4, Fig. 3.8.

We place the harmonic quantum dot in the lower arm s_2 of the ring. The quantum dot is coupled by resonant tunneling [107, 98, 99] to the waveguide s_2 . Within this configuration, transmission only takes place through the quantum dot when the Fermi energy hits a resonance (that is an eigenstates) of the quantum dot. Thus, we adjust the energy of the studied resonance of the quantum dot so that it is in the considered energy range $E_F \in [8.5, 9.5]$ meV. In the experimental setup, variations in the the energy levels of the embedded quantum dot are achieved by local gate voltages [126, 127]. A plot of the potential landscape of the setup is shown in Fig. 3.11. The strength of the confining potential is color-coded. The solid lines correspond to equipotential lines with an energy spacing of 5 meV. A zoom to the arm s_2 with the embedded quantum dot is shown in Fig. 3.11(b). The waveguide s_2 , which defines the lower arm of the ring, is closed by two rounded, harmonically confined caps in the proximity of the quantum dot. The closed waveguide configures the transport in the lower arm into the resonant tunneling regime. The distance between the center of the quantum dot and the harmonically confined caps of arm s_2 is set to 110 nm. This

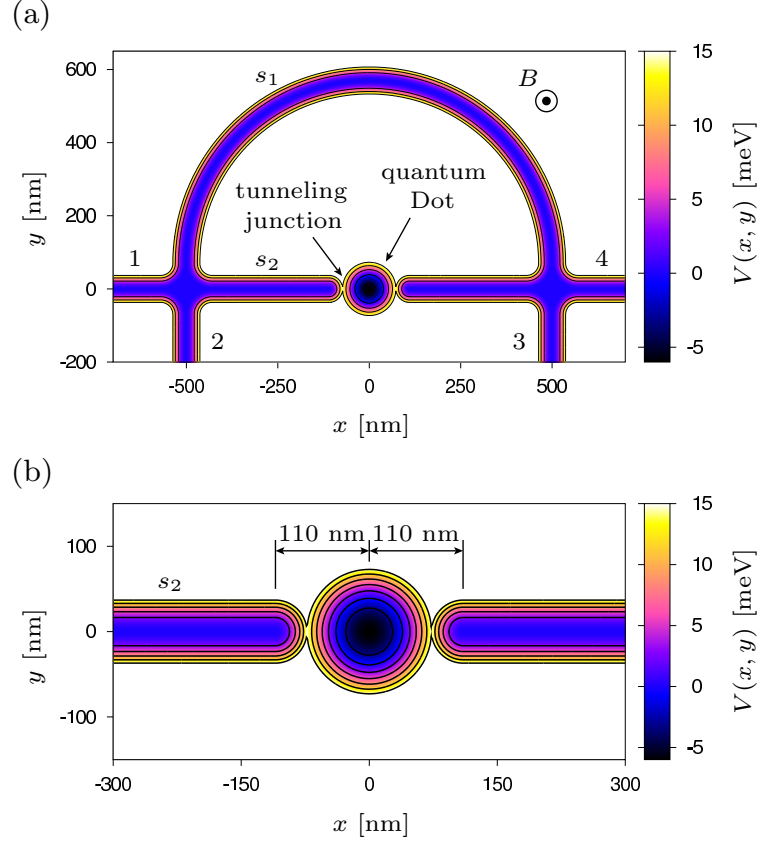


Figure 3.11: (a) Potential landscape of the AB interferometer configured as a transmission phase detector of an embedded quantum dot. We use an isotropic harmonic quantum dot with a frequency of $\hbar\omega_{\text{dot}} = 3$ meV which potential is shifted by $V_0 = -6$ meV. The ring is basically constructed in the same way as shown in Fig. 3.3. We use a harmonic transversal confinement of the leads with $\hbar\omega = 5$ meV. We set the radius of the ring to $R = 0.5 \mu\text{m}$ and use rounded cross-junctions with $R_{\text{right}} = R_{\text{left}} = 70$ nm. (b) shows a zoom to the lower arm of the ring. We configure the quantum dot into the resonant tunneling regime and close the waveguide s_2 in the proximity of the quantum dot with rounded caps. The distance between the caps and the center of the quantum dot adjusts the tunneling coupling. We use a distance of 110 nm.

parameter controls the potential barrier between the quantum dot and the closed waveguides which define the lower arm of the ring s_2 . The closer the waveguides are attached to the quantum dot, the larger the tunneling coupling becomes.

The potential of the harmonic quantum dot is given by

$$V_{\text{dot}} = \frac{1}{2}m^*\omega_{\text{dot}}^2(x^2 + y^2) + V_0, \quad (3.14)$$

where we set the frequency to $\hbar\omega_{\text{dot}} = 3$ meV and $V_0 = -6$ meV shifts the energy of the quantum dot with respect to the zero energy of the transversal confinement of the leads 1-4 and the arms of the ring s_1 and s_2 . The shift is chosen in such a way that the eigenstate corresponding to the quantum number $n = 4$ is located at the Fermi energy of $E_F = 9$ meV, which fits into the considered range of Fermi energies $E_F \in [8.5, 9.5]$ meV. The quantum number of the 2d harmonic oscillator $n = n_x + n_y$ is composed of the Cartesian quantum numbers n_x and n_y of the Cartesian coordinates x and y . In the presence of a homogeneous magnetic field perpendicular to the plane of the 2d harmonic quantum dot, the angular momentum states for a given quantum number n are no longer degenerate and split according to the Darwin-Fock spectrum. The Darwin-Fock spectrum is given by [98]

$$E_{n,m} = (n+1)\hbar\Omega + \frac{1}{2}\hbar\omega_c m + V_0, \quad \text{with} \quad \Omega = \sqrt{\omega^2 + \frac{\omega_c^2}{4}}, \quad (3.15)$$

where we do not include the Zeeman spin splitting and V_0 takes into account the zero energy shift of the harmonic quantum dot. We define $\omega_c = eB/m^*$ as the cyclotron frequency, $n = n_x + n_y$ corresponds to the main quantum number, and m denotes the $n+1$ angular momentum states with $m = -n, -n+2, \dots, n$. The eigenstates are given in polar coordinates $x = r \cos \phi$ and $y = r \sin \phi$ as follows [98]

$$\Phi_{n_r,m}(\mathbf{r}) = \frac{1}{\sqrt{2\pi}} e^{im\phi} \frac{1}{l_0} \sqrt{\frac{n_r!}{(n_r + |m|)!}} e^{-r^2/4l_0^2} \left(\frac{r}{\sqrt{2}l_0}\right)^{|m|} L_{n_r}^{|m|}(r^2/2l_0^2). \quad (3.16)$$

Here, n_r is the radial quantum number with $n_r = (n - |m|)/2$. We further define $l_0 = \sqrt{\hbar/m^*\Omega}$, and $L_{n_r}^{|m|}$ denotes the generalized Laguerre polynomials.

The Darwin-Fock spectrum is imprinted in the transmission through the quantum dot. To see this, we consider a two-terminal setup which only comprises of the lower arm s_2 with the embedded quantum dot. The zoom into the arm s_2 , Fig. 3.11(b), reflects such a setup in principle. In Fig. 3.12, we depict the transmission probability $T_{\text{QD}} = |t_{\text{QD}} e^{i\varphi_{\text{QD}}}|^2$ and the transmission phase φ_{QD} as functions of the Fermi energy E_F . Without the magnetic field, $B = 0$ mT (Fig. 3.12(a)), the angular momentum states m of the harmonic oscillator are degenerate. The transmission probability T_{QD} for transport through the quantum dot shows a Lorentz-shaped resonance around Fermi energy $E_F = 9$ meV, corresponding to the oscillator state with quantum number $n = 4$. The resonance is not exactly

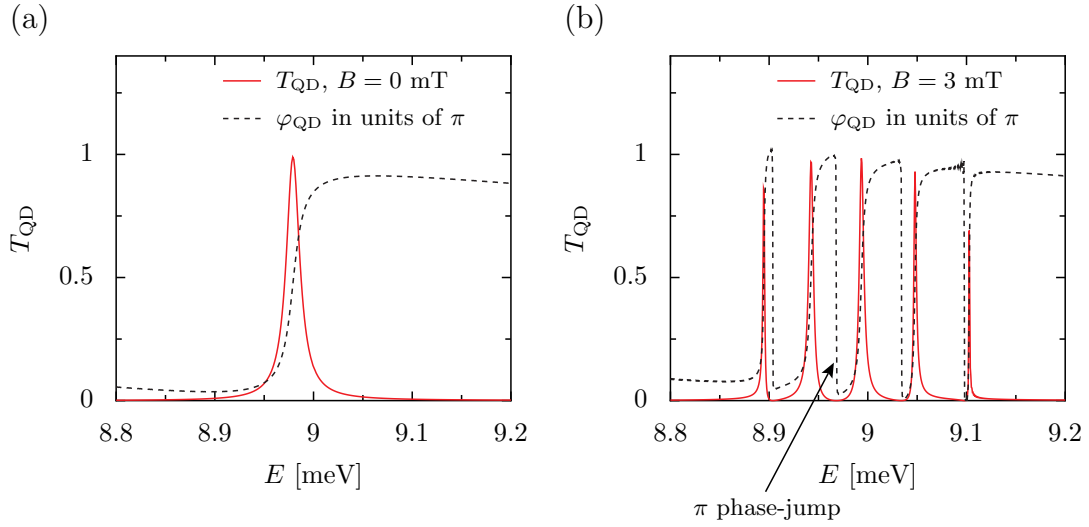


Figure 3.12: Transmission amplitude $T_{\text{QD}} = |t_{\text{QD}} e^{i\varphi_{\text{QD}}}|^2$ through the harmonic quantum dot as a function of the Fermi energy in a two-terminal resonant tunneling setup. The dashed line corresponds to the transmission phase φ_{QD} in units of π . The resonance for quantum number $n = 4$ of the harmonic quantum dot is shown. (a) For $B = 0$ mT, the angular momentum states m are degenerate and there is only a single resonance. (b) For $B = 3$ mT, the degeneracy is lifted and the momentum states split according to the Darwin-Fock spectrum eq. 3.15 into $n + 1$ resonances. The transmission phase evolves continuously while scanning through a resonance, but is interrupted by a π phase-jump between two consecutive resonances.

at $E_F = 9$ meV, and there is a slight shift of the resonance to lower energies. This is ascribed to the influence of the tunneling junctions. The transmission phase t_{QD} changes continuously by approximately π , while scanning the Fermi energy E_F through the resonance. The width of the Lorentz-shaped resonance depends on the strength of the tunneling coupling. The continuous shift of the transmission phase by π is a typical characteristic of resonant tunneling [129].

The situation is different for a finite magnetic field. Here, the degeneracy of the angular momentum m is lifted, and the single resonance, which was present for zero magnetic field $B = 0$ mT at the corresponding energy for the quantum number n , splits into $n + 1$ angular states. In Fig. 3.12(b), we illustrate the splitting of the resonance of the quantum number $n = 4$ into 5 individual peaks. Each peak in the transmission probability T_{QD} corresponds to a different angular momentum state m . For the applied magnetic field $B = 0.03$ mT, the energy splitting between two angular momentum states is given by $\hbar\omega_c = 0.052$ meV. Since the

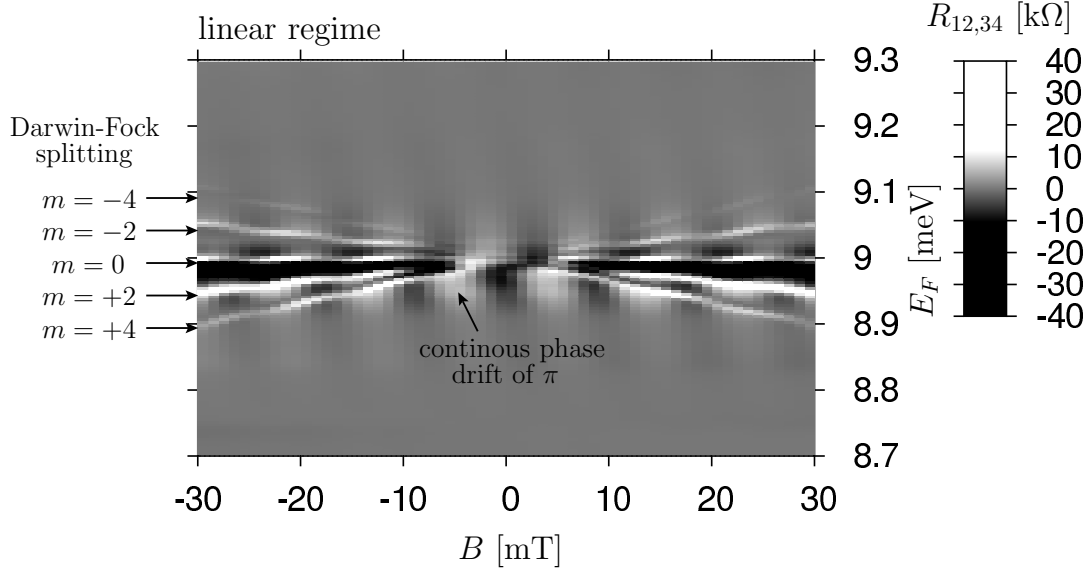


Figure 3.13: AB interferometer configured as phase transmission phase detector. Gray-scale plot of the oscillatory component of the resistance $R_{12,34}$ as a function of the magnetic field and the Fermi energy. AB oscillations only emerge when the Fermi energy E_F hits a resonance of the embedded quantum dot. The range of Fermi energies of the quantum state $n = 4$ of the harmonic quantum dot is depicted. The Darwin-Fock spectrum induces a splitting of the angular momentum states with an increasing magnetic field and induces *cat's whisker* like interference fringes. For small magnetic fields $|B| \leq 5$ mT, the resonances of the angular momentum states overlap, and form a single resonance at which the phase shows the expected continuous phase drift of π of the AB oscillations while scanning the Fermi energy through the resonance.

Darwin-Fock eigenstates have the same parity, see eq. (3.16), the transmission probability T_{QD} drops to zero between each resonance of the angular momentum states m . The continuous phase drift of π at each resonance is interrupted by an abrupt π phase-jump. Similar π -phase jumps between resonant states exhibiting the same parity are theoretically predicted in Ref. [131].

While the transmission amplitude is, in principle, already experimentally detectable by conductance measurements, the transmission phase is more complicated to attain. This is the idea behind embedding the quantum dot in a AB ring [126, 127] where the phase information is encoded in the interference fringes of the AB oscillations. We place the quantum dot in arm s_2 and run a simulation for the potential landscape depicted in Fig. 3.11(b). We evaluate

the non-local resistance $R_{21,34}$ within the linear regime, eq. (3.8). Current flows between leads 1 and 2, and leads 3 and 4 are configured as voltage probes. The oscillatory component of the non-local resistance as function of the magnetic field and the Fermi energy E_F is depicted in Fig. 3.13. Only when the Fermi energy hits the resonance of the embedded quantum dot does transport take place through both arms of the ring, resulting in AB oscillations in the non-local resistance $R_{21,34}$. Otherwise, the quantum dot blocks the transport through the lower arm s_2 . The only transfer path is then given by the upper arm s_1 and no AB interference emerges. In Fig. 3.13, we plot the oscillatory component of $R_{12,34}(B)$ as a function of the magnetic field and the Fermi energy. We consider a energy range between 8.9 meV and 9.1 meV which contains the resonance $n = 4$ of the harmonic quantum dot (see Fig. 3.12). The splitting of the angular momentum states m , with and increasing magnetic field B , is nicely visible in the oscillatory component of $R_{12,34}(B)$ as a function of the Fermi energy. In the AB interference fringes there emerge five lines reflecting the angular momentum states. The zeros in the transmission amplitude and the accompanied phase jumps of π create the unique *cat's whisker* like pattern in the non-local resistance $R_{12,34}$. For small magnetic fields $|B| \approx 5$ mT, the resonances of the angular momentum overlap with each other to form a single broad resonance that shows a continuous phase drift of π .

3.4 Summary

We investigated ballistic transport through four-terminal waveguide AB interferometers. The transport characteristics of such devices is based on quantum interference and might serve in future applications as low-power consuming switches. Furthermore, AB interferometers are used to detect the transmission phase of embedded quantum dots. All the applications require a continuous phase drift of the AB oscillations while scanning through the Fermi energy.

Recent four-terminal AB measurements for quantum rings show a continuous phase drift for the non-local arrangement of current and voltage probes. But, at certain energies, the continuous phase evolution is interrupted by abrupt π phase-jumps. Since the empty interferometer (without an embedded quantum dot) already shows complicated effects for the phase of the AB oscillations that are similar to the expected features of an embedded quantum dot, a detailed characterization of the experimental setup becomes necessary. Such characterization is provided by our accurate numerical simulations. We show that the π phase-jumps result from non-trivial scattering events at the geometry of the interferometer. In particular, multiple reflections between the junctions that connect the quantum waveguide ring to the asymptotic leads induce resonances in the arms of the ring. Those resonances cause a sensitive dependency of the

electron injection at the junctions on the Fermi energy. At certain Fermi energies, the resonances lead to drastic changes in the transmission properties of the junction and π phase-jumps emerge.

After the detailed characterization of the four-terminal AB-interferometer, we configure the four terminal quantum ring as a transmission phase detector. We embed a harmonic quantum via a tunneling junction in the lower arm of the ring. We carefully adjust the non-local setup to a suitable region of Fermi energies where the AB oscillations of the empty interferometer undergo a continuous phase drift. This ensures that the detected interference fringes in the AB oscillations are solely attributed to the influence of the transmission through the embedded quantum dot. We demonstrate that the transmission phase of the quantum dot is detectable in the interference pattern of the AB oscillations of the interferometer. We show that the Darwin-Fock spectrum of the harmonic quantum dot emerges as *cat's whisker* like interference fringes.

Summary and outlook

In this work, we provide new aspects on transport through complex networks. Here, we start with a brief summary of the first part of this thesis on photosynthesis, and point out possible future projects related to this topic. Recent experiments on 2d spectroscopy show evidence of long-lived electronic coherence in LHCs. The transfer process manifests itself in the dynamics of the diagonal- and cross-peak signals of the 2d spectra. In particular, a coherent dynamics shows unique oscillations in the cross-peaks. For the FMO complex, experiments reveal coherent oscillations lasting up to 0.3 ps at a temperature of 300 K, and even up to 1.2 ps at 150 K [20]. We address the challenging problem of reconciling three seemingly contradictory features within one consistent theoretical framework: (i) long-lasting electronic coherence, (ii) fast energy relaxation, and (iii) broad line-shapes in the optical spectra.

In Ref. [43], Ishizaki and Fleming propose that the finite time-scale of the relaxation of the protein vibrations prolongs coherence in the FMO complex. The inclusion of the finite phonon relaxation results in beatings in the site-basis population dynamics. Ishizaki and Fleming interpret these beatings as a signature for long-lasting electronic coherence. As we point out in this thesis, this interpretation is incorrect. In fact, the site-basis population-beatings do reflect reversible energy trade with the phonon bath rather than electronic coherence. In the experimentally accessible 2d-spectra the reversible energy trade is distinguishable from electronic coherence. While long-lived electronic coherence prolongs beatings in *cross peaks*, the reversible energy trade manifests itself as beatings in the *diagonal peaks*.

The Drude-Lorentz spectral density, which provides an insufficient approximation to the experimentally obtained spectral density for the FMO complex [48], is employed in Ref. [43]. The Drude-Lorentz spectral density does not adequately capture the coupling to the low-frequency modes. Precisely, it shows an Ohmic behavior for low frequencies, whereas the measured spectral density is initially super-Ohmic. Indeed, we demonstrate that the super-Ohmic character results in a prolonged coherent dynamics, while the strong coupling to higher frequency modes ensures a fast energy relaxation. We reproduce the experimentally observed broad peak-shapes in the 2d-spectra by the inclusion of static disorder. We find reasonable agreement of the numerical 2d-spectra with the experimen-

tal ones for static disorder of 94 cm^{-1} . Similar disorder values are estimated in Ref. [203]. In conclusion, our mechanism reproduces major features of the measured 2d spectra of the FMO complex including the long-lasting electronic coherence, the fast thermalization, and the peak-shapes in the spectra.

The physical mechanism causing the prolonged electronic coherence is based on the super-Ohmic nature of the spectral density. As we demonstrate the strongly coupled vibrational modes have only a minor influence. Our findings show that the explicit shape of the spectral density does not significantly affect the coherence life-times, provided that its initially super-Ohmic character is maintained. Thus, the mechanism might explain the obtained long-lived coherence of a wide class of LHCs. At this point measurements of the spectral density for other LHCs than the FMO complex might help to gain further insight into the question of whether or not the super-Ohmic property is a generic one of LHCs. We reproduce coherence life-times up to 0.3 ps at a temperature of 300 K. For the lower temperature of 150 K we predict electronic coherence up to 0.6 ps, which is two times shorter than in the experiment. Fidler *et al* in Ref. [237] provide simple estimates which suggest that spatially correlated vibration between different BChls results in a broadening of peak-shapes in the spectra, whereas coherence life-times increase. Hence, we expect that an even better agreement between our simulations and the experiments could be achieved by including spatial correlations in the vibrations. This could possibly give further strong evidence that the experiments indeed monitor long-lived *electronic* coherences, which would settle an outstanding question in the field.

Concerning the efficiency of the transport from the antenna to the reaction center, we show that noise-assisted transport [52, 55] embraces three mechanisms: (i) dephasing, which connects otherwise block-diagonal energy-subspaces, and allows for indirect transfer channels via energy exchange with the vibrational environment [52, 55], (ii) energy relaxation toward the energetically low-lying BChls, and (iii) bath-induced rearrangement of the distribution of coherence among the BChls to assist a directed coherent energy flow. We investigate the optimal transport condition with respect to changes in the electronic structure of the FMO complex, and demonstrate that high transfer efficiency is a consequence of an optimized balance between resonantly-coherent and environmentally-assisted energy transfer. Our analysis of environmentally-assisted transport is carried out for the Drude-Lorentz spectral density. However, we find that a realistic super-Ohmic spectral density shows an up to 10% faster transfer to the reaction center. Whether the faster transfer is due to the prolonged electronic coherence for the super-Ohmic spectral density remains an interesting question for a future analysis. This might yield promising insights into the role of long-lived electronic coherence for fast energy transfer in the FMO complex.

For the transport regime in LCHs, the energy scales of all parameters, such as the inter-site coupling, the exciton energies, and the coupling strengths to

the vibrations, are of the same order. Hence, there are no small parameters involved, and theoretical descriptions need to go beyond perturbation theory. In this thesis, the numerical simulations are carried out with the non-perturbative and non-Markovian hierarchical equations of motion (HEOM) technique [77]. Since simulations within HEOM are numerically expensive, we devised GPU-HEOM, which results in a 448-fold reduction in computation time compared to an analogous CPU implementation. Further, we extend the original version of HEOM, which is limited to a Drude-Lorentz spectral density, to more general spectral densities. We use the Meier-Tannor decomposition [82], and expand structured spectral densities in terms of a sum over shifted Drude-Lorentz peaks. Our GPU-HEOM provides an efficient infrastructure, and creates the technical basis for revealing the physical mechanisms of energy transfer in LHCs discussed and developed in this thesis.

Now we move on to the second part of this work, which is devoted to ballistic transport through semiconductor heterostructures. As a reminder, we recall some of the main concepts and techniques before giving an outlook on work in progress and interesting problems to address in the future. Electron transport in the ballistic regime is dominated by coherent scattering. According to the Landauer-Büttiker formalism the measured currents and voltages are given in terms of transmission amplitudes. Here we establish a time-dependent approach that allows one to compute the transmission amplitudes by wave-packet propagation. Employing GPU hardware we develop an efficient algorithm that speeds up the CPU implementation by a factor of 35. Propagation of a wave-packet pulse yields an intuitive picture of the intrinsic scattering processes. Under certain conditions the time evolution of the wave-packet is associated with the thermally averaged behavior of electrons moving through the device. The main advantage of the wave-packet approach is that the transmission amplitudes are computed for a large energy range withing a single wave-packet propagation. This makes it numerically very efficient. Moreover, with the wave-packet approach it is easy to include complicated device geometries.

In Part II, Chapter 3 we discuss electron transfer through four-terminal AB interferometers. The idea of those devices is to use the interference pattern to measure the transmission phase of an embedded quantum system [125]. At first, we characterize the empty interferometer, and relate the experimentally obtained π jumps in the phase of the AB oscillations at certain Fermi energy energies to complicated scattering at the device geometry. These phase jumps are intrinsic features of the interferometers. Thus, to configure the AB ring-structure as meter for the transmission phase requires a careful adjustment of the device. In the next step we embed a harmonic quantum dot in one of the arms in the resonant tunneling regime. The Darwin-Fock spectrum visible in the interference pattern has the form of *cat's whisker*.

The Darwin-Fock spectrum leads to an energy splitting of the angular momen-

tum states of the harmonic quantum dot, which becomes larger as the magnetic field increases. As a result one obtains a sequence of energy states of the same parity. Consequently the transmission phase, as a function of the Fermi energy, shows a continuous phase drift of π which is followed by abrupt π phase-lapses. For large occupation numbers of the quantum dot, the features in the transmission phase resemble the universal phase behavior reported in Refs. [126, 127]. Motivated by the observations for the Darwin-Fock states we put forward the idea that an energy splitting of the main quantum number into angular momentum states might lead to the observed universal phase behavior. In the Darwin-Fock spectrum this splitting is induced by the external magnetic field. The lifting of the degeneracy of the angular momentum states can alternatively be achieved by using different confinements of the quantum dot. For example, a stronger cosh-confinement, which comes closer to the experimental situation than the harmonic one, shows such an energy splitting. This is work in progress, and might lead to a better understanding of the observed universal phase behavior in Refs. [126, 127].

The advantages of the time-dependent approach might be exploited in future projects as well. One example is the investigation of transport measurements for four-terminal asymmetric cross-junctions. Recent experiments [104] measure a current-polarity-dependent Hall voltage, and obtain a break-down of the Onsager symmetry in the non-linear transport regime. The measured transport characteristics have not yet been confirmed by theoretical simulations. Numerical challenges arise due to the complicated geometry such as different confinements in the leads. Moreover, simulations of non-linear transport measurements require transmission amplitudes for a wide range of energies and for a large number of open lead modes. The wave-packet approach provides a very efficient algorithm for the problem at hand. Such studies might help to solve the open problem of whether the break-down of the Onsager symmetry is already incorporated in the non-linear evaluation of the Landauer-Büttiker formalism or if rather electron-electron interaction and non-trivial charging effects play a crucial role in the non-linear transport of asymmetric junctions.

Appendix

A Energy transfer in light-harvesting complexes

A.1 Microscopic picture of the Frenkel exciton Hamiltonian

We derive the Frenkel Hamiltonian by describing the exciton system in light-harvesting complexes (LHCs) from a microscopic picture. We highlight the underlying assumptions and simplifications that finally yield the effective Hamiltonian Part I chapter 2, eq. (2.1). The concepts presented in this section follow chapters two and eight of May and Kühn [32].

A.1.1 The Born-Oppenheimer approximation

The molecular Hamiltonian, which takes all degrees of freedom of the nuclei and the electrons of the protein into account, is given by

$$\mathcal{H}_{\text{mol}} = \mathcal{T}_{\text{el}} + \mathcal{V}_{\text{el-el}} + \mathcal{T}_{\text{nuc}} + \mathcal{V}_{\text{nuc-nuc}} + \mathcal{V}_{\text{el-nuc}}. \quad (\text{A.1})$$

\mathcal{T}_{el} and \mathcal{T}_{nuc} denote the kinetic energy of the electrons and the nuclei. $\mathcal{V}_{\text{el-el}}$ and $\mathcal{V}_{\text{nuc-nuc}}$ describe electron-electron and inter-nuclei interactions. The Coulomb interaction between the electrons and the nuclei $\mathcal{V}_{\text{el-nuc}}$ gives rise to an entangled motion of electrons and nuclei. Hence, the corresponding eigenfunctions $\psi_{\lambda}(\mathbf{r}, \mathbf{R})$ with

$$\mathcal{H}_{\text{mol}}\psi_{\lambda}(\mathbf{r}, \mathbf{R}) = \mathcal{E}_{\lambda}\psi_{\lambda}(\mathbf{r}, \mathbf{R}) \quad (\text{A.2})$$

do not factorize into electronic and nuclear components. We introduce $\mathbf{r} = (r_x^1, r_y^1, r_z^1, \dots, r_x^{N_e}, r_y^{N_e}, r_z^{N_e})$ for the coordinates of the N_e electrons, and $\mathbf{R} = (R_x^1, R_y^1, R_z^1, \dots, R_x^{N_n}, R_y^{N_n}, R_z^{N_n})$ for the coordinates of the N_n nuclei. The electron mass is much smaller than the mass of the nuclei, and the electron dynamics is fast when compared to the motions of the atoms. We assume that the electrons instantaneously follow the nuclei motion, and that the electron configuration is in the stationary state of the arrangement of the nuclei at any time. In this

regime, the nuclei coordinates enter the equation of motion for the electrons as parameters, and we obtain for the Hamiltonian of the electrons,

$$\mathcal{H}_{\text{el}}(\mathbf{R}) = \mathcal{T}_{\text{el}} + \mathcal{V}_{\text{el-el}} + \mathcal{V}_{\text{el-nuc}}(\mathbf{R}). \quad (\text{A.3})$$

The electronic eigenstates are given by

$$\mathcal{H}_{\text{el}}(\mathbf{R})\phi_{\alpha}(\mathbf{r}, \mathbf{R}) = E_{\alpha}(\mathbf{R})\phi_{\alpha}(\mathbf{r}, \mathbf{R}). \quad (\text{A.4})$$

The electronic states can be used as a basis for the wave functions of the total system

$$\psi(\mathbf{r}, \mathbf{R}) = \sum_{\alpha} \chi_{\alpha}(\mathbf{R})\phi_{\alpha}(\mathbf{r}, \mathbf{R}). \quad (\text{A.5})$$

Here, χ_{α} characterizes the arrangement of the nuclei if the electronic configuration is in state ϕ_{α} . Inserting this ansatz in the molecular Schrödinger equation (A.2), we find

$$\begin{aligned} \mathcal{H}_{\text{mol}}\psi(\mathbf{r}, \mathbf{R}) &= \sum_{\alpha} (E_{\alpha}(\mathbf{R}) + \mathcal{V}_{\text{nuc-nuc}}) \chi_{\alpha}(\mathbf{R})\phi_{\alpha}(\mathbf{r}, \mathbf{R}) + \sum_{\alpha} \mathcal{T}_{\text{nuc}}\chi_{\alpha}(\mathbf{R})\phi_{\alpha}(\mathbf{r}, \mathbf{R}) \\ &= \mathcal{E} \sum_{\alpha} \chi_{\alpha}(\mathbf{R})\phi_{\alpha}(\mathbf{r}, \mathbf{R}). \end{aligned} \quad (\text{A.6})$$

Multiplying eq. (A.6) with ϕ_{β}^{*} from the left and integrating over the electron degrees of freedom yields

$$(\mathcal{T}_{\text{nuc}} + E_{\alpha}(\mathbf{R}) + \mathcal{V}_{\text{nuc-nuc}} + \theta_{\alpha\alpha}(\mathbf{R}) - \mathcal{E})\chi_{\alpha}(\mathbf{R}) = - \sum_{\beta \neq \alpha} \theta_{\alpha\beta}(\mathbf{R})\chi_{\beta}(\mathbf{R}), \quad (\text{A.7})$$

which determines the state of the nuclei. Here, we define

$$\theta_{\alpha\beta}(\mathbf{R}) = \int d\mathbf{r} \phi_{\alpha}^{*}(\mathbf{r}, \mathbf{R}) \mathcal{T}_{\text{nuc}} \phi_{\beta}(\mathbf{r}, \mathbf{R}) + \sum_n \frac{1}{M_n} \left[\int d\mathbf{r} \phi_{\alpha}^{*}(\mathbf{r}, \mathbf{R}) \hat{P}_n \phi_{\beta}(\mathbf{r}, \mathbf{R}) \right] \hat{P}_n, \quad (\text{A.8})$$

where \hat{P}_n is the momentum operator of the n th atom with mass M_n . The right hand-side of eq. (A.7) stands for a nonadiabatic electron-nuclei coupling that induces transitions between different electronic states. In the following, we employ the adiabatic Born-Oppenheimer approximation in which such transitions are neglected and the electrons remain in the same quantum state. The wave function that describes electrons and nuclei is then expressed by

$$\psi_{\lambda,\alpha} = \chi_{\lambda,\alpha}(\mathbf{R})\phi_{\alpha}(\mathbf{r}, \mathbf{R}), \quad (\text{A.9})$$

with quantum number α for the electronic state, and quantum number λ for the nuclei configuration. The latter is obtained from

$$(\mathcal{T}_{\text{nuc}} + E_{\alpha}(\mathbf{R}) + \mathcal{V}_{\text{nuc-nuc}} + \theta_{\alpha\alpha}(\mathbf{R})) \chi_{\lambda,\alpha}(\mathbf{R}) = \mathcal{E}_{\lambda,\alpha} \chi_{\lambda,\alpha}(\mathbf{R}), \quad (\text{A.10})$$

which is deduced from eq. (A.7) by neglecting the nonadiabatic terms. The electronic energy, the nuclei-nuclei interaction, and $\theta_{\alpha\alpha}$ can be regarded as an effective potential

$$U_{\alpha}(\mathbf{R}) = E_{\alpha}(\mathbf{R}) + \theta_{\alpha\alpha}(\mathbf{R}) + \mathcal{V}_{\text{nuc-nuc}} \quad (\text{A.11})$$

which forms the potential energy surface (PES) of the nuclei motion.

A.1.2 Exciton model for coupled BChls

In the previous section, we started from a molecular Hamiltonian and derived separate equations for the electronic and nuclei motion within the adiabatic Born-Oppenheimer approximation. Here, we will discuss the electronic components, and in particular, introduce further approximations that finally result in the exciton Hamiltonian stated in Part I chapter 2, eq. (2.2). For further reading, we refer the reader to Ref. [163] chapter 2.

LHCs contain light-active BChls, the electronic configuration of which can be excited by the absorption of photons. Due to the Coulomb interaction, the electronic configurations between different BChls are coupled. The inter-Bchl coupling induces energy transfer, but no electron exchange. The latter is a consequence of the spatial separation of the BChls. The Hamiltonian for the electronic structure is then given by

$$\mathcal{H}_{\text{el}} = \sum_i \mathcal{H}_{\text{el}}^i + \sum_{i < j} V_{ij} \quad (\text{A.12})$$

where the sum goes over all BChls, and

$$V_{ij} = \frac{1}{4\pi\epsilon} \int d^3r \int d^3r' \frac{\rho_i(\vec{r})\rho_j(\vec{r}')}{|\vec{r} - \vec{r}'|} \quad (\text{A.13})$$

corresponds to the Coulomb interaction between charge densities $\rho_i(\mathbf{r})$ and $\rho_j(\mathbf{r})$ at different BChls. Note that the charge density at a certain Bchl implicitly depends on the arrangement of the nuclei of the protein. Since the distance between the BChls is large, we assume that the charge distribution is centered around the position \mathbf{r}_i of the i th Bchl. In this case, the Coulomb interaction can be approximated by dipole-dipole interaction, and eq. (A.13) reduces to

$$V_{ij} \approx \frac{1}{4\pi\epsilon} \left(\frac{\vec{\mu}_i \vec{\mu}_j}{r_{ij}^3} - \frac{3(\vec{\mu}_i \vec{r}_{ij})(\vec{\mu}_j \vec{r}_{ij})}{r_{ij}^5} \right), \quad (\text{A.14})$$

where we additionally assume that the BChls are uncharged. Here, $r_{ij} = |\vec{r}_j - \vec{r}_i|$ is the distance between two BChls, and the dipole moments are evaluated by

$$\vec{\mu}_i = \int d^3r \rho_i(\vec{r})(\vec{r} - \vec{r}_i). \quad (\text{A.15})$$

In the following, we introduce a suitable basis for the electronic structure of the coupled BChls. Since the BChls are spatially separated, there is a strong interaction with the protein environment in the vicinity of the individual BChls, whereas the inter-BChl coupling V_{ij} is weak and can be seen as a perturbation. As a consequence, the electronic configuration at a certain BChl is only weakly affected by neighboring BChls, and the electronic states of the isolated BChls

$$\mathcal{H}_{\text{el}}^i \phi_i^e = \varepsilon_i^e \phi_i^e, \quad \mathcal{H}_{\text{el}}^i \phi_i^g = \varepsilon_i^g \phi_i^g \quad (\text{A.16})$$

can be used to define a basis for the electronic configuration of the coupled system. $\mathcal{H}_{\text{el}}^i$ stands for the electronic Hamiltonian of the individual BChls, and ϕ_i^g (ϕ_i^e) denotes the electronic ground (excited) state of the isolated i th BChl with energy ε_i^g (ε_i^e). For energy transfer dynamics in LHCs, electronic excitations are created from the highest occupied molecular orbital (HOMO) to the lowest unoccupied molecular orbital (LUMO), and each BChl can be modeled by a two-level system. We expand the Hamiltonian eq. (A.12) of the coupled system in terms of basis functions that are built from eigenstates of the isolated BChls, eq. (A.16). Because of the weak inter-BChl coupling, we assume that the electronic wave function of the coupled BChls factorizes in components that describe the state of the individual BChls

$$\psi = \prod_i \phi_i^a \quad (\text{A.17})$$

where $a \in \{e, g\}$. We further assume that there is at most one excitation within the coupled BChls. In this case, the basis functions are given by

$$|i\rangle = \phi_1^g \dots \phi_i^e \dots \phi_N^g, \quad (\text{A.18})$$

which describes the state in which the electronic configuration at BChl i is excited, while all other BChls remain in the electronic ground state. We further introduce the ground state $|0\rangle = \prod_i \phi_i^g$ of the coupled system. The physical interpretation of this choice of basis functions is that the electronic states at the BChls are only weakly affected by the Coulomb coupling. Thus, eigenfunctions of isolated BChls, to some extent, still provide a good description of the electronic structure of the coupled BChls. We expand the Hamiltonian of the electronic structure of the coupled BChls into the basis functions $|i\rangle$

$$\mathcal{H}_{\text{el}} = \sum_{m,i,j} \langle i | \mathcal{H}_{\text{el}}^m | j \rangle |i\rangle \langle j| + \sum_{m>n,i,j} \langle i | V_{mn} | j \rangle |i\rangle \langle j|, \quad (\text{A.19})$$

with dipole-dipole matrix elements

$$\langle i | \frac{1}{4\pi\varepsilon} \left(\frac{\vec{\mu}_m \vec{\mu}_n}{r_{mn}^3} - \frac{3(\vec{\mu}_m \vec{r}_{mn})(\vec{\mu}_n \vec{r}_{mn})}{r_{mn}^5} \right) | j \rangle = J_{mn} \delta_{im} \delta_{jn}. \quad (\text{A.20})$$

The dipole-dipole couplings J_{mn} describe transitions from an electronic excitation at BChl m to an electronic excitation at BChl n . This mechanism allows a delocalized energy transfer among the coupled BChls. There is no exchange of electrons between the BChls, and the coupling between the BChls induces pure energy transfer. We assume real-valued dipole couplings and hence $J_{mn} = J_{nm}$ is symmetric. Equation (A.19) then reduces to the Frenkel exciton model Part I chapter 2, eq. (2.2)

$$\mathcal{H}_{\text{ex}} = \sum_m \varepsilon_m^e |m\rangle\langle m| + \sum_{m>n} J_{mn} (|m\rangle\langle n| + |n\rangle\langle m|). \quad (\text{A.21})$$

A.1.3 Coupling to the vibrational environment

So far, we have discussed the electronic structure of LHCs. Now, we focus on the dynamics of the nuclei, basically given as vibrations around the equilibrium positions of the nuclei. In the following, we derive the coupling term between the electronic degrees of freedom and vibrational coordinates. We follow the concepts of Ref. [32].

The molecular vibrations can be divided into intra-BChl, in which only the atoms of a certain BChl are in motion, and inter-BChl components. The latter are correlated vibrations between all atoms of the protein. Since the BChls are well separated and weakly coupled to each other, the intra-BChl vibrations are the dominant part. Nevertheless, the BChls are embedded in a protein mask, which can induce collective vibrations involving all BChls. This effect can be included by introducing spatial correlations between intra-BChl vibrations. The vibrations of the nuclear coordinates also lead to fluctuations in the charge distribution of the protein. Hence the dipole-dipole couplings J_{mn} fluctuate as well. For simplicity, we do not take this effect into account, and assume that changes in J_{mn} are small and, hence, negligible.

To characterize the intra-BChl vibrations, we consider the molecular Hamiltonian of a single BChl. This has the structure given in eq. (A.1). Within the adiabatic Born-Oppenheimer approximation, the dynamics of the nuclei are determined by the potential energy surface, eq. (A.10), which depends on the electronic configuration of the BChl. We approximate the PES of the electronic ground as well as the PES of the electronic excited state with a harmonic potential around the equilibrium position of the nuclear coordinates. The nuclei motion is then expressed in terms of vibrational normal modes. The potential energy surfaces for a specific vibrational normal mode q_ξ are illustrated in Fig. A.1. We assume that both, the ground state and the excited-state PESs are represented by the same coordinate q_ξ . In general, this assumption is not valid, since the geometry of the protein might be strongly influenced by changing the electronic configurations. However, in the case of LHCs, the PES does not change drastically, and the excited-state PES is still described by the normal

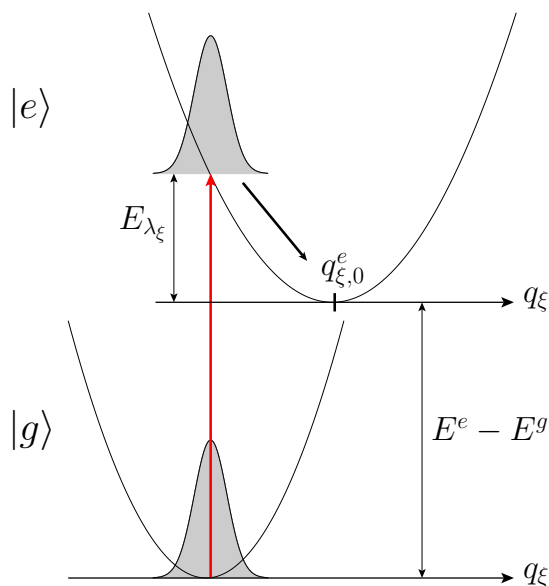


Figure A.1: Schematic sketch of the vertical Franck-Condon transition between the electronic ground-state PES of the vibrational coordinate q_ξ and the excited-state PES. After electronic excitation, the nuclei of the protein are tuned out of equilibrium, and the vibrational coordinates q_ξ are excited with the energy E_{λ_ξ} . Since the molecule couples with a thermal environment, the vibrations relax to the new equilibrium position $q_{\xi,0}^e$. During this reorganization process the reorganization energy E_{λ_ξ} is dissipated [32].

mode q_ξ [32]. However, the equilibrium position is shifted and the frequency of the vibrations may also change. Commonly, electronic excitations reduce the chemical bonding, and the excited-state PES is shifted to the right [32].

The timescale for creating an electronic excitation is much faster than the nuclei dynamics. The atoms remain in the same state during the excitation process. We describe excitations with a vertical Franck-Condon transition between the potential energy surfaces of the ground and the excited state. In Fig. A.1, this process is marked by the vertical arrow. Since the two PESs are shifted, electronic excitations tune the normal modes of the nuclei motion out of equilibrium and the BChls start to vibrate. To create electronic excitations, not only is the electronic excitation energy $E^e - E^g$ required but the nuclei also gain the reorganization energy E_{λ_ξ} . The protein is embedded in a thermal environment. Thus, energy is dissipated and the arrangement of the molecules approaches thermal equilibrium around the new equilibrium position $q_{\xi,0}^e$ of the excited-state PES. This is called reorganization process [32].

In the following, we demonstrate that a shift in the equilibrium position between the ground and excited-state PES results in a coupling between the exciton system and the molecular vibrations. The Hamiltonian for the vibrations in the electronic ground state is given by

$$\mathcal{H}_{\text{phon}} = \sum_{\xi} \left(\frac{p_{\xi}^2}{2m_{\xi}} + \frac{1}{2} m_{\xi} \omega_{\xi}^2 q_{\xi}^2 \right) = \sum_{\xi} \hbar \omega_{\xi} (b_{\xi}^{\dagger} b_{\xi} + \frac{1}{2}), \quad (\text{A.22})$$

where b_{ξ}^{\dagger} creates a phonon with energy $\hbar \omega_{\xi}$ for the normal mode q_{ξ} . In the following, we assume that the frequency of the vibrations remains the same for the excited-state PES, but that equilibrium configuration is shifted by $q_{0,\xi}$,

$$\begin{aligned} \mathcal{H}_{\text{phon}}^{\text{excited}} &= \sum_{\xi} \left(\frac{p_{\xi}^2}{2m_{\xi}} + \frac{1}{2} m_{\xi} \omega_{\xi}^2 (q_{\xi} - q_{0,\xi})^2 \right) \\ &= \sum_{\xi} \left(\frac{p_{\xi}^2}{2m_{\xi}} + \frac{1}{2} m_{\xi} \omega_{\xi}^2 q_{\xi}^2 + \frac{1}{2} m_{\xi} \omega_{\xi}^2 q_{0,\xi}^2 - m_{\xi} \omega_{\xi}^2 q_{0,\xi} q_{\xi} \right) \\ &= \mathcal{H}_{\text{phon}} + \sum_{\xi} \left(\frac{1}{2} m_{\xi} \omega_{\xi}^2 q_{0,\xi}^2 - m_{\xi} \omega_{\xi}^2 q_{0,\xi} q_{\xi} \right). \end{aligned} \quad (\text{A.23})$$

We use $q_{\xi} = \sqrt{\frac{\hbar}{2m_{\xi}\omega_{\xi}}} (b_{\xi}^{\dagger} + b_{\xi})$ and introduce the scaled displacements $d_{\xi} = -\sqrt{\frac{m_{\xi}\omega_{\xi}}{2\hbar}} q_{0,\xi}$. The vibrational part of the Hamiltonian for the excited state is then given by

$$\mathcal{H}_{\text{phon}}^{\text{excited}} = \mathcal{H}_{\text{phon}} + \sum_{\xi} \hbar \omega_{\xi} d_{\xi}^2 + \sum_{\xi} \hbar \omega_{\xi} d_{\xi} (b_{\xi}^{\dagger} + b_{\xi}). \quad (\text{A.24})$$

The last two terms are only present if there is an electronic excitation at the BChl. Hence, the electronic state $|\phi^e\rangle$ couples with the vibrations that are expressed by

$$\mathcal{H}_{\text{ex-phon}} = \sum_{\xi} \hbar \omega_{\xi} d_{\xi}^2 |\phi^e\rangle \langle \phi^e| + \sum_{\xi} \hbar \omega_{\xi} d_{\xi} (b_{\xi}^{\dagger} + b_{\xi}) |\phi^e\rangle \langle \phi^e|. \quad (\text{A.25})$$

The first term of the coupling describes the reorganization energy that is dissipated in the vibrations while the vibrational coordinates rearrange to the new equilibrium configuration. Generalization to a system of N electronically coupled BChls results in the exciton-phonon coupling term Part I, chapter 2, eqs. (2.4) and (2.5),

$$\mathcal{H}_{\text{ex-phon}} = \sum_{m=1}^N \sum_{\xi} \hbar \omega_{\xi,m} d_{\xi,m} (b_{\xi,m}^{\dagger} + b_{\xi,m}) |m\rangle \langle m|. \quad (\text{A.26})$$

The index m denotes vibrations at the m th BChl, and the reorganization energy is given by Part I, chapter 2, eq (2.3),

$$\mathcal{H}_{\text{reorg}} = \sum_{m=1}^N \sum_{\xi} \hbar \omega_{\xi,m} d_{\xi,m}^2 |m\rangle \langle m| = \sum_{m=1}^N \lambda_m |m\rangle \langle m|. \quad (\text{A.27})$$

Inter-BChl vibrations, which are delocalized over the BChls, induce correlations between the vibrations at different BChls. For the microscopic derivation of the exciton phonon interaction eq. (A.26), we only take into account shifts in the equilibrium position. We neglect changes in the frequencies of the vibrations that would lead to a quadratic coupling of the excitons with the intra-BChl vibrational modes. We further assume harmonic potential energy surfaces. Anharmonic effects in the molecular vibrations are neglected.

A.2 Masterequation approach

In this section we introduce the Masterequation approach [32, 3, 4], which assumes a weak coupling between the system and a dissipative environment. Furthermore, temporal correlations in the bath are neglected, and the Markov approximation is employed. The time-nonlocal integro-differential equation for the time evolution of the reduced density operator then condensates to simple rate equations, the Redfield equations. In section A.2.1, we derive the full Redfield equations that are obtained without any further approximations.

Often, the secular approximation is applied that neglects fast-fluctuating terms and brings the rate equations into a Lindblad form [32, 3]. The corresponding derivation is given in section A.2.2. Within the secular approximation, we also state a time-convolutionless (TCL) version of the Masterequation [238] that includes non-Markovian effects up to second-order perturbation theory.

A.2.1 Full Redfield equations

The time evolution of the total density operator in the interaction picture $\tilde{R}(t)$ is given by the Liouville equation

$$\frac{d}{dt}\tilde{R}(t) = -\frac{i}{\hbar}[\tilde{\mathcal{H}}_{\text{ex-phon}}(t), \tilde{R}(t)] = -\frac{i}{\hbar}\tilde{\mathcal{L}}(t)\tilde{R}(t) \quad (\text{A.28})$$

We expand the Liouville equation up to second-order in the exciton-phonon coupling term

$$\frac{d}{dt}\tilde{R}(t) = -\frac{i}{\hbar}[\tilde{\mathcal{H}}_{\text{ex-phon}}, \tilde{R}_0] - \frac{1}{\hbar^2} \int_0^t dt' [\tilde{\mathcal{H}}_{\text{ex-phon}}(t), [\tilde{\mathcal{H}}_{\text{ex-phon}}(t'), \tilde{R}(t')]]. \quad (\text{A.29})$$

Tracing out the bath degrees of freedom, and assuming that excitonic and vibrational degrees of freedom initially factorize $R(t_0) = \rho(t_0) \otimes \rho_{\text{phon}}$ results in a time-nonlocal integro-differential equation

$$\frac{d}{dt}\tilde{\rho}(t) = -\frac{1}{\hbar^2} \int_0^t dt' \text{Tr} \left\{ [\tilde{\mathcal{H}}_{\text{ex-phon}}(t), [\tilde{\mathcal{H}}_{\text{ex-phon}}(t'), \tilde{\rho}(t') \otimes \rho_{\text{phon}}]] \right\} \quad (\text{A.30})$$

for the reduced density operator in the interaction picture $\tilde{\rho}(t)$. We assume that the timescale of the phonon relaxation is fast compared to the exciton dynamics. We apply the Markov approximation, replace $\rho(t')$ by $\rho(t)$, and set the upper limit of the integration to $t \rightarrow \infty$. By transforming back to the Schrödinger picture and substituting the integration variable $t' \rightarrow \tau + t$, we finally obtain the Born-Markov equation

$$\frac{d}{dt}\rho(t) = -\frac{i}{\hbar}\mathcal{L}_{\text{ex}}\rho(t) - \frac{1}{\hbar^2} \int_0^\infty d\tau \text{Tr} \left\{ [\mathcal{H}_{\text{ex-phon}}, [\tilde{\mathcal{H}}_{\text{ex-phon}}(-\tau), \rho(t) \otimes \rho_{\text{phon}}]] \right\}, \quad (\text{A.31})$$

a time-local equation of motion for the reduced density operator. Here, $-i/\hbar \mathcal{L}_{\text{ex}} \rho(t) = -i/\hbar [\mathcal{H}_{\text{ex}}, \rho(t)]$ corresponds to the coherent exciton dynamics, whereas the second term takes into account the influence of the dissipative environment.

For the explicit evaluation of the Masterequation, we have to evaluate the exciton-phonon coupling in the interaction picture

$$\tilde{\mathcal{H}}_{\text{ex-phon}}(-\tau) = \sum_m \tilde{V}_m(-\tau) \tilde{B}_m(-\tau). \quad (\text{A.32})$$

The operators V_m and B_m are defined according to Part I chapter 2 eqs. (2.4) and (2.5). We use the exciton eigenbasis $\{|E_M\rangle\}$ with $\mathcal{H}_{\text{ex}}|E_M\rangle = E_M|E_M\rangle$, and express localized electronic excitations at BChl m by

$$|m\rangle = \sum_M c_m^*(E_M) |E_M\rangle. \quad (\text{A.33})$$

This then yields

$$\tilde{V}_m(-\tau) = \sum_{N,M} \langle E_M | V_m | N \rangle e^{-i/\hbar (E_M - E_N)\tau} |E_M\rangle \langle E_N| \quad (\text{A.34})$$

for the system part of the exciton-phonon coupling with $\langle E_M | V_m | N \rangle = c_m^*(E_M) c_m(E_N)$. For the bath component we obtain

$$\tilde{B}_m(-\tau) = \sum_{\xi} \hbar \omega_{\xi,m} d_{\xi,m} (b_{\xi,m}^\dagger e^{-i\omega_{\xi,m}\tau} + b_{\xi,m} e^{i\omega_{\xi,m}\tau}), \quad (\text{A.35})$$

where we use $\tilde{b}_{\xi,m}(t) = e^{-i\omega_{\xi,m}t}$. In the following, we introduce bath correlation functions

$$C_m(\tau) = \langle \tilde{B}_m(\tau) \tilde{B}_m(0) \rangle. \quad (\text{A.36})$$

The brackets denote expectation values over the vibrational degrees of freedom. We neglect correlations between vibrations at different BChls $\langle \tilde{B}_m(\tau) \tilde{B}_{m'}(0) \rangle = 0$ for $m \neq m'$ and, furthermore, use the properties $\langle \tilde{B}_m(\tau) \tilde{B}_m(0) \rangle = \langle \tilde{B}_m(0) \tilde{B}_m(-\tau) \rangle$, $\langle \tilde{B}_m(\tau) \tilde{B}_m(0) \rangle = \langle \tilde{B}_m(0) \tilde{B}_m(\tau) \rangle^*$ and $\tilde{V}_m(-\tau)^\dagger = \tilde{V}_m(-\tau)$, which allow us to cast the Born-Markov equation (A.31) into a compact form [32, 174]

$$\frac{d}{dt} \rho(t) = -\frac{i}{\hbar} \mathcal{L}_{\text{ex}} \rho(t) - \sum_m V_m^\times [\Lambda_m \rho(t) - \rho(t) \Lambda_m^\dagger], \quad (\text{A.37})$$

with $V_m^\times \bullet = [V_m, \bullet]$ and operator

$$\Lambda_m = \frac{1}{\hbar^2} \int_0^\infty d\tau C_m(\tau) \tilde{V}_m(-\tau). \quad (\text{A.38})$$

We introduce the Redfield rates

$$\Gamma_m(\omega) = \int_0^\infty d\tau C_m(\tau) e^{i\omega\tau} \quad (\text{A.39})$$

and expand eq. (A.38) in the eigenbasis. The matrix elements of Λ_m are then expressed by

$$\langle E_M | \Lambda_m | E_N \rangle = \frac{1}{\hbar^2} \langle E_M | V_m | E_N \rangle \Gamma_m((E_N - E_M)/\hbar). \quad (\text{A.40})$$

Inserting eq. (A.40) into the Born-Markov equation (A.37) yields rate equations for the matrix elements of the reduced density operator. These rate equations are referred to as Redfield equations.

In the following, we evaluate the Redfield rates $\Gamma_m(\omega)$ explicitly. The rates are expressed in terms of bath correlation functions

$$C_m(\tau) = \sum_{\xi} \hbar^2 \omega_{\xi,m}^2 d_{\xi,m}^2 (e^{i\omega_{\xi,m}\tau} \langle b_{\xi,m}^\dagger b_{\xi,m} \rangle + e^{-i\omega_{\xi,m}\tau} \langle b_{\xi,m} b_{\xi,m}^\dagger \rangle). \quad (\text{A.41})$$

The vibrational degrees of freedom are characterized by its thermal state. Hence, the bath expectation values appearing in eq. (A.41) can be written in terms of the Bose-Einstein distribution $n(\omega) = (\exp(\beta\hbar\omega) - 1)^{-1}$. The phonon mode-dependent exciton-phonon interaction is taken into account by the frequency dependent spectral density $J(\omega)$

$$J_m(\omega) = \pi \sum_{\xi} \hbar^2 \omega_{\xi,m}^2 d_{\xi,m}^2 \delta(\omega - \omega_{\xi,m}). \quad (\text{A.42})$$

We obtain

$$C_m(\tau) = \frac{1}{\pi} \int_0^\infty d\omega J_m(\omega) (e^{i\omega\tau} n(\omega) + e^{-i\omega\tau} (n(\omega) + 1)). \quad (\text{A.43})$$

We extend the spectral density to negative frequencies and define $J(-\omega) = -J(\omega)$. Equation (A.43) can be then written as

$$C_m(\tau) = \frac{1}{\pi} \int_{-\infty}^\infty d\omega J_m(\omega) n(\omega) e^{i\omega\tau}. \quad (\text{A.44})$$

To evaluate the integration over ω , we extend the integrand in eq. (A.44) to the complex plane and use Cauchy's residue theorem. The poles of the Bose-Einstein distribution $n(\omega)$ are on the imaginary axis and correspond to the Matsubara frequencies

$$\gamma_k = \frac{2\pi}{\beta\hbar} k \quad \text{with} \quad k \in \mathbb{Z}. \quad (\text{A.45})$$

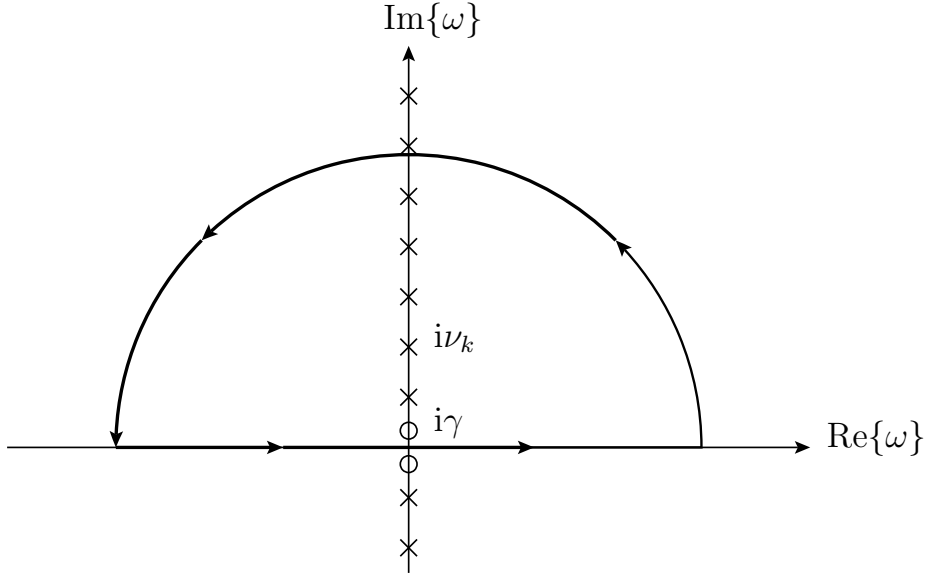


Figure A.2: Sketch of the integration contour for evaluating eq. (A.44). The crosses mark poles according to the Matsubara frequencies $\gamma_k = \frac{2\pi k}{\beta\hbar}$, and the small circles stand for the poles of the Drude-Lorentz spectral density.

The corresponding residues are given by

$$\text{Res}(i\gamma_k) = J(i\gamma_k) \frac{1}{\hbar\beta} e^{-\gamma_k\tau}. \quad (\text{A.46})$$

The remaining poles, and in particular the behavior of the integrand for $\omega = \gamma_0 = 0$, depends on the explicit form of the spectral density. In the following, we use a Drude-Lorentz spectral density

$$J_m(\omega) = 2\lambda \frac{\omega\nu}{\omega^2 + \nu^2}, \quad (\text{A.47})$$

with poles at $\omega = \pm i\nu$ and residues

$$\text{Res}(\pm i\nu) = \nu\lambda e^{\mp\nu\tau}. \quad (\text{A.48})$$

The zero-frequency component of the integrand is determined by the behavior of $n(\omega)$ and $J(\omega)$ for $\omega \rightarrow 0$. The Bose-Einstein distribution has a pole at $\omega = 0$, whereas the Drude-Lorentz spectral density goes to zero, $J(0) = 0$. We use l'Hopital's rule and obtain a finite value of the integrand as ω approaches zero

$$\lim_{\omega \rightarrow 0} J_m(\omega)n(\omega) = \frac{2\lambda}{\hbar k_B T}. \quad (\text{A.49})$$

According to eq. (A.39), the bath correlation function $C(\tau)$ has to be evaluated at positive times $\tau \geq 0$, and we close the integration contour along a semicircle within the upper complex plain. The semicircle is parameterized by $z = |\omega|e^{i\phi}$ with $\phi \in [0, \pi]$. The used contour and the corresponding poles of the integrand are illustrated in Fig. A.2. Since $\tau \geq 0$, the upper circle does not contribute to the integration for $|\omega| \rightarrow \infty$, and we get

$$C_m(\tau) = \frac{1}{\pi} \int_{-\infty}^{\infty} d\omega J_m(\omega) n(\omega) e^{i\omega\tau} = \frac{1}{\pi} \oint_C dz J_m(z) n(z) e^{iz\tau}. \quad (\text{A.50})$$

The integration is then easily done, and the result is given as a sum over the residues of all poles enclosed by the integration contour multiplied by $2\pi i$. The bath correlation is then expressed by [65]

$$C_m(\tau) = 2i\lambda\nu n(i\nu) e^{-\nu\tau} + \sum_{k=1}^{\infty} \frac{2i}{\beta\hbar} J(i\gamma_k) e^{-\gamma_k\tau}. \quad (\text{A.51})$$

The time integration in eq. (A.39) can be performed analytically, and the Redfield rates read

$$\Gamma(\omega) = \frac{2i\lambda\nu}{\hbar} n(i\nu) \frac{1}{\nu - i\omega} + \sum_{k=1}^{\infty} \frac{2i}{\beta\hbar^2} J(i\gamma_k) \frac{1}{\gamma_k - i\omega}. \quad (\text{A.52})$$

The summation can be evaluated explicitly, and the Redfield rates can be expressed in terms of the Digamma function $\psi(z)$. The real and imaginary part of the rates are then obtained by [65]

$$\text{Re}\{\Gamma(\omega)\} = \frac{1}{\hbar} J(\omega) (n(\omega) + 1) \quad (\text{A.53})$$

and

$$\text{Im}\{\Gamma(\omega)\} = -\frac{1}{\hbar\pi} J(\omega) \left(\frac{\pi\nu}{2\omega} + \frac{\pi}{\beta\hbar\nu} + \psi\left(\frac{\beta\hbar\nu}{2\pi}\right) - \text{Re}\psi\left(i\frac{\beta\hbar\omega}{2\pi}\right) \right). \quad (\text{A.54})$$

A.2.2 Secular approximation

In the previous section, we evaluated the Born-Markov equation in the Schrödinger picture, yielding the Redfield equations that can be formally written in a compact form eq. (A.37). Within the secular approximation, several terms of the full Redfield equations are neglected. In order to show which terms are omitted, and to point out the physical interpretation of the secular approximation, we will expand the Masterequation explicitly. In contrast to the derivation of the full Redfield equations, we remain in the interaction picture. We further deduce

the secular approximation from the more general TCL version of the quantum Masterequation approach. The TCL Masterequation

$$\frac{d}{dt}\tilde{\rho}(t) = -\frac{1}{\hbar^2} \int_0^t dt' \text{Tr} \left\{ [\tilde{\mathcal{H}}_{\text{ex-phon}}(t), [\tilde{\mathcal{H}}_{\text{ex-phon}}(t'), \rho(t) \otimes \rho_{\text{phon}}]] \right\} \quad (\text{A.55})$$

captures non-Markovian effects up to second-order perturbation theory with respect to the exciton-phonon coupling strength. Equation (A.55) is obtained from the Nakajima-Zwanzig approach in combination with the time-convolutionless projection operator technique [238].

In this section, we basically follow Ref. [185]. Analogous to the derivation of full Redfield equations, the evaluation of the TCL Masterequation requires an explicit form of the exciton-phonon coupling term in interaction picture. We introduce the operators

$$V_m(\omega) = \sum_{M,N} \langle E_M | V_m | E_N \rangle \delta(\hbar\omega - (E_M - E_N)) |E_M\rangle \langle E_N|, \quad (\text{A.56})$$

which yields

$$\tilde{\mathcal{H}}_{\text{ex-phon}}(t) = \sum_m \sum_{\omega} V_m(\omega) e^{i\omega t} \tilde{B}_m(t). \quad (\text{A.57})$$

This definition is equivalent to eq. (A.34). The bath operators $\tilde{B}_m(t)$ are given according to eq. (A.35). Inserting eq. (A.57) in the TCL Masterequation eq. (A.55) leads to

$$\begin{aligned} \frac{d}{dt}\tilde{\rho}(t) = -\frac{1}{\hbar^2} \sum_m \sum_{\omega, \omega'} \int_0^t ds \bigg(& V_m(\omega) V_m(\omega') \tilde{\rho}(t) C_m(s) e^{i(\omega+\omega')t} e^{-i\omega's} \\ & + \tilde{\rho}(t) V_m(\omega') V_m(\omega) C_m^*(s) e^{i(\omega+\omega')t} e^{-i\omega's} \\ & - V_m(\omega) \tilde{\rho}(t) V_m(\omega') C_m^*(s) e^{i(\omega+\omega')t} e^{-i\omega's} \\ & - V_m(\omega') \tilde{\rho}(t) V_m(\omega) C_m(s) e^{i(\omega+\omega')t} e^{-i\omega's} \bigg), \quad (\text{A.58}) \end{aligned}$$

where the bath correlation functions $C_m(t)$ are defined in eq. (A.36). The fast oscillatory terms $\sim e^{i(\omega+\omega')t}$ lead to mixing between exciton populations and exciton coherences. Within the secular approximation, these terms are neglected. This corresponds effectively to an averaging out of the fast oscillations. In eq. (A.58), the summation goes over the frequencies ω and ω' . In secular approximation, we replace $\sum_{\omega'}$ by $\delta(\omega + \omega')$. We use $V_m(-\omega) = V_m^\dagger(\omega)$ and obtain the TCL Masterequation in the secular approximation

$$\begin{aligned} \frac{d}{dt}\tilde{\rho}(t) = \sum_{m,\omega} \bigg(& iL_m(t, \omega) [V_m^\dagger(\omega) V_m(\omega), \tilde{\rho}(t)] + \gamma_m(t, \omega) (V_m(\omega) \tilde{\rho}(t) V_m^\dagger(\omega) \\ & - \frac{1}{2} V_m^\dagger(\omega) V_m(\omega) \tilde{\rho}(t) - \tilde{\rho}(t) \frac{1}{2} V_m^\dagger(\omega) V_m(\omega)) \bigg), \quad (\text{A.59}) \end{aligned}$$

where we introduce the time-dependent Lamb shift

$$L_m(t, \omega) = \frac{1}{\hbar^2} \text{Im} \int_0^t ds C_m(s) e^{-i\omega s} \quad (\text{A.60})$$

and time-dependent rates

$$\gamma_m(t, \omega) = \frac{2}{\hbar^2} \text{Re} \int_0^t ds C_m(s) e^{-i\omega s}. \quad (\text{A.61})$$

The Markov limit is obtained by $t \rightarrow \infty$, and both the Lamb-shift L_m and the rates γ_m become time-independent and are related to the Redfield rates defined in eq. (A.39),

$$L_m(\omega) = \frac{1}{\hbar^2} \text{Im}\{\Gamma_m(-\omega)\} \quad \text{and} \quad \gamma_m(\omega) = \frac{2}{\hbar^2} \text{Re}\{\Gamma_m(-\omega)\}. \quad (\text{A.62})$$

We neglect the Lamb-shift. The secular TCL Masterequation within the Born approximation is then given in the Schrödinger picture by

$$\frac{d}{dt} \rho(t) = -\frac{i}{\hbar} [\mathcal{H}_{\text{ex}}, \rho(t)] + \sum_{m, \omega} \gamma_m(t, \omega) \mathcal{D}[V_m(\omega)] \rho(t), \quad (\text{A.63})$$

where we introduce the Lindblad operator

$$\mathcal{D}[V] \rho = V \rho V^\dagger - \frac{1}{2} V^\dagger V \rho - \frac{1}{2} \rho V^\dagger V. \quad (\text{A.64})$$

The corresponding secular Born-Markov equations are obtained by replacing $\gamma_m(t, \omega)$ with its stationary value $\gamma_m(\omega) = \gamma_m(t \rightarrow \infty, \omega)$.

A.3 Combined Masterequation – HEOM approach (ME-HEOM)

Parts of this chapter have been published in Kreisbeck *et al.* Ref. [78].

To study the transfer efficiency within a non-Markovian and non-perturbative treatment of the excitation-phonon coupling, we modify the HEOM approach introduced in Part I section 3.3. This allows us to incorporate trapping and radiative decay.

In section A.3.1, we introduce a combined Masterequation (ME)-HEOM approach, in which trapping and the loss channel are described within the secular Born-Markov approximation, but which includes temporal correlations and higher-order phonon processes for the coupling to the molecular vibrations. In section A.3.2, we validate the ME-HEOM at hand of a simple example, in which we consider a dimer composed of two coupled BChls. One of the BChls interacts strongly and the other interacts weakly with vibrational modes of the BChls, fitting the setting of ME-HEOM.

A.3.1 ME-HEOM formalism

We consider a system \mathcal{H}_S coupling to two independent Bosonic environments

$$\mathcal{H}_{B_1} = \sum_{\xi_1} \hbar \omega_{\xi_1} b_{\xi_1}^\dagger b_{\xi_1} \quad \text{and} \quad \mathcal{H}_{B_2} = \sum_{\xi_2} \hbar \omega_{\xi_2} b_{\xi_2}^\dagger b_{\xi_2}. \quad (\text{A.65})$$

The structure of the coupling terms between the system and the environment is assumed to be of the form

$$\mathcal{H}_{S-B_k} = V_k \sum_{\xi_k} d_{\xi_k} (b_{\xi_k}^\dagger + b_{\xi_k}) \equiv V_k u_k \quad (\text{A.66})$$

where V_k is an operator acting only on the system degrees of freedom, and where d_{ξ_k} describes the coupling strength between the bath and the system. In the following, we treat \mathcal{H}_{S-B_1} as exact, whereas we use second-order perturbation theory and the Markov approximation for \mathcal{H}_{S-B_2} .

Analogous to the derivation of the HEOM approach in Part I section 3.3, we start with the Liouville equation for the total density operator in the interaction picture

$$\frac{d}{dt} \tilde{R}(t) = -\frac{i}{\hbar} [\tilde{\mathcal{H}}_{S-B_1} + \tilde{\mathcal{H}}_{S-B_2}, \tilde{R}(t)]. \quad (\text{A.67})$$

Operators in the interaction picture are given by

$$\tilde{\mathcal{O}}(t) = \exp\left(\frac{it}{\hbar} \mathcal{H}_S\right) \mathcal{O} \exp\left(-\frac{it}{\hbar} \mathcal{H}_S\right). \quad (\text{A.68})$$

We assume that the degrees of freedom of the system and the two individual baths factorize for the initial preparation time $t_0 = 0$

$$R(t_0) = \rho(t_0) \otimes \rho_{B_1} \otimes \rho_{B_2}. \quad (\text{A.69})$$

Following the steps of Part I section 3.3, the time evolution of the reduced density operator describing the system's degrees of freedom is then formally given by

$$\tilde{\rho}(t) = \tilde{\mathcal{U}}(t) = T_+ \exp \left(\int_0^t ds \tilde{W}_1(s) \right) \exp \left(\int_0^t ds \tilde{W}_2(s) \right) \rho(t_0). \quad (\text{A.70})$$

Analogous to Part I section 3.3, eq. (3.12) we define

$$\tilde{W}_k = -\frac{1}{\hbar^2} \int_0^t ds \tilde{V}_k(t)^\times [S_k(t-s) \tilde{V}_k(s)^\times - i \frac{\hbar}{2} \chi_k \tilde{V}_k(s)^\circ] \quad (\text{A.71})$$

with $V^\times \bullet = [V, \bullet]$ and $V^\circ \bullet = [V, \bullet]_+$. The symmetrized correlation function $S_k(t)$ and response function $\chi_k(t)$ are defined in the same way as Part I section 3.3, eqs. (3.13) and (3.14) with $C_k(t) = \langle u_k(t) u_k(0) \rangle$. The brackets denote expectation values with respect to the bath's degrees of freedom. The equation of motion for the reduced density matrix is time-nonlocal and reads

$$\frac{d}{dt} \tilde{\rho}(t) = T_+ \tilde{W}_1(t) \tilde{\rho}(t) + T_+ \tilde{W}_2(t) \tilde{\rho}(t). \quad (\text{A.72})$$

So far, we have just followed the steps of the derivation for the hierarchical equations of motion. Now, we are at the key point for the ME-HEOM, where we apply the Markov approximation in combination with second-order perturbation theory for the coupling to the bath B_2 . With this approximation, eq. (A.72) simplifies to

$$\frac{d}{dt} \tilde{\rho}(t) = T_+ \tilde{W}_1(t) \tilde{\rho}(t) + \tilde{\mathcal{L}}_{S-B_2} \tilde{\rho}(t), \quad (\text{A.73})$$

where the application $\tilde{\mathcal{L}}_{S-B_2}$ is time-local. In the Schrödinger picture we get

$$\mathcal{L}_{S-B_2} \rho(t) = -V_2^\times [\Lambda_2 \rho(t) - \rho(t) \Lambda_2^\dagger], \quad (\text{A.74})$$

where the operator Λ_2 is defined analogously to eq. (A.38). For the time-nonlocal part of eq. (A.73) we use the HEOM approach requiring a Drude-Lorentz shaped spectral density

$$J_1(\omega) = \pi \sum_{\xi_1} |d_{\xi_1}|^2 \delta(\omega - \omega_{\xi_1}) = 2\lambda_1 \frac{\nu_1 \omega}{\omega^2 + \nu_1^2}, \quad (\text{A.75})$$

where the response function $\chi(t)$ and the symmetrized correlation function $S(t)$ decay exponentially in time, see Part I section 3.3, eqs. (3.16) and (3.17). For

the time-local part, \mathcal{L}_{S-B_2} we do not need to restrict the spectral density used to a Drude-Lorentz form.

In order to rewrite the time-nonlocal effects for the coupling to the bath B_1 into a hierarchy of coupled equations, we define the auxiliary matrices

$$\tilde{\sigma}^{(n)}(t) = T_+ \left[\int_0^t ds e^{-\gamma_1(t-s)} \tilde{\theta}_1(s) \right]^n \exp \left[\int_0^t ds \tilde{W}_1(s) \right] \exp \left[\int_0^t ds \tilde{W}_2(s) \right]. \quad (\text{A.76})$$

The relaxation operator $\tilde{\theta}_1(s)$ is of the same form as Part I section 3.3, eq. (3.19). Note that, compared to the definition of the auxiliary matrices Part I section 3.3, eq. (3.20), there is only a single index n , since only the coupling to bath B_1 is incorporated in a time-nonlocal manner. This also manifests itself in the fact that only the parameters for the coupling to bath B_1 appear in front of the two exponential functions. Analogous to Part I section 3.3, the time evolution of the auxiliary matrices results in a hierarchy of equations of motion. However, the difference from the original version of the hierarchy is that now the application of $T_+ \tilde{W}_2(t)$ is replaced by its Markov limit $\tilde{\mathcal{L}}_{S-B_2}$. This results in a modified hierarchy of coupled equations. In Schrödinger picture, we obtain

$$\frac{d}{dt} \rho(t) = -\frac{i}{\hbar} [\mathcal{H}_S, \rho(t)] + \mathcal{L}_{S-B_2} \rho(t) + iV_1^\times \sigma(t)^{(1)} \quad (\text{A.77})$$

with

$$\begin{aligned} \frac{d}{dt} \sigma(t)^{(n)} = & -\frac{i}{\hbar} [\mathcal{H}_S, \sigma(t)^{(n)}] + \mathcal{L}_{S-B_2} \sigma(t)^{(n)} \\ & - n\nu_1 \sigma(t)^{(n)} + n\theta_1 \sigma(t)^{(n-1)} + iV_1^\times \sigma(t)^{(n+1)}. \end{aligned} \quad (\text{A.78})$$

A.3.2 Application of ME-HEOM to a dimer

In order to illustrate the ME-HEOM approach, we consider a dimer comprising two coupled BChls. The Hamiltonian is given by

$$\begin{aligned} \mathcal{H} = & \sum_{m=1}^2 (\varepsilon_m + \lambda_m) |m\rangle \langle m| + J_{12} (|1\rangle \langle 2| + |2\rangle \langle 1|) \\ & + \sum_{m=1, \xi}^2 |m\rangle \langle m| d_{\xi, m} (b_{\xi, m}^\dagger + b_{\xi, m}) + \sum_{m=1, \xi}^2 \hbar \omega_{m, \xi} b_{\xi, m}^\dagger b_{\xi, m} \end{aligned} \quad (\text{A.79})$$

The first part corresponds to the exciton system of the two coupled BChls. The second part takes into account the exciton-phonon coupling. The last term describes the phonon bath. One of the BChls (BChl 1, for example) interacts strongly with the molecular vibrations, whereas there is only a weak coupling to

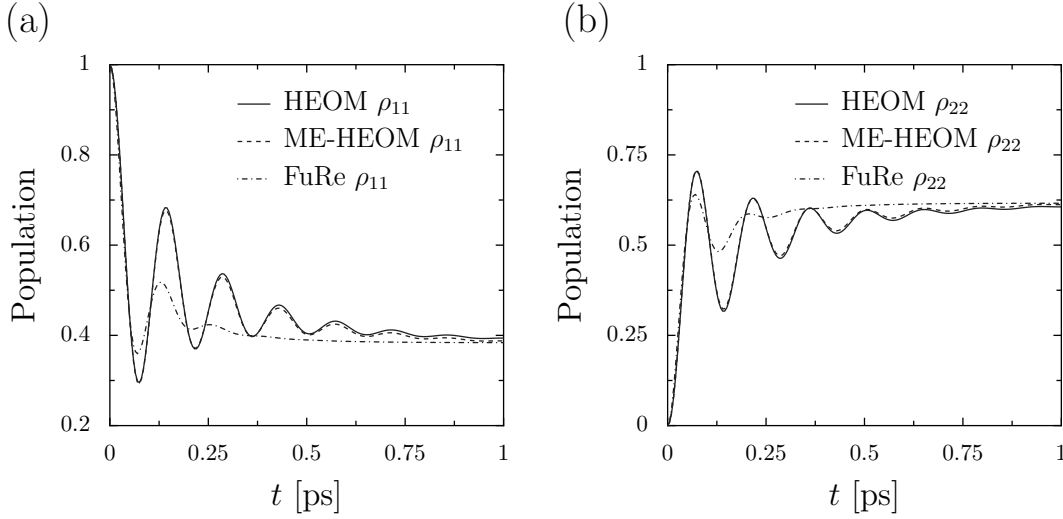


Figure A.3: Population dynamics for the dimer with an initial population at BChl 1, $\rho(t_0) = |1\rangle\langle 1|$, for different levels of approximation. HEOM (solid line) and ME-HEOM (dashed line) are almost on top of each other. (a) population at BChl 1 $\rho_{1,1}(t) = \langle 1|\rho(t)|1\rangle$, and (b) population at BChl 2 $\rho_{2,2}(t) = \langle 2|\rho(t)|2\rangle$. Parameters used: $\tau_c = 100$ fs, $\lambda_1 = 50$ cm $^{-1}$, $\lambda_2 = 2$ cm $^{-1}$ and $T = 300$ K.

the vibrations for the other BChl. This situation fulfills the requirements of the ME-HEOM approach.

We set the site energies to $\varepsilon_1 = 100$ cm $^{-1}$ and $\varepsilon_2 = 0$ cm $^{-1}$ and use an inter-site coupling $J_{12} = 100$ cm $^{-1}$. For the interaction with the vibrations, we use a Drude-Lorentz spectral density with the same phonon-relaxation timescale $\tau_c = 100$ fs but different reorganization energies $\lambda_1 = 50$ cm $^{-1}$ and $\lambda_2 = 2$ cm $^{-1}$ for both BChls. In the following, we explore the system dynamics under three different levels of approximation. Firstly, we use HEOM, which gives an exact solution for the exciton dynamics. Secondly, we use ME-HEOM, in which we treat the weaker coupling λ_2 within second-order perturbation theory. Finally we use the full Redfield approach, treating both system-bath interactions within the Born-Markov approximation. The corresponding results are shown in Fig. A.3. For ME-HEOM, we obtain excellent agreement with the exact HEOM results. In contrast to ME-HEOM, the full Redfield equations fail to reproduce the exact HEOM results.

B Lead eigenstates in the presence of a magnetic field

In the following we derive a formal expression for the asymptotic eigenstates. The leads are characterized by a confining potential in transversal direction and a free motion in the longitudinal direction. We set the coordinate system such that the confined direction points along the y -axis. The asymptotic Hamiltonian then reads

$$\mathcal{H} = \frac{1}{2m}(-i\hbar\nabla + e\mathbf{A}(x, y))^2 + V(y), \quad (\text{B.1})$$

where we introduced the vector potential \mathbf{A} which takes into account the homogeneous magnetic field perpendicular to the xy -plane. In Landau-gauche $\mathbf{A} = (-By, 0, 0)$, eq. (B.1) is given by

$$\mathcal{H} = -\frac{\hbar^2}{2m}(\partial_x^2 + \partial_y^2) + \frac{e^2}{2m}B^2y^2 + \frac{ie\hbar}{2m}By\partial_x + \frac{ie\hbar}{2m}\partial_x By + V(y). \quad (\text{B.2})$$

The longitudinal part of the eigenfunctions is given by plane waves

$$\psi_{k_x, n}(x, y) = \frac{1}{\sqrt{2\pi}} e^{ik_x x} \chi_{k_x, n}(y). \quad (\text{B.3})$$

We insert this ansatz in eq. (B.2) and get following equation for the transversal mode

$$\left(-\frac{\hbar^2}{2m}k_x^2 - \frac{\hbar^2}{2m}\partial_y^2 + \frac{e^2}{2m}B^2y^2 - \frac{e\hbar}{m}Byk_x + V(y) \right) \chi_{k_x, n}(y) = E_{k_x, n} \chi_{k_x, n}(y). \quad (\text{B.4})$$

Defining the cyclotron frequency $\omega_c = \frac{eB}{m}$, eq. (B.4) reduces to

$$\left(\frac{p_y^2}{2m} + V_{\text{eff}}(y, k_x) \right) \chi_{k_x, n}(y) = E_{k_x, n} \chi_{k_x, n}(y), \quad (\text{B.5})$$

where we introduce the effective potential

$$V_{\text{eff}}(y, k_x) = \frac{m \omega_c^2}{2} \left(y - \frac{\hbar k_x}{eB} \right)^2 + V(y). \quad (\text{B.6})$$

That is the transversal confinement is influenced by the longitudinal momentum and hence the transversal modes $\chi_{k_x, n}(y)$ depend on k_x . In the limiting case $B \rightarrow 0$ the effective confinement reduces to the original confining potential $V(y)$ and χ_n gets independent of the longitudinal motion. The lead eigenstates for reversed magnetic fields $B \rightarrow -B$ are given by $\psi_{k_x, n}^*(x, y) = e^{-ik_x x} \chi_{-k_x, n}(y)$.

Bibliography

- [1] A. O. Caldeira and A. J. Leggett. Influence of dissipation on quantum tunneling in macroscopic systems. *Phys. Rev. Lett.*, 46:211, 1981.
- [2] T. Dittrich, P. Hänggi, G.-L. Ingold, B. Kramer, G. Schön, and W. Zwerger. *Quantum Transport and Dissipation*. Wiley, 1998.
- [3] C. W. Gardiner and P. Zoller. *Quantum Noise*. Springer-Verlag, 2004.
- [4] H. Carmichael. *An Open System Approach to Quantum Optics*. Cambridge Studies in Semiconductor Physics and Microelectronic Engineering. Lecture Notes in Physics, Springer, 1993.
- [5] M. Grifoni and P. Hänggi. Driven quantum tunneling. *Phys. Rep.*, 304:229, 1998.
- [6] S. A. Gurvitz. Rate equations for quantum transport in multidot systems. *Phys. Rev. B*, 57:6602, 1998.
- [7] F. Sols. Scattering, dissipation, and transport in mesoscopic systems. *Ann. Phys.*, 214:386, 1992.
- [8] M. A. Nielsen and I. L. Chuang. *Quantum Computation and Quantum Information*. Cambridge University Press, 2000.
- [9] T. Michael and P. Hänggi. Decoherence and dissipation during a quantum XOR gate operation. *Phys. Rev. A*, 65:012309, 2001.
- [10] P. Zanardi and F. Rossi. Quantum information in semiconductors: Noiseless encoding in a quantum-dot array. *Phys. Rev. Lett.*, 81:4752, 1998.
- [11] P. Zanardi. Dissipation and decoherence in a quantum register. *Phys. Rev. A*, 57:3276, 1998.
- [12] D. P. DiVincenzo. The physical implementation of quantum computation. *Fortschr. d. Phys.*, 48.

- [13] S. Lloyd. Quantum coherence in biological systems. *J. Phys.: Conf. Ser.*, 302:012037, 2011.
- [14] L. Turin. A spectroscopic mechanism for primary olfactory. *Chem. Senses*, 21:773, 1996.
- [15] M. I. Franco, L. Turin, A. Mershin, and E. M. C. Skoulakis. Molecular vibration-sensing component in *Drosophila melanogaster* olfaction. *Proc. Nat. Acad. Sci.*, 108:3797, 2011.
- [16] G. S. Engel, T. R. Calhoun, E. L. Read, T.-K. Ahn, T. Mancal, Y.-C. Cheng, R. E. Blankenship, and G. R. Fleming. Evidence for wavelike energy transfer through quantum coherence in photosynthetic systems. *Nature*, 446:782, 2007.
- [17] H. Lee, Y.-C. Cheng, and G. R. Fleming. Coherence dynamics in photosynthesis: Protein protection of excitonic coherence. *Science*, 316:1462, 2007.
- [18] T. R. Calhoun, N. S. Ginsberg, G. S. Schlau-Cohen, Y.-C. Cheng, M. Balloottari, R. Bassi, and G. R. Fleming. Quantum coherence enabled determination of the energy landscape in light-harvesting complex II. *J. Phys. Chem. B*, 113:16291, 2009.
- [19] E. Collini, C. Y. Wong, K. E. Wilk, P. M. G. Curmi, P. Brumer, and G. D. Scholes. Coherently wired light-harvesting in photosynthetic marine algae at ambient temperature. *Nature*, 463:644, 2010.
- [20] G. Panitchayangkoon, D. Hayes, K. A. Fransted, J. R. Caram, E. Harel, J. Wen, R. E. Blankenship, and G. S. Engel. Long-lived quantum coherence in photosynthetic complexes at physiological temperature. *Proc. Natl. Acad. Sci.*, 107:12766, 2010.
- [21] R. E. Blankenship, M. T. Madigan, and C. E. Bauer. *Anoxygenic photosynthetic bacteria*. Kluwer Academic Publishers, 1995.
- [22] R. E. Blankenship. *Molecular mechanisms of photosynthesis*. Blackwell Science, 2002.
- [23] H. M. Berman, J. Westbrook, Z. Feng, G. Gilliland, T. N. Bhat, H. Weissig, I. N. Shindyalov, and P. E. Bourne. The protein data bank. *Nucl. Acids Res.*, 28:235, 2000.
- [24] T. Förster. Zwischenmolekulare Energiewanderung und Fluoreszenz. *Ann. Phys.*, 437:55, 1948.

-
- [25] G. D. Scholes. Green quantum computers. *Nature Physics*, 6:402, 2010.
- [26] G. D. Scholes, G. R. Fleming, A. Olaya-Castro, and R. van Grondelle. Lessons from nature about solar light harvesting. *Nature Chemistry*, 3:763, 2011.
- [27] J. M. Olson and C. A. Romano. A new chlorophyll from green bacteria. *Biochim. Biophys. Acta*, 59:726, 1962.
- [28] R. E. Fenna and B. W. Matthews. Chlorophyll arrangement in a bacteriochlorophyll protein from *Chlorobium limicola*. *Nature*, 258:573, 1975.
- [29] M. Ø. Pedersen, J. Linnanto, N.-U. Frigaard, N. C. Nielsen, and M. Miller. A model of the protein-pigment baseplate complex in chlorosomes of photosynthetic green bacteria. *Photosynth. Res.*, 104:233, 2010.
- [30] N.-U. Frigaard and D. A. Bryant. Seeing green bacteria in a new light: Genomics-enabled studies of the photosynthetic apparatus in green sulfur bacteria and filamentous anoxygenic phototrophic bacteria. *Arch. Microbiol.*, 182:265, 2004.
- [31] G. T. Oostergetel, H. van Amerongen, and E. J. Boekema. The chlorosome: A prototype for efficient light harvesting in photosynthesis. *Photosynth. Res.*, 104:245, 2010.
- [32] V. May and O. Kühn. *Charge and energy transfer dynamics in molecular systems*. Wiley-VCH, 2004.
- [33] S. Mukamel. *Principles of nonlinear optical spectroscopy*. Oxford University Press, 1999.
- [34] M. Cho. *Two-dimensional optical spectroscopy*. CRC Press, 2009.
- [35] M. Cho, T. Brixner, I. Stiopkin, H. Vaswani, and G. R. Fleming. Two dimensional electronic spectroscopy of molecular complexes. *J. Chin. Chem. Soc.*, 53:15, 2006.
- [36] S. Mukamel. Multidimensional femtosecond correlation spectroscopies of electronic and vibrational excitations. *Annu. Rev. Phys. Chem.*, 51:691, 2000.
- [37] D. M. Jonas. Two-dimensional femtosecond spectroscopy. *Annu. Rev. Phys. Chem.*, 54:425, 2003.
- [38] W. Zhuang, T. Hayashi, and S. Mukamel. Coherent multidimensional vibrational spectroscopy of biomolecules; concepts, simulations and challenges. *Angew. Chem. Int. Ed.*, 48:3750, 2009.

- [39] M. Cho, H. M. Vaswani, T. Brixner, J. Stenger, and G. R. Fleming. Exciton analysis in 2d electronic spectroscopy. *J. Phys. Chem. B*, 109:10542, 2005.
- [40] M. Schmidt am Busch, F. Müh, M. E. Madjet, and T. Renger. The eighth bacteriochlorophyll completes the excitation energy funnel in the FMO protein. *J. Phys. Chem. Lett.*, 2:93, 2011.
- [41] L. Z. Sharp, D. Egorova, and W. Domcke. Efficient and accurate simulations of two-dimensional electronic photon-echo signals: Illustration for a simple model of the Fenna-Matthews-Olson complex. *J. Chem. Phys.*, 132:014501, 2010.
- [42] T. Brixner, J. Stenger, H. M. Vaswani, M. Cho, R. E. Blankenship, and G. R. Fleming. Two-dimensional spectroscopy of electronic couplings in photosynthesis. *Nature*, 434:625, 2005.
- [43] A. Ishizaki and G. R. Fleming. Theoretical examination of quantum coherence in a photosynthetic system at physiological temperature. *Proc. Natl. Acad. Sci.*, 106:17255, 2009.
- [44] P. Nalbach, D. Braun, and M. Thorwart. Exciton transfer dynamics and quantumness of energy transfer in the Fenna-Matthews-Olson complex. *Phys. Rev. E*, 84:041926, 2011.
- [45] A. W. Chin, J. Prior, R. Rosenbach, F. Caycedo-Soler, S. F. Huelga, and M. B. Plenio. Vibrational structures and long-lasting electronic coherence. *arXiv:1203.0776v1*, 2012.
- [46] B. Hein, C. Kreisbeck, T. Kramer, and M. Rodríguez. Modelling of oscillations in two-dimensional echo-spectra of the Fenna-Matthews-Olson complex. *New J. Phys.*, 14:023018, 2012.
- [47] L. Chen, R. Zheng, Y. Jing, and Q. Shi. Simulation of the two-dimensional electronic spectra of the Fenna-Matthews-Olson complex using the hierarchical equations of motion method. *J. Chem. Phys.*, 134:194508, 2011.
- [48] M. Wendling, T. Pullerits, M. A. Przyjalowski, S. I. E. Vulto, T. J. Aartsma, R. van Grondelle, and H. van Amerongen. Electron-vibrational coupling in the Fenna-Matthews-Olson complex of *Prosthecochloris aestuarii* determined by temperature-dependent absorption and fluorescence line-narrowing measurements. *J. Phys. Chem. B*, 104:5825, 2000.
- [49] J. Adolphs and T. Renger. How proteins trigger excitation energy transfer in the FMO complex of green sulfur bacteria. *Biophys. J.*, 91:2778, 2006.

-
- [50] N. Christensson, H. F. Kauffmann, T. Pullerits, and T. Mancal. Origin of long lived coherences in light-harvesting complexes. *arXiv:1201.6325v1*, 2012.
- [51] D. Hayes, J. Wen, G. Panitchayangkoon, R. E. Blankenship, and G. S. Engel. Robustness of electronic coherence in the Fenna-Matthews-Olson complex to vibronic and structural modifications. *Faraday Discuss.*, 150:459, 2011.
- [52] P. Rebentrost, M. Mohseni, I. Kassal, S. Lloyd, and A. Aspuru-Guzik. Environment-assisted quantum transport. *New J. Phys.*, 11:033003, 2009.
- [53] P. Rebentrost, M. Mohseni, and A. Aspuru-Guzik. Role of quantum coherence and environmental fluctuations in chromophoric energy transport. *J. Phys. Chem. B*, 113:9942, 2009.
- [54] M. B. Plenio and S. F. Huelga. Dephasing-assisted transport: Quantum networks and biomolecules. *New J. Phys.*, 10:113019, 2008.
- [55] F. Caruso, A. W. Chin, A. Datta, S. F. Huelga, and M. B. Plenio. Highly efficient energy excitation transfer in light-harvesting complexes: The fundamental role of noise-assisted transport. *J. Chem. Phys.*, 131:105106, 2009.
- [56] A. W. Chin, A. Datta, F. Caruso, S. F. Huelga, and M. B. Plenio. Noise-assisted energy transfer in quantum networks and light-harvesting complexes. *New J. Phys.*, 12:065002, 2010.
- [57] M. Mohseni, P. Rebentrost, S. Lloyd, and A. Aspuru-Guzik. Environment-assisted quantum walks in photosynthetic energy transfer. *J. Chem. Phys.*, 129:174106, 2008.
- [58] M. Mohseni, A. Shabani, S. Lloyd, and H. Rabitz. Optimal and robust energy transport in light-harvesting complexes: (II) A quantum interplay of multichromophoric geometries and environmental interactions. *arXiv:1104.4812v1*, 2011.
- [59] J. Wu, F. Liu, Y. Shen, J. Cao, and R. J. Silbey. Efficient energy transfer in light-harvesting systems, I: Optimal temperature, reorganization energy, and spatial-temporal correlations. *New J. Phys.*, 12:105012, 2010.
- [60] J. Wu, F. Liu, J. Ma, R. J. Silbey, and J. Cao. Efficient energy transfer in light-harvesting systems, II: Quantum-classical comparison, flux network, and robustness analysis. *arXiv:1109.5769v1*, 2011.

- [61] S. Hoyer, M. Sarovar, and K. B. Whaley. Limits of quantum speedup in photosynthetic light harvesting. *New. J. Phys.*, 12:065041, 2010.
- [62] F. Fassioli and A. Olaya-Castro. Distribution of entanglement in light-harvesting complexes and their quantum efficiency. *New. J. Phys.*, 12:085006, 2010.
- [63] L. K. Grover. Quantum mechanics helps in searching for a needle in a haystack. *Phys. Rev. Lett.*, 79:325, 1997.
- [64] S. Hoyer, A. Ishizaki, and K. B. Whaley. Propagating quantum coherence for a biological advantage. *arXiv:1106.2911v1*, 2011.
- [65] A. Ishizaki and Y. Tanimura. Nonperturbative non-Markovian quantum master equation: Validity and limitation to calculate nonlinear response functions. *Chem. Phys.*, 347:185, 2008.
- [66] S. I. E. Vulto, M. A. de Baat, R. J. W. Louwe, H. P. Permentier, T. Neef, M. Miller, H. van Amerongen, and T. J. Aartsma. Exciton simulations of optical spectra of the FMO complex from the green sulfur bacterium *Chlorobium tepidum* at 6 K. *J. Phys. Chem. B*, 102:9577, 1998.
- [67] M. Wendling, M. A. Przyjalowski, D. Gülen, S. i. E. Vulto, T. J. Aartsma, R. van Grondelle, and H. van Amerongen. The quantitative relationship between structure and polarized spectroscopy in the FMO complex of *Prosthecochloris aestuarii*: Refining experiments and simulations. *Photosynth. Res.*, 71:99, 2002.
- [68] M. T. W. Milder, B. Brüggemann, R. van Grondelle, and J. L. Herek. Revisiting the optical properties of the FMO protein. *Photosynth. Res.*, 104:257, 2010.
- [69] F. Müh, M. E. Madjet, J. Adolphs, A. Abdurahman, B. Rabenstein, H. Ishikita, E.-W. Knapp, and T. Renger. α -helices direct excitation energy flow in the Fenna-Matthews-Olson protein. *Proc. Natl. Acad. Sci.*, 104:16862, 2007.
- [70] J. Adolphs, F. Müh, M. E.-A. Madjet, and T. Renger. Calculation of pigment transition energies in the FMO protein. *Photosynth. Res.*, 95:197, 2008.
- [71] C. Olbrich, T. L. C. Jansen, J. Liebers, M. Aghtar, J. Strumpfer, K. Schulten, J. Knoester, and U. Kleinekathoefer. From atomistic modeling to excitation transfer and two-dimensional spectra of the FMO light-harvesting complex. *J. Phys. Chem. B*, 115:8609, 2011.

-
- [72] S. Shim, P. Rebentrost, S. Valleau, and A. Aspuru-Guzik. Atomistic study of the long-lived quantum coherences in the Fenna-Matthews-Olson complex. *Biophys. J.*, 102:649, 2012.
- [73] A. Kolli, A. Nazir, and A. Olaya-Castro. Electronic excitation dynamics in multichromophoric systems described via a polaron-representation master equation. *J. Chem. Phys.*, 135:154112, 2011.
- [74] J. Roden, G. Schulz, A. Eisfeld, and J. Briggs. Electronic energy transfer on a vibronically coupled quantum aggregate. *J. Chem. Phys.*, 131:044909, 2009.
- [75] J. Roden, A. Eisfeld, W. Wolff, and W. T. Strunz. Influence of complex exciton-phonon coupling on optical absorption and energy transfer of quantum aggregates. *Phys. Rev. Lett.*, 103:058301, 2009.
- [76] S. F. Huelga J. Prior, A. W. Chin and M. B. Plenio. Efficient simulation of strong system-environment interactions. *Phys. Rev. Lett.*, 105:050404, 2010.
- [77] Y. Tanimura and R. Kubo. Time evolution of a quantum system in contact with a nearly Gaussian-Markoffian noise bath. *J. Phys. Soc. Jpn.*, 58:101, 1989.
- [78] C. Kreisbeck, T. Kramer, M. Rodríguez, and B. Hein. High-performance solution of hierarchical equations of motion for studying energy transfer in light-harvesting complexes. *J. Chem. Theory Comput.*, 7:2166, 2011.
- [79] T. Yamasaki, T. Yamakawa, Y. Yamane, H. Koike, K. Satoh, and S. Katoh. Temperature acclimation of photosynthesis and related changes in photosystem II electron transport in winter wheat. *Plant Physiol.*, 128:1087, 2002.
- [80] J. Strümpfer and K. Schulten. Light harvesting complex II B850 excitation dynamics. *J. Chem. Phys.*, 131:225101, 2009.
- [81] J. Strümpfer and K. Schulten. Open quantum dynamics calculations with the hierarchy equations of motion on parallel computers. *J. Chem. Theory Comput.*, 8:2808, 2012.
- [82] C. Meier and D. J. Tannor. Non-Markovian evolution of the density operator in the presence of strong laser fields. *J. Chem. Phys.*, 111:3365, 1999.
- [83] C. Kreisbeck and T. Kramer. Long-lived electronic coherence in dissipative exciton-dynamics of light-harvesting complexes. *arXiv:1203.1485v3*, 2012.

- [84] A. P. Micolich, A. M. See, B. C. Scannel, C. A. Marlow, T. P. Martin, I. Pilgrim, A. R. Hamilton, H. Linke, and R. P. Taylor. Is it the boundaries or disorder that dominates electron transport in semiconductor ‘billiards’? *Fortschr. Phys.*, 60:1, 2012.
- [85] T. Saku, Y. Hirayama, and Y. Horikoshi. High electron mobility in AlGaAs/GaAs modulation-doped structures. *Jpn. J. Appl. Phys.*, 30:902, 1991.
- [86] D. Stich, J. Zhou, T. Korn, R. Schulz, D. Schuh, W. Wegscheider, M. W. Wu, and C. Schüller. Dependence of spin dephasing on initial spin polarization in a high-mobility two-dimensional electron system. *Phys. Rev. B*, 76:205301, 2007.
- [87] C. Riedesel, D. Reuter, and A. D. Wieck. Laterally patterned high mobility two-dimensional electron gases obtained by overgrowth of focused ion beam implanted $\text{Al}_{1-x}\text{Ga}_x\text{As}$. *Physica E*, 21:592, 2004.
- [88] R. Völkl, M. Griesbeck, S. A. Tarasenko, D. Schuh, W. Wegscheider, C. Schüller, and T. Korn. Spin dephasing and photoinduced spin diffusion in a high-mobility two-dimensional electron system embedded in a GaAs-(Al,Ga)As quantum well grown in the [110] direction. *Phys. Rev. B*, 83:241306, 2011.
- [89] C. J. B. Ford, S. Washburn, M. Büttiker, C. M. Knoedler, and J. M. Hong. The Hall effect in ballistic junctions. *Surface Science*, 229:298, 1990.
- [90] H. U. Baranger and A. D. Stone. Quenching of the Hall resistance in ballistic microstructures: A collimation effect. *Phys. Rev. Lett.*, 63:414, 1989.
- [91] H. U. Baranger, D. P. DiVincenzo, R. A. Jalabert, and A. D. Stone. Classical and quantum ballistic-transport anomalies in microjunctions. *Phys. Rev. B*, 44:10637, 1991.
- [92] J. H. Davies. *The physics of low dimensional semiconductors: An introduction*. Cambridge University Press, Cambridge, 1997.
- [93] P. Harrison. *Quantum Wells, Wires and Dots*. Wiley, 2009.
- [94] T. Ihn. *Semiconductor nanostructures: Quantum states and electronic transport*. Oxford University Press, 2010.
- [95] K. von Klitzing. The quantized Hall effect. *Rev. Mod. Phys.*, 58:519, 1986.

-
- [96] B. J. van Wees, H. van Houten, C. W. J. Beenakker, J. G. Williamson, L. P. Kouwenhoven, D. van der Marel, and C. T. Foxon. Quantized conductance of point contacts in a two-dimensional electron gas. *Phys. Rev. Lett.*, 60:848, 1988.
 - [97] K. E. Aidala, R. E. Parrott, T. Kramer, E. J. Heller, R. M. Westervelt, M. P. Hanson, and A. C. Gossard. Imaging magnetic focusing of coherent electron waves. *Nature Physics*, 3:464, 2007.
 - [98] D. K. Ferry and S. M. Goodnick. *Transport in nanostructures*. Cambridge University Press, 1997.
 - [99] I. V. Krive, A. Palevski, R. I. Shekhter, and M. Jonson. Resonant tunneling of electrons in quantum wires (review). *Low Temp. Phys.*, 36:119, 2010.
 - [100] M. A. Kastner. Artificial atoms. *Physics Today*, 46:24, 1993.
 - [101] L. Worschech, D. Hartmann, S. Reitzenstein, and A. Forchel. Nonlinear properties of ballistic nanoelectronic devices. *J. Phys. Condens. Matter*, 17:775, 2005.
 - [102] H. Lüth. Nanostructures and semiconductor electronics. *Phys. Stat. Sol. (b)*, 192:278, 1995.
 - [103] C. J. B. Ford, A. B. Fowler, J. M. Hong, C. M. Knoedler, S. E. Laux, J. J. Wainer, and S. Washburn. Gated, asymmetric rings as tunable electron interferometers. *Surface Science*, 229:307, 1990.
 - [104] U. Wieser, M. Knop, U. Kunze, D. Reuter, and A. D. Wieck. Magnetoballistic effects in non-centrosymmetric GaAs/AlGaAs cross junctions. *Physica E: Low-dimensional Systems and Nanostructures*, 40(6):2179, 2008.
 - [105] M. Büttiker. Four-terminal phase-coherent conductance. *Phys. Rev. Lett.*, 57:1761, 1986.
 - [106] M. Büttiker. Absence of backscattering in the quantum Hall effect in multiprobe conductors. *Phys. Rev. B*, 38:9375, 1988.
 - [107] S. Datta. *Electronic transport in mesoscopic systems*. Cambridge University Press, 1995.
 - [108] S. Rotter, J.-Z. Tang, L. Wirtz, J. Trost, and J. Burgdörfer. Modular recursive Green’s function method for ballistic quantum transport. *Phys. Rev. B*, 62:1950, 2000.

- [109] S. Rotter, B. Weingartner, F. Libisch, F. Aigner, and J. Feist. A modular method for the efficient calculation of ballistic transport through quantum billiards. *Springer lecture notes in computer science*, 3743:586, 2006.
- [110] K. Kazymyrenko and X. Waintal. Knitting algorithm for calculating Green functions in quantum systems. *Phys. Rev. B*, 77:115119, 2008.
- [111] M. Wimmer and K. Richter. Optimal block-tridiagonalization of matrices for coherent charge transport. *J. Comp. Phys.*, 228:8548, 2009.
- [112] T. Kramer, E. J. Heller, and R. E. Parrott. An efficient and accurate method to obtain the energy-dependent Green function for general potentials. *J. Phys. conf. ser.*, 99:012010, 2008.
- [113] D. E. Weeks and D. J. Tannor. A time-dependent formulation of the scattering matrix for the collinear reaction $\text{H} + \text{H}_2(\nu) \rightarrow \text{H}_2(\nu') + \text{H}$. *Chem. Phys. Lett.*, 224:451, 1994.
- [114] D. H. Zhang and J. Z. H. Zhang. Quantum reactive scattering with a deep well: Time-dependent calculation for $\text{H} + \text{O}_2$ reaction and bound state characterization for HO_2 . *J. Chem. Phys.*, 101:3671, 1994.
- [115] J. Dai and J. Z. H. Zhang. Time-dependent wave packet approach to state-to-state reactive scattering and application to $\text{H} + \text{O}$ reaction. *J. Phys. Chem.*, 100:6898, 1996.
- [116] S. Garashchuk and D. J. Tannor. Correlation function formulation for the state selected total reaction probability. *J. Chem. Phys.*, 109:3028, 1998.
- [117] D. J. Tannor and S. Garashchuk. Semiclassical calculation of chemical reaction dynamics via wavepacket correlation functions. *Annu. Rev. Phys. Chem.*, 51:553, 2000.
- [118] S. C. Althorpe. Quantum scattering calculations on chemical reactions. *Annu. Rev. Phys. Chem.*, 54:493, 2003.
- [119] C. Kreisbeck, T. Kramer, S. S. Buchholz, S. F. Fischer, U. Kunze, D. Reuter, and A. D. Wieck. Phase shifts and phase π jumps in four-terminal waveguide Aharonov-Bohm interferometers. *Phys. Rev. B*, 82:165329, 2010.
- [120] V. Krueckl and K. Richter. Switching spin and charge between edge states in topological insulator constrictions. *Phys. Rev. Lett.*, 107:086803, 2011.
- [121] Y. Aharonov and D. Bohm. Significance of electromagnetic potentials in the quantum theory. *Phys. Rev.*, 115:485, 1959.

-
- [122] G. Cernicchiaro, T. Martin, K. Hasselbach, D. Mailly, and A. Benoit. Channel interference in a quasiballistic Aharonov-Bohm experiment. *Phys. Rev. Lett.*, 79:273, 1997.
- [123] S. Pedersen, A. E. Hansen, A. Kristensen, C. B. Sørensen, and P. E. Lindelof. Observation of quantum asymmetry in an Aharonov-Bohm ring. *Phys. Rev. B*, 61:5457, 1999.
- [124] L. C. Mur, C. J. P. M. Harmans, and W. G. van der Wiel. Competition between h/e and $h/2e$ oscillations in a semiconductor Aharonov-Bohm interferometer. *New J. Phys.*, 10:073031, 2008.
- [125] A. Yacoby, M. Heiblum, D. Mahalu, and H. Shtrikman. Coherence and phase sensitive measurements in a quantum dot. *Phys. Rev. Lett.*, 74:4047, 1995.
- [126] R. Schuster, E. Buks, M. Heiblum, D. Mahalu, V. Umansky, and H. Shtrikman. Phase measurement in a quantum dot via a double-slit interference experiment. *Nature*, 385:417, 1997.
- [127] M. Avinun-Kalish, M. Heiblum, O. Zarchin, D. Mahalu, and V. Umansky. Crossover from 'mesoscopic' to 'universal' phase for electron transmission in quantum dots. *Nature*, 436:529, 2005.
- [128] D. C. Langreth. Friedel sum rule for Anderson's model of localized impurity states. *Phys. Rev.*, 150:516, 1966.
- [129] G. Hackenbroich. Phase coherent transmission through interacting mesoscopic systems. *Physics Reports*, 343:463, 2001.
- [130] R. A. Molina, R. A. Jalabert, D. Weinmann, and P. Jacquod. Scattering phase of quantum dots: Emergence of universal behavior. *Phys. Rev. Lett.*, 108:076803, 2012.
- [131] Analysis of the phase lapse problem in closed interferometers. *Phys. Lett. A*, in press, 2012.
- [132] Y. Oreg. Universal phase lapses in a noninteracting model. *New J. Phys.*, 9:122, 2007.
- [133] D. I. Golosov and Y. Gefen. Transmission through quantum dots: Focus on phase lapses. *Phys. Rev. B*, 74:205316, 2006.
- [134] K. Kobayashi, H. Aikawa, S. Katsumoto, and Y. Iye. Probe-configuration-dependent decoherence in an Aharonov-Bohm ring. *J. Phys. Soc. Jpn.*, 71:2094, 2002.

- [135] S. S. Buchholz, S. F. Fischer, U. Kunze, M. Bell, D. Reuter, and A. D. Wieck. Control of the transmission phase in an asymmetric four-terminal Aharonov-Bohm interferometer. *Phys. Rev. B*, 82:045432, 2010.
- [136] Y. Gefen, Y. Imry, and M. Ya. Azbel. Quantum oscillations and the Aharonov-Bohm effect for parallel resistors. *Phys. Rev. Lett.*, 52:129, 1984.
- [137] M. Büttiker, Y. Imry, and M. Ya. Azbel. Quantum oscillations in one-dimensional normal-metal rings. *Phys. Rev. A*, 30:1982, 1984.
- [138] P. Vasilopoulos, O. Kálmán, F. M. Peeters, and M. G. Benedict. Aharonov-Bohm oscillations in a mesoscopic ring with asymmetric arm-dependent injection. *Phys. Rev. B*, 75:035304, 2007.
- [139] E. R. Hedin, Y. S. Joe, and A. M. Satanin. Resonance and phase shift in an open Aharonov-Bohm ring with an embedded quantum dot. *J. Phys. Condens. Matter*, 21:015303, 2009.
- [140] Y. Ying, G. Jin, and Y.-Q. Ma. Transmission phase and spin filter effect in a four-terminal interferometer. *Europhys. Lett.*, 84:67012, 2008.
- [141] M. L. Ladrón de Guevara, G. A. Lara, and P. A. Orellana. Quantum interference effects in two double quantum dots-molecules embedded in an Aharonov-Bohm ring. *Physica E*, 42:1637, 2010.
- [142] S. S. Buchholz, S. F. Fischer, U. Kunze, D. Reuter, and A. D. Wieck. Non-local Aharonov-Bohm conductance oscillations in an asymmetric quantum ring. *Appl. Phys. Lett.*, 94:022107, 2009.
- [143] G. Hernandez. *Fabry-Perot interferometers*. Cambridge Studies in Modern Optics Vol.3 (Cambridge University Press), 1998.
- [144] C. B. Field, M. J. Behrenfeld, J. T. Randerson, and P. Falkowski. Primary production of the biosphere: Integrating terrestrial and oceanic components. *Science*, 281:237, 1998.
- [145] J. C. Pommerville. *Alcamo's fundamentals of microbiology*. Jones and Bartlett Publishers, 2010.
- [146] T. A. Evans and J. J. Katz. Evidence for 5- and 6-coordinated magnesium in bacterio-chlorophyll *a* from visible absorption spectroscopy. *Biochim. Biophys. Acta*, 396:414, 1975.
- [147] J. M. Olson and J. P. Pedersen. Bacteriochlorophyll-c monomers, dimers, and higher aggregates in dichlormethane, chloroform, and carbon-tetrachloride. *Photosynth. Res.*, 25:25, 1990.

-
- [148] H. J. Trurnit and G. Colmano. Chloroplast studies: I. absorption spectra of chlorophyll monolayer at liquid interfaces. *Biochim. Biophys. Acta*, 31:434, 1959.
- [149] P. Hugenholtz, C. Pitulle, K. L. Hershberger, and N. R. Pace. Novel division level bacterial diversity in a yellowstone hot spring. *J. Bacteriol.*, 180:366, 1998.
- [150] D. M. Ward, M. J. Ferris, S. C. Nold, and M. M. Beteson. A natural view of microbial biodiversity within hot spring cyanobacterial mat communities. *Microbiol. Mol. Biol. Rev.*, 62:1353, 1998.
- [151] A. K. Manske, J. Glaeser, M. M. M. Kuypers, and J. Overmann. Physiology and phylogeny of green sulfur bacteria forming a monospecific phototrophic assemblage at a depth of 100 meters in the black sea. *Appl. Environ. Microbiol.*, 71:8049, 2005.
- [152] A. J. Hoff and J. Deisenhofer. Photophysics of photosynthesis. structure and spectroscopy of reaction centers of purple bacteria. *Photosynth. Res.*, 287:1, 1997.
- [153] G. Hauska, T. Schoedl, H. Remigy, and G. Tsiotis. The reaction center of green sulfur bacteria. *Biochim. Biophys. Acta*, 1507:260, 2001.
- [154] P. C. Nelson. *Biological physics*. W. H. Freeman and Company, 2004.
- [155] J. P. Allen and J. C. Williams. Photosynthetic reaction centers. *FEBS Lett.*, 438:5, 1998.
- [156] B. W. Matthews, R. E. Fenna, Bolognesi M. C., and M. F. Schmid. Structure of bacteriochlorophyll *a*-protein from the green photosynthetic bacterium *prothecochloris aestuarii*. *J. Mol. Biol.*, 131:259, 1979.
- [157] J. M. Olson. The FMO protein. *Photosynth. Res.*, 80:181, 2004.
- [158] J. Wen, H. Zhang, M. L. Gross, and R. E. Blankenship. Membrane orientation of the FMO antenna protein from *Chlorobaculum tepidum* as determined by mass spectrometry-based footprinting. *Proc. Natl. Acad. Sci.*, 106:6134, 2009.
- [159] A. Ben-Shem, F. Frolov, and N. Nelson. Evolution of photosystem I - from symmetry through pseudosymmetry to asymmetry. *FEBS Lett.*, 564:274, 2004.

- [160] D. E. Tronrud, J. Wen, L. Gay, and R. E. Blankenship. The structural basis for the difference in absorbance spectra for the FMO antenna protein from various green sulfur bacteria. *Photosynth. Res.*, 100:79, 2009.
- [161] J. A. Leegwater. Coherent versus incoherent energy transfer and trapping in photosynthetic antenna complexes. *J. Phys. Chem.*, 100:14403, 1996.
- [162] T. Ritz, S. Park, and K. Schulten. Kinetics of excitation migration and trapping in the photosynthetic unit of purple bacteria. *J. Phys. Chem. B*, 105:8259, 2001.
- [163] H. van Amerongen, L. Valkunas, and R. van Grondelle. *Photosynthetic excitons*. World Scientific Publishing Co. Pte. Ltd., 2000.
- [164] S. I. E. Vulto, M. A. de Baat, S. Neerken, F. R. Nowak, H. van Amerongen, J. Amesz, and Aartsma T. J. Excited state dynamics in FMO antenna complexes from photosynthetic green sulfur bacteria: A kinetic model. *J. Phys. Chem. B*, 103:8153, 1999.
- [165] J. Overmann and C. Tuschak. Phylogeny and molecular fingerprinting of green sulfur bacteria. *Arch. Microbiol*, 167:302, 1997.
- [166] A. Ishizaki and G. R. Fleming. On the adequacy of the Redfield equation and related approaches to the study of quantum dynamics in electronic energy transfer. *J. Chem. Phys.*, 130:234110, 2009.
- [167] T. Renger and V. May. Ultrafast exciton motion in photosynthetic antenna systems: The FMO-complex. *J. Phys. Chem. A*, 102:4381, 1998.
- [168] A. V. Pisiakov, T. Mancal, and G. R. Fleming. Two-dimensional optical three-pulse photon echo spectroscopy. II. Signatures of coherent electronic motion and exciton population transfer in dimer two-dimensional spectra. *J. Chem. Phys.*, 124:234505, 2006.
- [169] F. Milota, J. Sperling, A. Nemeth, D. Abramavicius, S. Mukamel, and H. F. Kauffmann. Excitonic couplings and interband energy transfer in a double-wall molecular aggregate imaged by coherent two-dimensional electronic spectroscopy. *J. Chem. Phys.*, 131:054510, 2009.
- [170] P. Rebentrost and A. Aspuru-Guzik. Communication: Exciton-phonon information flow in the energy transfer process of photosynthetic complexes. *J. Chem. Phys.*, 134:101103, 2011.
- [171] Y. Yan, F. Yang, Y. Liu, and J. Shao. Hierarchical approach based on stochastic decoupling to dissipative systems. *Chem. Phys. Lett.*, 395:216, 2004.

-
- [172] R.-X. Xu, P. Cui, X.-Q. Li, Y. Mo, and Y. Yan. Exact quantum master equation via the calculus on path integrals. *J. Chem. Phys.*, 122:041103, 2005.
- [173] A. Ishizaki and Y. Tanimura. Quantum dynamics of system strongly coupled to low-temperature colored noise bath: Reduced hierarchy equations approach. *J. Phys. Soc. Jpn.*, 74:3131, 2005.
- [174] A. Ishizaki and G. R. Fleming. Unified treatment of quantum coherent and incoherent hopping dynamics in electronic energy transfer: Reduced hierarchy equation approach. *J. Chem. Phys.*, 130:234111, 2009.
- [175] Y. Tanimura. Stochastic Liouville, Langevin, Fokker-Planck, and Master equation approaches to quantum dissipative systems. *J. Phys. Soc. Jpn.*, 75:082001, 2006.
- [176] Q. Shi, L. Chen, G. Nan, R.-X. Xu, and Y. Yan. Efficient hierarchical Liouville space propagator to quantum dissipative dynamics. *J. Chem. Phys.*, 130:084105, 2009.
- [177] J. Zhu, S. Kais, P. Rebentrost, and A. Aspuru-Guzik. Modified scaled hierarchical equation of motion approach for the study of quantum coherence in photosynthetic complexes. *J. Phys. Chem. B*, 115:1531, 2011.
- [178] L. Chen, R. Zheng, Q. Shi, and Y.-J. Yan. Two-dimensional electronic spectra from the hierarchical equations of motion method: Application to model dimers. *J. Chem. Phys.*, 132:024505, 2010.
- [179] J. Xu, R.-X. Xu, D. Abramavicius, H.-D. Zhang, and Y.-J. Yan. Advancing hierarchical equations of motion for efficient evaluation of coherent two-dimensional spectroscopy. *Chin. J. Chem. Phys.*, 24:497, 2011.
- [180] A. G. Dijkstra and Y. Tanimura. Non-Markovian entanglement dynamics in the presence of system-bath coherence. *Phys. Rev. Lett.*, 104:250401, 2010.
- [181] J. Hu, R.-X. Xu, and Y. Yan. Communication: Padé spectrum decomposition of Fermi function and Bose function. *J. Chem. Phys.*, 133:101106, 2010.
- [182] J. Hu, M. Luo, F. Jiang, R.-X. Xu, and Y. Yan. Padé spectrum decompositions of quantum distribution functions and optimal hierarchical equations of motion construction for quantum open systems. *J. Chem. Phys.*, 134:244106, 2011.

- [183] A. Ishizaki and G. R. Fleming. Quantum coherence in photosynthetic light harvesting. *Annu. Rev. Condens. Matter Phys.*, 3:10.1, 2012.
- [184] U. Zürcher and P. Talkner. Quantum-mechanical harmonic chain attached to heat baths. I. Equilibrium properties. *Phys. Rev. A*, 42:3267, 1990.
- [185] P. Rebentrost, R. Chakraborty, and A. Aspuru-Guzik. Non-markovian quantum jumps in excitonic energy transfer. *J. Chem. Phys.*, 131:184102, 2009.
- [186] R. van Grondelle and V. I. Novoderezhkin. Quantum design for a light trap. *Nature*, 463:614, 2010.
- [187] N. Shenvi, J. Kempe, and K. B. Whaley. Quantum random-walk search algorithm. *Phys. Rev. A*, 67:052307, 2003.
- [188] J. Cao and R. J. Silbey. Optimization of exciton trapping in energy transfer processes. *J. Phys. Chem. A*, 113:13825, 2009.
- [189] M. O. Scully and S. Zubairy. *Quantum optics*. Cambridge University Press, 1997.
- [190] F. Fassioli, A. Nazir, and A. Olaya-Castro. Quantum state tuning of energy transfer in a correlated environment. *J. Phys. Chem. Lett.*, 1:2139, 2010.
- [191] W. K. Wootters. Entanglement of formation of an arbitrary state of two qubits. *Phys. Rev. Lett.*, 80:2245, 1998.
- [192] M. Tiersch, S. Popescu, and H. J. Briegel. A critical view on transport and entanglement in models of photosynthesis. *Phil. Trans. R. Soc. A*, 370:3771.
- [193] J. Yuen-Zhou and A. Aspuru-Guzik. Quantum process tomography of excitonic dimers from two-dimensional electronic spectroscopy. I. General theory and application to homodimers. *J. Chem. Phys.*, 134:134505, 2011.
- [194] S. Mukamel and R. F. Loring. Nonlinear response function for time-domain and frequency-domain four-wave mixing. *J. Opt. Soc. Am. B*, 3:595, 1985.
- [195] P. Hamm. Principles of nonlinear optical spectroscopy: A practical approach. <http://www.mitr.p.lodz.pl/evu/lectures/Hamm.pdf>, 2005.
- [196] D. Abramavicius, B. Palmieri, D. V. Voronine, F. Šanda, and S. Mukamel. Coherent multidimensional optical spectroscopy of excitons in molecular aggregates; quasiparticle versus supermolecule perspectives. *Chem. Rev.*, 109:2350, 2009.

-
- [197] G. Panitchayangkoon, D. V. Voronine, D. Abramavicius, J. R. Caram, N. H. C. Lewis, S. Mukamel, and G. S. Engel. Direct evidence of quantum transport in photosynthetic light-harvesting complexes. *Proc. Natl. Acad. Sci.*, 108:20908, 2011.
- [198] B. Brüggemann, P. Kjellberg, and T. Pullerits. Non-perturbative calculation of 2d spectra in heterogeneous systems: Exciton relaxation in the FMO complex. *Chem. Phys. Lett.*, 444:192, 2007.
- [199] C. Olbrich, J. Strümpfer, K. Schulten, and U. Kleinekathöfer. Theory and simulation of the environmental effects on FMO electronic transitions. *J. Phys. Chem. Lett.*, 2:1771, 2011.
- [200] M. Thorwart, J. Eckel, J. H. Reina, P. Nalbach, and S. Weiss. Enhanced quantum entanglement in the non-Markovian dynamics of biomolecular excitons. *Chem. Phys. Lett.*, 478:234, 2009.
- [201] U. Weiss. *Quantum dissipative systems*. World Scientific Publishing Co. Pte. Ltd., 3rd edition, 2008.
- [202] D. B. Kirk and W. W. Hwu. *Programming Massively Parallel Processors: A Hands-on Approach*. Elsevier, 2010.
- [203] D. Gülen. Interpretation of the excited-state structure of the Fenna-Matthews-Olson pigment protein complex of *Prosthecochloris aestuarii* based on the simultaneous simulation of the 4 K absorption, linear dichroism, and singlet-triplet absorption difference spectra: A possible excitonic explanation? *J. Phys. Chem.*, 100:17683, 1996.
- [204] V. V. Mitin, V. A. Kochelap, and M. A. Strosio. *Introduction to nano-electronics: Science, nanotechnology, engineering, and applications*. Cambridge University Press, 2008.
- [205] L. P. Kadanoff and G. Baym. *Quantum statistical mechanics*. W. A. Benjamin, 1962.
- [206] L. V. Keldysh. Diagram technique for nonequilibrium processes. *Sov. Phys. JETP*, 20:1018, 1965.
- [207] R. A. Craig. Perturbation expansion for real-time Green's functions. *J. Math. Phys.*, 9:605, 1968.
- [208] D. S. Fisher and P. A. Lee. Relation between conductivity and transmission matrix. *Phys. Rev. B*, 23:6851, 1981.

- [209] T. Kramer. *Matter waves from localized sources in homogeneous force fields*. Dissertation, Technische Universität München, 2003.
- [210] David J. Tannor. *Introduction to quantum mechanics: A time-dependent perspective*. University Science Books, 2007.
- [211] J. A. Jr. Fleck, J. R. Morris, and M. D. Feit. Time-dependent propagation of high energy laser beams through the atmosphere. *J. Comp. Phys.*, 47:412, 1982.
- [212] M. D. Feit, J. A. Jr. Fleck, and A. Steiger. Solution of the Schrödinger equation by a spectral method. *J. Comp. Phys.*, 47:412, 1982.
- [213] H. Tal-Ezer and R. Kosloff. An accurate and efficient scheme for propagating the time dependent Schrödinger equation. *J. Chem. Phys.*, 81:3967, 1984.
- [214] C. Leforestier, R. H Bisseling, C. Cerjan, M. D. Feit, R. Friesner, A. Guldborg, A. Hammerich, G. Jolicard, W. Karrlein, H.-D. Meyer, N. Lipkin, O. Roncero, and R. Kosloff. A comparison of different propagation schemes for the time dependent Schrödinger equation. *J. Comput. Phys.*, 94:59, 1991.
- [215] A. G. Borisov and S. V. Shabanov. Wave packet propagation by the Faber polynomial approximation in electrodynamics of passive media. *J. Comput. Phys.*, 216:391, 2006.
- [216] E. J. Heller, K. E. Aidala, B. J. LeRoy, A. C. Bleszynski, A. Kalben, R. M. Westervelt, K. D. Maranowski, and A. C. Gossard. Thermal averages in a quantum point contact with a single coherent wave packet. *Nano Lett.*, 5:1285, 2005.
- [217] B. Szafran and F. M. Peeters. Time-dependent simulations of electron transport through a quantum ring: Effect of the Lorentz force. *Phys. Rev. B*, 72:165301, 2005.
- [218] A. Chaves, G. A. Farias, F. M. Peeters, and B. Szafran. Wave packet dynamics in semiconductor quantum rings of finite width. *Phys. Rev. B*, 80:125331, 2009.
- [219] R. Kalina, B. Szafran, S. Bednarek, and F. M. Peeters. Magnetic-field asymmetry of electron wave packet transmission in bent channels capacitively coupled to a metal gate. *Phys. Rev. Lett.*, 102:066807, 2009.
- [220] V. Krueckl and T. Kramer. Revivals of quantum wave packets in graphene. *New. J. Phys.*, 11:093010, 2009.

-
- [221] T. Kramer, C. Kreisbeck, V. Krueckl, E. J. Heller, R. E. Parrott, and C.-T. Liang. Theory of the quantum Hall effect in finite graphene devices. *Phys. Rev. B*, 81:081410(R), 2010.
- [222] B. Donner and M. Kleber. A simple method for simulating scanning tunneling images. *Am. J. Phys.*, 73:690, 2005.
- [223] T. Kramer, C. Kreisbeck, and V. Krueckl. Wave packet approach to transport in mesoscopic systems. *Phys. Scr.*, 82:038101, 2010.
- [224] H. Bauke and C. H. Keitel. Accelerating the Fourier split operator method via graphics processing units. *Comp. Phys. Comm.*, 182:2454, 2011.
- [225] R. Kosloff and D. Kosloff. Absorbing boundaries for wave propagation problems. *J. Comp. Phys.*, 63:363, 1986.
- [226] U. V. Riss and H.-D. Meyer. Investigation on the reflection and transmission properties of complex absorbing potentials. *J. Chem. Phys.*, 105:1409, 1996.
- [227] Jäckle A. and H.-D. Meyer. Time-dependent calculation of reactive flux employing complex absorbing potential: General aspects and application within the multiconfiguration time-dependent Hartree wave approach. *J. Chem. Phys.*, 105:6778, 1996.
- [228] NVIDIA. CUFFT Library. http://developer.download.nvidia.com/compute/DevZone/docs/html/CUDALibraries/doc/CUFFT_Library.pdf, 2011.
- [229] M. Harris. Optimizing parallel reduction in CUDA. http://developer.download.nvidia.com/compute/cuda/1_1/Website/projects/reduction/doc/reduction.pdf, 2011.
- [230] M. Zaffalon, A. Bid, M. Heiblum, D. Mahalu, and V. Umansky. Transmission phase of a singly occupied quantum dot in the Kondo regime. *Phys. Rev. Lett.*, 100:226601, 2008.
- [231] B. L. Altshuler, A. G. Aronov, and B. Z. Spivak. The Aharonov-Bohm effect in disordered conductors. *JETP Lett.*, 33:94, 1981.
- [232] L. Onsager. Reciprocal relations in irreversible processes. II. *Phys. Rev.*, 38:22659, 1931.
- [233] J. Wurm, M. Wimmer, H. U. Baranger, and K. Richter. Graphene rings in magnetic fields: Aharonov-Bohm effect and valley splitting. *Semicond. Sci. Technol.*, 25:034003, 2010.

- [234] Y. Yamauchi, M. Hashisaka, S. Nakamura, K. Chida, S. Kasai, T. Ono, R. Leturcq, K. Ensslin, D. C. Driscoll, A. C. Gossard, and K. Kobayashi. Universality of bias- and temperature-induced dephasing in ballistic electronic interferometers. *Phys. Rev. B*, 79:161306, 2009.
- [235] T. Ihn, M. Sigrist, K. Ensslin, W. Wegscheider, and M. Reinwald. Interference in a quantum dot molecule embedded in a ring interferometer. *New J. Phys.*, 9:1367, 2007.
- [236] S. S. Buchholz, U. Kunze, D. Reuter, A. D. Wieck, and S. F. Fischer. Mode-filtered electron injection into a waveguide interferometer. *Appl. Phys. Lett.*, 98:102111, 2011.
- [237] A. F. Fidler, J. R. Caram, D. Hayes, and G. S. Engel. Towards a coherent picture of excitonic coherence in the Fenna-Matthews-Olson complex. *J. Phys. B*, 45, 2012.
- [238] H. P. Breuer and F. Petruccione. *The theory of open quantum systems*. Oxford University Press, 2002.

Acknowledgements

While working on this thesis I have been supported by many people. Now it is time to thank all of them.

First and foremost, I would like to express my gratitude to *Dr. Tobias Kramer* for being such a supportive and encouraging advisor. He knows the perfect balance between giving guidance, and leaving me free to develop my own ideas. I enjoyed our numerous discussions and informal group meetings, as well as the frequent opportunities to gain insight into the world of science at international conferences.

Many thanks to *Prof. Dr. Thomas Niehaus* for writing a report on my thesis, and to *Prof. Dr. Milena Grifoni* and *Prof. Dr. John Lupton* for their willingness to join my doctoral committee.

I would like to thank my colleague *Dr. Birgit Hein* for her helpful contribution to the evaluation of 2d-spectra. I really enjoyed our time together as office mates.

I am happy about the fruitful collaboration with the group of *Prof. Dr. Ulrich Kunze* at Ruhr-Universität Bochum. In particular, I thank *Prof. Dr. Saskia Fischer* and *Dr. Sven Buchholz* for sharing their experimental data, and for many helpful discussions.

The collaboration with *Dr. Mirta Rodríguez* and *Dr. Rafael Molina* from the Instituto de Estructura de la Materia - CSIC in Madrid was supported by the *DAAD-project 50240755*, which is thankfully acknowledged.

Part of the computations of 2d-spectra was done on the *Harvard SEAS "Resonance" GPU cluster*. I am grateful to the SEAS computing team for providing these resources.

I appreciate the funding by the *DFG Emmy-Noether program* through the grant KR 2889/2, and thank *Prof. Dr. Klaus Richter* for hosting our research group at Universität Regensburg.

Moreover, I thank the team of *Korrektur+Lektorat*, in particular Jonathan Andrews and Christian Kelly, for their quick response and professional proof-reading.

I am grateful to my *parents* and my *parents-in-law* for their permanent encouragement during the years of my Ph. D. project.

My final thanks go to my wife *Carolín* for her support and love ♥

Publications

- ◇ C. Kreisbeck and T. Kramer, *Long-lived electronic coherence in dissipative exciton-dynamics of light-harvesting complexes*, arXiv:1203.1485 (2012)
- ◇ B. Hein, C. Kreisbeck, T. Kramer and M. Rodríguez, *Modelling of oscillations in two-dimensional echo-spectra of the Fenna-Matthews-Olson complex*, New J. Phys., **14**, 023018 (2012)
- ◇ C. Kreisbeck, T. Kramer, M. Rodríguez and B. Hein, *High-performance solution of hierarchical equations of motion for studying energy transfer in light-harvesting complexes*, J. Chem. Theory Comput., **7**, 2166 (2011)
- ◇ C. Kreisbeck, T. Kramer, S. S. Buchholz, S. F. Fischer, U. Kunze, D. Reuter and A. D. Wieck, *Phase shifts and phase π jumps in four-terminal waveguide Aharonov-Bohm interferometers*, Phys. Rev. B, **82**, 165329 (2010)
- ◇ T. Kramer, C. Kreisbeck and V. Krückl, *Wave packet approach to transport in mesoscopic systems*, Phys. Scr., **82**, 038101 (2010)
- ◇ C. Kreisbeck, F. J. Kaiser and S. Kohler, *Phase readout of a charge qubit capacitively coupled to an open double quantum dot*, Phys. Rev. B, **81**, 125404 (2010)
- ◇ T. Kramer, C. Kreisbeck, V. Krückl, E. J. Heller, R. E. Parrott and C.-T. Liang, *Theory of the quantum Hall effect in finite graphene devices*, Phys. Rev. B, **81**, 081410(R) (2010)

Selected conferences and research visits

Quantum biology

- ◇ Workshop on quantum effects in biological systems (QuEBS 2012), University of California at Berkeley, USA, June 4 - 8, 2012 (poster)
- ◇ Research visit to Harvard University, USA, April 18 - 22, 2012 (talk)
- ◇ Research visit to Instituto de Estructura de la Materia - CSIC, Madrid, Spain, October 24 - 30, 2011 and September 12 - 24, 2010 (talk)
- ◇ 489. Wilhelm and Else Heraeus-Seminar, Quantum effects in biological systems (QuEBS 2011), Universität Ulm, Germany, August 1 - 5, 2011 (poster)
- ◇ CECAM-Workshop, Spectroscopy and quantum phenomena in large molecular aggregates, Universität Bremen, Germany, June 27 - July 1, 2011 (poster)
- ◇ Workshop on quantum effects in biological systems (QuEBS 2010), Harvard University, USA, June 17 - 20, 2010 (poster)

Mesoscopic physics

- ◇ Aharonov-Bohm effect and Berry phase anniversary 50/25, University of Bristol, UK, December 14 - 15, 2009 (poster)
- ◇ Workshop on semiconductor-nanobalistic, Ruhr-Universität Bochum, Germany, June 25 - 27, 2009 (talk)

DPG spring meetings

- ◇ DPG spring meeting 2011, TU Dresden, Germany, March 13 - 18, 2011 (poster and talk)
- ◇ DPG spring meeting 2010, Universität Regensburg, Germany, March 21 - 26, 2010 (poster and talk)
- ◇ DPG spring meeting 2009, TU Dresden, Germany, March 22 - 27, 2009 (poster and talk)

Christoph Kreisbeck (Dipl. Phys. Univ.)

Kontakt

Anschrift: Gotenstr. 15
93138 Lappersdorf
Telefon: 0941/28005191
E-mail: Christoph.Kreisbeck@physik.uni-r.de

Persönliche Daten

Geburtsdatum: 15.05.1981
Geburtsort: Nördlingen
Staatsangehörigkeit: deutsch
Familienstand: verheiratet

Lebenslauf

- ◇ Wissenschaftlicher Mitarbeiter in der Emmy-Noether Nachwuchsgruppe von Dr. Tobias Kramer am Institut für Theoretische Physik der Universität Regensburg (seit Mai 2008)
- ◇ Promotionsstudium in Physik an der Universität Regensburg (seit Mai 2008)
Titel der Dissertation: *Quantum transport through complex networks - from light-harvesting proteins to semiconductor devices*
Betreuer: Dr. Tobias Kramer
- ◇ Studium der Physik (Diplom) mit Nebenfach Mathematik an der Universität Augsburg (Oktober 2002 - April 2008)
Titel der Diplomarbeit: *Auslesen von Ladungsqubits mit Hilfe eines Zweiniveau-Einzelelektronentransistors*
Betreuer: PD. Dr. Sigmund Kohler
Abschlussnote: 1.00
- ◇ Hans-Leipelt Berufsoberschule Donauwörth (September 2000 - Juli 2002)
Abschluss: Allgemeine Hochschulreife
- ◇ Ausbildung zum Industriemechaniker bei AGCO Bäumenheim (September 1997 - Juli 2000)
- ◇ Realschule Hl. Kreuz Donauwörth (September 1991 - August 1997)
Abschluss: Mittlere Reife